3-30-2012

Efficiency and Power Density Improvement of Grid-Connected Hybrid Renewable Energy Systems utilizing High Frequency-Based Power Converters

Mahmoud Amin
Florida International University, mneam001@fiu.edu

DOI: 10.25148/etd.FI12050211

FLORIDA INTERNATIONAL UNIVERSITY

Miami, Florida

EFFICIENCY AND POWER DENSITY IMPROVEMENT OF GRID-CONNECTED HYBRID RENEWABLE ENERGY SYSTEMS UTILIZING HIGH FREQUENCY-BASED POWER CONVERTERS

A dissertation submitted in partial fulfillment of

the requirements for the degree of

DOCTOR OF PHILOSOPHY

in

ELECTRICAL ENGINEERING

by

Mahmoud Amin

2012

To: Dean Amir Mirmiran
College of Engineering and Computing

This dissertation, written by Mahmoud Amin, and entitled Efficiency and Power Density Improvement of Grid-Connected Hybrid Renewable Energy Systems utilizing High Frequency-Based Power Converters, having been approved in respect to style and intellectual content, is referred to you for judgment.

We have read this dissertation and recommend that it be approved.

_____
Nezih Pala

_____
Mark Roberts

_____
Berrin Tansel

_____
Jean Andrian

_____
Osama A. Mohammed, Major Professor

Date of Defense: March 30, 2012

The dissertation of Mahmoud Amin is approved.

_____
Dean Amir Mirmiran
College of Engineering and Computing

_____
Dean Lakshmi N. Reddi
University Graduate School

Florida International University, 2012

DEDICATION

If this research is well organized, accomplished, and written, it is due mostly to the prayer of my parents, and their continuous encouragement. I dedicate this dissertation to my wife, Heba Moussa and my daughter, Sana Amin. Without their patience, understanding, support, sacrifice, and most of all love, the completion of this work would not have been possible.

ACKNOWLEDGMENTS

First and foremost, I would like to give my sincere appreciation and thanks to my major Professor Dr. Osama A. Mohammed for his support, guidance, expert assistance and significant contributions through the period of the research and dissertation development, without which this dissertation would not have been possible. I will always remember his belief in my abilities to work hard work to produce at a high level. I do appreciate Professor Mohammed's many constructive suggestions while the material was being developed and tested in the lab. I am indebted for his willingness to accept me in his laboratory and for providing significant research facilities to develop this work in addition to his expert guidance and continued assistance, without which, I wouldn't have been able to successfully accomplish my experimental work. I also thank Professor Mohammed for his tremendous efforts in reading and correcting this dissertation. His gentle but firm direction and guidance are most appreciated.

I wish to also thank the members of my committee for their support, patience and valuable discussions, in particular, Dr. Nezih Pala, Dr. Mark Roberts, Dr. Berrin Tansel, and Dr. Jean Andrian.

I would like to acknowledge the research support provided through the projects funded by the Office of Naval Research and the US Department of Energy throughout my years of dissertation research. I also acknowledge the dissertation year fellowship from the FIU graduate school during the last year of dissertation research.

I would like to give thanks to all my colleagues at the Energy Systems Research Laboratory of the Electrical and Computer Engineering Department, especially the undergraduate and graduate student interns who helped me with some of the test setups. I do appreciate all of my other colleagues with whom I had many fruitful discussions.

ABSTRACT OF THE DISSERTATION

EFFICIENCY AND POWER DENSITY IMPROVEMENT OF

GRID-CONNECTED HYBRID RENEWABLE ENERGY SYSTEMS

UTILIZING HIGH FREQUENCY-BASED POWER CONVERTERS

by

Mahmoud Amin

Florida International University, 2012

Miami, Florida

Professor Osama A. Mohammed, Major Professor

High efficiency of power converters placed between renewable energy sources and the utility grid is required to maximize the utilization of these sources. Power quality is another aspect that requires large passive elements (inductors, capacitors) to be placed between these sources and the grid. The main objective is to develop higher-level high frequency-based power converter system (HFPCS) that optimizes the use of hybrid renewable power injected into the power grid. The HFPCS provides high efficiency, reduced size of passive components, higher levels of power density realization, lower harmonic distortion, higher reliability, and lower cost.

The dynamic modeling for each part in this system is developed, simulated and tested. The steady-state performance of the grid-connected hybrid power system with battery storage is analyzed. Various types of simulations were performed and a number of algorithms were developed and tested to verify the effectiveness of the power conversion topologies. A modified hysteresis-control

strategy for the rectifier and the battery charging/discharging system was developed and implemented. A voltage oriented control (VOC) scheme was developed to control the energy injected into the grid. The developed HFPCS was compared experimentally with other currently available power converters. The developed HFPCS was employed inside a microgrid system infrastructure, connecting it to the power grid to verify its power transfer capabilities and grid connectivity. Grid connectivity tests verified these power transfer capabilities of the developed converter in addition to its ability of serving the load in a shared manner.

In order to investigate the performance of the developed system, an experimental setup for the HF-based hybrid generation system was constructed. We designed a board containing a digital signal processor chip on which the developed control system was embedded. The board was fabricated and experimentally tested. The system's high precision requirements were verified. Each component of the system was built and tested separately, and then the whole system was connected and tested. The simulation and experimental results confirm the effectiveness of the developed converter system for grid-connected hybrid renewable energy systems as well as for hybrid electric vehicles and other industrial applications.

TABLE OF CONTENTS

LIST OF TABLES

LIST OF FIGURES

LIST OF ACRONYMS

ACRONYM	DETAILS
HFPCS	High Frequency Power Converter System
DG	Distributed Generation
SMES	Superconducting Magnetic Energy Storage
CAES	Compressed Air Energy Storage
AC	Alternating Current
DC	Direct Current
PWM	Pulse Width Modulation
ASD	Adjustable Speed Drive
UPS	Uninterruptible Power Supply
IGBT	Insulated Gate Bipolar Transistor
VSI	Voltage Source Inverter
CSI	Current Source Inverter
MOSFET	Metal Oxide Silicon Field Effect Transistor
BJT	Bipolar Junction Transistor
SEPIC	Single-ended Primary Inductance Converter
HEV	Hybrid Electric Vehicle
EMS	Energy Management System
NPT	Non-Punch Through
VAR	Voltage-Ampere Reactive
WECS	Wind Energy Conversion System

VSWT	Variable Speed Wind Turbine
DFIG	Double-Fed Induction Generator
WRIG	Wound Rotor Induction Generator
EESG	Electrically-Excited Synchronous Generator
PMs	Permanent Magnets
SEIG	Self-Excited Induction Generator
PMSG	Permanent-Magnet Synchronous Generator
THD	Total Harmonic Distortion
BBR	Bridge Boost Rectifier
PV	Photovoltaic
FC	Fuel Cell
BESS	Battery Energy Storage System
HESS	Hybrid Energy Storage System
VOC	Voltage Oriented Control
VSPM	Variable Speed Prime Mover
SPLL	Software Phase Locked Loop
UPF	Unity Power Factor
PID	Proportional Integral Derivative
SVC	Static VAR Compensator
HF	High Frequency
LF	Low Frequency
EMI	Electromagnetic Interference

PMWGS	Permanent Magnet Wind Generation System
HB	Hysteresis Band
MIBC	Multi-Input Boost Converter
PFC	Power Factor Correction
MIBBC	Multi-Input Bridgeless Boost Converter
BBC	Bridge Boost Converter
BPFCC	Bridgeless Power Factor Correction Converter
RDA	Digital Redesign Approach
DDC	Direct Digital Control
ZOH	Zero-Order-Hold
WAMS	Wide Area Measurement System
PMU	Phasor Measurement Units
PDC	Phasor Data Concentrator
RTSM	Real-Time System Monitoring
RTC	Real-Time Control
HIL	Hardware-in-The loop
DSC	Digital Signal Controller
UPQC	Unified Power Quality Conditioner
GPS	Global Positioning System
DFT	Discrete Fourier Transform
UTP	Unshielded Twisted Pair
SCADA	Supervisory Control and Data Acquisition

LIST OF SYMBOLS

SYMBOL	DESCRIPTION
C_p	The Power Coefficient
λ	The Tip Speed Ratio
ω	The Angular Speed of The Turbine Shaft
V	The Wind Speed
R_t	The Length of each Blade
P_t	The Turbine Mechanical Power
ρ	The Air Density
A	The Area of The Rotor Blades
T_t	The Turbine Torque
C_t	The Torque Coefficient
V_{ds} and V_{qs}	The Generated Voltages along The *d*-axis and *q*-axis, Respectively
T_e	The Electromagnetic Torque
V_{ds} and V_{qs}	The *d*-*q* Stator Voltages, Respectively
i_{ds} and i_{qs}	The *d*-*q* Stator Currents, Respectively
V_{dr} and V_{qr}	The *d*-*q* Rotor Voltages, Respectively
i_{dr} and i_{qr}	The *d*-*q* Rotor Currents, Respectively
p	The Derivative Operator, i.e. $p=d/dt$
K_d and K_q	The Residual Voltage Inside The Induction Generator
V_{cd} and V_{cq}	The Initial Voltages of The Self-Excitation Capacitor Bank
ω_e and ω_r	The Synchronous and Rotor Angular Speed, Respectively

P	The Number of Poles
λ_{dr} and λ_{qr}	The *d-q* Rotor Fluxes, Respectively
λ_{ds} and λ_{qs}	The *d-q* Stator Fluxes, Respectively
C	The External Self-Excitation Capacitance
R_s and L_{ls}	The Resistance and Self Inductance of The Stator, Respectively
R_r and L_{lr}	The Resistance and Self Inductance of The Rotor, Respectively
L_s and L_r	The Stator and Rotor Inductances, Respectively
L_m	The Mutual Inductance
v_d and v_q	The Two-Axis Machine Voltages, Respectively
i_d and i_q	The Two-Axis Machine Currents, Respectively
R_g, L_d, and L_q	The PMSG Resistance and *d-q* Inductances, Respectively
λ_m	The PMSG Flux Linkage Amplitude
I_o	The PV-Cell Output Current
V_o	The PV-Cell Output Voltage
P_o	The PV-Cell Output Power
I_λ	The Photon Current
I_d	The Shockley Temperature-Dependent Diode Current
V_d	The Shockley Temperature-Dependent Diode Voltage
I_p	The PV Cell Leakage Current
λ	The Light Wavelength
I_{sc}	The PV Cell Short-Circuit Current
V_{oc}	The PV Cell Open-Circuit Voltage

R_p	The PV Parallel Resistance
R_s	The PV Series Resistance
R_a	The FC Activation and Concentration Equivalent Resistance
R_r	The FC Membrane and Contact Ohmic Resistance
E_{oc}	The FC Open Circuit Voltage
V_{fc}	The FC Output Voltage Of A Single Cell
P_{fc}	The FC Instantaneous Electrical Power
μ_f	The FC Utilization Factor
V_c	The Output Voltage across The Terminals of Every Single Cell Belonging to The FC Stack
E_0	The Constant Voltage
Exp(s)	The Exponential Zone Dynamics
Sel(s)	The Battery Mode
K	The Polarization Constant or Polarization Resistance
*i**	The Low Frequency Current Dynamics
i	The Battery Current
it	The Extracted Capacity
Q	The Maximum Battery Capacity
E	The Maximum Amplitude of The Generator AC Voltage
R, L	The Line Inductor and Resistance Between Generator and The Converter Terminal, Respectively
e_a, v_a	The Generator Phase Voltage and Converter Voltage, Respectively
i_a, i_c, i_L	The Line, DC-Link Capacitor, and Load Currents, Respectively
i_{dc}, v_{dc}	The DC-Output Current and Controlled Voltage, Respectively

θ	The Rotating Angle of *abc-dq* Transformation
S, P, Q	The Complex, Active, and Reactive Powers, Respectively
K_p^v, K_i^v	The Constant Gains of The PI-Voltage Controller
K_p^i, K_i^i	The Constant Gains of The PI-Current Controllers
$v_d^r(t)$, $v_q^r(t)$	The *d* and *q* Voltage References, Respectively
U_d^v, U_q^v	The *d* and *q* Effective Voltage References, Respectively
F_{osc}, θ_{osc}	Frequency and Phase Angle of VCO, Respectively
F_{ref}, θ_{ref}	Reference Frequency and Phase Angle, Respectively
K_v, K_ϕ, K_f	VCO, Phase Frequency Detector, Filter Gains, Respectively
K_p, K_i	Loop Filter Gains, Respectively
ω_n, ξ	Natural Frequency and Damping Ratio, Respectively
$v_a(t)$, $v_b(t)$, $v_c(t)$	The VSI Phase Potentials
$u_a^g(t)$, $u_b^g(t)$, $u_c^g(t)$	The Utility Grid Phase Potentials
ω_g	The Grid Voltage Angular Frequency
$i_a(t)$, $i_b(t)$, $i_c(t)$	The Currents Flowing from DC-Link to VSI
$P^r(t)$, $Q^r(t)$	The Active and Reactive Power Commands, Respectively
$v_d^r(t)$, $v_q^r(t)$	The *d*-Axis and *q*-Axis Voltage Commands, Respectively
U_d^v, U_q^v	The Effective Voltage Commands, Respectively
$i_d^r(t)$, $i_q^r(t)$	The *d*-Axis and *q*-Axis Current Commands, Respectively
U_d^c, U_d^c	The Effective Current Commands

k_p^c , k_i^c	The PI-Gains of The Capacitor Voltage Controllers, Respectively
$F_s^{\max}$	The Maximum Switching Frequency
h	The HB Magnitude
η	The System Efficiency
P_{in}	The Input Power
P_{out}	The Output Power
P_{loss}	The Total Losses
P_S	The Switch Losses
P_D	The Diode Losses
P_{LC}	The Passive Element Losses
ϕ_m	The Phase Margin
ω_{cz}	The Critical Frequency

Chapter 1 Introduction

Today, the world's energy supply is based largely on fossil fuels and nuclear power. These sources of energy will not last forever and have proved to be a major cause of environmental issues. Environmental effects of energy use are not new, but it is increasingly well known that they range from deforestation to local and global pollution. In less than three centuries since the industrial revolution, humankind has burned away roughly half of the fossil fuels accumulated under earth's surface during hundreds of millions of years. Nuclear power is also based on limited resources such as uranium, and the use of nuclear power creates such incalculable risks that nuclear power plants cannot be insured.

Renewable sources of energy are in line with an overall strategy of sustainable development. They help reduce dependence on energy imports and do not create a dependence on energy imports, thereby ensuring a sustainable security of supply. Furthermore, renewable energy sources can improve the competitiveness of industries, at least in the long run, and have a positive effect on regional development and employment. Renewable energy technologies are suitable for off-grid services; they can serve remote areas of the world without expensive and complicated grid infrastructure.

Integration of renewable energy sources involves integrating in a system any energy resource naturally over a short period of time. This time scale is derived directly from the sun (such as for thermal, photochemical, and photosynthetic energy), indirectly from the sun (such as for wind, hydropower, and photosynthetic energy stored in biomass), or from other natural movements and mechanisms of the environment (such as for geothermal and tidal energy). In the long term, renewable energies will necessarily

dominate the world's energy supply system for the simple reason that there is no alternative. Humankind cannot survive indefinitely off the consumption of finite energy resources, concentrate supplies on some points on earth, or carelessly spread its population over the world.

1.1 Renewable Energy Sources….Overview

Renewable sources such as solar, wind, biomass, geothermal, ocean (wave, and tidal) energy are practically inexhaustible or can be regenerated or recycled. Figure 1.1 shows photographs for renewable source. Next an overview on some renewable energy sources is given [1-3].

1.1.1 Solar

Solar energy, radiant light and heat from the sun, has been harnessed by humans since ancient times using a range of ever-evolving technologies. Solar radiation, along with secondary solar-powered resources such as wind and wave power, hydroelectricity and biomass, account for most of the available renewable energy on earth. Only a minuscule fraction of the available solar energy is used.

Solar powered electrical generation relies on heat engines and photovoltaic. Solar energy's uses are limited only by human ingenuity. A partial list of solar applications includes space heating and cooling through solar architecture, potable water via distillation and disinfection, day-lighting, solar hot water, solar cooking, and high temperature process heat for industrial purposes. To harvest the solar energy, the most common way is to use solar panels.

Solar technologies are broadly characterized as either passive solar or active solar depending on the way they capture, convert and distribute solar energy. Active solar

techniques include the use of photovoltaic panels and solar thermal collectors to harness the energy. Passive solar techniques include orienting a building to the Sun, selecting materials with favorable thermal mass or light dispersing properties, and designing spaces that naturally circulate air.

1.1.2 Wind

The Earth is unevenly heated by the sun, such that the poles receive less energy from the sun than the equator; along with this, dry land heats up (and cools down) more quickly than the seas do. The differential heating drives a global atmospheric convection system reaching from the Earth's surface to the stratosphere which acts as a virtual ceiling. Most of the energy stored in these wind movements can be found at high altitudes where continuous wind speeds of over 160 km/h (99 mph) occur. Eventually, the wind energy is converted through friction into diffuse heat throughout the Earth's surface and the atmosphere.

Wind power is the conversion of wind energy into a useful form of energy, such as using wind turbines to make electricity, wind mills for mechanical power, wind pumps for pumping water or drainage, or sails to propel ships.

At the end of 2009, worldwide nameplate capacity of wind-powered generators was 159.2 gigawatts (GW). Energy production was 340 TWh, which is about 2% of worldwide electricity usage; and is growing rapidly, having doubled in the past three years. Several countries have achieved relatively high levels of wind power penetration (with large governmental subsidies), such as 13% in Spain and Portugal, and 7% in Germany and the Republic of Ireland in 2008. As of May 2009, eighty countries around the world are using wind power on a commercial basis.

Large-scale wind farms are connected to the electric power transmission network; smaller facilities are used to provide electricity to isolated locations. Utility companies increasingly buy back surplus electricity produced by small domestic turbines. Wind energy as a power source is attractive as an alternative to fossil fuels, because it is plentiful, renewable, widely distributed, clean, and produces no greenhouse gas emissions during operation. However, the construction of wind farms is not universally welcomed because of their visual impact and other effects on the environment.

1.1.3 Biomass

Biomass is a biological material derived from living, or recently living organisms, such as wood, waste, (hydrogen) gas, and alcohol fuels. Biomass is commonly plant matter grown to generate electricity or produce heat. In this sense, living biomass can also be included, as plants can also generate electricity while still alive. The most conventional way on how biomass is used however, still relies on direct incineration. Forest residues for example (such as dead trees, branches and tree stumps), yard clippings, wood chips and garbage are often used for this. However, biomass also includes plant or animal matter used for production of fibers or chemicals. Biomass may also include biodegradable wastes that can be burned as fuel. It excludes organic materials such as fossil fuels which are transformed by geological processes into substances such as coal or petroleum.

1.1.4 Geothermal

Geothermal power (from the Greek roots geo, meaning earth, and thermos, meaning heat) is power extracted from heat stored in earth. This geothermal energy originates from the original formation of the planet, from radioactive decay of minerals, and from

solar energy absorbed at the surface. It was used for bathing since Paleolithic times and for space heating since ancient Roman times, but is now better known for generating electricity. Worldwide, about 10,715 megawatts (MW) of geothermal power is online in 24 countries. An additional 28 gigawatts of direct geothermal heating capacity is installed for district heating, space heating, spas, industrial processes, desalination and agricultural applications.

Geothermal power is cost effective, reliable, sustainable, and environmentally friendly, but has historically been limited to areas near tectonic plate boundaries. Recent technological advances have dramatically expanded the range and size of viable resources, especially for applications such as home heating, opening a potential for widespread exploitation.

The Earth's geothermal resources are theoretically more than adequate to supply humanity's energy needs, but only a very small fraction of it may be profitably exploited. Drilling and exploration for deep resources costs tens of millions of dollars, and success is not guaranteed. Forecasts for the future penetration of geothermal power depend on assumptions about technology growth, the price of energy, subsidies, and interest rates.

1.1.5 Ocean Energy

Ocean energy, also referred to as marine renewable energy, marine power, marine energy, and ocean power, refers to the energy carried by ocean waves and tides. The movement of water in the world’s oceans creates a vast store of kinetic energy, or energy in motion. This energy can be harnessed to create electricity to power homes, transport and industries.

The term marine energy encompasses both wave energy and tidal energy obtained from oceans, seas, and, in general, other large bodies of water. Offshore wind energy is also sometimes included under the description of marine energy. Marine energy is similar to hydroelectric power, although that term usually refers to energy generated by dammed rivers or waterfalls.

The oceans have a tremendous amount of energy and are close to many if not most concentrated populations. Many researches show that ocean energy has the potential of providing for a substantial amount of new renewable energy around the world.

1.1.6 Hydro

Hydroelectricity is electricity generated by hydropower, i.e., the production of electrical power through the use of the gravitational force of falling or flowing water. It is the most widely used form of renewable energy. Once a hydroelectric complex is constructed, the project produces no direct waste, and has a considerably lower output level of the greenhouse gas carbon dioxide (CO2) than fossil fuel powered energy plants. Worldwide, an installed capacity of 777 GWe supplied 2998 TWh of hydroelectricity in 2006. This was approximately 20% of the world's electricity, and accounted for about 88% of electricity from renewable sources.

Most hydroelectric power comes from the potential energy of dammed water driving a water turbine and generator. In this case the energy extracted from the water depends on the volume and on the difference in height between the source and the water's outflow. This height difference is called the head. The amount of potential energy in water is proportional to the head. To deliver water to a turbine while maintaining pressure arising from the head, a large pipe called a penstock may be used.

Solar

PV

Wind

Biomass

Geothermal

Wave

Tidal

Hydro

Fig. 1.1 Renewable energy sources

1.2 Energy Storage Systems….Overview

Electrical energy storage has long been considered a critical technology. At the beginning of the twentieth century, electrochemical batteries were used to power telephones and telegraphs, and enormous, heavy flywheels were common in rotating generators to smooth out load oscillations. Electric vehicles were more common than gasoline-powered vehicles. Batteries were important in such transportation applications because they could store energy to give reasonable transportation autonomy to vehicles. Even longer ago, water dams were used to store potential energy.

Today, energy storage systems play the important role of unifying, distributing, and augmenting the capabilities of alternative and renewable energy-distributed generating systems. The average central electrical generation, transmission, and distribution system is large enough not to be affected by residential and commercial load changes. On the other hand, distributed generation (DG) is exposed to the fluctuations of individual loads; it does not experience the averaging effect seen by large generators [4].

Figure 1.2 shows mature and emerging storage technologies organized in categories of ride-through, power quality, and energy management. Applications include lead–acid batteries, advanced batteries, low- and high-energy flywheels, ultra capacitors, superconducting magnetic energy storage (SMES) systems, heating systems, pumped hydro, geothermal underground, and compressed air energy storage (CAES). Hydrogen storage is not included in this section.

1.3 Literature Review

The integration of renewable sources of energy poses a challenge because their output is intermittent and variable and must be stored for use when there is demand. If only one

renewable energy source is considered, the electric power system is simple. The source can be connected to a storage system to deliver electricity for stand-alone use or interconnected with the grid. In the grid-connected application, the grid acts as energy storage. However, if multiple renewable energy sources are used, the electric power system can be rather complex and a microgrid will be formed.

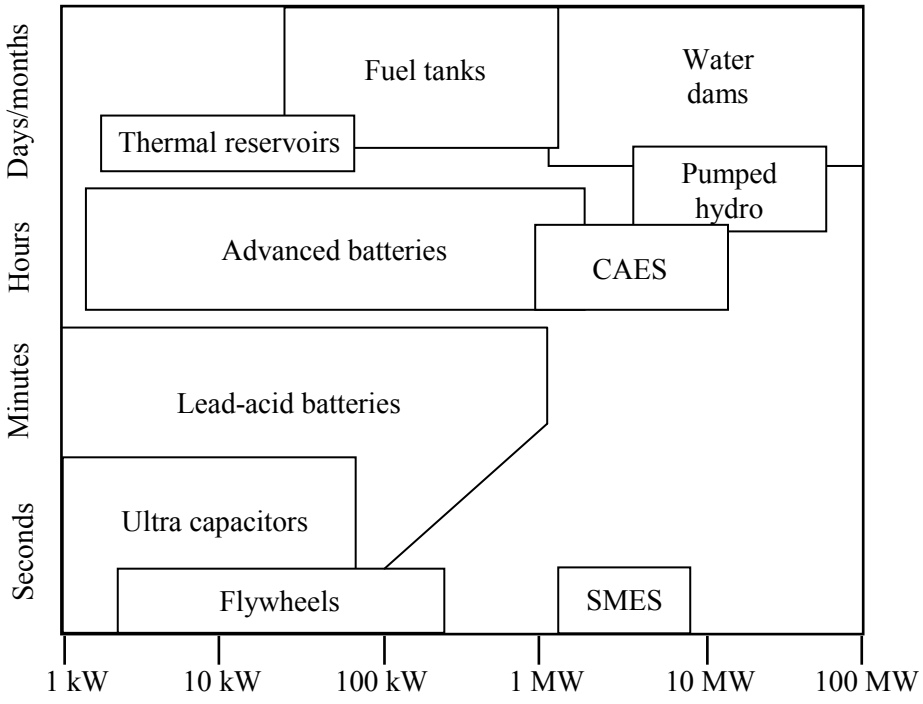

Fig. 1.2 Energy management, power quality, and ride-through storage applications

1.3.1 Converting Technologies

Power electronics is the enabling technology that allows the conversion of energy and injection of power from renewable energy sources to the grid. Therefore, it is suggested that the reader review some background information on power electronics from the technical literature to complement this material. Figure 1.3 illustrates the main electrical conversion technologies required for injection of renewable energy power. If only photovoltaic and fuel cell systems are used, a DC-link bus might be used to aggregate

them. AC power can be integrated through DC–AC conversion (inverter) systems. If only hydro or wind power is used, a variable-frequency AC voltage control must be aggregated into an AC link through an AC–AC conversion system.

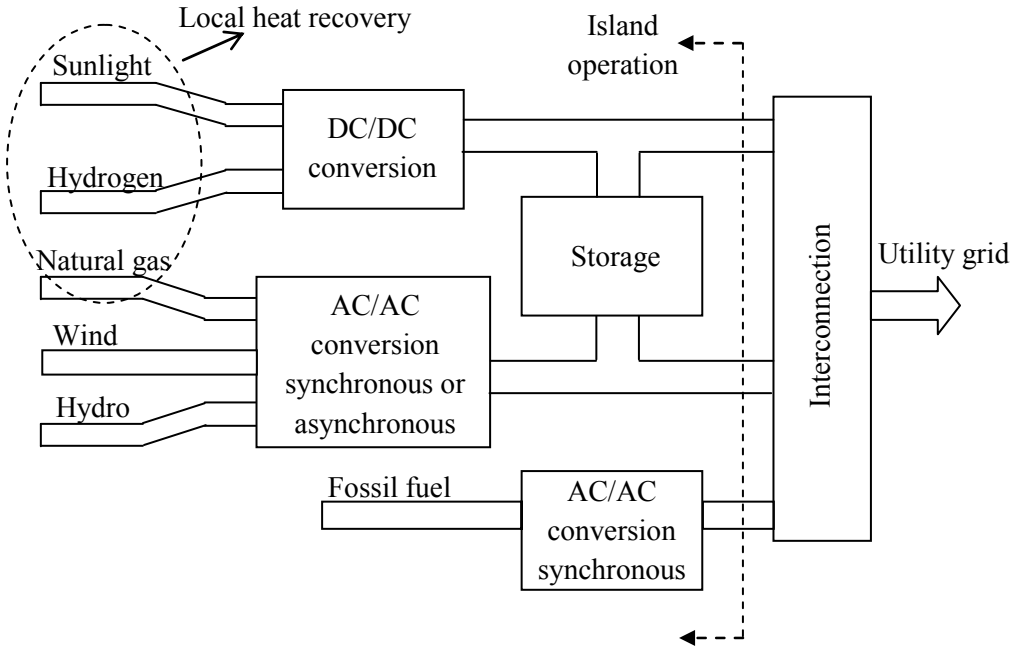

Fig. 1.3 Alternative energy conversion technologies for injection of alternative energy power to the grid

1.3.1.1 AC/DC Power Conversion Topologies

There are several ways for converting the AC power to DC, as a first stage of interfacing with the utility. Commonly, diode rectifiers shown in Fig. 1.4a are used to convert the input AC voltage into DC in an uncontrolled manner. This type of rectifiers has the advantage of being simple, robust and low cost. However, it allows only unidirectional power flow. Therefore, energy returned from the grid must be dissipated on power resistor controlled by chopper connected across the DC link. The diode input circuit also results in lower power factor and draw highly distorted current from the source. Furthermore, a large size DC link capacitor is required for smoothing the DC

voltage. In addition, the diode rectifier is working in uncontrolled manner, thus, the DC output voltage level is strongly depending on the amplitude of the AC input voltage level.

Besides the six-diode bridge rectifier, a few other conversion topologies are known. The topology shown in Fig. 1.4b presents a simple solution of boost type converter with the possibility to increase DC output voltage. The main drawback of this solution, besides existing the diode rectifier's drawbacks, is stress on the boost power switch.

In the line frequency phase-controlled converter (Thyristors), shown in Fig. 1.4c, for a given AC input voltages, delaying the instants at which the thyristor is allowed to start conduction can control the magnitude of the average output voltage. The main disadvantage is the injection of large harmonics into the source. At a small value of output power, compared to its maximum possible value, these converters operate at very poor power factor and producing notches in the line-voltage waveform.

In recent years, development in Pulse Width Modulation (PWM) controlled AC/DC rectifier (Converter) made it the most popular topology used in ASD, UPS…etc. This universal topology, shown in Fig. 1.4d, has the advantage of using a low-cost three-phase module with a bi-directional energy flow capability as well as high quality controlled DC output voltage.

The converter stack, Fig. 1.4d, consist of six switches, where the upper switches (S1, S3, S5) and the lower switches (S2, S4, S6) should not conduct simultaneously to prevent each converter arm from being short circuited. Hence the dead-time must be introduced between the conduction of the upper switch and that of the lower switch [5].

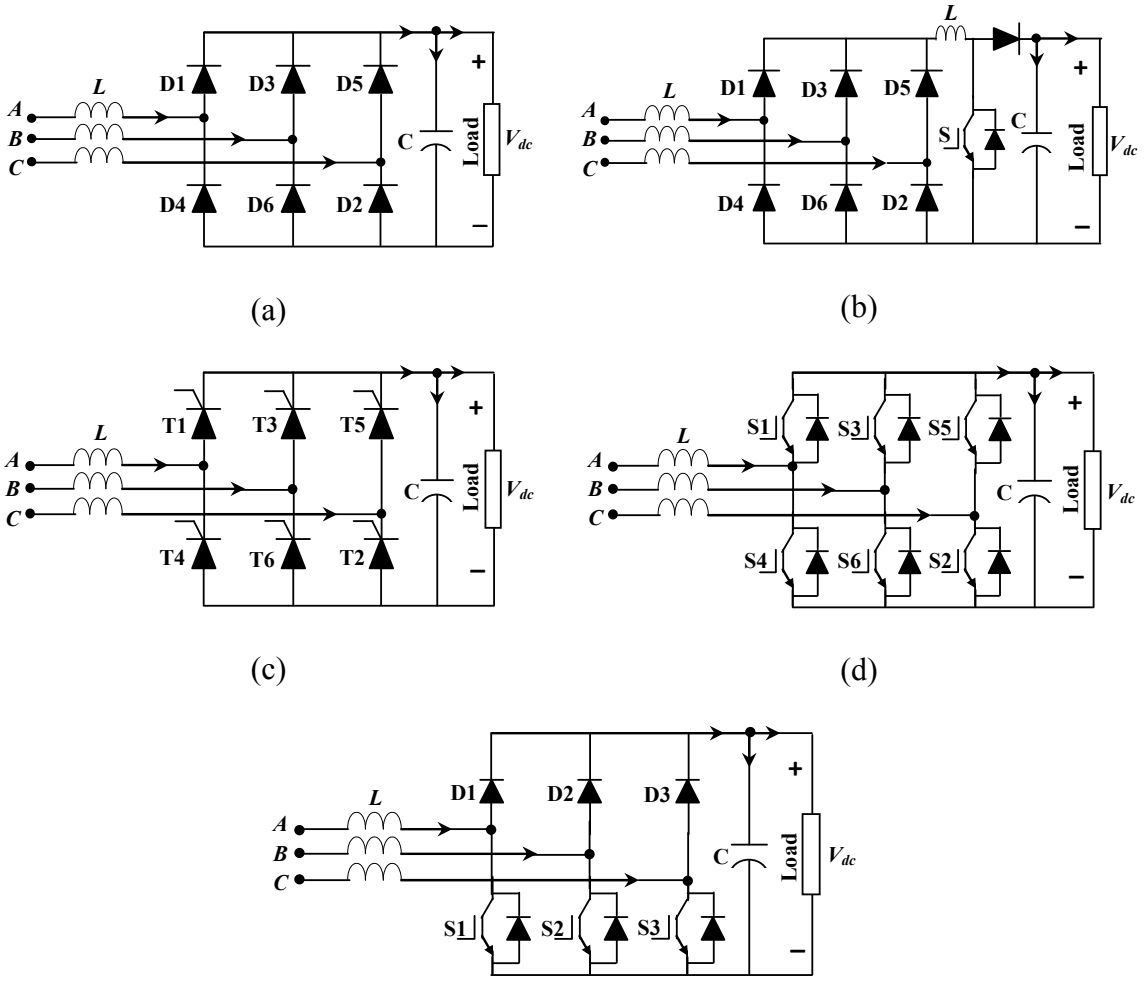

Fig. 1.4 Different rectifier topologies

The semi-controlled rectifier structure uses three insulated-gate bipolar transistors (IGBTs) and three diodes is shown in Fig. 1.4e [6]. The main advantages of this topology when compared to standard topologies are that all switches are connected to the same reference in rectifier stage which simplifying the command circuit, there are no switches in series in the rectifier stage which discharging the possibility of short-circuit through a leg, and the small number of power stages increases efficiency when compared to the topology shown in Fig. 1.4b. The main disadvantage of this topology is the higher

harmonic content when compared to the fully controlled topology shown in Fig. 1.4d, since only the positive half-cycle can be modulated.

1.3.1.2 DC/AC Power Conversion Topologies

It is possible to use the line frequency phase controlled converter presented in the previous section where the converter always operates in an inverter mode and the polarity of the input DC power is considered. However, AC side filters and the reactive power compensation would be needed, since the output current will contain harmonics and will be at lagging power factor, which is not required to interface with the utility grid.

Alternatively, switch mode DC/AC power converter (Inverter) used in motor control and UPS can be utilized where the objective is to produce a sinusoidal AC output voltage whose magnitude and frequency can both be controlled. For renewable energy interconnection, the inverter output voltage must be synchronized with the utility grid.

In general, two basic types, Fig. 1.5, of inverters exist that are totally different in their behavior. The first is referred as a voltage link PWM or Voltage Source Inverter (VSI) while the second referred as a current link PWM or Current Source Inverter (CSI). The basic difference between the VSI and the CSI is the following;

In the VSI, the DC input appears as a stiff DC voltage source to the inverter (ideally with no internal impedance) by the use of a large DC electrolytic capacitor in parallel to its input terminals. It creates a relatively well-defined switched voltage waveform at its output terminals. The resulting current waveform is then governed by the loads on the grid utility. By the use of recent inverter control algorithms, the supplied current can be controlled to be lagging or leading to the grid voltage, which leads to fully controlled reactive power.

In the CSI, the DC input appears as a stiff DC current source to the inverter (ideally with internal impedance approaching infinity). While a true DC current source can never be a reality, it is reasonably approximated by a controlled rectifier or chopper with a current control loop as well as a large inductor in series with its terminal to smooth the current. It creates relatively well defined-switched current waveforms at its output terminals. Here, the resulting voltage waveform is governed by the loads on the grid utility. Again with the inverter control algorithms, the supplied voltages can be controlled.

Current source inverters have several advantages over variable-voltage inverters because they can operate under a wide input voltage range and a boost converter stage may not be required. They provide protection against short circuits in the output stage and can easily handle temporary overrating situations such as wind gusts or faulty turbines. In addition, CSIs have relatively simple control circuits and good efficiency. As disadvantages, CSIs produce torque pulsations at low speed, cannot handle undersized motors, and are large and heavy. The phase-controlled bridge rectifier CSI is less noisy than its chopper-controlled counterpart, losses are smaller, and it does not need high-speed switching devices, but it cannot operate efficiently from direct DC voltage. The chopper-controlled CSI can operate from batteries and produces more noise as a result of its need for high-speed switching devices. With the advent of fast, high-power controlled devices, VS inverters have become popular, but much R&D is needed before they are applied to very high power systems.

For most small- and medium-power applications, VS inverters are used, with some inherent constraints. For example, a VS inverter might be a buck converter that cannot

produce an output voltage greater than the source voltage. This limitation often requires an additional DC-DC boost converter for stationary applications such as batteries, photovoltaics, and fuel cells, which make the power conversion have lower efficiency, larger size, and higher cost [7-11].

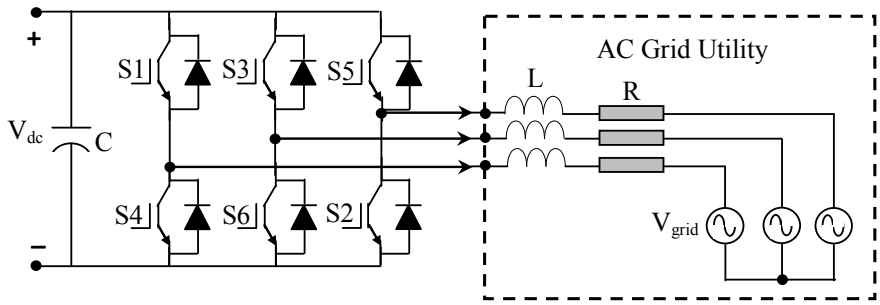

(a)

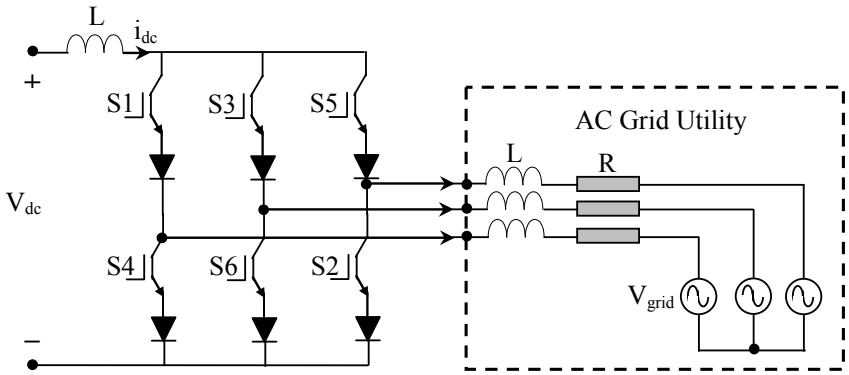

(b)

Fig. 1.5 Basic DC/AC converter topologies: (a) Voltage source inverter, and (b) Current source inverter

A new type of power conversion circuit, known as an impedance-source (Z-source) power converter, is designed to overcome the characteristics associated with the conventional V-source and I-source converters [12]. A Z-source inverter can produce any

desired voltage regardless of its input voltage, which greatly reduces system complexity, cost, size, and power loss.

Figure 1.6 shows the concept of a Z-source converter. In it, there is a unique LC network in the DC link, making it possible for buck and boost operation. Even though such topology has gained attention in the past few years (with some interesting features such as application to almost all the conversion circuits: DC-AC inversion, AC-AC conversion, and DC-DC conversion). In this dissertation, we concentrate on the analysis of DC-link voltage source conversion because of a vast and solid application to the field of renewable energy-based conversion systems. In addition, a Z-source converter has more passive components in the link, and an economical breakthrough analysis must be carried out for high-power applications [13].

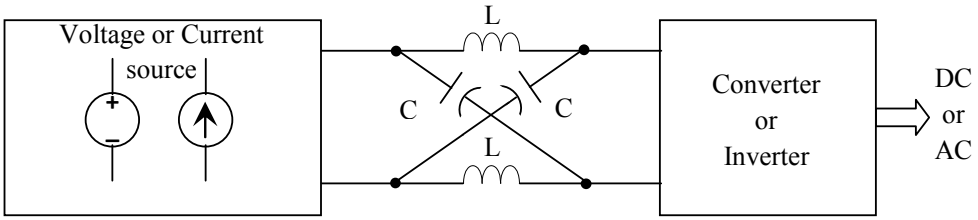

Fig. 1.6 Z-source converter system

1.3.1.3 DC/DC Power Conversion Topologies

DC-DC power converters are employed in a variety of applications, including power supplies for personal computers, office equipment, spacecraft power systems, laptop computers, renewable energy conversion systems and telecommunications equipment, as well as DC motor drives. The input to a DC-DC converter is an unregulated DC voltage V_g. The converter produces a regulated output voltage V, having a magnitude (and possibly polarity) that differs from V_g. For example, in a computer off-line power supply,

the 120 V or 240 V AC utility voltages is rectified, producing a DC voltage of approximately 170 V or 340 V, respectively. A DC-DC converter then reduces the voltage to the regulated 5 V or 3.3 V required by the processor ICs.

High efficiency is invariably required, since cooling of inefficient power converters is difficult and expensive. The ideal DC-DC converter exhibits 100% efficiency; in practice, efficiencies of 70% to 95% are typically obtained. This is achieved using switched-mode, or chopper, circuits whose elements dissipate negligible power. PWM allows control and regulation of the total output voltage. This approach is also employed in applications involving alternating current, including high-efficiency DC-AC power converters (inverters and power amplifiers), AC-AC power converters, and some AC-DC power converters (low-harmonic rectifiers).

A large number of DC-DC converter circuits are known that can increase or decrease the magnitude of the DC voltage and/or invert its polarity [14-18]. Figure 1.7 illustrates several commonly used DC-DC converter circuits, along with their respective conversion ratios. In each example, the switch is realized using a power MOSFET and diode; however, other semiconductor switches such as IGBTs, BJTs, or thyristors can be substituted if desired.

The first converter is the buck converter, which reduces the DC voltage and has conversion ratio $M(D) = D$. In a similar topology known as the boost converter, the positions of the switch and inductor are interchanged. This converter produces an output voltage V that is greater in magnitude than the input voltage V_g. Its conversion ratio is $M(D) = 1/(1-D)$.

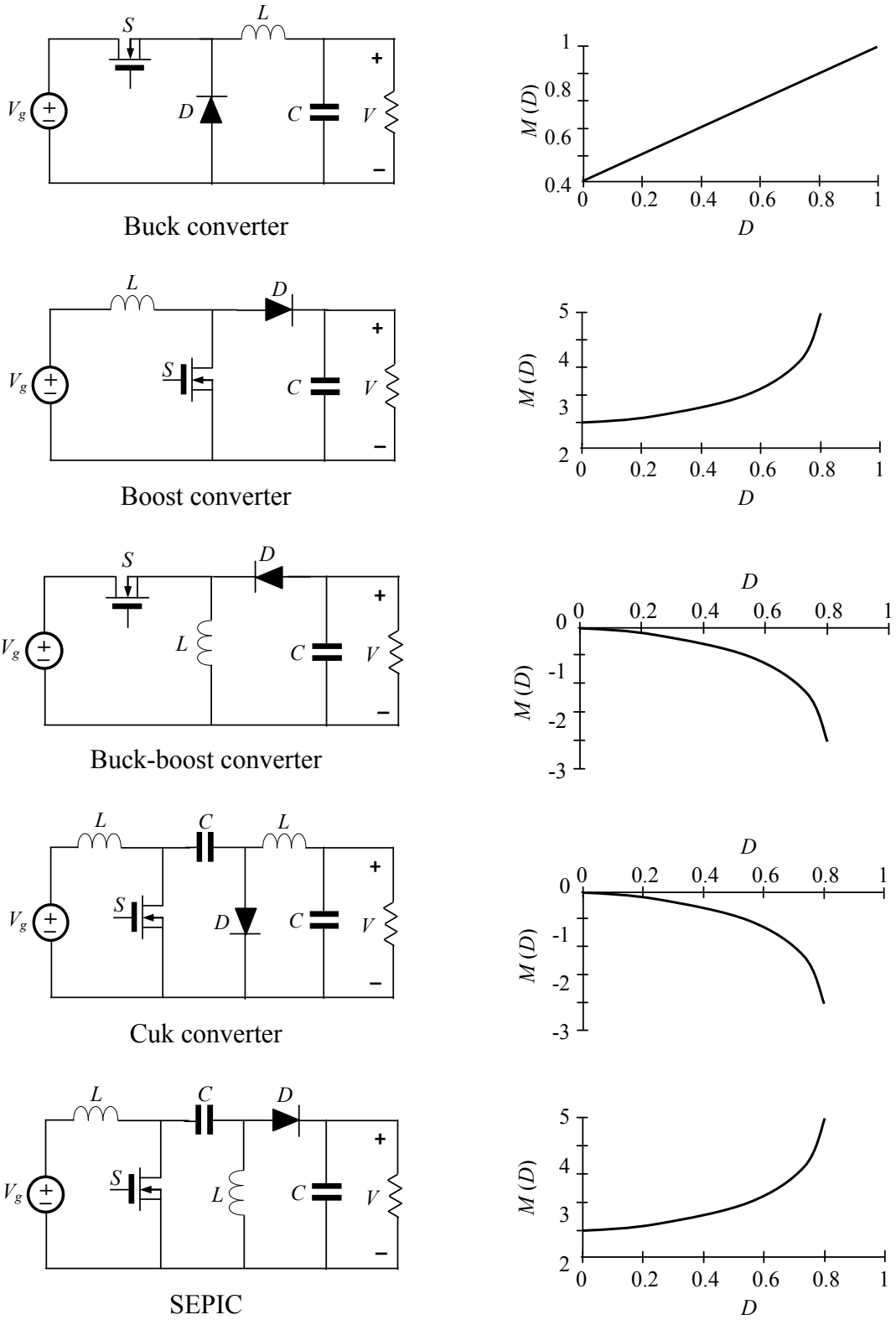

Fig. 1.7 Several basic DC-DC converters and their DC conversion ratios $M(D) = V / V_g$

In the buck-boost converter, the switch alternately connects the inductor across the power input and output voltages. This converter inverts the polarity of the voltage, and can either increase or decrease the voltage magnitude. The conversion ratio is $M(D) = -D/(1-D)$.

The Cuk converter contains inductors in series with the converter input and output ports. The switch network alternately connects a capacitor to the input and output inductors. The conversion ratio $M(D)$ is identical to that of the buck-boost converter. Hence, this converter also inverts the voltage polarity, while either increasing or decreasing the voltage magnitude. The single-ended primary inductance converter (SEPIC) can also either increase or decrease the voltage magnitude. However, it does not invert the polarity. The conversion ratio is $M(D) = D/(1-D)$.

1.3.1.4 PWM Strategies

Application of power converter topologies are still expanding due to continuous improvements in semiconductor technology, which offer higher voltage and current ratings as well as better switching characteristics. On the other hand, the main advantages of modern power electronic converters such as: high efficiency, low weight and small dimensions, fast operation and high power densities are being achieved through the use of the so called “switch mode operation”, in which power semiconductor devices are switched on and off to control power instead of continuous conduction [5, 6].

In the power converter system, a good choice of the switching manner (modulation technique) is very important, however, it should perform some general demands like:

[1] Minimal number of switches to keep low switching losses in power components.

[2] Low content of high order harmonics in voltage and current, because they produce additional losses and noise in load.

[3] Elimination of low order harmonics.

[4] Simplicity and fast response because the modulator is one of the most time-consuming part of control algorithm and reducing of computations intensity with high performance is the main point for industry, to give the possibility for using simple and inexpensive microprocessors.

Pulse Width Modulation, is the basic energy processing technique applied in power converter systems. Among the different types of PWM, Space Vector Pulse Width Modulation (SVPWM), based on space vector representation, becomes very popular due to its simplicity and higher utilization of DC-bus voltage [19, 20]. A three-phase two-level converter provides eight possible switching states, made up of six active and two zero switching states, Fig. 1.8. Active vectors divide the plane in six sectors where a reference voltage vector V^r (t) is obtained by switching ON two adjacent vectors for proper time. Generally, to implement any vector, the phase angle of the vector should be defined, and in which sector the vector exists, finally, referring the vector to the two adjacent vectors for that sector. The switching states and the converter output voltages are summarized in Table 1.1; where '1' represents the conduction of the upper switch and '0' do that of the lower switch. In the dissertation, through the simulation and the experimental verifications, the SVPWM strategy will be studied.

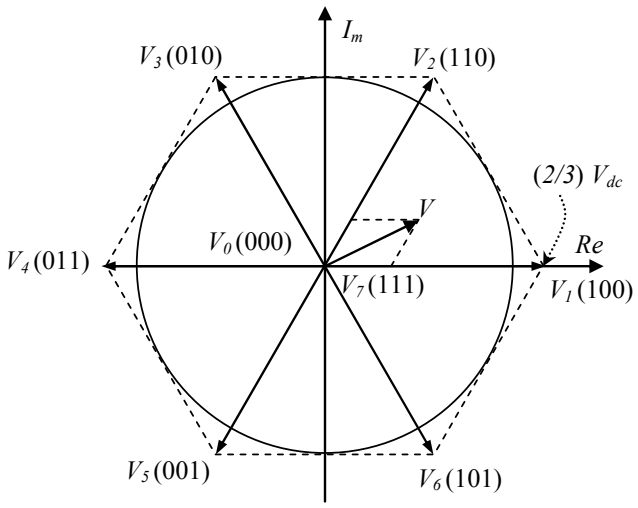

Fig. 1.8 Space vector representation of three-phase converter

Table 1.1 Switching states and converter output voltages

	V_1	V_2	V_3	V_4	V_5	V_6	V_7	V_0
S1	1	1	0	0	0	1	1	0
S2	1	1	1	0	0	0	0	1
S3	0	1	1	1	0	0	1	0
S4	0	0	1	1	1	0	0	1
S5	0	0	0	1	1	1	1	0
S6	1	0	0	0	1	1	0	1
V_a	$\frac{2}{3}V_{dc}$	$\frac{1}{3}V_{dc}$	$-\frac{1}{3}V_{dc}$	$-\frac{2}{3}V_{dc}$	$-\frac{1}{3}V_{dc}$	$\frac{1}{3}V_{dc}$	0	0
V_b	$-\frac{1}{3}V_{dc}$	$-\frac{2}{3}V_{dc}$	$-\frac{1}{3}V_{dc}$	$\frac{1}{3}V_{dc}$	$\frac{2}{3}V_{dc}$	$\frac{1}{3}V_{dc}$	0	0
V_c	$-\frac{1}{3}V_{dc}$	$\frac{1}{3}V_{dc}$	$\frac{2}{3}V_{dc}$	$\frac{1}{3}V_{dc}$	$-\frac{1}{3}V_{dc}$	$-\frac{2}{3}V_{dc}$	0	0

1.3.2 Energy Integration Link Technologies

The integration of multiple renewable energy sources can be considered a facet of distributed generation (DG). DG systems consist of small generators, typically 1kW to 10MW, scattered throughout the system to provide electrical and, sometimes, heat energy close to consumers. When interconnected with distribution systems, these small, modular generation technologies can form a new type of power system, the microgrid.

The microgrid concept assumes a cluster of loads and micro-sources operating as a single controllable system that can provide power and heat to the local area. The electrical connection of sources and loads can be done through a DC link, an AC link, or an HFAC link. Converters are usually connected in parallel, although series arrangements of sources and loads are possible to allow better use of high voltages and currents. An example of series connection is a group of small run-of-river hydroelectric systems that drive induction generators connected in. All configurations require a controlled voltage at the load link bus that is capable of supplying power to all the loads with reasonable power quality. On the other hand, a controlled current source is more convenient to adjust the voltage of every electrical source to the common voltage of the source bus, according to the strategy of power control.

In the configurations depicted in Fig. 1.9, thyristors or GTOs are still recommended for their robustness, guaranteed reliability, handling of higher power levels, low cost, easy control, and high efficiency. The major problem with these components is that they cannot operate easily with frequencies much higher than 1 kHz. Furthermore, GTOs demand a high control current to interrupt their load currents. Even so, for very high-power applications, they are absolute in the industry.

1.3.2.1 DC-Link Integration

The simplest and oldest type of electrical energy integration is through a DC link (see Fig. 1-9a). An example is the straightforward connection of a DC source to a battery and load scheme. Most of the first cars used this type of integration. With the advent of power diode rectifiers and controlled rectifiers, DC-link integration has widened its capabilities with AC–DC connections, controlled links, voltage-matching levels, and DC transmission and distribution.

The advantages of DC-link integration include:

- Synchronism is not required.
- There are lower distribution and transmission losses than with AC-link.
- It has high reliability because of parallel sources.
- Although the terminal needs of a DC link are more complex, the DC transmission infrastructure per km is simpler and cheaper than in AC links.
- Long-distance transmission (for high-voltage links) is possible, which enables integration of offshore wind turbines and other energies with inland networks.
- The converters required are easily available.
- Single-wired connections allow balanced terminal AC systems.

The disadvantages are:

- The need for careful compatibility of voltage levels to avoid current recirculation between the input sources.
- The need for robust forced commutation capabilities in circuits at high power levels.
- Corrosion concerns with the electrodes.
- A large number of components and controls.

- More complex galvanic isolation.
- Higher costs of terminal equipment.
- Difficulties with multi-terminal or multi-voltage-level operation for transmission and distribution.

In the rotatory generation with synchronous or induction generators of Fig. 1.9a, two separate converters would be necessary to feed the DC link. For stationary generation, it is used only in a diode scheme to prevent back-feeding to the DC source. In some cases, such as for fuel cell stacks, a DC–DC converter with filtering features is required for voltage matching and smoothing out undesirable ripples. The DC–AC converter connecting the DC link to the 60-Hz grid is necessary if the grid is used to store energy; otherwise, it could be an ordinary thyristor inverter. Control is exerted individually on each source because current contribution to the DC link can occur just by raising the output voltage above other sources.

The same solution can be used to store energy in a battery, making sure that the battery can supply energy when the bus voltage is lower or receive energy when the bus voltage is higher. A typical case of a current control source is that of a small wind power plant for a boat or remote load. Other alternatives have to be adapted according the needs of the generating system.

1.3.2.2 AC-Link Integration

Another possibility for integrating renewable energy sources is the AC-link bus operating at either 50 or 60 Hz, as indicated in Fig. 1.9b. This bus can be the public grid or a local grid for islanded operation. In this case, the interconnection of a local bus to the public bus must follow the standards and requirements for interconnection.

The positive features of this configuration include:

- Utility regulation and maintenance of the operational voltage, which makes it easier to inject power into the grid.
- The possibility, in some cases, of eliminating the electronic converters (e.g., by using synchronous or induction generators that establish their own operating point)
- Easy multi-voltage and multi-terminal matching.
- Easy galvanic isolation.
- Well-established scale economy for consumers and existing utilities.

The negative points include:

- The need for rigorous synchronism, voltage-level matching, and correct phase sequence between sources during interconnection as well as during operation.
- Leakage inductances and capacitances in addition to the skin and proximity effects that cause losses in long distributions.
- Electromagnetic compatibility concerns.
- The possibility of current recirculation between sources.
- The need for power factor and harmonic distortion correction.
- Reduced limits for transmission and distribution.

The rotatory generation in Figure 1.9b is feeding the AC link to the grid directly. The stationary generation will need a DC–AC inverter or, in some cases, a DC–DC booster and then a DC–AC converter to allow minimum levels of efficient conversion. No DC loads are assumed in this case. Volt-amperes reactive compensation and harmonic compensation are easily implemented in this scheme using the storage facilities and the *p–q* theory concepts.

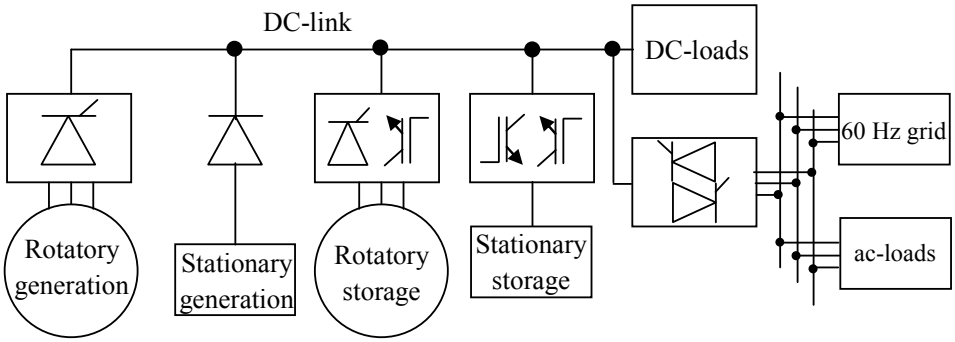

(a)

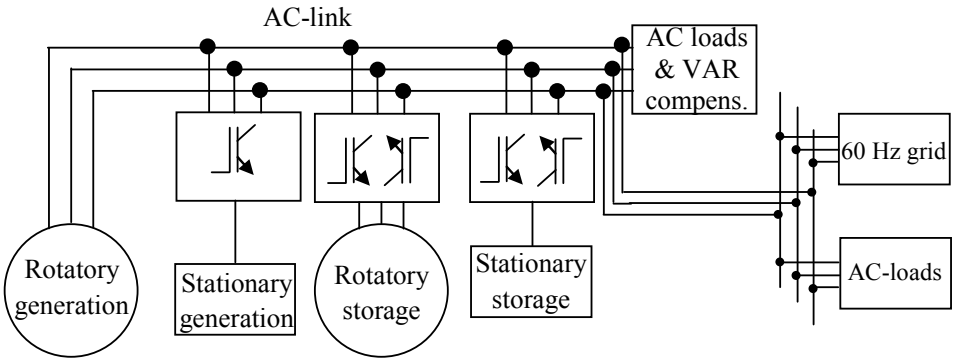

(b)

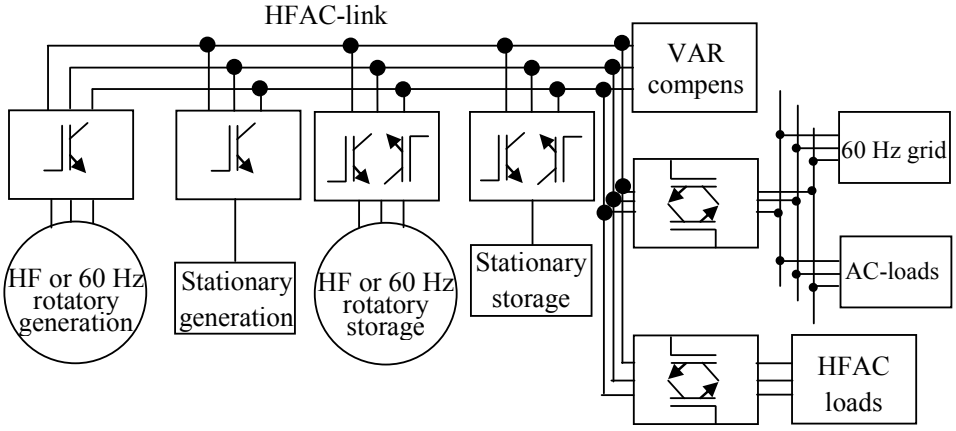

(c)

Fig. 1.9 Varieties of energy integration: (a) DC-link integration, (b) AC-link integration and (c) HFAC-link integration

1.3.2.3 HFAC Link Integration

An HFAC microgrid system is a power electronics solution that is promising as an interface for the utility grid and stand-alone operation. It provides embedded fault protection, small dimensions, and a configuration to serve various power quality functions. Frequencies in industrial use are 400 Hz, as is the case in spaceships, boats, buses, planes, submarines, and other loads of the kind. Researchers are investigating increased levels of these frequencies for high-power electronic circuits and devices.

Power electronic-based systems connected with the grid can be controlled and monitored remotely to allow real-time optimization of power generation and power flow, which allows aggregation of distributed power generation resources into a ‘‘virtual utility.’’ Several HFAC power distribution systems were implemented for aerospace applications, and NASA evaluated this scheme for space station applications [9, 10]. It was developed as a workable power distribution system for hybrid electric vehicles (HEVs) as well [11] using traditional AC–AC conversion through semiconductor switches. This is performed in two stages, from AC–DC and then from DC–AC (DC-link converters), or directly by cycloconverters. A microgrid is illustrated in Fig. 1.9c.

Series resonant converters, using zero-voltage or zero-current switching, can be used with each of the sources to generate the HFAC link [9]. In this way, the overall losses in the converters can be reduced. An HFAC microgrid system has the following inherent advantages:

- The harmonics are of higher orders and are easily filtered out.
- Fluorescent lighting will experience improvement because, with higher frequency, the luminous efficiency is improved, flicker is reduced, and dimming is accomplished

directly. The ballast inductance is reduced proportionally to the frequency, with a corresponding reduction in size and weight.

- High-frequency induction motors can be used for compressors, high-pressure pumps, high-speed applications, and turbines. AC frequency changers based on matrix converters can be used to soft start high-frequency induction motors. A safe operating area is not a restriction for soft switching, and therefore modern power electronic devices will be advantageous.
- Harmonic ripple current in electric machines will decrease, improving efficiency.
- High-frequency power transformers, harmonic filters for batteries, and other passive circuit components become smaller.
- Auxiliary power supply units are easily available by tapping the AC link. They would be smaller with higher efficiencies.
- Batteries have been the traditional energy storage source, but in HFAC microgrids, dynamic storage is an alternative.

The disadvantages are:

- The high cost of transformers.
- The large number of devices (because of the use of bipolar AC switches).
- Very complex control.
- The dependence on future advances of power electronic components.
- Concerns about electromagnetic compatibility.
- Extremely reduced limits and technological problems for transmission and distribution at high frequencies.

1.4 Problem Statement

High efficiency of power converters between renewable energy sources (wind, photovoltaic, fuel cells, etc.) and the utility grid is strongly recommended to maximize the utilization of these sources. The power quality is also another aspect that requires large passive elements (inductors, capacitors, filters) to be placed between these sources and the grid. In that respect, the new equipment and modern control systems can provide new possibilities for improving present control strategies, performance, and utilization of the installation. Furthermore, an improved control system should provide overall higher level of safety and reliability. The present state-of-the-art tools and methods for analyzing combined power systems does only to a limited extent utilize the possibilities for increased knowledge available in the more advanced models and methods developed and used within each of the machinery and electrical engineering disciplines [21-26]. To be able to analyze increasingly more complex systems of interest, the ability to easily combine models and methods to develop more fundamental insight into the total systems behavior, its characteristics and limitations will be an advantage in design of new systems. Accordingly, it is first necessary to design the grid-connected renewable power generation system simulation model that should include mathematical models of electrical and mechanical machinery components to the required level of complexity. Renewable power generation system simulation model should be used to explore possibilities of energy management system (EMS) as the control from the highest level and to provide means of developing methods of local-optimization and plant control. Various kinds of simulations should be performed and various algorithms should be

tested and verified with the aim of such model, including different power conversion topologies.

1.5 Research Objectives

Optimum utilization of the hybrid renewable power injected into the grid is essential for safe operation with minimum operational costs (fuel consumption). In the next generation systems, power converter topologies and the control systems are an integrated part of the system to an even higher level than found today. The main objective is to develop higher-level high frequency-based power converter system (HFPCS) which optimize the utilization of the hybrid renewable power injected into the local grid and has the overall control functionality of the power system and which will be the integrating element in a totally integrated power system as shown in Fig. 1.10. HFPCS should provide means of optimal topologies of energy conversion subject to operating conditions, safety requirements and operational availability. The high-level HFPCS have to be well integrated functionally with low level controllers which interact with producers and consumers of electrical energy, as well as control and protection of the overall power system.

A key activity is to develop and establish a complete power system simulation model for overall system performance verifications. Such a model can, to a large extent, be based on models (modules) already available at the various research groups, but there is a need to adapt and combine the various models into one unified system model. A main challenge in this respect is to create a functional and modular system model where all critical components are adequately represented. This means that each type of component in the system, ranging from mechanical drive trains to purely electrical loads and

converters, is represented by models with the same level of complexity from an integrated system point of view. The system model serves a number of purposes, including:

- Design and testing of the overall control system including the HFPCS and individual controllers for the local power consumers and power generating units.
- Design of different conversion topologies which can be utilized to optimize utilization from the renewable sources, but also to include analysis of dynamic behavior in extreme operational cases for the total system.
- Development and testing of a digital signal controller (DSC) for controlling the HFPCS with high precision.

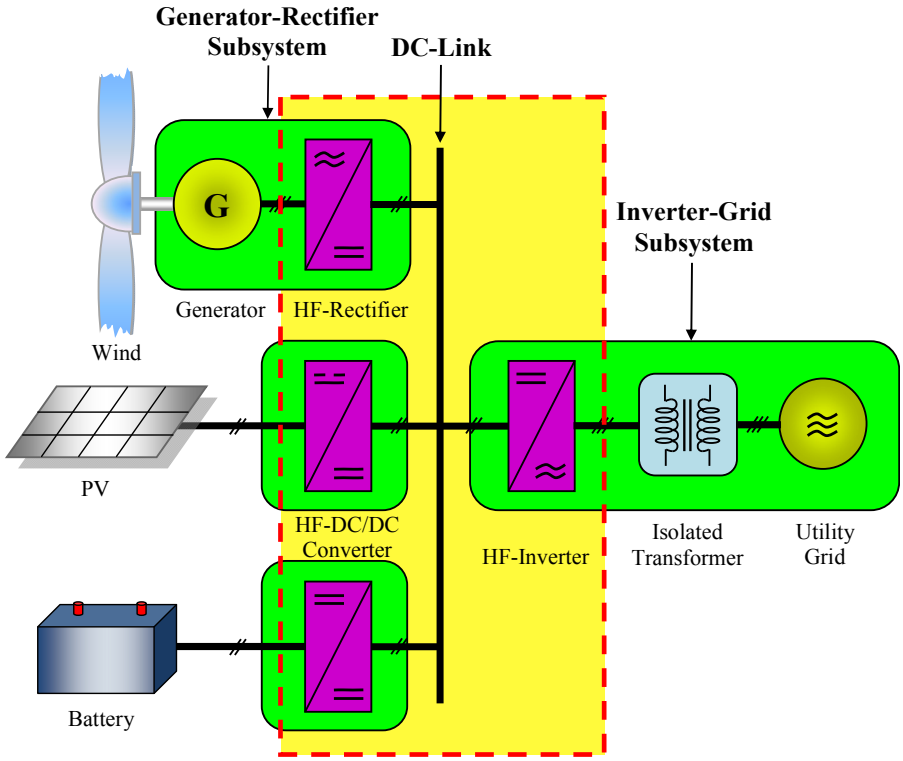

Fig. 1.10 The developed grid-connected hybrid generation system schematic diagram

Before carrying out any testing, under different possible operational cases, it is imperative to test the developed system of "HFPCS" in fixed and controlled environment. This will verify the conceptual integrity of the methods developed before the added complexity of testing with different scenarios is implemented.

1.6 Originality and Significance

In the past few years, the use of high switching frequency for high power converters was very limited due to the absence of this technology for the high power switches (IGBT) which had a switching capability less than 20-kHz. The main reason for this limitation was the power losses (conduction and switching losses) dissipated in each switch which is increasing proportionally to the frequency. On the other hand, MOSFET switches had higher switching capability than IGBT but only for low power applications.

Recently, a new generation of IGBT switch technology was produced to open the horizon for utilizing the power converters for high switching frequencies above 20 kHz. This new generation is bulk-diffused silicon, rather than the epitaxial material that both IGBTs and MOSFETs have historically used. This technology is called "non-punch through" (NPT) technology.

Studying the high frequency power converters is the special task of this dissertation in order to optimize the utilization of the hybrid renewable power injected into the grid. Nowadays, a large part of power electronics system volume is occupied by heat dissipation unit and the passive components, i.e. heat sinks, magnetic components and capacitors. Therefore, reduction of power losses and increase of switching frequency are major technological direction. This is because the reduction of losses directly reduces the

heat sink volume. The increase of switching frequency reduces the passive component volume as well. The reduction of the power loss also improves the system efficiency [27].

In the next 10 years, the power density will be 10 times larger according to data traced by NTT [28]. According to the relation between output power density and power loss, the power losses of the power electronics systems is expected to be reduced by half, and the switching frequency will be 10 times higher than that for present converters. To achieve lower loss and higher switching frequency for higher output power density systems, the improvement of the semiconductor power device is a key issue. This is because the power loss generated in the power semiconductors shares about a half of the total losses in the present power electronics system. Also, an increase of switching frequency directly increases the semiconductor power loss [29-31].

The developed HFPCS hybrid generation system control should provide an improvement in the overall efficiency for the energy conversion stages if it works under high switching frequency control levels. The system is implemented with different conversion topologies to select the optimum design which provide low number of switches in order to decrease the switching losses for HFPCS. Moreover, the developed method should increase the overall power density (decrease the size for the energy conversion stages while handling the same power rating when compared to other traditional larger size circuits) if it works under high switching frequency control levels; since the power circuit passive elements (inductors, capacitors, harmonic filters, etc) are reduced proportionally to the frequency, with a corresponding reduction in size and weight.

1.7 Organization of Dissertation

The dissertation is organized into twelve chapters including this chapter.

Chapter 1 introduces an overview for the renewable energy sources. Classifications of energy storage systems are presented. Different topologies for the power electronics parts in which renewable energy can be injected into the grid are discussed. The PWM strategies applied on the power converters are introduced, focusing on the SVPWM technique. Mutli-renewable energy sources integration link technologies are well defined. In addition to the problem statement, research objectives, originality and significance, and the outline of the work in this chapter, the other chapters include:

Chapter 2 presents background material for renewable energy sources characteristics and dynamic modeling involving battery energy storage system.

Chapter 3 discusses the dynamic performance of the SEIG driven by a variable speed wind turbine. Also, loading effect on the stator terminal voltage of the SEIG is presented.

Chapter 4 focuses on the modeling and control design of a controlled voltage DC-DC boost converters. The DC-bus is designed to meet the needs of house loads and future wide use of hybrid systems. The system being implemented in the laboratory is designed to operate at 318V DC.

Chapter 5 proposes a SEIG-based WECS with VOC strategy for a three-phase voltage-source PWM inverter is used as a dynamic VAR compensator system for weak grids to provide full control of active and reactive power injected into the grid.

Chapter 6 presents a simple simulation comparative study between high frequency (HF) and low frequency (LF) switching to verify the advantages resulting from HF-operation

and to confirm the effectiveness of the hybrid generation system with high frequency-high power converters for grid connection operation.

Chapter 7 introduces a new grid-connected dual-boost converter feasible for low speed direct-driven PMWGSs. A three-phase high frequency semi-controlled boost rectifier is used as the first interface stage for grid connection.

Chapter 8 presents a design of a novel modularized multi-input bridgeless boost converter (MIBBC) for possibility of reducing the size and weight of the passive components.

Chapter 9 addresses the design and implementation of a real-time digital signal controller printed circuit board for high frequency converters to achieve a fast response during transient operation.

Chapter 10 focuses on the practical implementation of the developed HFPCS compared to the other conventional power converters and discusses the grid connectivity issues.

Chapter 11 introduces an application example study for WAMS network utilizing this type of data collection to check the health state of hybrid power system networks. The purpose is to increase the overall system reliability for all power stages via significant dependence on WAMS as distributed intelligence agents with improved monitoring, protection, and control capabilities of the power networks.

Chapter 12 provides general discussions of the results of this work and includes the conclusions of this dissertation as well as provides suggestions and recommendations for further research.

Chapter 2 Characteristics and Dynamic Modeling of Renewable Energy Sources and Battery Energy Storage Systems

2.1 Introduction

A renewable energy source cannot run out and causes so little damage to the environment that its use does not need to be restricted. No energy system based on mineral resources is renewable because, one day, the mineral deposits will be used up. This is true for fossil fuels and uranium. The debate about when a particular mineral resource will run out is irrelevant in this context. A renewable energy source is replenished continuously.

There is no shortage of renewable energy because it can be taken from the sun, wind, water, plants, and garbage to produce electricity and fuels. For example, the sunlight that falls on the United States in one day contains more than twice the energy the country normally consumes in a year. California has enough wind gusts to produce 11% of the world's wind electricity [32].

Because every source is more or less intensive in what it produces, special measures have to be considered when considering global energy solutions. These include availability, capability, extraction costs, emissions, and durability [33]. This chapter addresses the characteristics and the dynamic modeling of the renewable energy sources involving the battery energy storage system.

2.2 Wind Turbine Characteristics

The effective power extracted from wind is derived from the airflow speed just reaching the turbine and the velocity just leaving it. The number of blades must also be considered. Only part of the full energy available from the wind can be extracted for

energy generation, quantified by the power coefficient, C_p. The power coefficient is the relationship of the power extraction possible to the total amount of power contained in the wind [34, 35]. Figure 2.1 relates the power coefficient to the tip speed ratio, λ, defined as the relationship between the rotor blade tip speed and the free speed of the wind for several wind power turbines. As stated earlier, in quantitative terms, the tip speed ratio is defined as $\lambda = \omega R_t / V$, where ω is the angular speed of the turbine shaft, V is the wind speed, and R_t is the length of each blade. It emphasizes the importance of knowing the purpose for which the energy will be used, to allow determination of the best selection for wind power extraction.

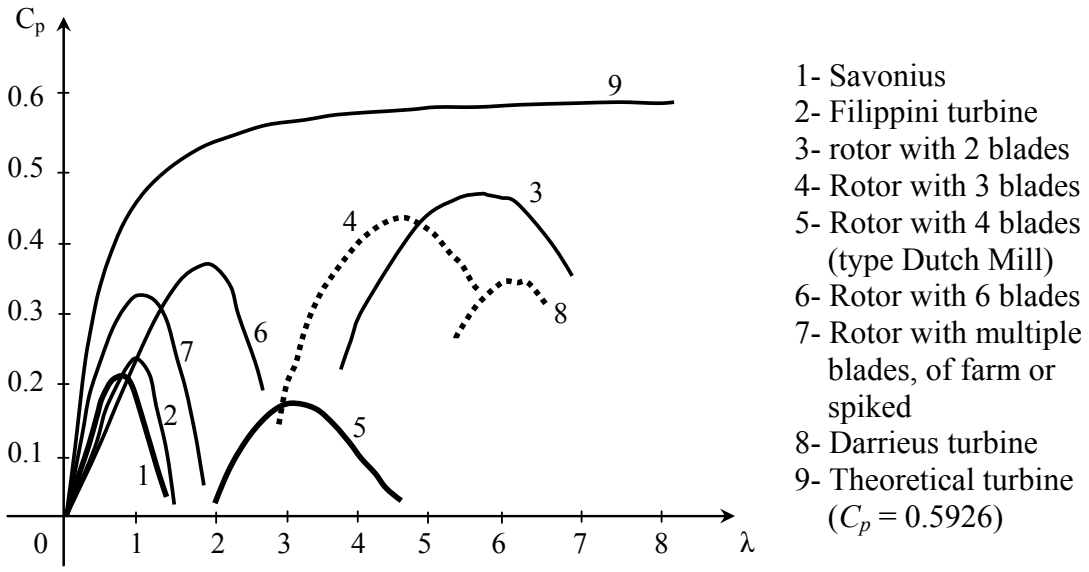

Fig. 2.1 Output characteristics of various turbines

According to Betz theory, the turbine mechanical power (P_t) can be given by [1]:

$$P_t = 0.5 C_p \rho A V^3 \quad kg \cdot m / s \tag{2-1}$$

Where ρ is the air density and A is the area of the rotor blades. So, from (1), the turbine torque (T_t) is given by:

$$T_t = \frac{P_t}{\omega} = 0.5\,\rho\,A\,R_t\,V^2\,C_t \tag{2-2}$$

Where the torque coefficient is defined as $C_t = C_p / \lambda$.

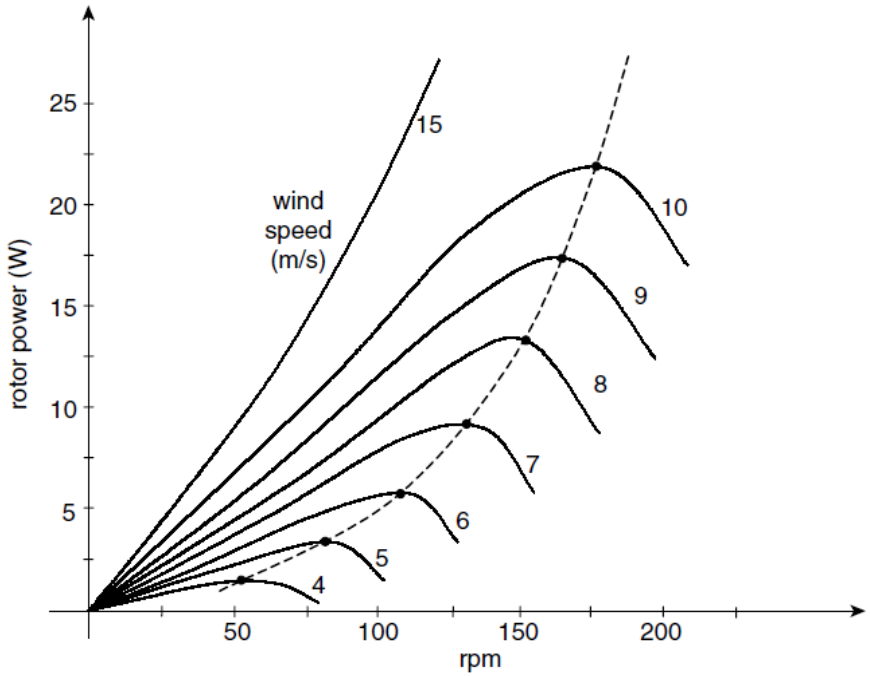

Fig. 2.2 Turbine rotation versus power characteristic related to wind speed

Considering the wind speed, the wind energy conversion system (WECS) can be divided into no load, partial load and full load state. When the wind speed is below the cut-in wind speed or above the cut-out wind speed, wind turbine operates in the no load region. When the WECS is in the full load region, the output power must be regulated at rated power, which can be achieved by changing the pitch angle. In order to maximize the captured power, the tip speed ratio needs to be controlled. As the rotor speed must change according to the wind intensity, the speed control of the turbine has to command low speed at low winds and high speed at high winds, so as to follow the maximum power operating point as indicated in Fig. 2.2. It is observed that the maximum power output occurs at different generator speeds for different wind velocities [36].

2.3 Wind Turbine Generators

Variable speed wind turbine (VSWT) systems are preferred for the higher output power generation. The first configuration shown in Fig. 2.3 is known as the double-fed induction generator (DFIG) concept, which corresponds to a VSWT with a wound rotor induction generator (WRIG) and a partial-scale power converter on the rotor circuit. One of the advantages for DFIG is that the rotor energy, instead of being dissipated, can be fed into the grid by the power electronic converter. Moreover, the power converter system can perform reactive power compensation and smooth grid connection. However, the DFIG system has the following disadvantages: a multi-stage gearbox is still necessary in the drive train because the speed range is far from a common turbine speed of 10–25 rpm, slip ring is used to transfer the rotor power by means of a partial-scale converter which requires a regular maintenance, large stator currents due to grid fault condition result in large rotor currents then converter needs to be protected from destroy, control strategies are complicated [37].

In [38], the electrically excited synchronous generator (EESG) is another generation topology which is usually built with a rotor carrying the field system provided with a DC excitation as shown in Fig. 2.4. The voltage amplitude and frequency can be fully controlled by the power electronics at the generator side, so that the generator speed is fully controllable over a wide range, even to very low speeds. In addition, EESG has the opportunities of controlling the flux for a minimized loss in different power ranges. Moreover, it does not require the use of permanent magnets (PMs), which would represent a large fraction of the generator costs, and might suffer from performance loss in harsh atmospheric conditions. Including the disadvantages of direct-drive wind

turbines compared with geared-drive wind turbines, some disadvantages of direct-drive EESG systems can be summarized as follows: It is necessary to excite the rotor winding with DC and the field losses are inevitable, a larger number of parts and windings probably make it a heavy weight and expensive solution.

In recent years, the use of PMs is more attractive than before, because the performance of PMs is improving and the cost of PM is decreasing. The trends make PM machines with a full-scale power converter more attractive for direct-drive wind turbines [39]. The scheme of a grid-connected permanent-magnet synchronous generator (PMSG) for direct-drive wind turbines is shown in Fig. 2.5. The advantages of PMSGs over EESGs and DFIGs can be summarized as follows: higher efficiency and energy yield, no additional power supply for the magnet field excitation, improvement in the PM machine thermal characteristics due to the absence of the field losses, higher reliability due to the absence of mechanical components such as slip rings, lighter and therefore higher power to weight ratio. However, PM machines have some disadvantages such as: high cost of PM material, difficulties to handle in manufacture, and demagnetization of PM at high temperature.

In order to fulfill the variable speed operation with a self-excited induction generator (SEIG), an alternative generator system that might replace the capacitor bank and soft-starter of 'Danish concept' is a variable speed multiple-stage geared SEIG with a full-scale converter, as shown in Fig. 2.6 [39]. Compared with 'Danish concept' as mentioned above, this concept has advantages of the flexible control with a full-scale power, such as variable speed operation, better performances of reactive power compensation and smooth grid connection. Presently, Siemens is using this concept with the rated power of

3.6 MW (Bonus 107) in the market, and the generator speed range is designed to be 595–1547 rpm. The decreasing cost of power electronics (roughly a factor of 10 over the past 10 years) and the absence of brushes may make variable speed multiple-stage geared concepts (both PMSG and SEIG as mentioned above) more attractive.

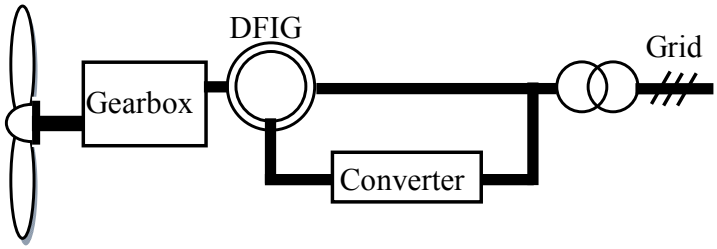

Fig. 2.3 VSWT with a gear-drive DFIG system

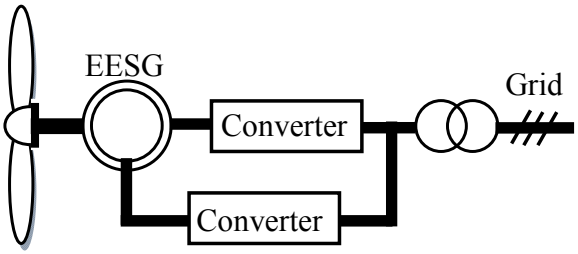

Fig. 2.4 VSWT with a direct-drive EESG system

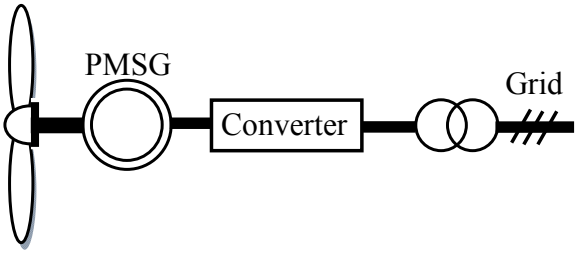

Fig. 2.5 VSWT with a direct-drive PMSG system

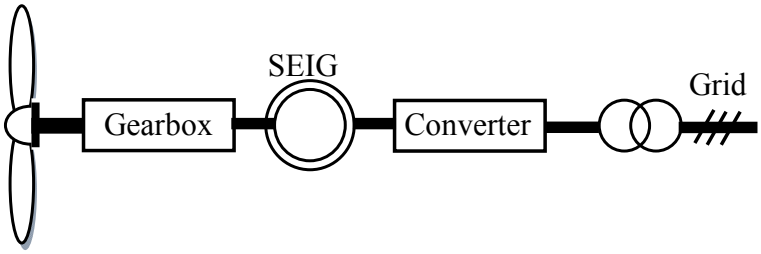

Fig. 2.6 VSWT with a geared SEIG system

2.3.1 SEIG Dynamic Model

The model of an induction generator is helpful to analyze all its characteristics. The induction machine used as SEIG is a three- phase squirrel-cage machine. In this section the model, shown in Fig. 2.7, is used because it provides a complete solution (transient and steady state) of the self-excitation process [40].

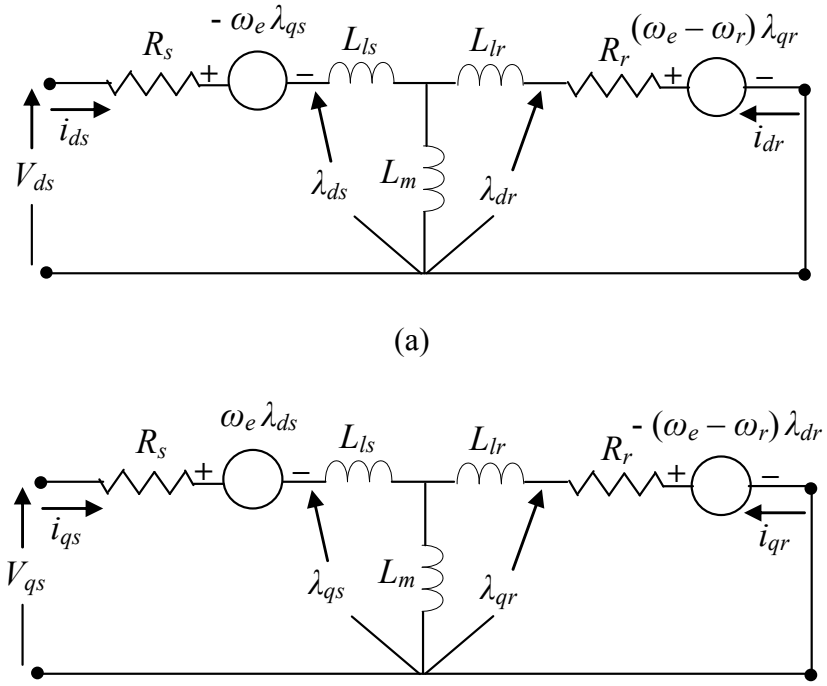

Fig. 2.7 The *d-q* model of an induction machine in the synchronously rotating reference frame: (a) *d*-axis and (b) *q*-axis

In the *d-q* model of the induction machine, V_{ds} and V_{qs} are the generated voltages along the *d*-axis and *q*-axis, respectively. The voltage of an induction machine in the synchronous reference frame, which can be obtained as follows:

$$v_{ds} + R_s i_{ds} - \omega_e \lambda_{qs} + L_{ls} p i_{ds} + L_m p i_{ds} + L_m p i_{dr} = 0 \tag{2-3}$$

$$K_d - (\omega_e - \omega_r)\lambda_{qr} + R_r i_{dr} + L_{lr} p i_{dr} + L_m p i_{ds} + L_m p i_{dr} = 0 \tag{2-4}$$

$$v_{qs} + R_s i_{qs} + \omega_e \lambda_{ds} + L_{ls} p i_{qs} + L_m p i_{qs} + L_m p i_{qr} = 0 \tag{2-5}$$

$$K_q + (\omega_e - \omega_r)\lambda_{dr} + R_r i_{qr} + L_{lr} p i_{qr} + L_m p i_{qs} + L_m p i_{qr} = 0 \tag{2-6}$$

Where:

$$\begin{aligned} \lambda_{ds} &= L_s i_{ds} + L_m i_{dr} \\ \lambda_{dr} &= L_m i_{ds} + L_r i_{dr} \\ \lambda_{qs} &= L_s i_{qs} + L_m i_{qr} \\ \lambda_{qr} &= L_m i_{qs} + L_r i_{qr} \end{aligned} \tag{2-7}$$

The voltage equation of the *d-q* model is based on the stator and rotor currents are given as:

$$\begin{bmatrix} 0 \\ 0 \\ 0 \\ 0 \end{bmatrix} = \begin{bmatrix} (R_s + pL_s) & \omega_e L_s & pL_m & \omega_e L_m \\ -\omega_e L_s & (R_s + pL_s) & -\omega_e L_m & pL_m \\ pL_m & (\omega_e - \omega_r)L_m & (R_r + pL_r) & (\omega_e - \omega_r)L_r \\ (\omega_r - \omega_e)L_m & pL_m & (\omega_r - \omega_e)L_r & (R_r + pL_r) \end{bmatrix} \begin{bmatrix} i_{qs} \\ i_{ds} \\ i_{qr} \\ i_{dr} \end{bmatrix} + \begin{bmatrix} V_{qs} \\ V_{ds} \\ K_q \\ K_d \end{bmatrix} \tag{2-8}$$

$$V_{qs} = \frac{1}{C} \int i_{qs} dt + V_{cq} \Big]_{t=0} \tag{2-9}$$

$$V_{ds} = \frac{1}{C} \int i_{ds} dt + V_{cd} \Big]_{t=0} \tag{2-10}$$

The electromagnetic torque (T_e) is given by:

$$T_e = -\frac{3}{2}\frac{P}{2}\frac{L_m}{L_r}(\lambda_{dr} i_{qs} - \lambda_{qr} i_{ds}) \tag{2-11}$$

Where V_{ds}, V_{qs}, i_{ds}, and i_{qs} are the stator voltages and currents, respectively. V_{dr}, V_{qr}, i_{dr}, and i_{qr} are the rotor voltages and currents, respectively. p is the derivative operator, i.e. $p=d/dt$. K_d and K_q are the residual voltage inside the induction generator. V_{cd} and V_{cq} are the initial voltages of the self-excitation capacitor bank. ω_e and ω_r are the synchronous

and rotor angular speed, respectively. P is the number of poles. λ_{dr}, λ_{qr}, λ_{ds}, and λ_{qs} are the rotor and stator fluxes, respectively. C is the external self-excitation capacitance. R_s, L_{ls}, R_r, and L_{lr} are the resistance and the self inductance of the stator and the rotor, respectively. L_s and L_r are the stator and rotor inductances, respectively. L_m is the mutual inductance. The mathematical equation that relates the wind turbine output torque (T_t) with the electromagnetic torque of the induction generator is given by:

$$T_t = J\frac{d}{dt}\omega + \beta\omega + T_e \tag{2-12}$$

Where J and β are the effective inertia of the wind turbine and the induction generator, and friction coefficient, respectively. From (2-8)-(2-12), the state equations of the SEIG and turbine can be accomplished as in (2-13) and (2-14):

$$\frac{d}{dt}\begin{bmatrix} i_{qs} \\ i_{ds} \\ i_{qr} \\ i_{dr} \end{bmatrix} = \frac{1}{L}\begin{bmatrix} -R_s L_r & (\omega_e-\omega_r)L_m^2 - \omega_e L_s L_r & R_r L_m & -\omega_r L_m L_r \\ \omega_e L_s L_r - (\omega_e-\omega_r)L_m^2 & -R_s L_r & \omega_r L_m L_r & R_r L_m \\ R_s L_m & \omega_r L_s L_m & -R_r L_s & \omega_e L_m^2 - (\omega_e-\omega_r)L_s L_r \\ -\omega_r L_s L_m & R_s L_m & (\omega_e-\omega_r)L_s L_r - \omega_e L_m^2 & -R_r L_s \end{bmatrix}\begin{bmatrix} i_{qs} \\ i_{ds} \\ i_{qr} \\ i_{dr} \end{bmatrix} + \frac{1}{L}\begin{bmatrix} L_m K_q - L_r V_{qs} \\ L_m K_d - L_r V_{ds} \\ L_m V_{qs} - L_s K_q \\ L_m V_{ds} - L_s K_d \end{bmatrix} \tag{2-13}$$

$$\frac{d}{dt}\omega = \frac{1}{J}T_t - \frac{\beta}{J}\omega - \frac{1}{J}T_e \tag{2-14}$$

Where $L = L_s L_r - L_m^2$

2.3.2 Power Conversion Topologies with SEIGs

In order to supply a constant-voltage DC-link of the inverter stage, a DC–DC stage is introduced between the conventional diode rectifier and the output stage [9], as shown in

Fig. 2.8. However, the rectifier stage of the power converter causes high distortion of the current and voltage of SEIGs, implying several undesirable effects to the generator, such as [41], which are as follows:

- Increased heating due to iron and copper losses at the harmonic frequencies
- Reduction in machine efficiency
- Loss of the torque production
- Increased audible noise emission
- Eventual occurrence of mechanical oscillations

In order to avoid these problems, it is interesting to use systems capable of emulating resistive loads for the SEIG, resulting in low total harmonic distortion (THD). In grid-connected applications, a step-up DC-DC converter, with current–source input characteristic, can be used in the WECS of Fig. 2.8. The simplicity of control, the reduced number of components, and the predominant need to increase the generated voltage make the boost converter the main choice [42] in this WECS. However, one can see that there are always three semiconductors in the current path from the generator side to the DC-link side, which reduces the efficiency of this topology. Also, power factor correction is achieved only in discontinuous-conduction mode. Then, this structure becomes feasible for small WECSs.

Another option to achieve high power factor in the generator side is to use a PWM rectifier in the WECS. The traditional topology applied in high-power WECS is shown in Fig. 2.9 and uses the back-to-back converter [43]. In the rectifier stage of this structure, the currents can be modulated in both half cycles. However, the half-bridge connected switches demand the use of bootstrap-integrated circuits and the occurrence of eventual

short-circuits through the leg is possible. Fig. 2.10 shows a WECS that uses a variation of the back-to-back converter [44]. Only four semiconductors are used in the rectifier stage of this topology. On the other hand, the small number of components and voltage balance across the DC-link capacitors limit the use of modified modulation techniques for the optimization of losses [45, 46].

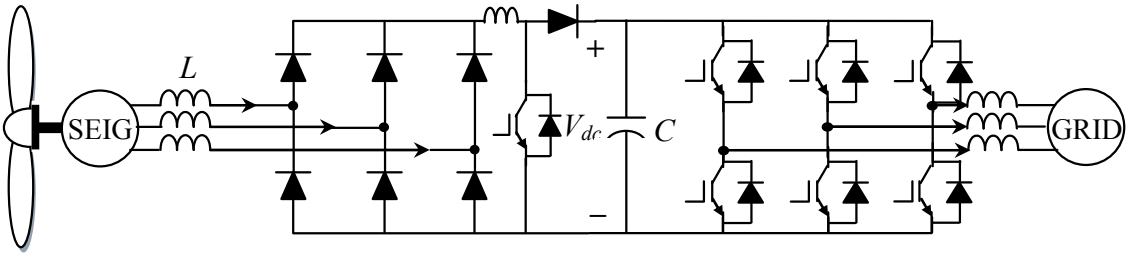

Fig. 2.8 WECS with PF correction using intermediate DC–DC stage

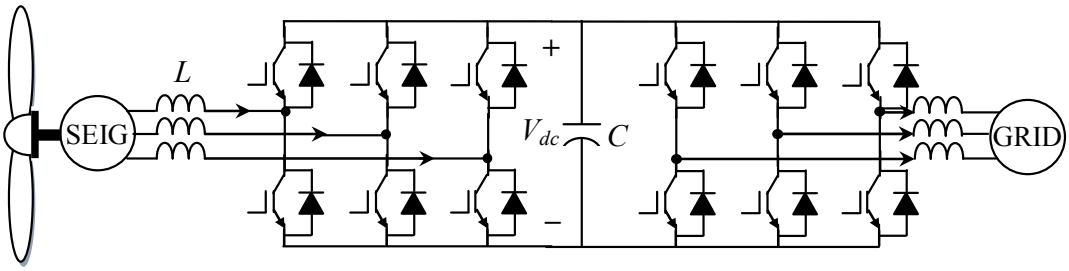

Fig. 2.9 WECS with back-to-back converter

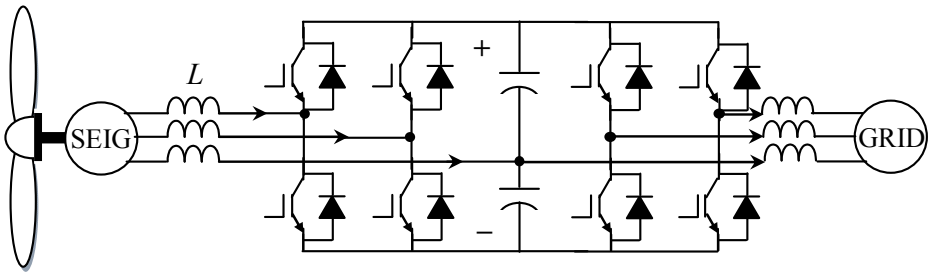

Fig. 2.10 WECS with modified back-to-back converter

2.3.3 PMSG Dynamic Model

Theoretical models for generator producing power from a wind turbine have been previously developed [47]. The PMSG dynamic equations are expressed in the *d-q*

reference frame. The model of electrical dynamics in terms of voltage and current can be given as:

$$v_q = -\left(\frac{R_g + dL_q}{dt}\right) i_q - \omega_r L_d i_d + \omega_r \lambda_m \tag{2-15}$$

$$v_d = -\left(\frac{R_g + dL_d}{dt}\right) i_d + \omega_r L_q i_q \tag{2-16}$$

Where v_d, v_q, i_d, and i_q are the two-axis machine voltages and currents, respectively. R_g, L_d, and L_q are the PMSG resistance and *d*-*q* inductances, respectively. λ_m is the PMSG flux linkage amplitude. The aforementioned equations are derived assuming that the *q*-axis is aligned with the stator terminal voltage phasor (i.e., $V_d = 0$). The expression for the electromagnetic torque in the rotor is written as:

$$T_e = \left(\frac{3}{2}\right)\left(\frac{P}{2}\right)\left[(L_d - L_q) i_q i_d - \lambda_m i_q\right] \tag{2-17}$$

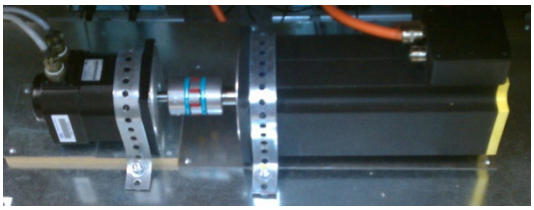

Fig. 2.11 PMSG in the laboratory

The PMSG was physically tested under varying load conditions at different rotational speeds. The 5-kW test setup for measuring the voltage variation with the load current is as illustrated in Fig. 2.11. The machine was coupled to a brushless motor simulating the characteristic of a wind turbine and was tested with a three-phase resistive load.

2.3.4 Power Conversion Topologies with PMSGs

Low-speed high-torque PMSGs are used as the preferred solution in variable-speed high-power direct-driven wind generators [48]. However, low speed operation produces

low voltage profile at the generator terminals. As the electrical power available from the wind generation system cannot be delivered directly to the grid, power electronics plays a decisive role in overcoming this limitation [49]. In order to optimize the wind turbine system, many kinds of power conversion systems to connect between the generator and the grid line have been proposed and utilized [50-54]. Figure 2.12 shows a bridge boost rectifier (BBR) in cascaded with VSI topology. A step-up transformer is used for grid connection; since VSI produces low voltage profile due to low speed direct-driven generator operation. This topology has same features as the topology that was previously shown in Fig. 2.8 in addition to the grid-tie-transformer [50].

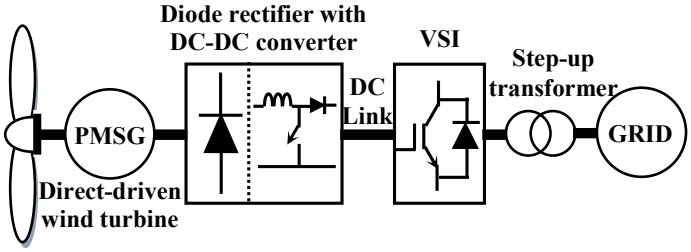

Fig. 2.12 PMSG with BBR and VSI topologies

Another option to achieve high power factor in the generator side is to use a VSC in cascaded with VSI topology in the WECS as shown in Fig. 2.13. The transformer stage still required to boost the inverter output voltage level to the grid voltage level [51]. In Fig. 2.14, a semi-controlled rectifier topology was proposed to achieve same VSC topology advantages with higher efficiency; since less switching losses can be obtained through reducing the number of switching devices. However, it will produce larger current harmonic distortion because only one half cycle is controlled [52]. The common drawback for the previous configurations is the use of the transformer for grid connection

which increases the size and weight of the power converter circuit. Then, this structure becomes feasible for small WECSs.

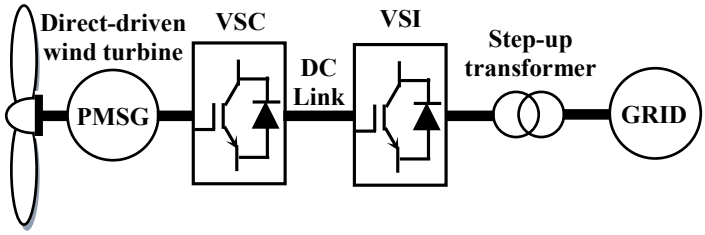

Fig. 2.13 WECS with VSC-VSI converter structure

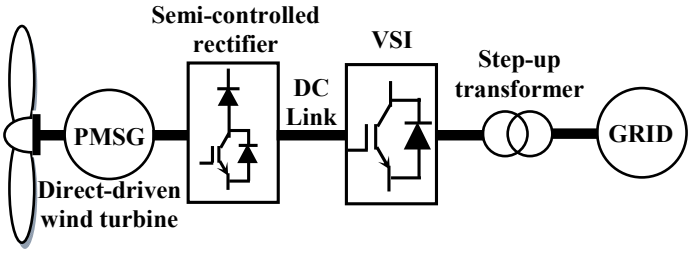

Fig. 2.14 WECS with semi-controlled rectifier and VSI

On the other hand, the same rectifier topologies can be efficiently utilized with CSI topology feasible for low-speed direct-driven PMSGs. Figure 2.15 shows same configuration as the other in Fig. 2.12 but with CSI working as a boost inverter stage. This configuration has the same drawbacks as illustrated previously. However, omitting the step-up transformer is representing an additional advantage which reduces the size and weight of the system [53].

In Fig. 2.16, the VSC topology can be used with CSI topology in order to achieve same advantages as the configuration in Fig. 2.13. Dual boost feature is obtained with low harmonic distortion. However, larger losses are expected through increasing the number of switching devices (12-switches) which reduce the overall converter-inverter efficiency. The CSI increases the voltage towards the mains by itself, so the output voltage of the VSC must be lower than the lowest rectified line to line voltage. In

practical implementations, a CSI requires a DC current source that should behave as a constant (as required by PWM CSIs) or variable (as square-wave CSIs) current source. Such current sources should be implemented as separate units [54].

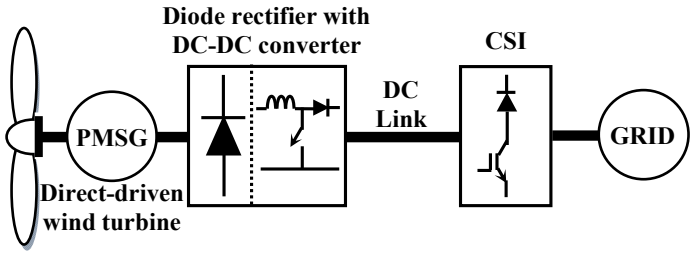

Fig. 2.15 WECS with BBR stage and CSI topology

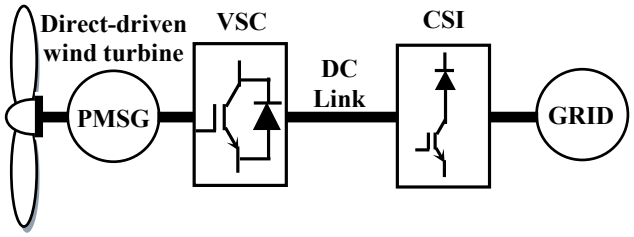

Fig. 2.16 WECS with VSC-CSI structure

2.4 Photovoltaic Cells Characteristics

Semiconductor materials have bands of allowed and forbidden energy in their spectrum of electronic energy (the energy gap). Inside the allowed band, there are valence and conduction bands, separated by such an energy gap. The electrons occupy the valence band and can be excited in the conduction band by thermal energy or by absorption of photons with energy quantum higher than the energy gap. The bandwidth of the energy gap is characteristic for each semiconductor.

When an electron passes from one band to other, it leaves in its place a hole that can be considered a positive charge. When voltage is applied across the semiconductor, the electrons and their holes contribute to the electrical current, since the presence of that

electric field makes those particles move in opposite directions with respect to each other. Therefore, an electrostatic potential inside the material is created to separate positive from negative charges. Now, when the semiconductor is illuminated, it behaves like a battery; in other words, the charges accumulate in opposite areas of the chip. If an external wire connects the two areas, there will be a circulation of electric current. In solar cells made of crystalline silicon, the processes of controlled and selective contamination of the semiconductor material originate the electric field [55, 56].

The equivalent electrical circuit of a single cell is represented in Fig. 2.17, from where the following equation for the cell output current (I_o) can be derived:

$$I_o = I_\lambda - I_d - I_p \tag{2-18}$$

Where I_λ is the photon current, which depends on the light intensity and its wavelength. I_d is the Shockley temperature-dependent diode current. I_p is the PV cell leakage current. The photon current is proportional to the illumination intensity and depends on the light wavelength (λ). The parameters of this current are related to the cell short-circuit current (I_{sc}) and to the cell open-circuit voltage (V_{oc}). The short circuit current may be obtained from the *I–V* characteristic for a given PV cell when the cell output voltage is $V_o = 0$. In its turn, the open-circuit voltage is obtained for zero output current, $I_o = 0$ (no load).

Figure 2.19 shows very useful characteristics typically used for control design of power electronic systems connected to PV arrays: the output power versus the load voltage and the output power versus the load current at different illumination and temperature levels. Voltage-based power control is clearly better, as suggested by Fig. 2.19a, where the family of curves are smoother and evenly spaced [57].

Cell temperature also plays an important role in the efficiency of solar panels. Figure 2.19c and d show that for a cell illuminated by 0.6 sun under two different temperatures, t_1 = 50°C and t_2 = -25°C, the cell short-circuit current decreases whereas the open-circuit voltage increases.

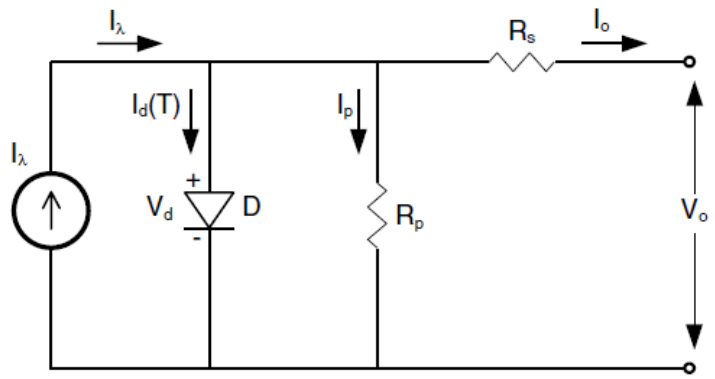

Fig. 2.17 Equivalent electrical circuit of a single PV cell

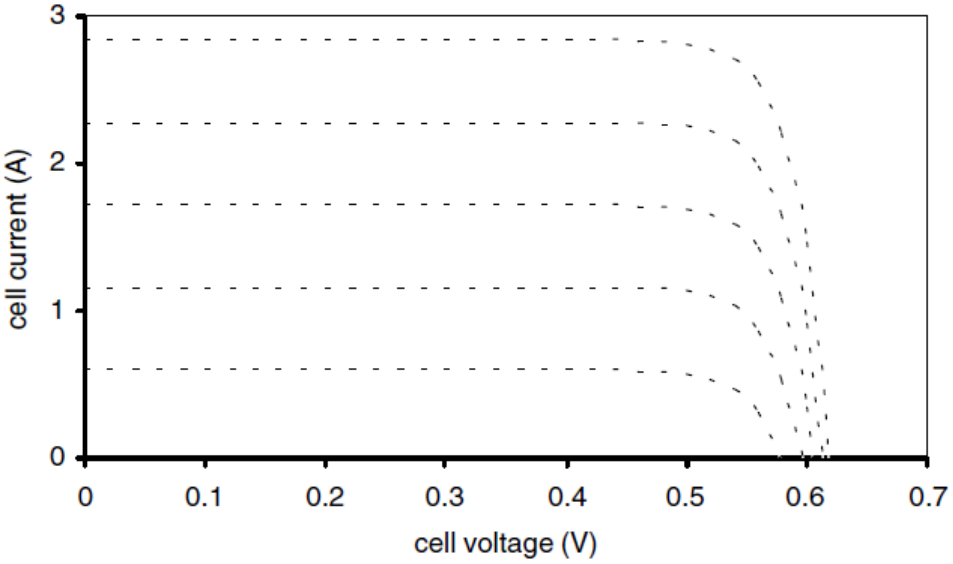

Fig. 2.18 Typical *I–V* characteristic of a PV cell

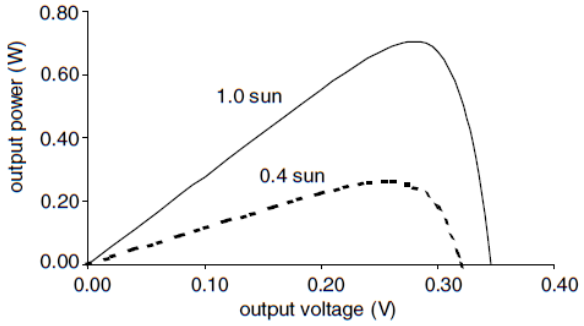

(a) Effects of the illumination level on the power versus voltage characteristic

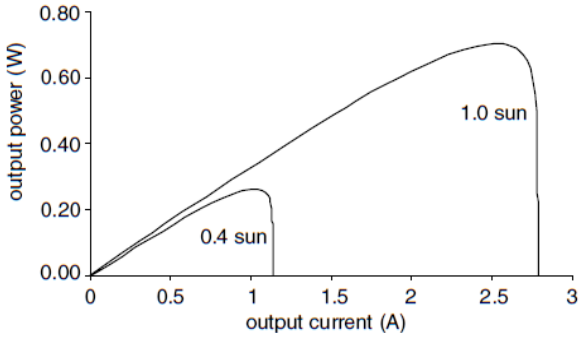

(b) Effects of the illumination level on the power versus current characteristic

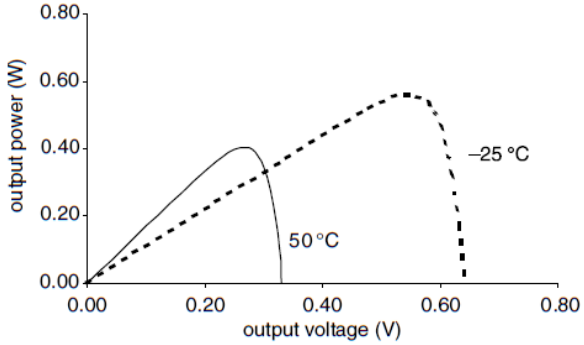

(c) Effects of the temperature on the power versus voltage characteristic

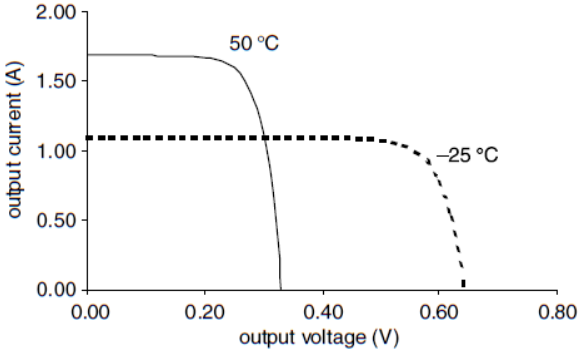

(d) Effects of the temperature on the voltage versus current characteristic

Fig. 2.19 Effects at 0.6 sun of illumination and distinct temperature on output power

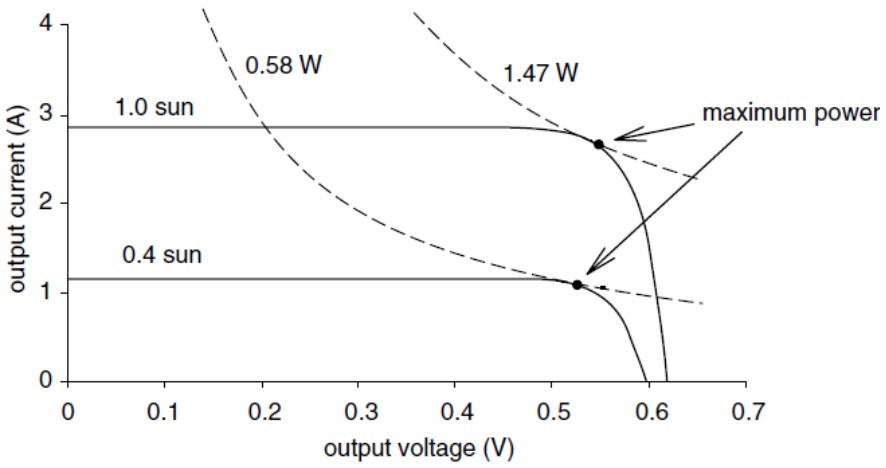

Fig. 2.20 Conditions of maximum power for various illumination levels

Equation (2.19) supports the fact that the output power of a PV cell increases with the illumination level, generating a locus of maximum power. Figure 2.20 represents the maximum output power locus for an individual PV cell. Comparing this figure with Fig. 2.19, it is interesting to observe that neither the maximum voltage nor the maximum current are the same for different levels of illumination at the maximum power point. As the output power (P_o) is given as:

$$P_o = V_o I_o \tag{2-19}$$

then the peak power may be given from the following condition:

$$\frac{dP_o}{dV_o} = V_o + I_o \frac{dV_o}{dI_o} = 0$$

that is:

$$\frac{dV_o}{dI_o} = -\frac{V_o}{I_o} \tag{2-20}$$

The meaning of this expression is that the dynamical internal resistance of the source should match the external load resistance, leading to special power peak tracking control approaches.

2.4.1 Model of a PV Panel Consisting of *n* Cells in Series

When integrating a group of PV cells in series, it is assumed that the cells are identical, resulting in the equivalence evolution of Fig. 2.21. This assumption is usually well accepted if it is taken into account that individual cells inside the panel are manufactured with very similar characteristics, to avoid circulation of internal currents among the cells. With this in mind, it is acceptable to make the assumption:

$$I_{\lambda 1} = I_{\lambda 2} = \cdots = I_{\lambda n} \qquad R_{s1} = R_{s2} = \cdots = R_{sn}$$

$$I_{d1} = I_{d2} = \cdots = I_{dn} \qquad R_{p1} = R_{p2} = \cdots = R_{pn}$$

$$V_{d1} = V_{d2} = \cdots = V_{dn}$$

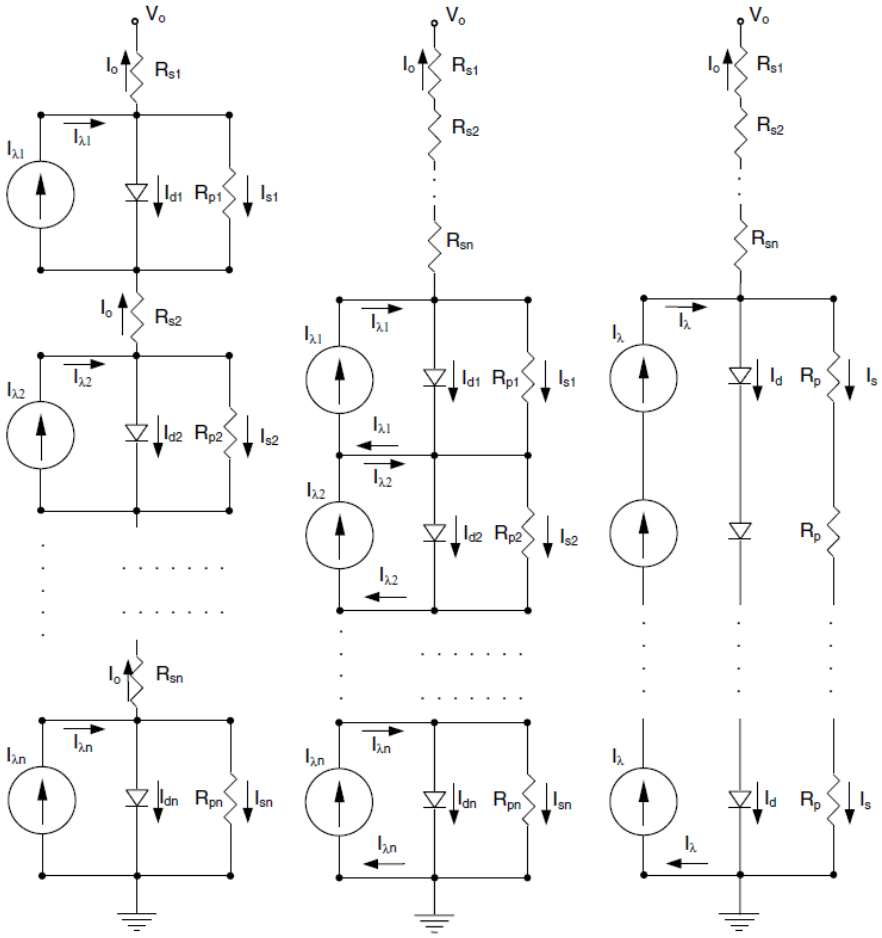

Fig. 2.21 Equivalence evolution of a series PV panel

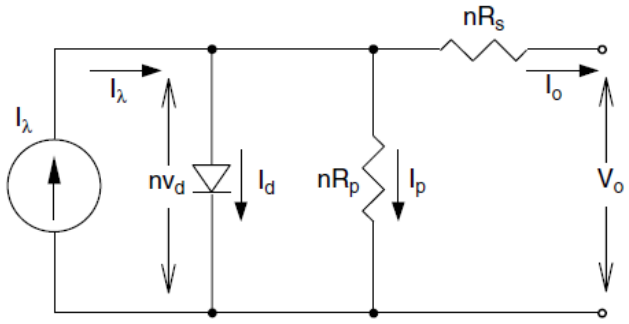

Fig. 2.22 Equivalent model of a PV panel with identical cells in series

The respective output voltage and current of the group are:

$$V_o = nV_{oi} \qquad I_o = I_{oi} \tag{2-21}$$

Where V_{oi} and I_{oi} are the average voltage and current in the individual cell I, respectively.

2.4.2 Model of a PV Panel Consisting of *n* Cells in Parallel

Assuming that the PV cells of a panel are connected in parallel across common terminals *a* and *b* as in Fig. 2.23. In these conditions, there is no direct interaction among current sources or individual diode voltages because they are considered exactly the same. Therefore, this equivalent model may assume a more compact form, as shown in Fig. 2.24.

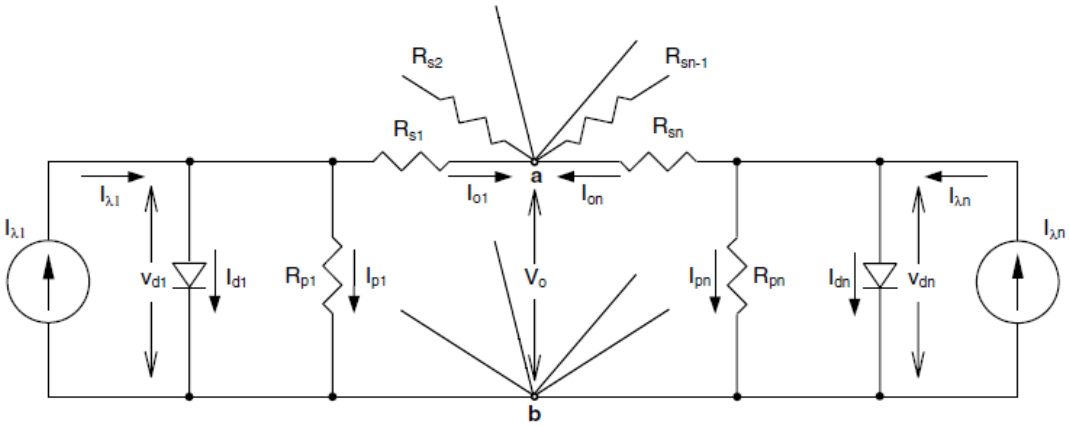

Fig. 2.23 Group of identical PV cells connected in parallel

Tests of this equivalent model can be seen as a test carried out on a single panel with individual output voltage and current for the same cell:

$$V_o = V_{oi} \qquad I_o = nI_{oi} \tag{2-22}$$

The method just described can be extended to equivalent models of series–parallel combinations of PV panels or other arrangements of interest. The PV characteristic is emulated and tested in the laboratory using a Magna-Power XR-6 kW programmable DC power supply.

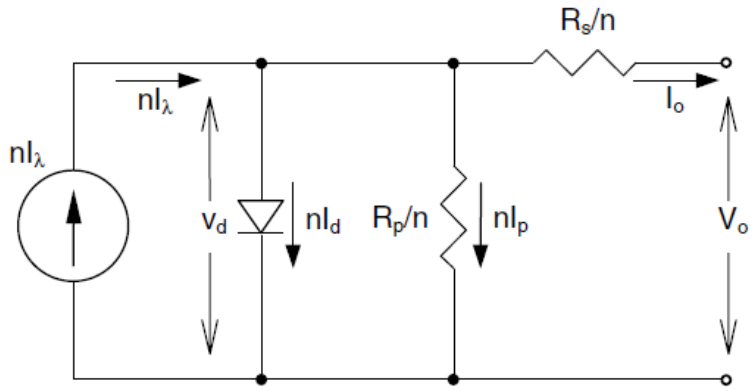

Fig. 2.24 Equivalent model of a PV panel with cells in parallel

2.5 Fuel Cells Characteristics and Dynamic Modeling

Evaluation of the dynamic performance of fuel cells for studies of electrical energy generation systems is important to reduce cost and time at the design and testing stages. An electrical model may be derived from the electrochemical equations to enable determination of the open-circuit voltage and voltage drops of cells for a specified operating point [58–61]. In power generation systems, the dynamic response is of extreme importance for the control planner and system management, especially when energy is injected into the grid. Accordingly, special attention has to be given to the dynamic response of FCs. For energy injection into the grid, the generation control has to

set the amount of power the FC will supply as a function of the load demand. As such, the dynamic FC response should be compatible with a fast variation in the random load curve, which is not always the case [62–64].

Figure 2.25 shows the FC construction of an equivalent circuit model which represents FC dynamic behavior. C is the equivalent capacitance of the system and R_a is the equivalent variable resistance to the activation and concentration losses (ohms). The membrane and contact ohmic losses are represented by R_r. The FC open circuit voltage is represented by E_{oc}. The output voltage of a single cell can be defined as V_{fc}. The instantaneous electrical power supplied by the cell to the load (P_{fc}) can be determined by:

$$P_{fc} = V_{fc} I_{fc} \tag{2-23}$$

Figure 2.26 shows the performance curves for a typical membrane used in fuel cells, which may be superimposed on the theoretical curves described by equation (2-23) for P_{fc} and V_{fc}. The efficiency (η) is defined as the relationship between the electric output power and the energy corresponding to the fuel input. When the water product is in liquid form, it is usually given as:

$$\eta = \mu_f \frac{V_c}{1.48} \tag{2-24}$$

On the other hand, when the water product is in vapor form, the efficiency is generally given as:

$$\eta = \mu_f \frac{V_c}{1.25} \tag{2-25}$$

Where μ_f is the fuel utilization factor, generally about 95%, and 1.48 and 1.25 V are the maximum voltages that can be obtained using the highest and lowest values, respectively,

of the cell enthalpy. V_c is the output voltage across the terminals of every single cell belonging to the FC stack.

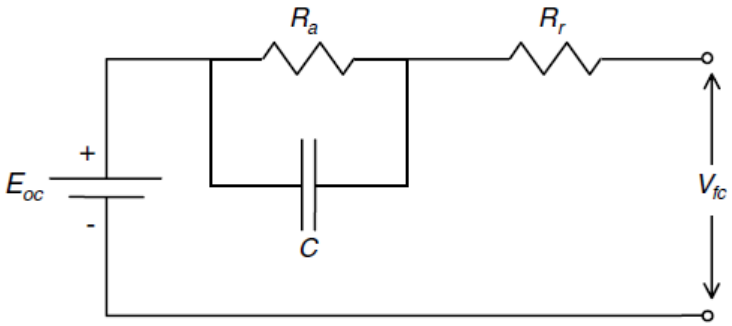

Fig. 2.25 Equivalent circuit of the dynamic behavior of a fuel cell

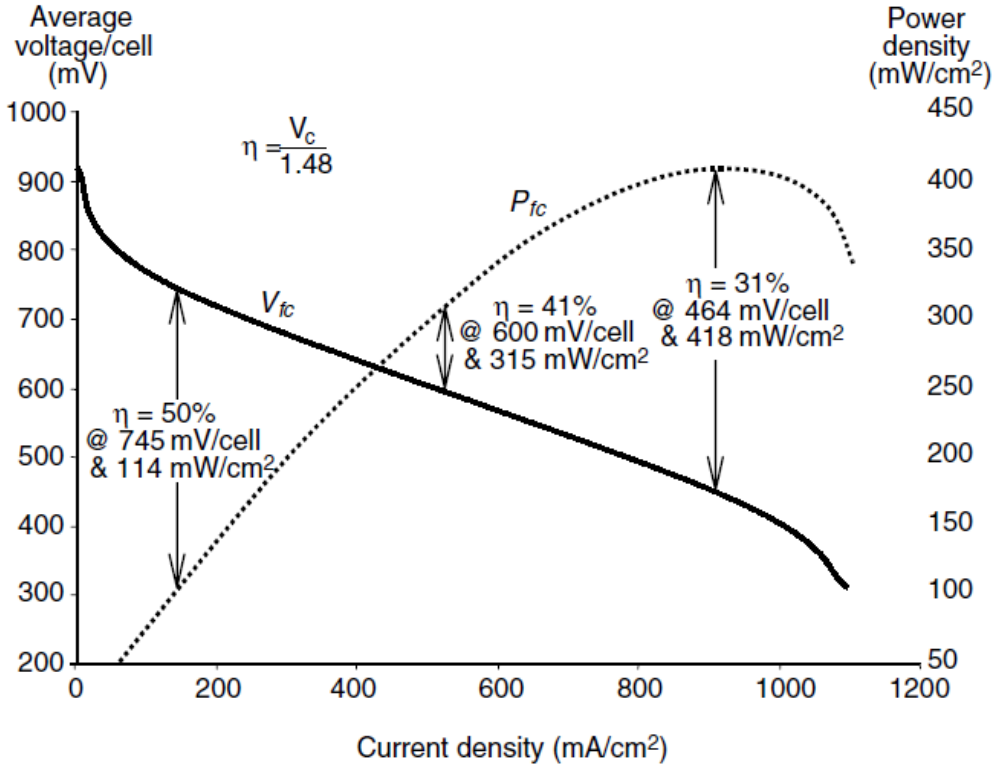

Fig. 2.26 Typical curves of fuel cells

2.6 Battery Energy Storage System Characteristics and Dynamic Modeling

Although most of the battery energy storage systems (BESSs) currently available on the market are equipped with small size battery modules; such as Ni-MH batteries, the

lead-acid batteries are still attractive and used for hybrid systems, which have relatively restricted functions and require consideration of cost effectiveness. Also, lead-acid batteries represent both reasonable cost and high reliability in automotive applications, but they generally show some drawbacks in cycle life, power characteristics, and weight, etc. Studies to improve their performance are being continuously performed, and different viewpoints have arisen providing resolutions other than strictly improving the battery itself [65-68]. Moreover, further improvement could be achieved when a proper storage device is selectively used corresponding to respective charging status and operation conditions, which can be called an advanced Hybrid Energy Storage System (advanced HESS) [69].

Figure 2.27 shows how the terminal voltage depends on the charge or discharge rate and the state of charge for a typical lead–acid battery [1]. The charge capacity of a battery is referred to as *C*. Thus, if a load is connected to a battery such that it will discharge in *n* hours, the discharge rate is *C*/*n*.

It is extremely difficult to measure accurately the state of charge of a lead–acid battery and predict the remaining capacity. In a battery, the rate at which input or output current is drawn affects the overall energy available from the battery. For example, a 100-Ah battery at a 20-hour rate means that over 20 hours, 100 Ah is available (i.e., the user can expect to draw up to 5 A per hour for up to 20 hours). If a quick discharge is imposed, the effective ampere-hours will be fewer.

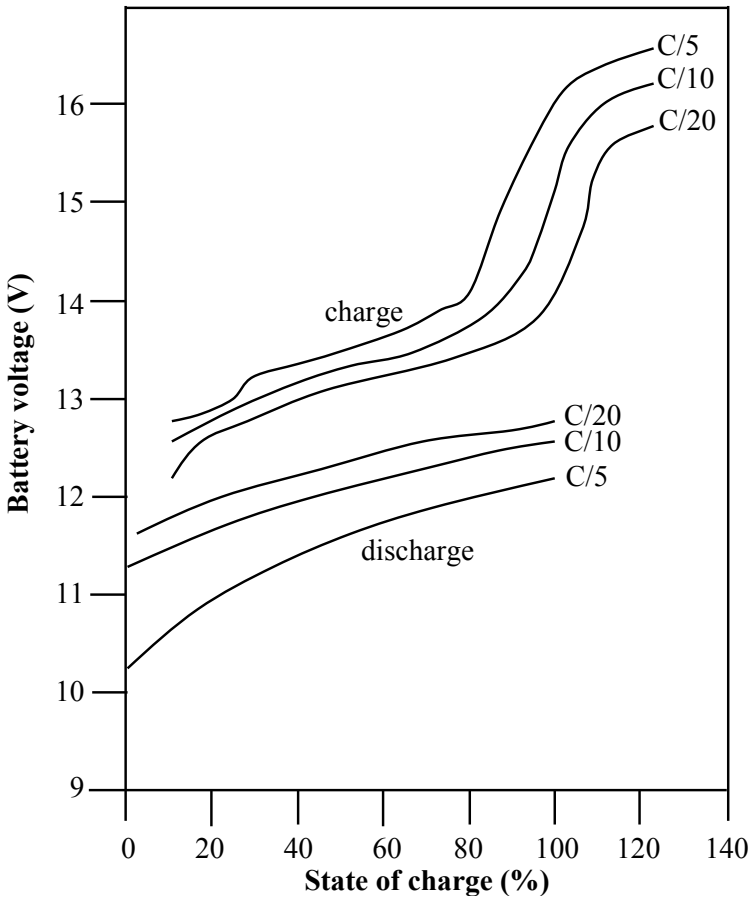

Fig. 2.27 Terminal voltage as a function of charge–discharge rate and state of charge

Figure 2.28 represents the equivalent circuit of a generic battery dynamic model parameterized to represent most popular types of rechargeable batteries [70]. Lead-acid batteries are used here which can be modeled as:

Discharge model ($i^*>0$)

$$f_1(it, i^*, i, Exp) = E_0 - K \cdot \frac{Q}{Q - it} \cdot i^* - K \cdot \frac{Q}{Q - it} \cdot it + Lapalace^{-1}\left(\frac{Exp\ (s)}{Sel\ (s)} \cdot 0 \right) \quad (2\text{-}26)$$

Charge model ($i^*<0$)

$$f_2(it, i^*, i, Exp) = E_0 - K \cdot \frac{Q}{it + 0.1Q} \cdot i^* - K \cdot \frac{Q}{Q - it} \cdot it + Lapalace^{-1}\left(\frac{Exp\ (s)}{Sel\ (s)} \cdot \frac{1}{s} \right) (2\text{-}27)$$

Where E_0 is constant voltage, *Exp(s)* is exponential zone dynamics, *Sel(s)* represents the battery mode, K is the polarization constant or Polarization resistance, i^* is the low frequency current dynamics, i is the battery current, it is the extracted capacity, and Q is the maximum battery capacity.

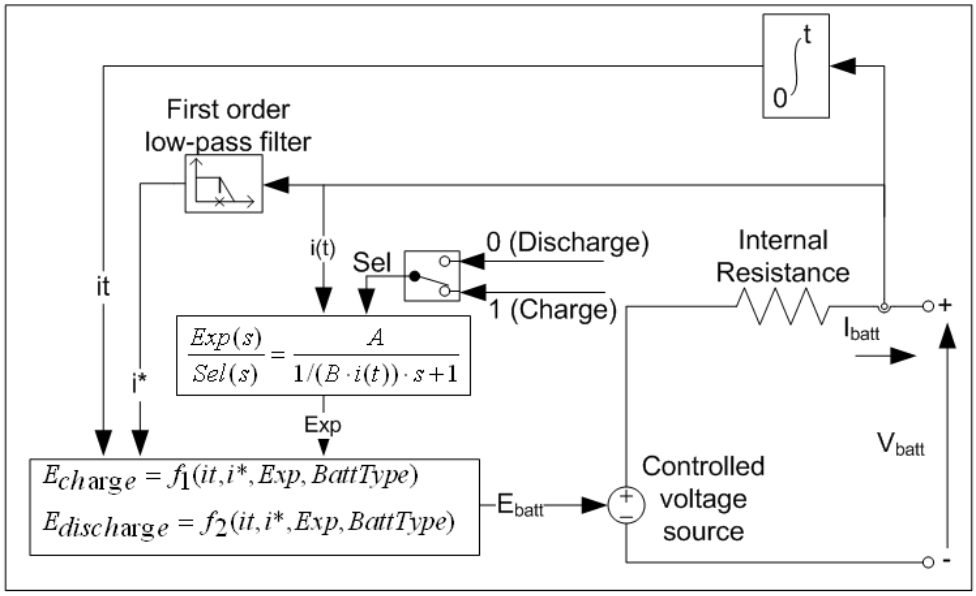

Fig. 2.28 BESS simplified model

As an example, a ten-cell battery bank has the following characteristic voltage set points:

- Quiescent (open-circuit) voltage: 12.6 V
- Discharging end voltage: 11.8 V
- Charge: 13.2 to 14.4 V
- Recommended floating voltage for charge preservation: 13.2 V

After full charge, the terminal voltage drops quickly to 13.2 V and then slowly to 12.6 V. Figure 2.29 shows a schematic of a 12 kW battery bank that was built and connected to our test bed to study the energy storage under different mode of operation.

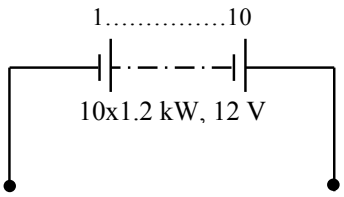

Fig. 2.29 A group of 10-batteries (each 1.2 kW) connected in series

Chapter 3 DC-Bus Voltage Control of Three-Phase Full Bridge PWM Converters Connected to Wind Powered Induction Generator

3.1 Introduction

Recently, wind generation systems are attracting attention as a clean and safe renewable energy source. The three-phase induction machine with a squirrel cage rotor or a wound rotor could work as a three-phase induction generator either connected to the utility AC power distribution line or operated in the self-excitation power generation mode with an additional stator terminal excitation capacitor bank [71].

Variable speed operation of wind turbines has many advantages that are well documented in the literature [72, 73]. Induction machines have many advantageous characteristics such as high robustness, reliability and low cost. The induction machines may be used as a motor or a generator. These machines are good candidates for wind-power electricity generation especially in remote areas, because they do not need an external power supply to produce the excitation magnetic fields [74, 75]. The excitation can be provided by a capacitor bank connected to the stator windings of the induction generator.

Many research results focusing on control point of view were reported [76-78]. Reference [76] analyzed the design methods and the performance of the voltage and current proportional plus integral (PI) controllers, which are as usually made up of inner current control loops and an outer voltage control loop in a cascade structure. The cascade control structure is not so effective for the system control of which both dynamics are close to each other. In references [77] and [78], the PWM converters have been modeled in a single nonlinear system using a power balance concept between the

input and output sides. However, the nonlinear system was analyzed and the controllers were designed using small-signal analysis, which is valid only around specified operating points, not in the whole operating range.

The difficulty in controlling the converters is mainly due to the nonlinearity. There are several ways of dealing with the nonlinearity. The simplest way is to use two PI controllers to control the DC-term and the reactive power independently [79].

Particularly, the voltage-oriented control (VOC), which guarantees high dynamic and static performance via internal current control loops. This method has become very popular and has constantly been developed and improved [80]. A conventional PI-compensator can be applied to the variables in the rotating reference frame so as to achieve a zero steady-state error in response to step commands. Then, variables in the rotating reference frame must be restored in the stationary three-phase reference frame using the inverse– transformation [81].

In this chapter, we discuss the dynamic performance of the self-excited induction generator (SEIG) driven by a variable speed wind turbine. Also, loading effect on the stator terminal voltage of the SEIG is presented. There was a tendency to operate AC/DC converters with PWM switching patterns to improve the input and output performance of the converter. In addition, a control strategy for a three-phase voltage-source PWM AC/DC converter is used in the synchronous *dq* frame. The PI-current controllers in *dq* axes are designed and analyzed to meet the time domain specification: minimum overshot, minimum settling time and minimum steady-state error. A PI voltage controller is designed to accomplish the specifications of the voltage control loop based on the dynamic of the DC-bus. In order to investigate the performance of the overall developed

system, an experimental setup for wind energy conversion system was constructed and connected to a DC-load. A digital board containing dSPACE DS1104 R&D controller board was used as the interface part of the system.

3.2 System Description

Wind is a result of the movement of atmospheric air. The prime mover for the induction generator is the wind turbine connected via a gear box as shown in Fig. 3.1. It shows only the overall mechanical and electrical connections; the controller part is not shown. The machine parameters which are used as a simulator to the wind generator are listed in Table 3.1.

3.3 Dynamic Model of the Vector Controlled PWM Converter

A power circuit and a per-phase equivalent circuit of a fully-controlled PWM voltage-source converter are shown in Fig. 3.2. It is assumed that a resistive load R_L is connected to the output terminal.

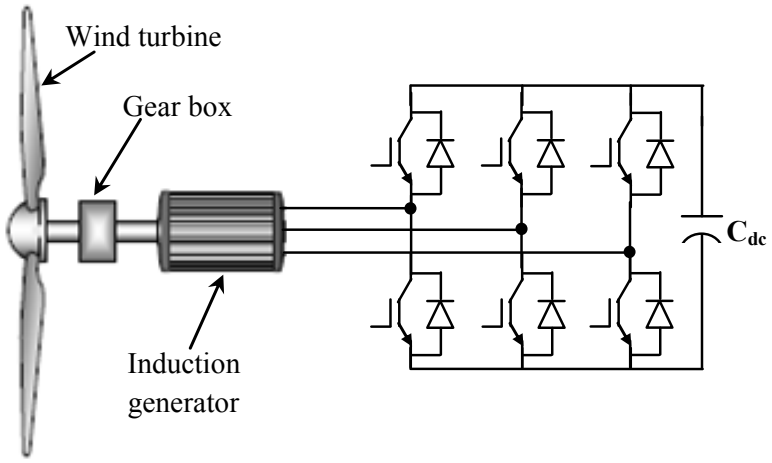

Fig. 3.1 Electrical and mechanical connections

Table 3.1 Induction generator IM-100 parameters

Symbol	Quantity	Value
hp	Output power	1/3
V_n	Nominal voltage	208 V L-L
rpm	Nominal speed	1800
I_n	Nominal current	1.7 A
R_r	Rotor resistance	3.592 Ω
R_s	Stator resistance	6.294 Ω
L_{ls}	Stator self-inductance	0.0168 H
L_{lr}	Rotor self-inductance	0.0168 H
L_m	Mutual inductance	0.464 H
J	Moment of inertia	0.03338 Kg.m^2

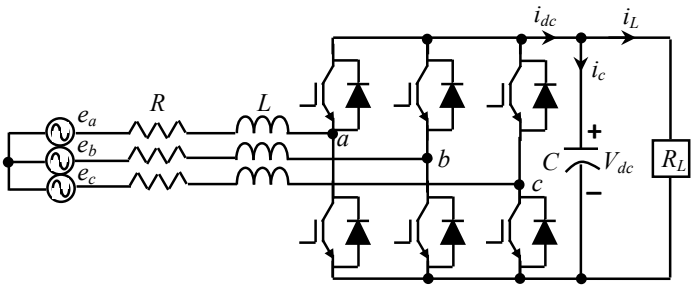

(a)

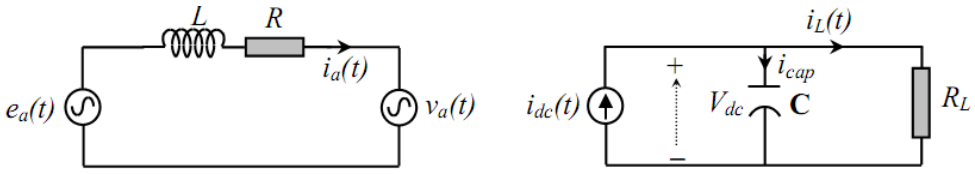

(b) (c)

Fig. 3.2 AC/DC PWM converter: (a) Power circuit, (b) Per-phase input equivalent circuit, and (c) Per-phase output equivalent circuit

From the equivalent circuit shown in Fig. 3.2.b, assuming generator voltage is 3-phase balanced voltage source and its state equations are:

$$\begin{bmatrix} e_a(t) \\ e_b(t) \\ e_c(t) \end{bmatrix} = \begin{bmatrix} E\sin\omega t \\ E\sin(\omega t - 2\pi/3) \\ E\sin(\omega t + 2\pi/3) \end{bmatrix} \tag{3-1}$$

Where E is the maximum amplitude of the generator AC voltage, (R, L) are the line inductor and resistance between generator and the converter terminal, respectively, e_a is the generator phase voltage, v_a is the bridge converter voltage controllable according to the demanded DC-voltage level, i_a is the line current, i_{dc} is the converter DC-output current, v_{dc} is the converter DC-output controlled voltage, i_c is the DC-link capacitor current, and i_L is the load current. From Fig. 3.2.b., the dynamic equation for the input side of the three phase converter system can be written as:

$$e_{abc}(t) - v_{abc}(t) = L\frac{di_{abc}(t)}{dt} + Ri_{abc}(t) \tag{3-2}$$

Referring to Fig. 3.2.c., the dynamic equation for the output side of the three phase converter system can be written as,

$$i_c(t) = i_{dc}(t) - i_L(t) = C\frac{dv_{dc}(t)}{dt} \tag{3-3}$$

The line voltage, the phase current, and the terminal voltage of the PWM converter can be transformed to a synchronous reference frame using the transformation matrix H(θ) as follows:

$$\begin{aligned} v_{abc}(t) &= H(\theta).v_{dq}(t) \\ v_{dq}(t) &= H^{-1}(\theta).v_{abc}(t) \end{aligned} \tag{3-4}$$

$$H^{-1}(\theta)=\begin{bmatrix}\cos\theta & \frac{1}{\sqrt{3}}\sin\theta & \frac{-1}{\sqrt{3}}\sin\theta \\ \sin\theta & \frac{-1}{\sqrt{3}}\cos\theta & \frac{1}{\sqrt{3}}\cos\theta\end{bmatrix} \tag{3-5}$$

Where θ is the rotating angle of transformation. Now, the dynamic equation (3-2) can be transformed directly from the *abc* frame to the synchronous reference frame resulting in a mathematical model for the PWM converter in a synchronous rotating coordinates:

$$e_{dq}(t)-v_{dq}(t)=R.i_{dq}(t)+L\frac{di_{dq}(t)}{dt}-L.\omega.M.i_{dq}(t) \tag{3-6}$$

Where $M=\begin{bmatrix}0 & 1 & 0\\ -1 & 0 & 0\\ 0 & 0 & 0\end{bmatrix}$

For more simplification, we assume that the three-phase voltage source is balanced without zero sequence component. Therefore, (3-6) can be written as:

$$\begin{aligned} v_d(t)&=e_d(t)-L\frac{di_d(t)}{dt}-R.i_d(t)+L.\omega.i_q(t)\\ v_q(t)&=e_q(t)-L\frac{di_q(t)}{dt}-R.i_q(t)-L.\omega.i_d(t)\end{aligned} \tag{3-7}$$

The converter system in the s-domain can be obtained by applying Laplace transformation to the dynamic equations in the synchronous frame directly such as:

$$\begin{aligned} i_d(s)&=\frac{1}{Ls+R}.\left[e_d(s)-v_d(s)+\omega.L.i_q(s)\right]\\ i_q(s)&=\frac{1}{Ls+R}.\left[e_q(s)-v_q(s)-\omega.L.i_d(s)\right]\end{aligned} \tag{3-8}$$

For the converter output side:

$$v_{dc} = \frac{R_L}{1 + CR_L s} . i_{dc} \tag{3-9}$$

Now, we should derive the active and reactive power to get the relation between i_d and i_{dc} where the complex power S is the sum of the active power P and reactive power Q, and is defined as:

$$S = \underline{E}.\underline{I}^* = P + jQ \tag{3-10}$$

Where the subscript * means complex conjugate, in the synchronous frame:

$$\begin{aligned} P &= \frac{3}{2}\mathrm{Re}\{[\underline{E_d} + j\underline{E_q}].[\underline{I_d} + j\underline{I_q}]^*\} \\ P(t) &= \frac{3}{2}[e_d(t).i_d(t) + e_q(t).i_q(t)] \\ Q &= \frac{3}{2} I_m\{[\underline{E_d} + j\underline{E_q}].[\underline{I_d} + j\underline{I_q}]^*\} \\ Q(t) &= \frac{3}{2}[e_q(t).i_d(t) - e_d(t) i_q(t)] \end{aligned} \tag{3-11}$$

In a balanced case and unity power factor operation, the q-component for the generator voltage and current are zero. Therefore, (3-11) can be modified to:

$$P(t) = \frac{3}{2} . e_d(t).i_d(t) \tag{3-12}$$

Assuming no power dissipation in the converter power switches, the converter input power is equal to the output, thus:

$$P(t) = v_{dc}(t).i_{dc}(t) \tag{3-13}$$

Then, from (3-12), (3-13):

$$i_{dc} = \frac{3}{2}\frac{e_d(t)}{v_{dc}(t)} . i_d \tag{3-14}$$

The converter plant model in s-domain representation is shown in Fig. 3.3.

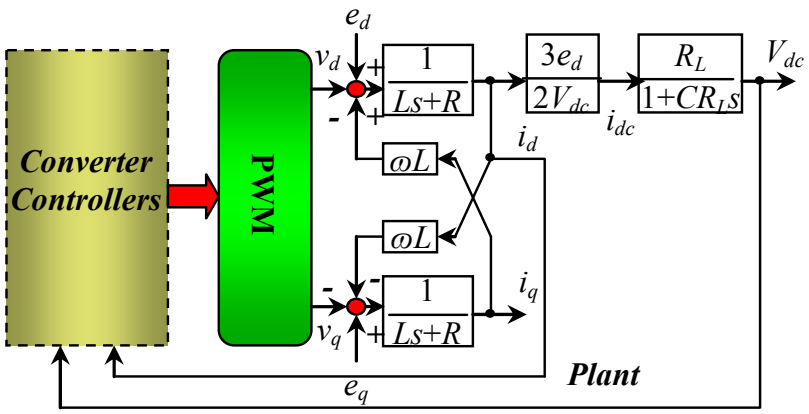

Fig. 3.3 Converter model block diagram

3.4 Voltage Oriented Control Technique

The block diagram of the wind power generation system studied in this section involving the developed VOC technique is shown in Fig. 3.4. The wind turbine is coupled to the shaft of a SEIG through a gear box. The generator is connected to current regulated PWM voltage source converter with current and voltage regulation utilizing VOC control of the supply. In this control scheme, the output DC voltage is controlled by a voltage loop, where a PI controller acts on the DC-voltage error to generate references for the AC currents in the stationary (*abc* or *dq*) or rotating (*dq*) frames. PI current regulators ensure that the input AC currents track these references. Note that the current loop uses two PI regulators in the rotating *dq* frame in these approaches.

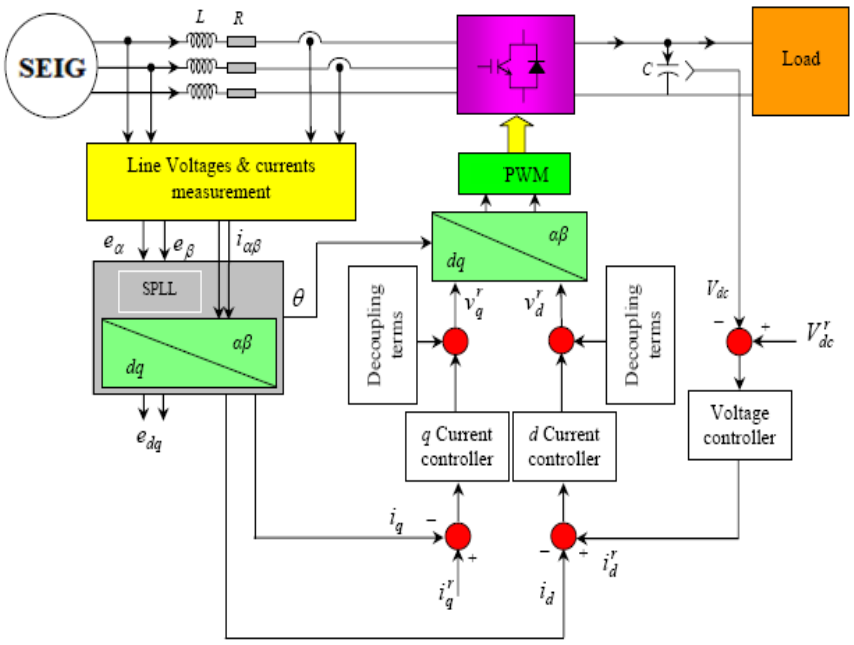

Fig. 3.4 SEIG wind energy conversion system

From the converter dynamic equations in synchronous frame, (3-7), there are coupling terms between these equations. This degrades the dynamic performance (slow the controller transient and cause high overshoots) of the system. These terms are the coupling q-current componenet ($\omega L i_q$) and generator voltage on the d-axis equation, e_d , while coupling d-current component ($\omega L i_d$) and e_q on the q-axis. The vector controller will decouple these terms, giving the ability to control each current component separately without any effect from the other component.

The two current components, i_d and i_q, could be oriented to control the converter operation via internal current control loops. Consequently, the system performance is largely depending on the quality of applied current control technique.

Two current controllers are utilized as inner controllers. The first is q-current controller with reference i_q^r which determines the reactive power. By setting $i_q^r = 0$, the unity power factor operation is achieved. The other is the d-current controller with i_d^r set

by the outer DC-voltage controller and decides the active power flow between the wind generator and the DC-bus. The converter DC-voltage is determined by $i_{dc}(t)$-$i_L(t)$, as shown in Fig. 3.2.c., such that:

$$V_{dc}(t) = \frac{1}{c}\int [i_{dc}(t) - i_L(t)]dt \tag{3-15}$$

Using the PI-voltage controller, the DC-voltage can be regulated by choosing the DC current reference, $i_{dc}{}^r(t)$ such that:

$$i_{dc}{}^r(t) = K_p{}^v.[V_{dc}{}^r - V_{dc}(t)] + K_i{}^v \int [V_{dc}{}^r - V_{dc}(t)]dt \tag{3-16}$$

Where $V_{dc}{}^r$ is the desired DC voltage, $K_p{}^v$, $K_i{}^v$ are the constant gains of the PI-voltage controller. From (3-15):

$$\begin{aligned} i_d{}^r(t) &= \frac{2V_{dc}}{3e_d}.i_{dc}{}^r \\ i_q{}^r(t) &= 0 \end{aligned} \tag{3-17}$$

From (3-12), the current can be constructed to give the suitable voltage drop across the inductor $L\dfrac{di_{dq}(t)}{dt}$ as follows:

$$\begin{aligned} v_d{}^r(t) &= e_d(t) - U_d{}^v - R.i_d(t) + L.\omega.i_q(t) \\ v_q{}^r(t) &= e_q(t) - U_q{}^v - R.i_q(t) - L.\omega.i_d(t) \end{aligned} \tag{3-18}$$

Where $v_d{}^r(t)$, $v_q{}^r(t)$ are the d and q voltage references, respectively, and $U_d{}^v$, $U_q{}^v$ are the effective voltage reference which can be obtained using PI-current controllers as follows:

$$\begin{aligned} U_d{}^v &= K_p{}^i.[i_d{}^r(t) - i_d(t)] + K_i{}^i.\int [i_d{}^r(t) - i_d(t)]dt \\ U_q{}^v &= K_p{}^i.[i_q{}^r(t) - i_q(t)] + K_i{}^i.\int [i_q{}^r(t) - i_q(t)]dt \end{aligned} \tag{3-19}$$

Where K_p^i, K_i^i are the constant gains of the PI-current controllers. The structure of the PI-voltage and current controllers for the rectifier system is shown in Fig. 3.5.

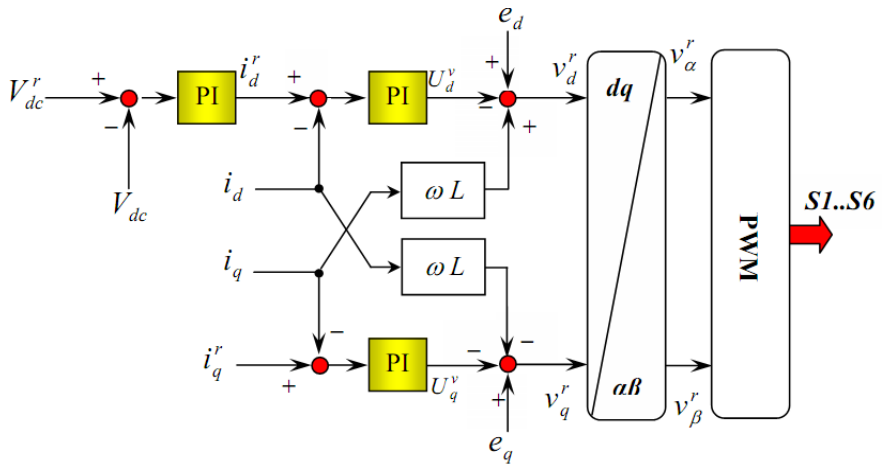

Fig. 3.5 The structure of the PI-voltage and decoupled current controllers for the PWM converter

3.5 Simulation and Experimental Results

In order to investigate the dynamic performance of the VOC algorithm, a simulation program using Matlab/Simulink™ was carried out using simulation parameters shown in Table 3.2. The PWM studied in this section was used with a 5-kHz switching frequency. The vector converter control strategy discussed in section 3.4 is utilized in the simulation. Two inner PI-controllers are used as current controllers; one for the *d*-component and the other for the *q*-component. The outer PI is the voltage controller. Fig. 3.6 shows the experimental setup for the overall WECS. The wind generator is represented by variable speed prime mover (VSPM) coupled with SEIG. A photograph for the experimental WECS connected to DC-load is shown in Fig. 3.7.

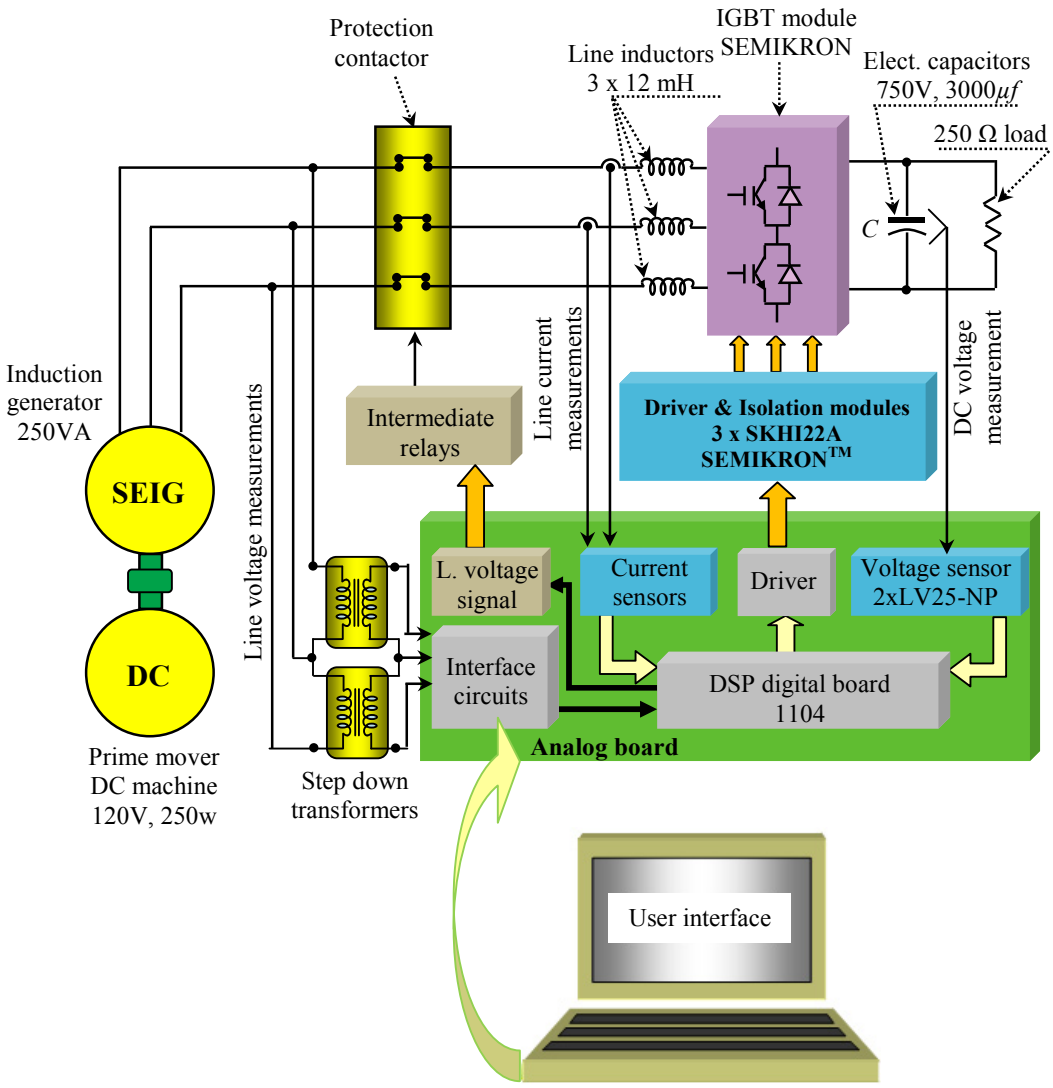

Fig. 3.6 Wind energy model drives a PWM voltage source converter laboratory setup

Table 3.2 Simulation parameters for the PWM converter

Parameter	Value	Parameter	Value
Generator frequency	60 Hz	Generator voltage	120 Vrms
DC link voltage	400 V	DC-link capacitor	1200 *uF*
Resistive load	250 *Ohm*	Line inductor	12 *m*H
Switching frequency	5 kHz	Internal Resistance	2.7 Ω

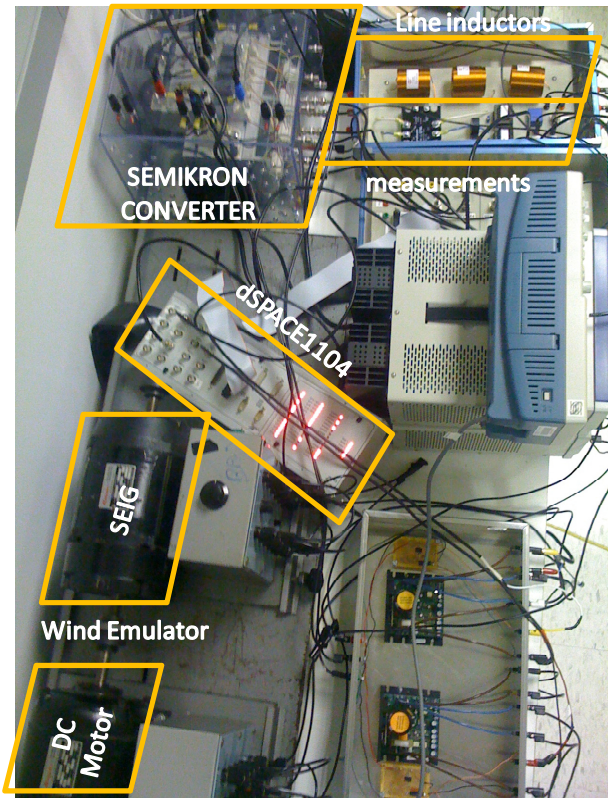

Fig. 3.7 Experimental setup laboratory for the WECS

3.5.1 The Software Design Flow Chart

This section is concerned with formulating a software program code designed using Matlab/Simulink that will instruct the DSP Controller to control the DC-bus voltage under UPF operation. Programming DSPs using Simulink provides portability and maintainability. Preparing and testing the program in Matlab is relatively easier than using an assembly language and the program can be optimized to this particular processor architecture. The software design is the main heart of the control system, as it includes all theories introduced in previous sections. The DSP controller commands the operation of the experiment setup by the use of the software design. The flowchart shown in Fig.

3.8 describes the software experimental steps. The initialization section is where all the variables and constants that will be used in the program are initialized.

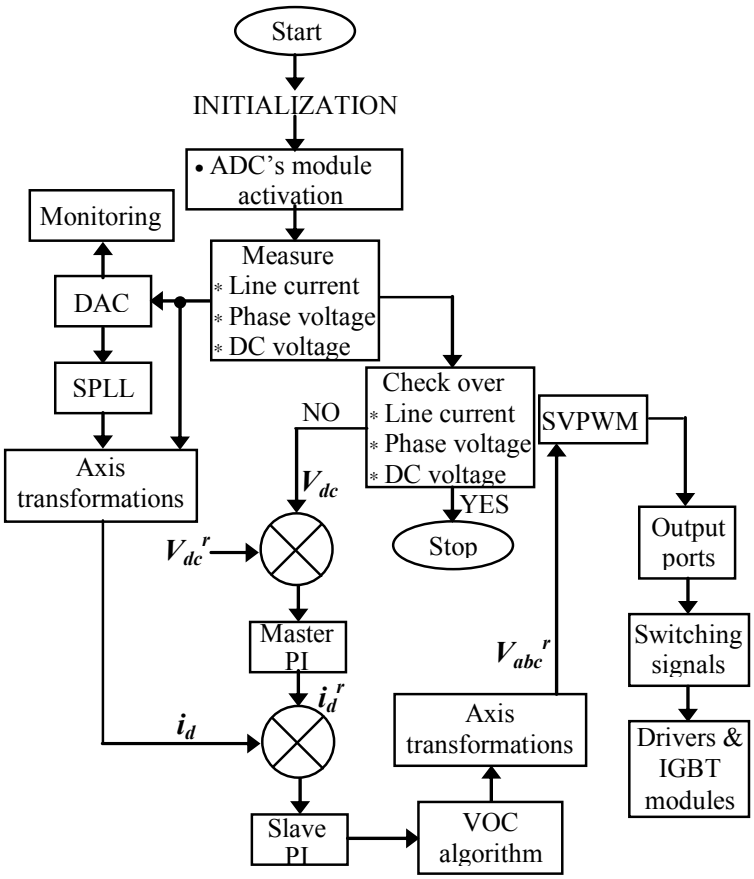

Fig. 3.8 Rectifier control software flow chart

3.5.2 Characteristics of Magnetizing Inductance

To model an induction machine when used for motoring application, it is important to determine the magnetizing inductance at rated voltage. In the SEIG, the variation of magnetizing inductance is the main factor in the dynamics of voltage buildup and stabilization. In this investigation, the magnetizing inductance is calculated by driving the induction machine at synchronous speed. The magnetizing inductance L_m used in this test is given in Fig. 3.9. It is based on the rated frequency (60 Hz) of the induction machine where the curve is a fourth-order curve fit given by:

$$L_m = -1.62\times10^{-11}V_{ph}^4 + 2.67\times10^{-8}V_{ph}^3 - 1.381\times10^{-5}V_{ph}^2 + 1.76\times10^{-3}V_{ph} + 0.23 \quad (3\text{-}20)$$

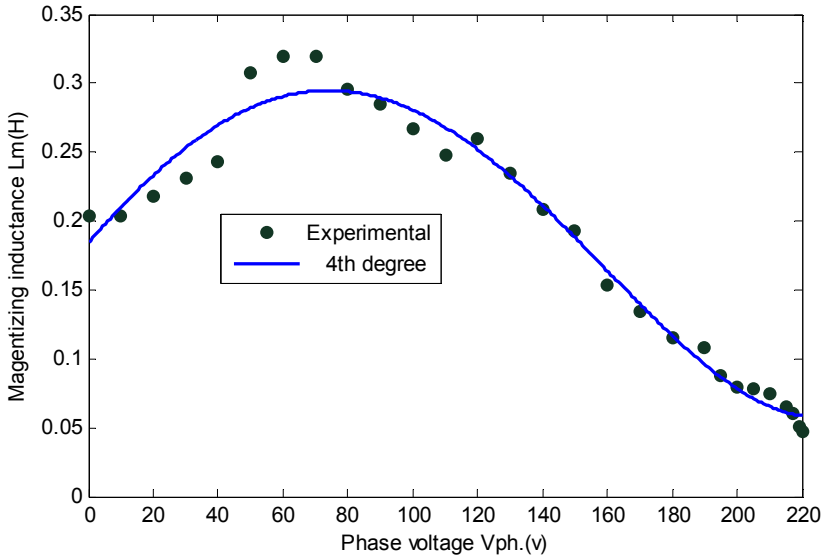

Fig. 3.9 Variation of magnetizing inductance with phase voltage at rated frequency

3.5.3 Process of Self-Excitation

The following figure shows the process of self-excitation in an induction machine under no-load condition. From Fig. 3.10, we can say that the self-excitation follows the process of magnetic saturation of the core and a stable output is reached only when the machine core is saturated.

3.5.4 Effect of Load Variation

When an induction machine operates as a motor at a constant frequency, the speed of the air-gap rotating magnetic field is fixed. When this motor is loaded the rotor speed will be varied relative to the synchronous speed. For a SEIG with constant rotor speed, the speed of the rotating magnetic field lags behind the rotor speed. When the load of the SEIG is increased from (1.5 to 2A), the magnitude of the negative slip also increases. In this case, as the rotor speed is the input, the increase in slip is due to a decrease in the speed of the rotating magnetic field. The generated frequency and voltage are

proportional to the speed of the rotating magnetic field. A decrease in the speed of the rotating magnetic field will inevitably decrease the generated voltage and its frequency. The simulation and experimental results given in Fig. 3.11, respectively, confirm this. It can be seen that for the same speed, the voltage and frequency drop with load.

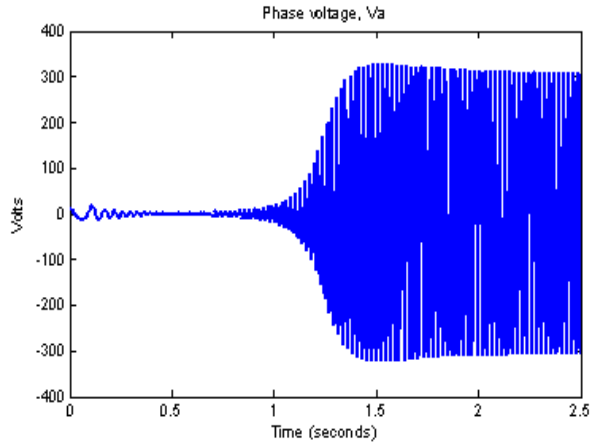

(a)

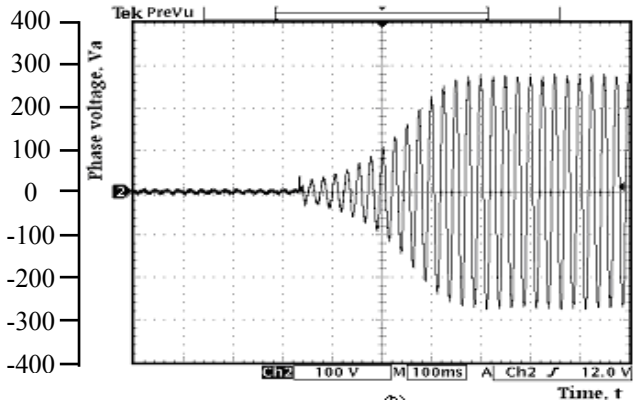

(b)

Fig. 3.10 Voltage build up in a self-excited induction generator: (a) simulation and (b) experimental

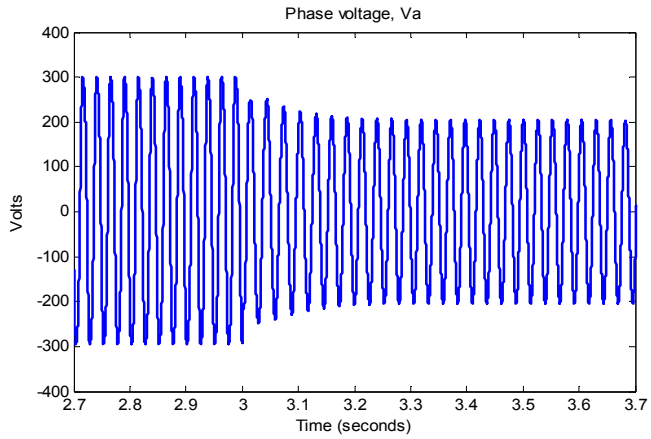

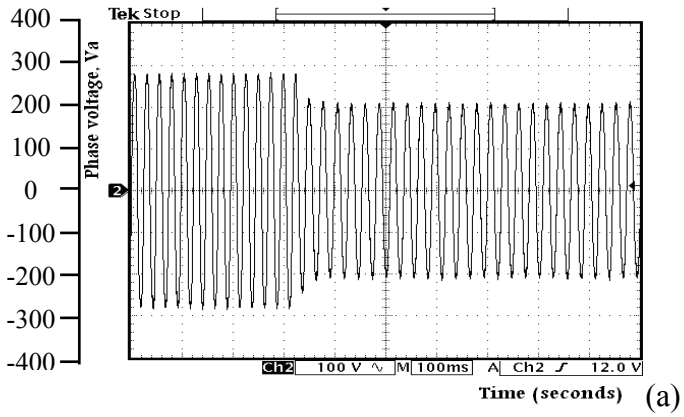

(a)

(b)

Fig. 3.11 Loading of SEIG after the voltage has developed to its steady-state value: (a) simulation and (b) experimental

3.5.5 2nd Order Software Phase Locked Loop for Phase Angle Detection

A good detection of the phase angle of the generated power is highly recommended in WECSs utilizing converter-inverter unites. A zero-voltage crossing detection method, where the zero voltage must be accurately detected each half period, can be used. However, the synchronization must be updated, not just at the zero voltage, but continuously during the whole period, because multi-zero crossing can occur with the existence of noise [82]. The Phase Locked Loop (PLL) technique can be applied here for precise detection of the phase angle. PLL is widely used in communication engineering

because of its excellent noise rejection capability [83]. A hybrid (hardware & software) PLL was introduced by Jovan [84] for synchronizing a single-phase PWM inverter (UPS) with the grid. However, this technique needs software and hardware implementations. A fully software PLL for the phase angle detection of the three phase generator voltage is used here using the *dq* synchronous reference frame [85]. Fig. 3.12 shows a basic block diagram of the applied PLL. The output of the voltage controlled oscillator (VCO), F_{ref}, is fed-back to the phase frequency detector input, and comparison continue until both frequency and phase are made the same and the phase and frequency of the VCO are in locked state with reference signal i.e. $F_{osc} = F_{ref}$, $\theta_{osc} = \theta_{ref}$. The closed loop transfer function of the PLL system of Fig. 3.12 can be expressed as:

$$W(s) = \frac{\theta_{osc}(s)}{\theta_{ref}(s)} = \frac{K_{\phi} K_f(s) K_v(s)}{1 + K_{\phi} K_f(s) K_v(s)} \tag{3-21}$$

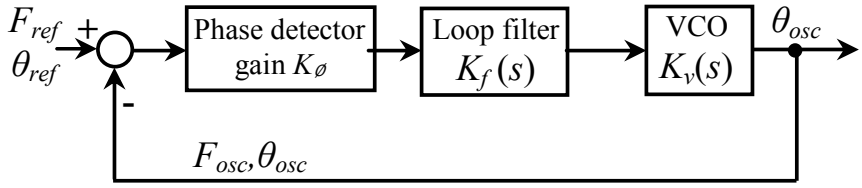

Fig. 3.12 Basic PLL block diagram

The VCO transfer gain $K_v(s)$ is a function of time, since phase is the time integral of frequency, it may be written as:

$$K_v(s) = \frac{K_v}{s} \tag{3-22}$$

The phase frequency detector gain, K_{ϕ}, is assumed to be independent of frequency. With unity VCO gain, K_v=1, (3-21) can be rewritten as:

$$W(s) = \frac{K_\phi K_s(s)}{s + K_\phi K_s(s)} \tag{3-23}$$

There are several methods to design the loop filter. The 2nd order loop filter is commonly used as a good trade-off of the filter performance and system stability [86]. The 2nd order PI-loop filter can be expressed in the form:

$$K_f(s) = K_p + K_i / s \tag{3-24}$$

Therefore, the SPLL transfer function will be:

$$W(s) = \frac{K_\phi K_p s + K_\phi K_i}{s^2 + K_\phi K_p s + K_\phi K_i} \tag{3-25}$$

The general form of the closed loop transfer function of the second order system is given by:

$$W(s)_{General} = \frac{\omega_n^2}{s^2 + 2\xi\omega_n s + \omega_n^2} \tag{3-26}$$

Comparing (3-25) with (3-26):

$$K_i = \frac{\omega_n^2}{K_\phi} \qquad \text{and} \qquad K_p = \frac{2\xi\omega_n}{K_\phi} \tag{3-27}$$

The configuration of the PLL system using the *dq* components in the synchronous reference frame of the three phase input voltage is shown in Fig. 3.13. Figure 3.14 shows the simulated and experimental response of the SPLL system at 60Hz, 120V. The synchronous reference frame *dq*-voltage appears as DC-values. This technique achieved high accuracy (error=0.04) which leads to better performance for the control system and very fast transient response within a fraction of millisecond (0.1 msec) during frequency step change due to wind speed

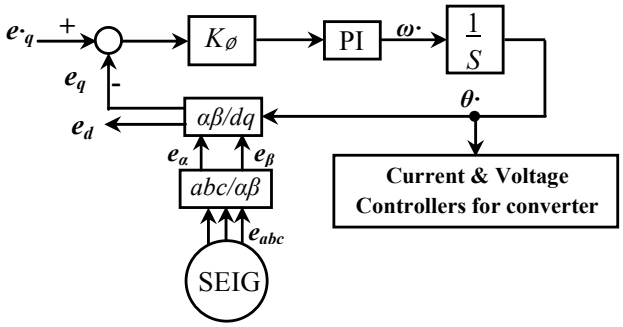

Fig. 3.13 SPLL applied for wind generation converter

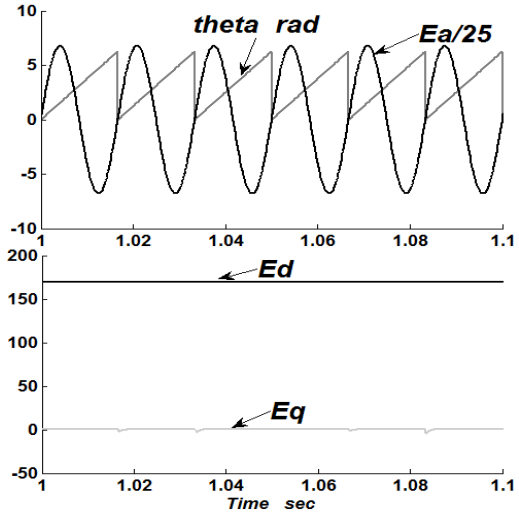

(a)

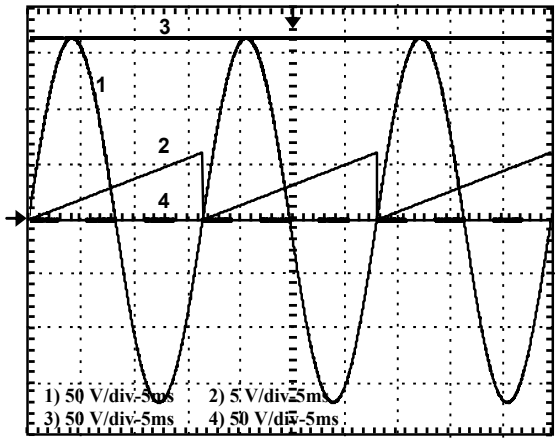

(b)

Fig. 3.14 The SPLL response: (a) Simulation and (b) Experimental (1-Generator voltage, phase angle, and 3, 4-synchronous frame *dq* voltage waveforms for phase "a")

3.5.6 Converter Experimental Setup and Evaluation Results

The system experimental setup is constructed of a three phase converter IGBT full wave bridge connected to a three phase SEIG (Hampden™, 1/3 hp). A three line inductors each with inductance 12 mH are mounted in series between the generator terminals and the converter. The wind turbine is modeled by a DC motor (Hampden™ 120V, 1/3 hp) working as a prime mover. In order to evaluate the performance of developed emulator in turbulent wind speed condition an experimental test was carried out. Fig. 3.15 shows the daily average wind speed at Chicago City during 2009.

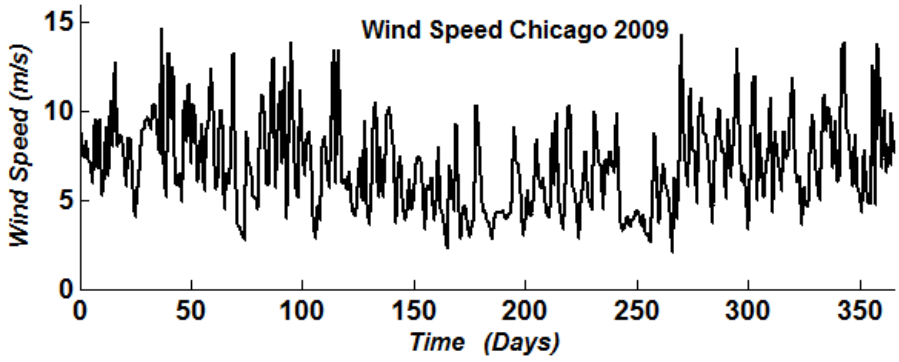

Fig. 3.15 Daily average wind speed in Chicago 2009

The SPWM technique used in the converter simulation was investigated. Fig. 3.16 shows the generator output voltages e_{abc}, at 60 Hz with the converter terminal phase voltages v_{abc}. The converter terminal line voltages v_{L_abc} are shown in Fig. 3.17.

3.5.7 DC Reference Change Test

In order to confirm the transient behavior of the DC-voltage controller used in the built converter system, it was exposed to step changes in the DC-voltage from 400V to 500V. The experimental results compared with the simulation results are shown in Fig. 3.18. The simulation results shown with the experimental results give great agreement. The generator phase voltage and line current are shown in Fig. 3.19.

It is clear from these results that good tracking and regulation performance are attained due to the presence of the VOC technique for converter system. The voltage controller provides a rapid and accurate response for the reference. The unity power factor (UPF) demand was investigated in Fig. 3.20, where the generator line current and the phase voltage are in phase.

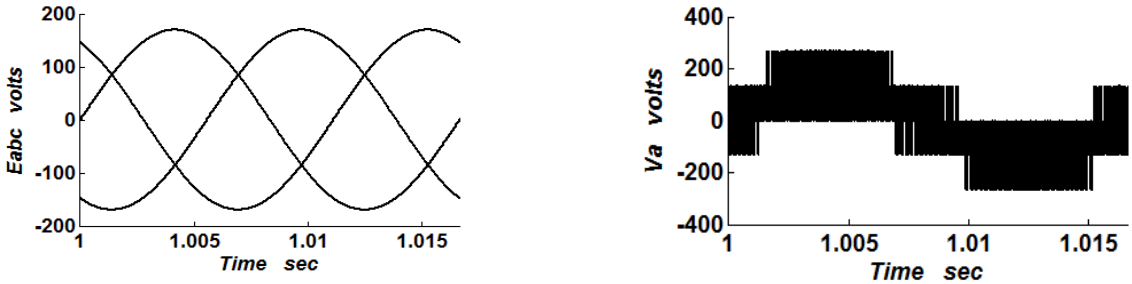

(a)

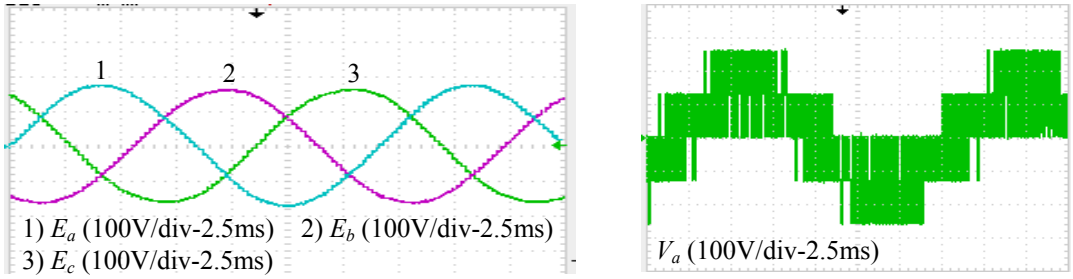

(b)

Fig. 3.16 Generator output voltages and converter terminal phase voltages: (a) Simulation and (b) Experimental

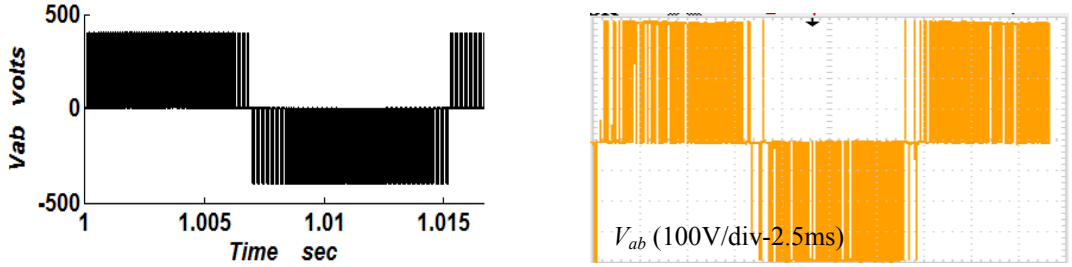

(a) (b)

Fig. 3.17 Converter terminal line voltages: (a) Simulation and (b) Experimental

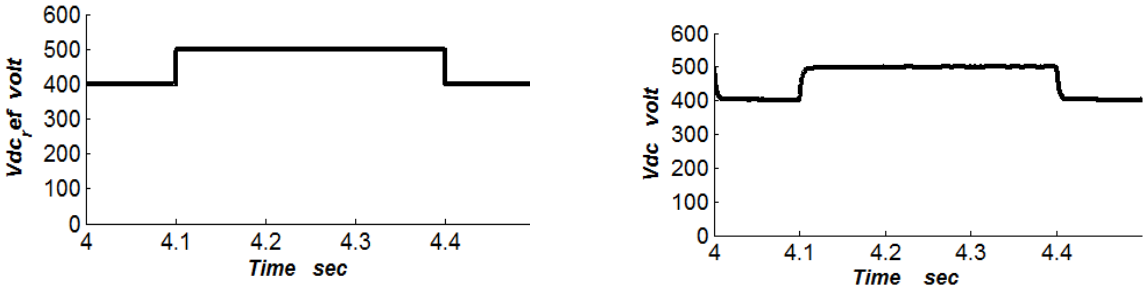

(a)

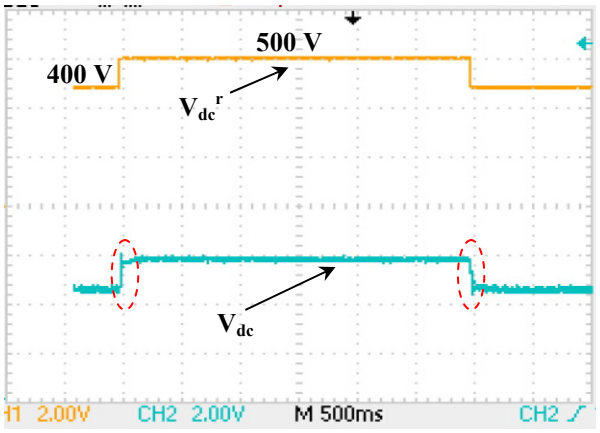

(b)

Fig. 3.18 Converter output response for reference & actual DC-voltage: (a) Simulation and (b) Experimental

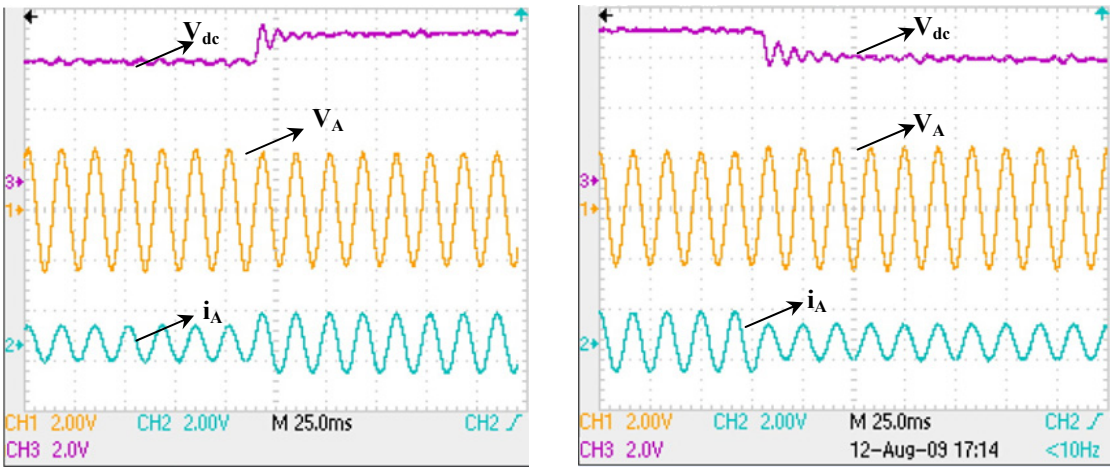

(a) (b)

Fig. 3.19 The zooming window for the generator phase voltage and line current: (a) positive edge and (b) negative edge

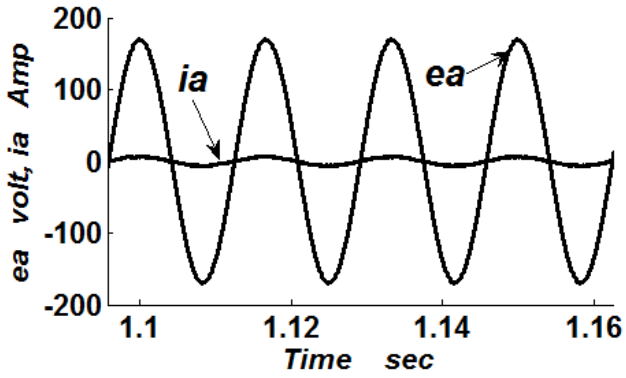

(a)

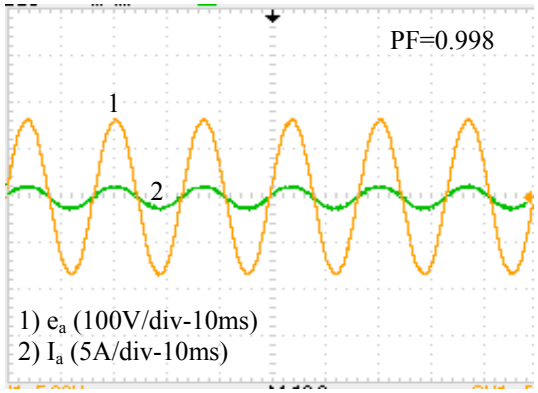

(b)

Fig. 3.20 The generator phase voltage and line current showing the unity power factor at 60Hz: (a) Simulation and (b) Experimental

3.5.8 DC-Output Voltage under Load Variation

The converter response under load variations is shown in Fig. 3.21. We started loading the DC-bus by R_L=40 Ω and at 3.2 sec load changed to be 60 Ω. At 3.8 sec, the load returns to its initial value of 40 Ω. From DC-output voltage waveform, we can notice that the system gives a good and fast transient performance during loading change instants and returns to its reference value within 0.1 sec. Since the load resistance increases at 3.2 sec, the generator current should produce less current while the load and DC-output current decreases.

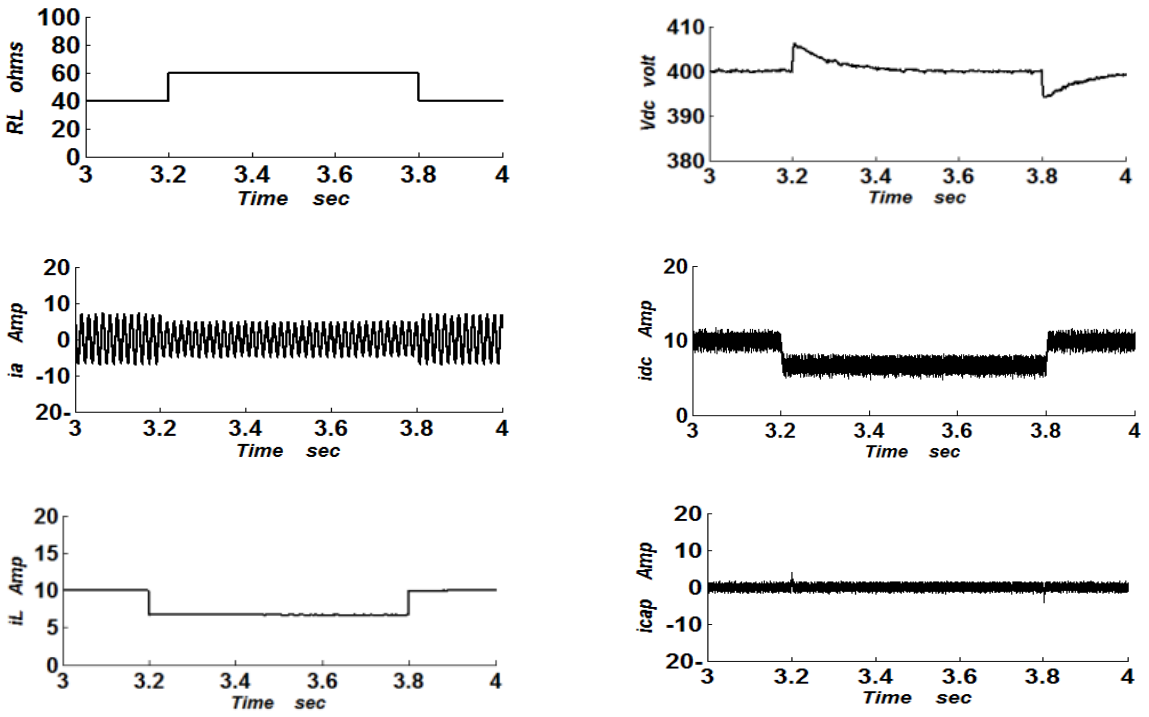

Fig. 3.21 Converter's variables response under load step change

3.5.9 Generator Voltage and Frequency Variation Test

Imitating the variation in wind speed, which leads to variation in the generator output voltage and frequency, is shown in Fig. 3.22. The Figure shows the converter output DC-voltage under step change in the generator output voltage and frequency. Fig. 3.22.a represents the falling response in the DC-voltage with the line current and phase voltage, while Fig. 3.22.b shows the rising response.

3.6 Conclusion

In this chapter, the dynamic mathematical model of the full-bridge PWM converter was derived for the SEIG-based WECS. The VOC technique was used for high performance control operation. The synchronous frame SPLL was used to give a fast detection for the phase and frequency variation resulting by the variable speed operation. The simulation results investigated the response of the converter at different generator

outputs. All results obtained confirm the effectiveness of the developed control system for the SEIG feeding PWM voltage source converter. An experimental setup was designed and implemented including a dSPACE DS1104 R&D controller board as an interface element. The experimental results showed agreement with the simulation results to a great extend.

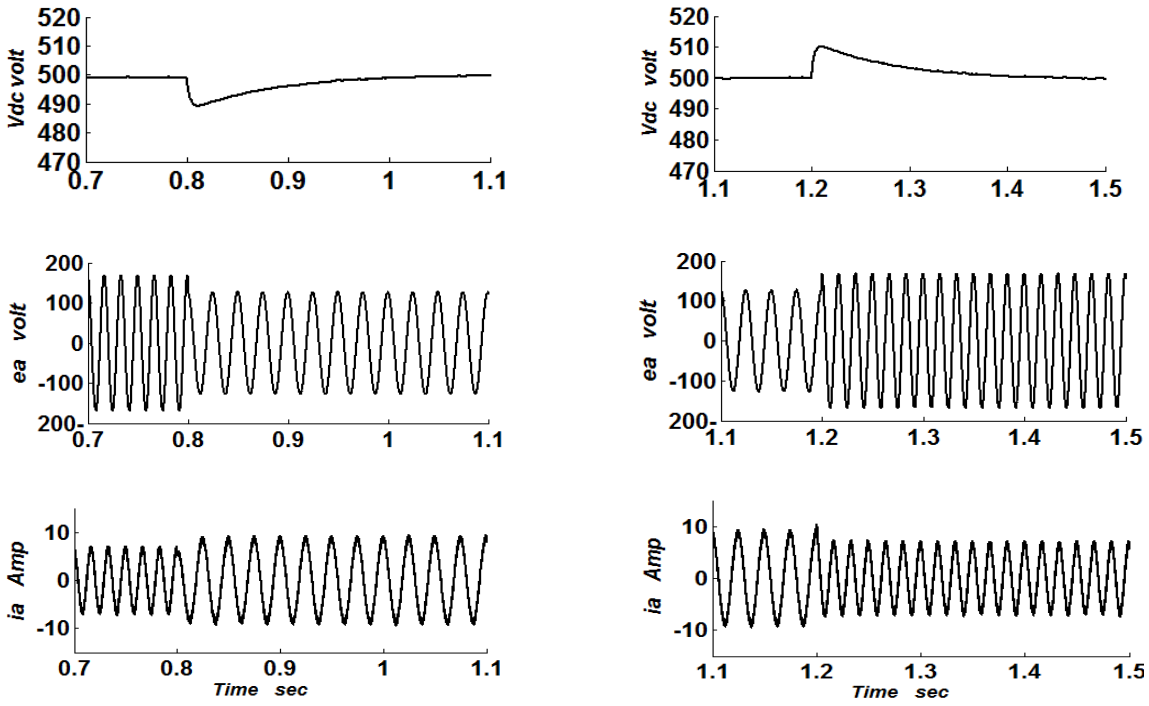

(a) (b)

Fig. 3.22 Converter response under wind speed variation: (a) Falling edge response and (b) Rising edge response

Chapter 4 DC-Bus Voltage Control for PV Sources in Hybrid DC-Distribution System Infrastructure

4.1 Introduction

The utilization of PV energy in hybrid systems has become more practical, feasible and realizable at sizable levels. One of the most common control strategies applied to the grid-connected system is based on VOC technique employing a controller for the DC-link voltage and a controller to regulate the injected current to the system [87].

In order to extract the maximum amount of energy, the PV system must be capable of tracking the solar arrays maximum power point that varies according to the solar radiation and temperature values [88]. These control requirements have been generally achieved by means of voltage and current control loops based on analog linear controllers [89].

A DC-DC converter is required to regulate the voltage feed from a PV source. The DC/DC converter is achieved by constantly adjusting the amount of energy absorbed from the source and that is injected into the load which is in turn controlled by the relative durations of the absorption and injection intervals [90].

The control is made possible by using an IGBT which acts as a switch in the circuit. The gate of the IGBT is feed a PWM signal that is generated based on the output voltage and the input current of the boost circuit. A conventional proportional integral-derivative (PID)-type controller is most widely used in industry due to its simple control structure, ease of design and low cost [91].

4.2 Description of Controlled Voltage DC-Bus

This chapter focuses on the modeling and control design of a controlled voltage DC-DC boost converters. The DC-bus is designed to meet the needs of house loads and future wide use of hybrid systems. The system being implemented in the laboratory is designed to operate at 318V DC. As an example, the schematic diagram of the PV-source connected to the utility hybrid power system is shown in Fig. 4.1 [92]. The system includes a distribution zone which has four houses (1, 2, 3, and 4); each house has its own generations which are represented by three renewable energy sources (PV, wind, and fuel cells) and each source should be connected to a boost converter in order to obtain a regulated (constant) DC-voltage of 318V. Furthermore, each of those houses is connected to a group of battery banks which are used as backup energy storage in case of any overload which can occur by each house or neighbor's house. This battery storage also should be connected to the battery charger which operates in two modes. The first is the charging mode which will draw the charging current from the DC-bus and the second is the discharging mode which will be useful in case of overloading or loss of grid generation due to any fault condition.

The input from the PV source is a variable DC-voltage. Based on the PV-cells characteristics, shown in Fig. 4.2, the input voltage range for the bus is designed and the range of the operating load is set. The PV generates 1.2 kW at varying voltage range of 100-200V.

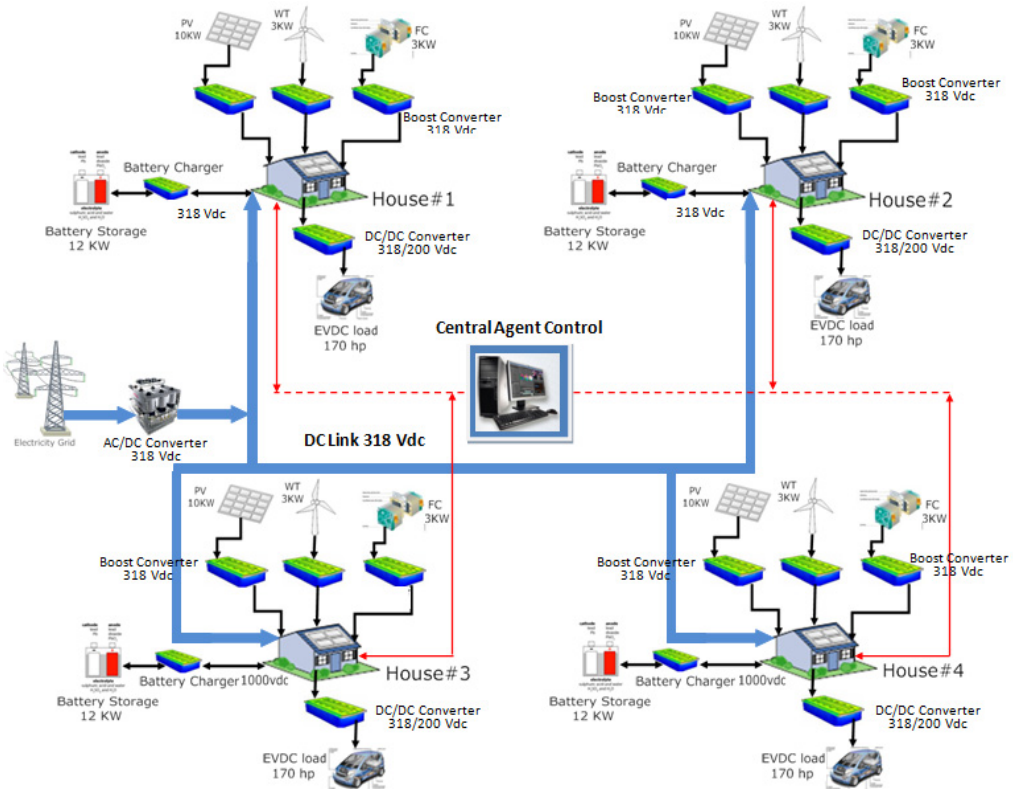

Fig. 4.1 The schematic diagram for the PV source connected to utility hybrid power system and local DC-distribution system

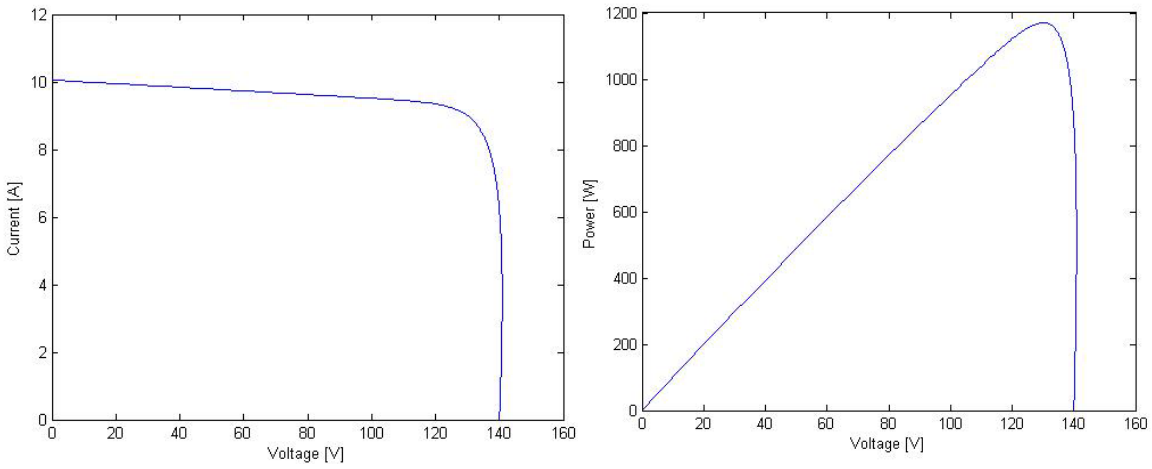

(a) (b)

Fig. 4.2 PV-cells characteristics: (a) V-I and (b) P-I

4.3 DC-DC Boost Converter Operation

As shown in Fig. 4.3, the boost converter consists of DC-input voltage source V_i, boost inductor L, IGBT switch, diode, filter capacitor C, and load resistance R. When the IGBT is in the on state, the current in the boost inductor increases linearly and the diode is off at that time. When the IGBT is turned off, the energy stored in the inductor is released through the diode to the output RC-circuit [54].

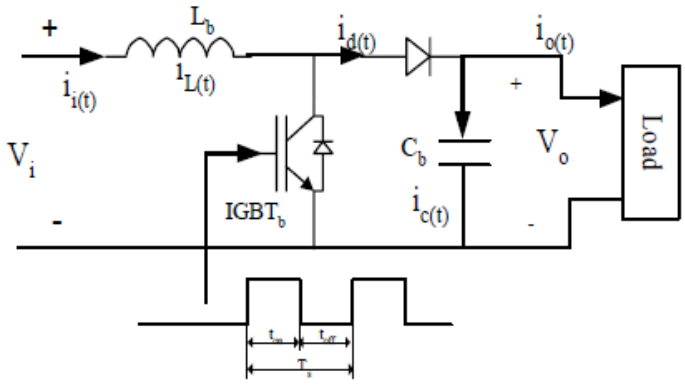

Fig. 4.3 Circuit schematic of DC-DC boost converter circuit

Using Faraday's law, the following equation can be derived for the boost inductor:

$$V_i DT = (V_o - V_i)(1-D)T \tag{4-1}$$

The DC-voltage transfer function is illustrated in (4-1). The boost circuit voltage gain (M_v) is deduced in (4-2). The parameters of the inductor and capacitor are calculated based on (4-3) and (4-4), respectively. The boost converter operates in the common emitter mode for $L > L_b$. The filter capacitor must provide the output DC-current to the load when the diode is off. The minimum value of the filter capacitance that results in the voltage ripple V_r is given by (4-4). The value of the capacitor is inversely proportional to the voltage ripple V_r.

$$M_v = \frac{V_o}{V_i} = \frac{1}{1-D} \tag{4-2}$$

$$L_b = \frac{(1-D)^2 DR}{2f} \tag{4-3}$$

$$C_{\min} = \frac{DV_o}{V_r Rf} \tag{4-4}$$

Where V_o is the output voltage, D is the duty cycle of the PWM, C_{min} is the minimum capacitance needed, L_b is the minimum inductance needed, f is the switching frequency.

4.4 DC-DC Boost Converter Controller

The control signal for the IGBT is generated based on the inductor current and the load voltage. As seen in Fig. 4.4, the analog to digital (ADC) block, which is termed as inductor current, is reading the analog voltage signal from the current sensor. This signal is multiplied by a gain value to read the actual current measured. The analog voltage signal from the voltage sensor is obtained via the ADC, which is termed as load voltage. This signal is multiplied by a gain value to read the actual measured load voltage. A PI controller is used to control the duty ratio of the IGBT. The integrator for the PI controller has a lower saturation limit of 0.05 and an upper saturation limit of 0.95. The current limiter control is essential in this experiment as a protection for the circuit against high current. This is activated when the input current to the boost converter is larger than the maximum allowable current of 10 A. A comparator block is used to compare the instantaneous inductor current. If the inductor current is larger than 10A, then a signal with a fixed duty ratio will be activated while the calculated controlled PWM is deactivated. While supplying the boost converter input current within its range, the PI-controller will be on. The saturation block connected to the PI-controller is used to limit

the output. The output of the saturation block is subtracted by a saw tooth signal of amplitude 0.45 and frequency of 2 kHz. The subtraction result is used to create the pulse signal to the IGBT.

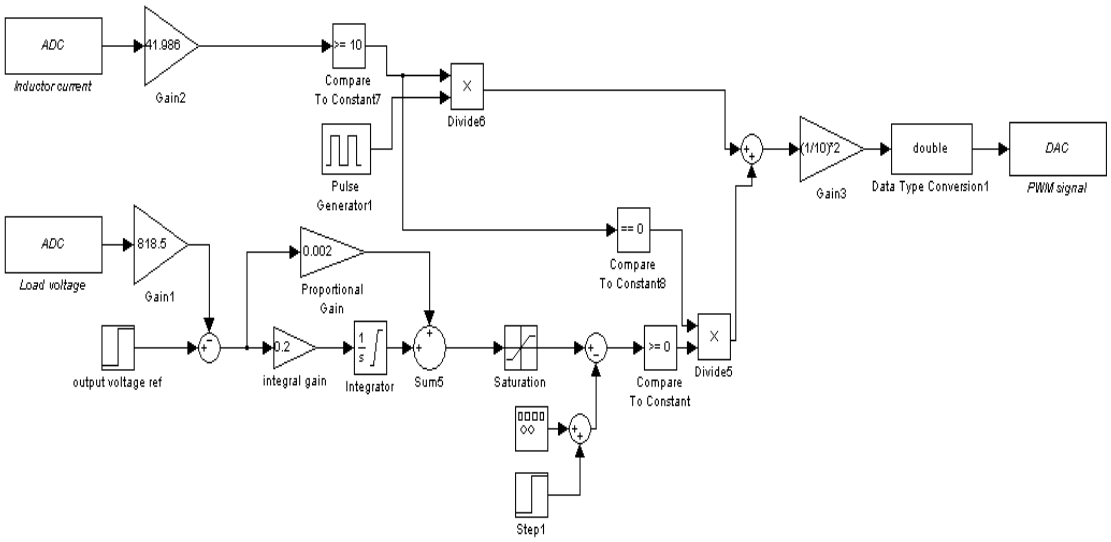

Fig. 4.4 Simulink model of the voltage controller

4.5 Simulation Results

Simulation was performed to verify the effectiveness of the control strategy. The parameters of the boost converter are listed as follows: L=2.7 mH, C=1200 μf, R_L=250 Ω

4.5.1 Simulated Input Voltage Variation Effect

The input voltage is suddenly changed from 70 to 100V. The output voltage remained constant while tracking the reference value (318V) with a very short disturbance time to reach its desired value in 0.2 sec, as shown in Fig. 4.5. Also, the load current is affected by this variation of the input voltage for the same period of time (0.2 sec) then returning back again to be constant, as shown in Fig. 4.6.

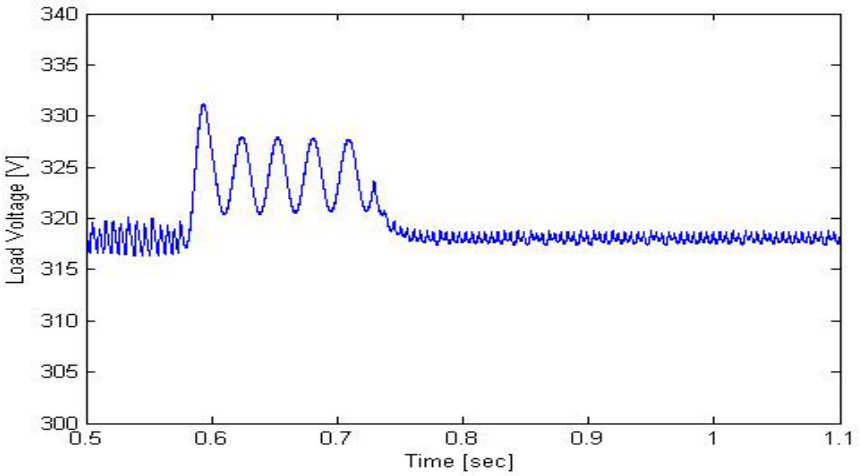

Fig. 4.5 Simulated results for the output voltage transient response during the input voltage variation (30V)

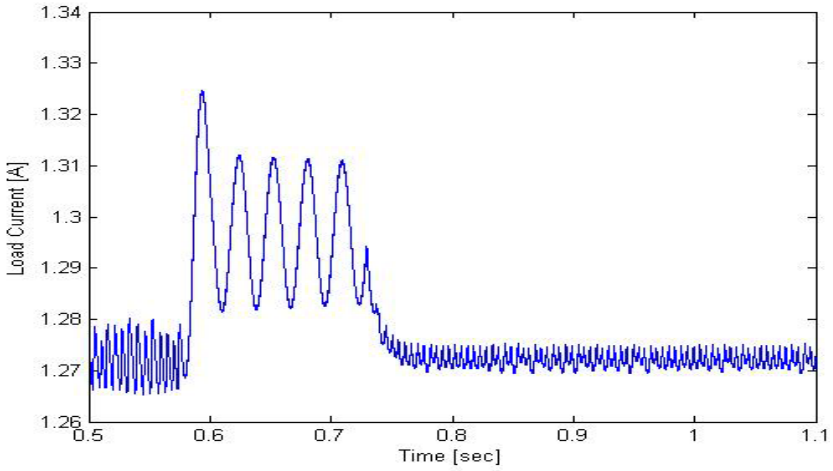

Fig. 4.6 Simulated results for the load current transient response during the input voltage variation (30V)

From the previous figures, the voltage increases by 15V for 0.2 sec due to 30V variation in the input voltage.

The simulation results for the pulse, inductor current and load current are illustrated in Figs. 4.7-9; since it shows the steady state response. A 100V input voltage and 250 Ω resistive load applied to the boost converter. The generated pulse has constant frequency

since the input voltage and the load does not vary. The inductor current is also symmetric and the load current is constant at a value of 1.272A.

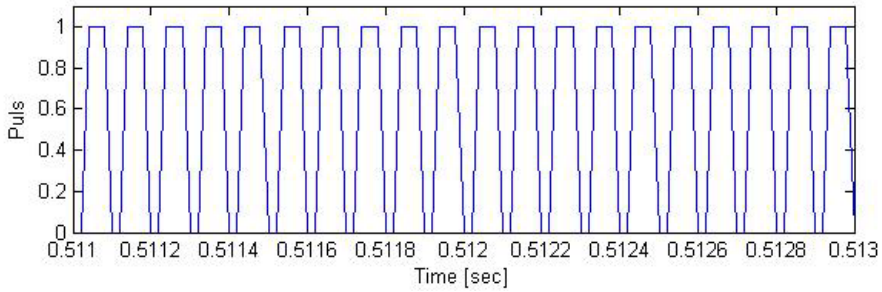

Fig. 4.7 Simulated results for generated pulse at steady state and 100V input

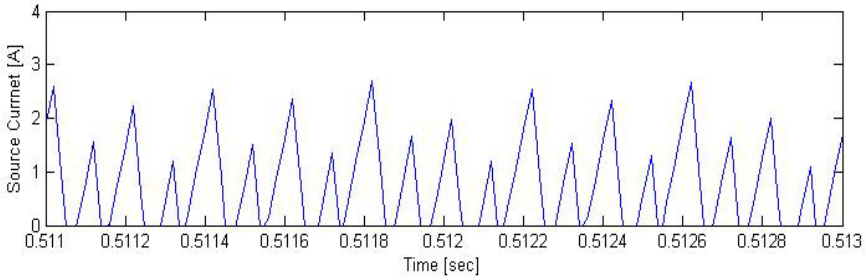

Fig. 4.8 Simulated results for inductor current at steady state and 100V input

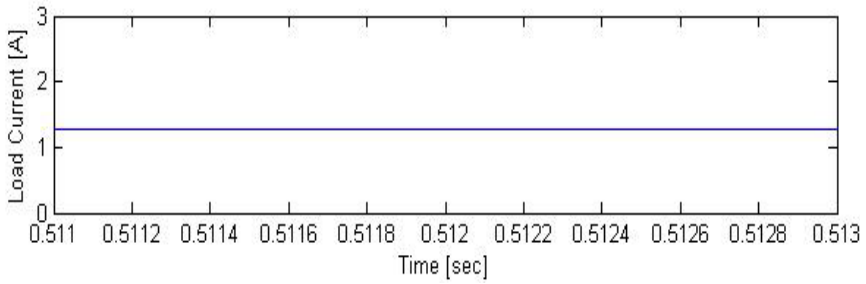

Fig. 4.9 Simulated results for load current at steady state and 100V input

4.6 Experimental Results

Figure 4.10 illustrates an enlarged schematic for the whole developed system. The PV is acting as a source for the boost converter. The controller reads the instantaneous inductor current and the instantaneous load voltage. Based on the values, the controller will calculate a pulse signal to control the IGBT. A picture of the experimental setup

showing the DC-Bus voltage control for PV source using boost converter is depicted in Fig. 4.11.

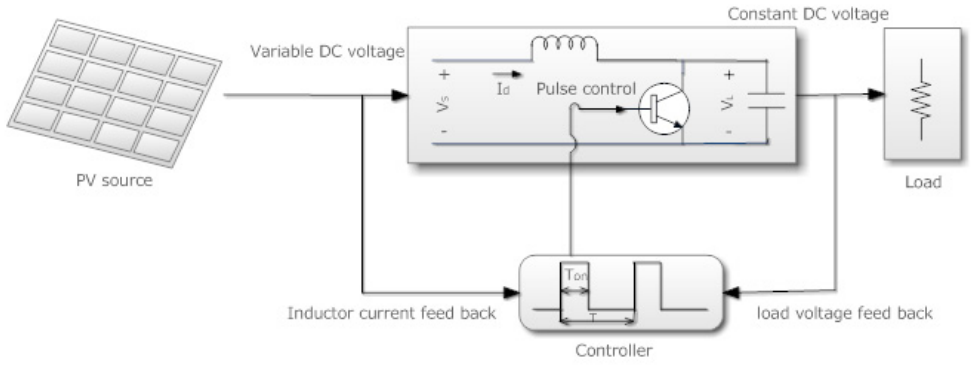

Fig. 4.10 Schematic diagram of the boost converter

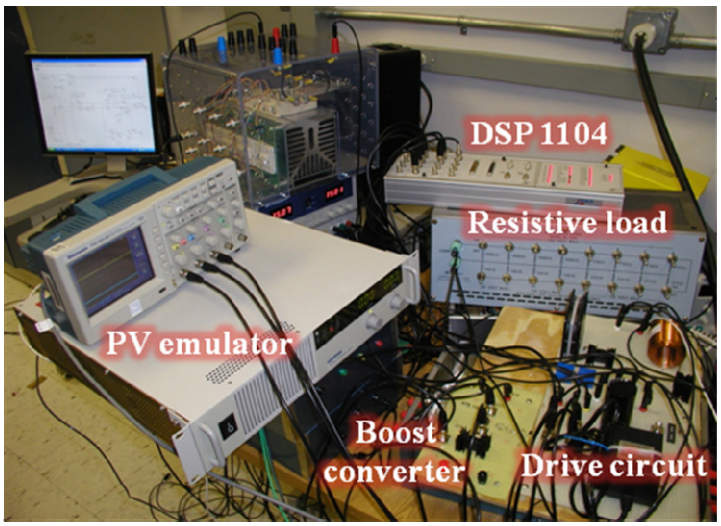

Fig. 4.11 The experimental setup in our energy systems research laboratory

The experimental results for the PWM pulses, the inductor, and output current response in the boost circuit are illustrated in Figs. 4.12 and 4.13, respectively. The signal seen in the graph is multiplied by a gain to get the actual current signal. Therefore, the inductor current is 2.1A. This test is done while a load of 250 Ω resistance is applied to the boost converter. Figure 4.12 illustrates the pulse signal that is used to switch ON and OFF the IGBT. We can notice that the inductor current is operating in the discontinuous

mode (DCM); which means a reduced need to a large inductor. On the other hand, the instantaneous value of the inductor current cannot be controlled in DCM.

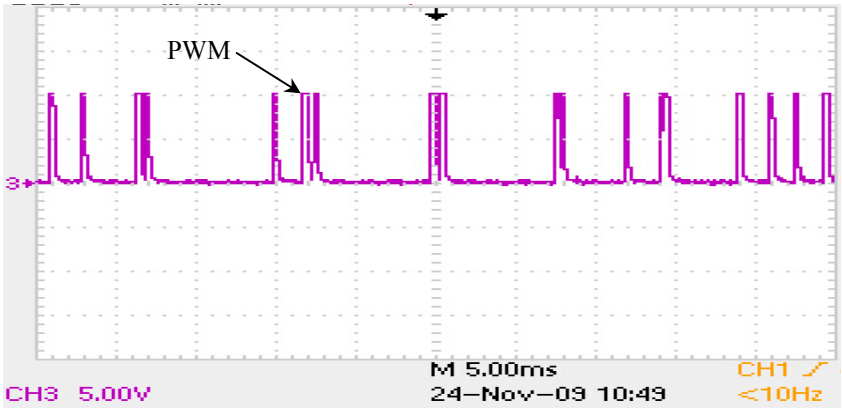

Fig. 4.12 Experimental results of generated PWM at steady state (5V-div)

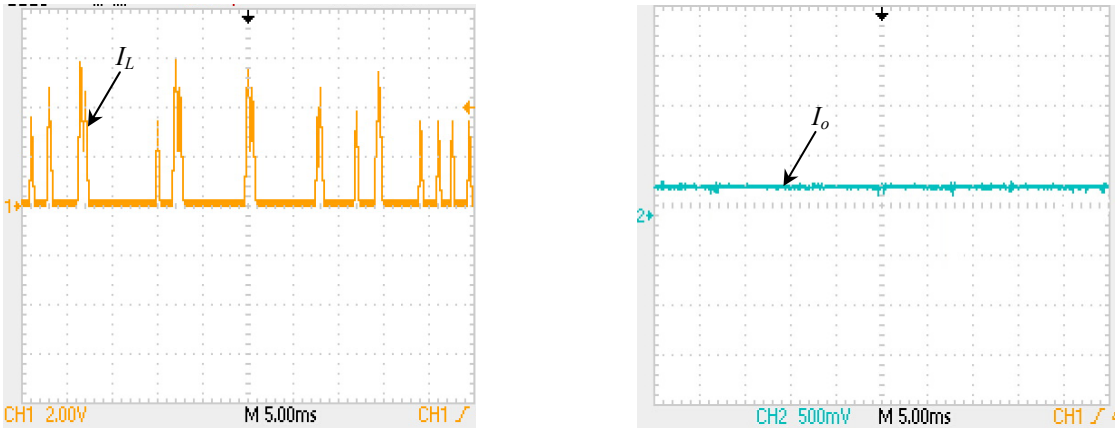

(a) (b)

Fig. 4.13 Experimental steady state results of: (a) Inductor current (5A-div) and (b) Load current (5A-div)

4.6.1 Loading Change Effect

A load of 1000 ohms resistance is applied to the boost circuit and then the load resistance is reduced. Figures 4.14 and 4.15 shows the PWM signal, inductor and load currents, respectively. The Figure clearly shows that the switching frequency increased due to increasing the load current to compensate the output voltage drop.

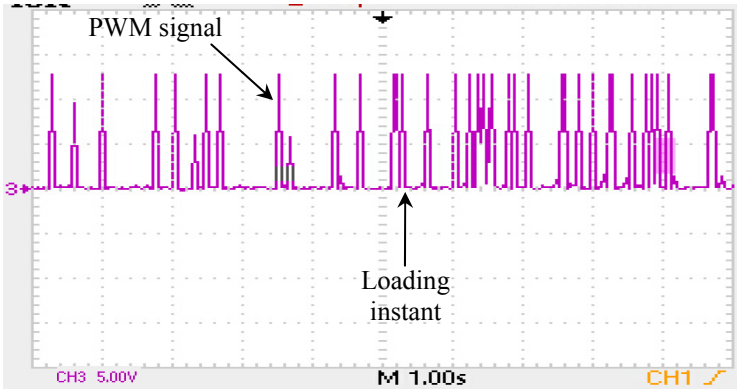

Fig. 4.14 Experimental results of generated PWM during loading change (5V-div)

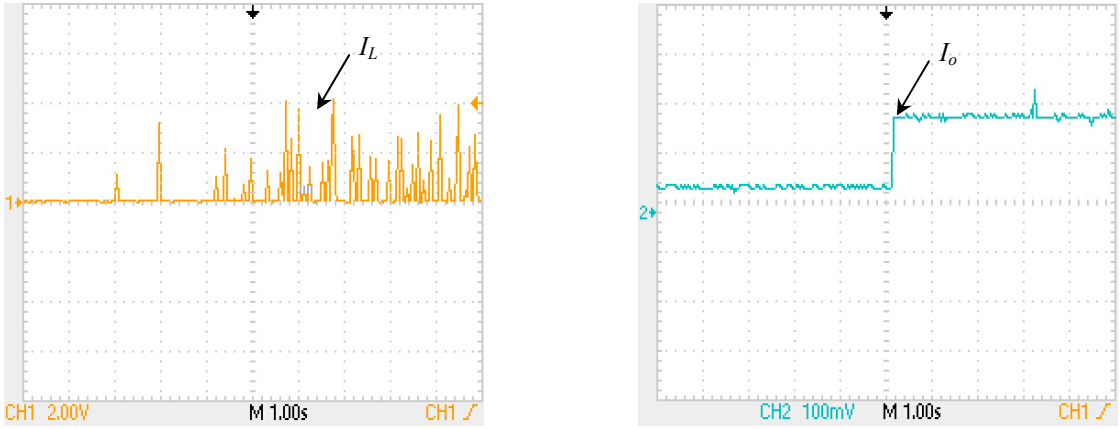

(a) (b)

Fig. 4.15 Loading change experimental results of: (a) Inductor current (5A-div) and (b) Load current (1A-div)

4.6.2 Experimental Input Voltage Variation

The next test is to change the input voltage and monitor the output voltage of the boost converter. The input voltage changes from 66V to 200 while operating the circuit at a load with resistance 333.3 Ω. Figure 4.16 shows that the output voltage still kept constant and tracking the desired output value (318V).

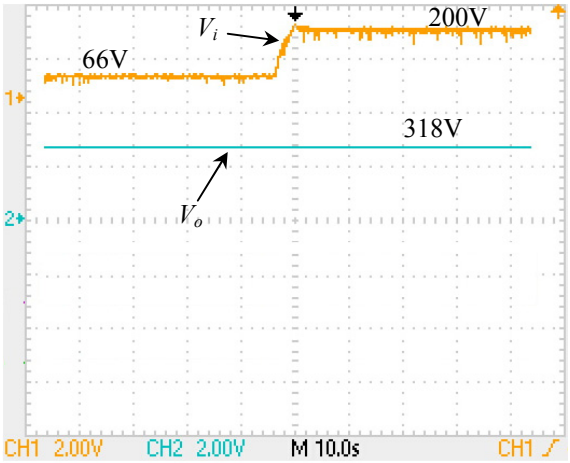

Fig. 4.16 Experimental results of input and output voltages

4.6.3 DC-Output Voltage Reference Change

In order to confirm the effectiveness of the developed control system, we should test it under different values of the reference output voltage. The boost converter is running at 100V input voltage and load resistance of 250 Ω. Figure 4.17 shows the output voltage change with respect to the change of the reference voltage. The reference is changed from 318V to 200V in the first step. The second step is from 200V to 150V. Then, it increased from 150V to 350V to 400V to 500V. From Fig. 4.17, we can notice that the output voltage is tracking the reference value. Also, the response time is 0.1 sec (fast response).

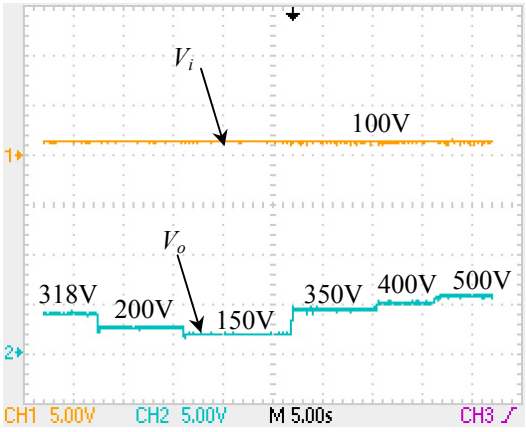

Fig. 4.17 Experimental results of varying the reference output voltage

4.7 Conclusion

In this chapter, the mathematical model of the boost converter connected to DC-bus system was introduced. The simulation results showed how the control scheme succeeded in injecting the PV-power to feed the DC-distribution system with the available power from the PV-source.

A laboratory experimental setup was developed and implemented. All the interfacing circuits to the analog power circuits were connected. The system was experimentally tested under different possible conditions. All results obtained confirm the effectiveness of the developed control system for the PV-source system feeding the small utility power system. The experimental results showed good transient and steady state performance for each part of the system as well as the overall system.

Chapter 5 Active and Reactive Power Control Strategies through Grid-Tie-Inverter as a Dynamic VAR Compensator for WECS

5.1 Introduction

Nonlinear devices, such as power electronics converters, are injecting harmonic currents in the AC system and increase the overall reactive power demanded by the equivalent load. Also, the number of sensitive loads that require ideal sinusoidal supply voltages for their proper operation has increased [93].

The power quality can be improved for grid-connected WECSs for a more economical system. In order to keep the power quality under the limits proposed by standards, it is necessary to include compensation. There are several technical issues arising from compensation techniques and the complexity of implementing their control operation [94-96].

In [94], an LC filter design for medium voltage applications of PWM inverters was proposed. The filter capacitor compensates the reactive power of the motor which allows the utilization of standard industrial motors without de-rating. However, the filter becomes heavy and expensive because of the low switching frequency (below 1 kHz) of inverter switches. Also, the designed filter was always excited at resonance frequency. A damping function integrated in the inverter control could be a solution.

A three-phase AC-to-DC resonant converter operating in high input power factor mode was introduced in reference [95]. This design offers several advantages such as high power factor and low THD operation. However, high switching losses for high frequency operation will reduce the overall efficiency. The control complexity is one of the main drawbacks for this proposed system.

The static VAR compensator (SVC) technique for the voltage regulation or reactive power control of the wind powered self-excited induction generator (SEIG) is investigated in [96]. The SVC has some known problems as switching capacitors and injection of harmonics to the grid due to the use of the thyristor-based switching devices.

In this chapter, a SEIG-based WECS with VOC strategy for a three-phase voltage-source PWM inverter is used as a dynamic VAR compensator system for weak grids to provide full control of active and reactive power injected into the grid [97]. A second order SPLL technique for phase angle detection of the grid voltage in synchronous reference frame is utilized same as in chapter 3. An analytical model for the VSI connected to the grid with L and LC-filters and the operating principle of the developed vector controllers were introduced. Finally, the simulation and experimental results for VSI connected to the grid with L and LC-filters are presented and compared to confirm the validity of the developed technique and show its practical superiority in renewable energy applications.

5.2 Grid-Connected System Architecture

The developed topology is shown in Fig. 5.1. With this topology, boost converter is omitted without any change in the WECS objectives. The advantages of the developed system are; simplicity and high efficiency. Since there are no switches in the rectifier stage, the reliability of the system is greatly improved. This is because it has the ability of full active and reactive power control. The high injected power quality is achieved by employing LC filter between the inverter and grid [98]. Better dynamic performance under different possible conditions is accomplished by utilizing the decoupled VOC control scheme.

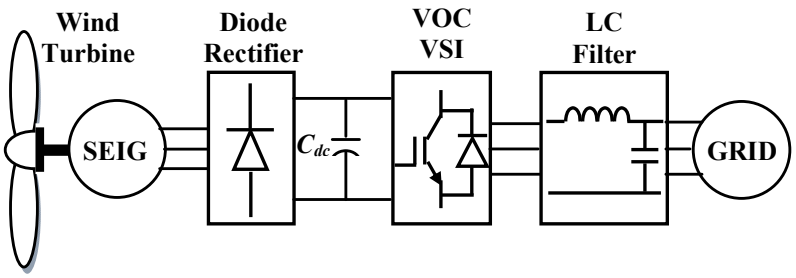

Fig. 5.1 SEIG-based WECS with VOC VSI structure

5.3 Dynamic Model of the Converter-Inverter System

5.3.1 Three-Phase Diode Bridge Rectifier

Three-phase diode bridge rectifiers are commonly used for high-power applications. It is very efficient and popular wherever both DC-voltage and current requirements are high. In many applications, no additional filter is required because the output ripple voltage is only 4.2%. Even if a filter is required, the size of the filter is relatively small because the ripple frequency is increased to six times the input frequency. The circuit of a three-phase bridge rectifier is shown in Fig. 5.2. The voltage waveforms of the rectifier are shown in Fig. 5.3. The line voltage is $\sqrt{3}$ times the phase voltage of a three-phase generator voltage. The average value of the output can be found as:

$$V_{dc} = \frac{6}{2\pi} \int_{\pi/3}^{2\pi/3} \sqrt{3} V_m \sin\theta \cdot d\theta \tag{5-1}$$

or $$V_{dc} = \frac{3\sqrt{3}}{\pi} V_m = 1.654 V_m \tag{5-2}$$

Where L, C_{dc} are input inductance and output filter capacitance, respectively. Here, V_m is the maximum value for the generator output phase voltage. θ is the angle of the generator voltage. V_{dc} is the DC-link output voltage.

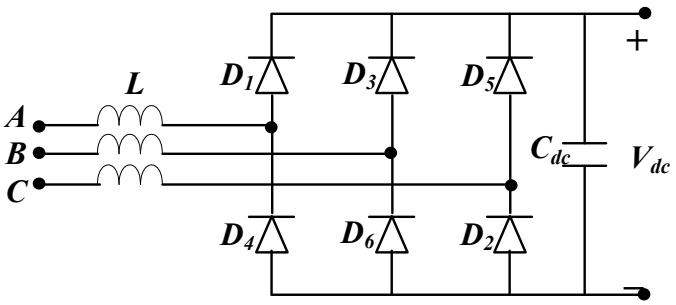

Fig. 5.2 Three-phase diode bridge rectifier

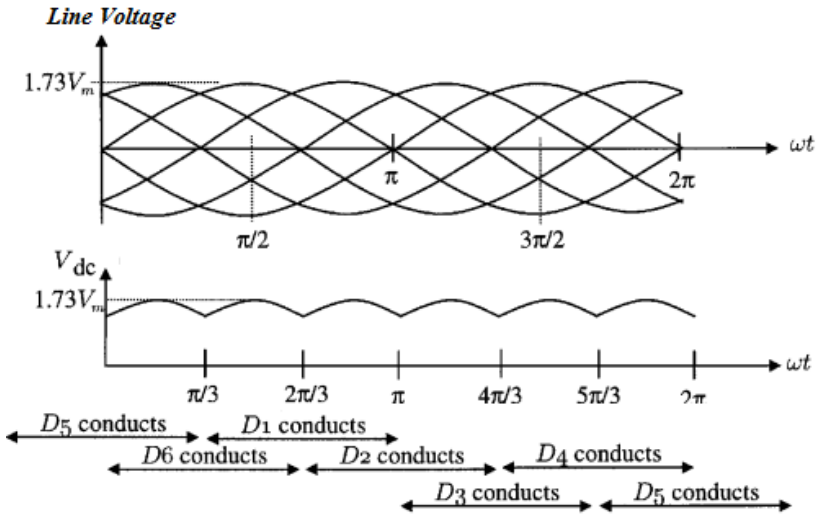

Fig. 5.3 Voltage waveforms of the three-phase diode bridge rectifier

5.3.2 Voltage Source Inverter

The main circuit of the VSI connected to a three phase grid is shown in Fig. 5.4. An inductance L that works as line filter is mounted between the utility grid and the VSI having an internal resistance R. The phase potentials of the VSI denoted as $v_a(t)$, $v_b(t)$ and $v_c(t)$. The phase potentials of the utility grid denoted $u_a^g(t)$, $u_b^g(t)$ and $u_c^g(t)$. ω_g is the grid voltage angular frequency. The currents flowing from the DC-link to the VSI denoted as $i_a(t)$, $i_b(t)$ and $i_c(t)$ while the DC-link current and voltage are denoted as $i_{dc}(t)$ and $V_{dc}(t)$ respectively.

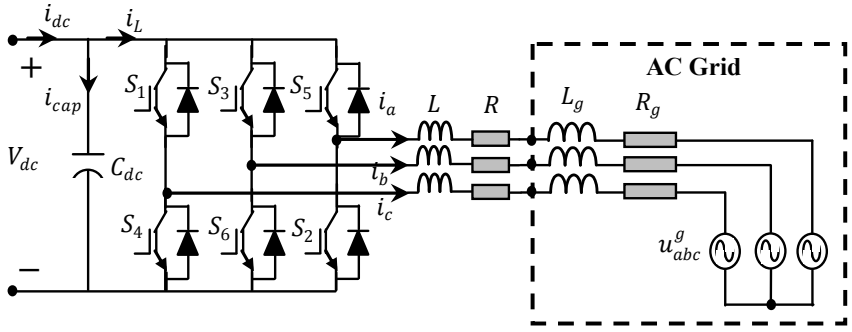

Fig. 5.4 The main electric circuit of the VSI connected to the utility grid

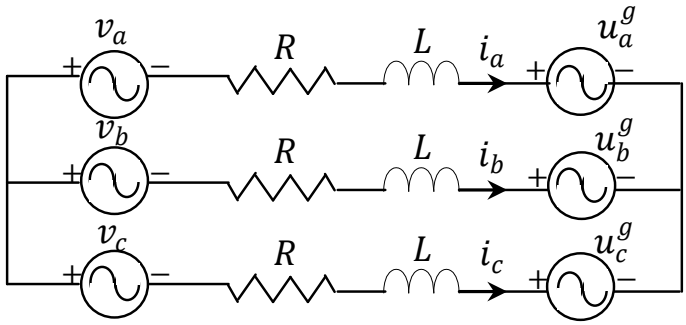

Fig. 5.5 Simplified circuit of a grid connected VSI

In order to design a VSI control systems, mathematical models are important tools for predicting dynamic performance and stability limits of different control laws and system parameters. The system modeled is shown in Fig. 5.5. In this figure, the grid inductance L_g is assumed to be zero. The assumption of the balanced state of the grid is presented. The AC-side of the inverter system is modeled by the differential equations for three-phases such that:

$$\frac{di_{abc}(t)}{dt} + Ri_{abc}(t) = v_{abc}(t) - u^g_{abc}(t) \tag{5-3}$$

Using vector notation, the last equation can be written in the $\alpha\beta$ stationary frame such as:

$$\frac{di_{\alpha\beta}(t)}{dt} + Ri_{\alpha\beta}(t) = v_{\alpha\beta}(t) - u^g_{\alpha\beta}(t) \tag{5-4}$$

Equation (5-4) can be written in the rotating reference frame synchronized with grid voltage using Park's transformation such as [40]:

$$\frac{di_{dq}(t)}{dt} + (R + j\omega_g L) i_{dq}(t) = v_{dq}(t) - u^g_{dq}(t) \tag{5-5}$$

The decoupled equation can be written in the state space form as:

$$\frac{dX}{dt} = A \cdot X - B \cdot Y \tag{5-6}$$

Where the state vector and the input vector are defined by:

$$X = \begin{bmatrix} i_d & i_q \end{bmatrix}^T \tag{5-7}$$

$$Y = \begin{bmatrix} V_d & V_q & u^g_d & u^g_q \end{bmatrix}^T \tag{5-8}$$

Respectively, the system matrix and the input matrix are given by:

$$A = \begin{bmatrix} -R/L & \omega_g \\ -\omega_g & -R/L \end{bmatrix} \tag{5-9}$$

$$B = \begin{bmatrix} 1/L & 0 & -1/L & 0 \\ 0 & 1/L & 0 & -1/L \end{bmatrix} \tag{5-10}$$

The DC-side of the system is modeled by the equation:

$$C_{dc} \frac{dV_{dc}(t)}{dt} = i_{dc}(t) - i_L(t) \tag{5-11}$$

5.4 VCO Strategy for VSI as Dynamic VAR Compensator

Until recently, most wind power plants and utility operations have utilized capacitor banks to correct the power factor to near unity. The capacitors are switched in and out by means of mechanical contactors. Unfortunately, because these contactors are relatively slow, they are unable to react to sudden momentary dips in the voltage commonly seen in

the weak grid and can add greater stress on the utility grid. The VOC VSI is used here as a dynamic VAR compensator system.

The dynamic VAR systems detect and instantaneously compensate for voltage disturbances by injecting leading or lagging reactive power at key points on power transmission grids. Through the VAR control system, the reactive power is supplied to the grid in a fraction of a second, regulating the system voltage and stabilizing a weak grid. The controller measures the utility line voltage, compares it to the desired level, and computes the amount of reactive power needed to bring the line voltage back to the specified range [99].

The active and reactive power in the synchronous frame given by:

$$\begin{aligned} P(t) &= \frac{3}{2}\left[u_d^j(t)\cdot i_d(t) + u_q^j(t)\cdot i_q(t)\right] \\ Q(t) &= \frac{3}{2}\left[u_q^j(t)\cdot i_d(t) - u_d^j(t)\cdot i_q(t)\right] \end{aligned} \tag{5-12}$$

The power of the DC-side is given by:

$$P_{dc} = V_{dc}\cdot i_{dc} \tag{5-13}$$

The basic principle of the VOC method is to control the instantaneous active and reactive grid currents. Consequently, the active and reactive power by separate controllers that are independently of each other. The grid voltages and currents are first sensed. By means of the SPLL, the grid phase angle and frequency can be detected in order to synchronize the VSI output with grid. The demanded amount of power is first estimated from the utility grid at the desired power factor. As a result, the reference currents in the synchronous frame synchronized with the grid voltage are calculated.

Consequently, the current controllers are trying to bring the actual currents to its references.

The reference currents i_d^r and i_q^r could be calculated from the power equation (5-13), such that:

$$\begin{aligned} i_d^r(t) &= \frac{3}{3\Pi}\left[u_d^j(t)\cdot P^r(t) + u_q^j(t)\cdot Q^r(t)\right] \\ i_q^r(t) &= \frac{3}{3\Pi}\left[u_q^j(t)\cdot P^r(t) - u_d^j(t)\cdot Q^r(t)\right] \end{aligned} \tag{5-14}$$

Where $\Pi = u_d^{j\,2}(t) + u_q^{j\,2}(t)$, and $P^r(t)$, $Q^r(t)$ are the active and reactive power commands, respectively. With the assumption of zero reactive power command, the current command equations can be simplified such that:

$$\begin{aligned} i_d^r(t) &= \frac{2\cdot P^r(t)}{3\cdot u_d^j(t)} = \frac{2\cdot V_{dc}\cdot i_{dc}^r(t)}{3\cdot u_d^j(t)} \\ i_q^r(t) &= 0 \end{aligned} \tag{5-15}$$

From the state equation (5-6), the current controllers can be constructed such that:

$$\begin{aligned} v_d^r(t) &= u_d^j(t) - \omega_g L i_q(t) + R\cdot i_d(t) + U_d^v \\ v_q^r(t) &= u_q^j(t) + \omega_g L i_d(t) + R\cdot i_q(t) + U_q^v \end{aligned} \tag{5-16}$$

Where $v_d^r(t)$ and $v_q^r(t)$ are the *d*-axis and *q*-axis voltage commands, respectively, U_d^v and U_q^v are the effective voltage commands.

The coupling term between the *d*-axis and *q*-axis is cancelled out by feed-forward controller $\omega_g L i_d(t)$, $\omega_g L i_q(t)$. The effective voltage commands are obtained by using PI-controller such that:

$$U_d^r(t) = k_p^i \cdot [i_d^r(t) - i_d(t)] + k_i^i \cdot \int [i_d^r(t) - i_d(t)]dt$$
$$U_q^r(t) = k_p^i \cdot [i_q^r(t) - i_q(t)] + k_i^i \cdot \int [i_q^r(t) - i_q(t)]dt \quad (5\text{-}17)$$

(29)

Where k_p^i and k_i^i are the proportional and integral gains of the current controllers, respectively. The schematic diagram of the VSI connected to the grid and its decoupled vector current controller is shown in Fig. 5.6.

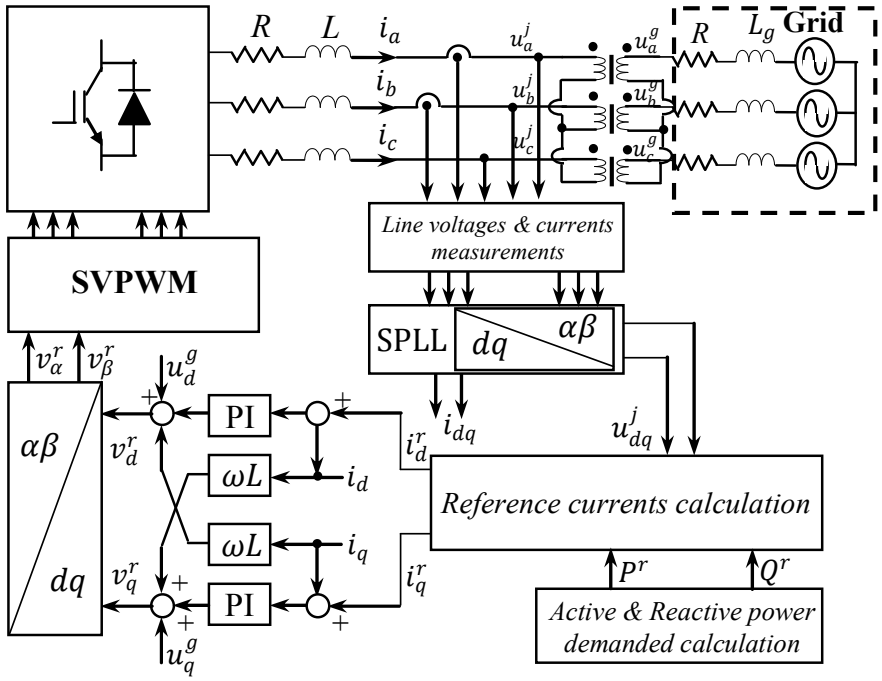

Fig. 5.6 Schematic diagram of the VOC VSI connected to the grid

5.5 Grid-Connected VSI with LC-Filter

The per-phase equivalent circuit for the VSI connected to the grid with LC-filter is shown in Fig. 5.7. The inverter dynamic should have additional voltage controller in front of the current controller to control the filter capacitor voltage. According to the equivalent circuit, the system dynamic equations can be written as:

$$L_f \frac{di_{abc}(t)}{dt} = v_{abc}(t) - R_f \cdot i_{abc}(t) - u^c_{abc}(t) \tag{5-18}$$

$$C_f \frac{du^c_{abc}(t)}{dt} = i_{abc}(t) - i^j_{abc}(t) \tag{5-19}$$

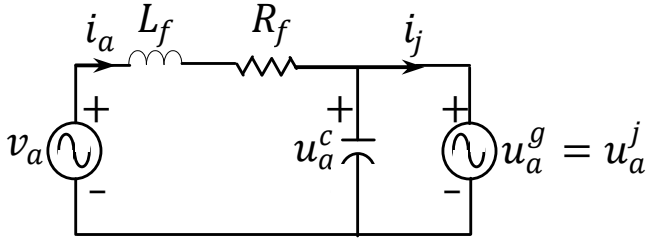

Fig. 5.7 VSI with LC filter equivalent circuit

The three phase model of the system transformed to a synchronous reference frame, where the *d*-axis is oriented with the grid voltage vector, can be described by the state equations:

$$\begin{aligned} L_f \frac{di_d(t)}{dt} &= v_d(t) - R_f \cdot i_d(t) - u^c_d(t) + \omega_g L_f i_q(t) \\ L_f \frac{di_q(t)}{dt} &= v_q(t) - R_f \cdot i_q(t) - u^c_q(t) - \omega_g L_f i_d(t) \end{aligned} \tag{5-20}$$

$$\begin{aligned} C_f \frac{du^c_d(t)}{dt} &= i_d(t) - i^j_d(t) + \omega_g C_f u^c_q(t) \\ C_f \frac{du^c_q(t)}{dt} &= i_q(t) - i^j_q(t) - \omega_g C_f u^c_d(t) \end{aligned} \tag{5-21}$$

The system utilizes an inner control loop to control the current through the filter inductor, and an outer control loop to control the filter capacitor voltage, which in turn will be applied to the primary terminals of the isolation transformer between the grid and the inverter. The capacitor voltage could be controlled by controlling the filter inductor current since the injected current, i^j_{dq}, may be considered as a disturbance. Therefore, the controller could be constructed such that:

$$
\begin{aligned}
i_d^r(t) &= i_d^j(t) - \omega_g C_f u_q^c(t) + U_d^c \\
i_q^r(t) &= i_q^j(t) + \omega_g C_f u_d^c(t) + U_q^c
\end{aligned}
\tag{5-22}
$$

Where $i_d^r(t)$ and $i_q^r(t)$ are the *d*-axis and *q*-axis current commands, respectively, U_d^c and U_d^c are the effective current commands. If PI-controller is used, $U_{dq}^c(t)$ could be controlled such that:

$$
\begin{aligned}
U_d^c &= k_p^c \cdot [u_d^{c^r}(t) - u_d^c(t)] + k_i^c \cdot \int [u_d^{c^r}(t) - u_d^c(t)] dt \\
U_q^c &= k_p^c \cdot [u_q^{c^r}(t) - u_q^c(t)] + k_i^c \cdot \int [u_q^{c^r}(t) - u_q^c(t)] dt
\end{aligned}
\tag{5-23}
$$

Where k_p^c, and k_i^c are the proportional and integral gains of the capacitor voltage controllers, respectively. The inner current controller has the same dynamics as the controller of L-filter discussed in section 5.4, so it can be used here. The overall VSI controllers are shown in Fig. 5.8.

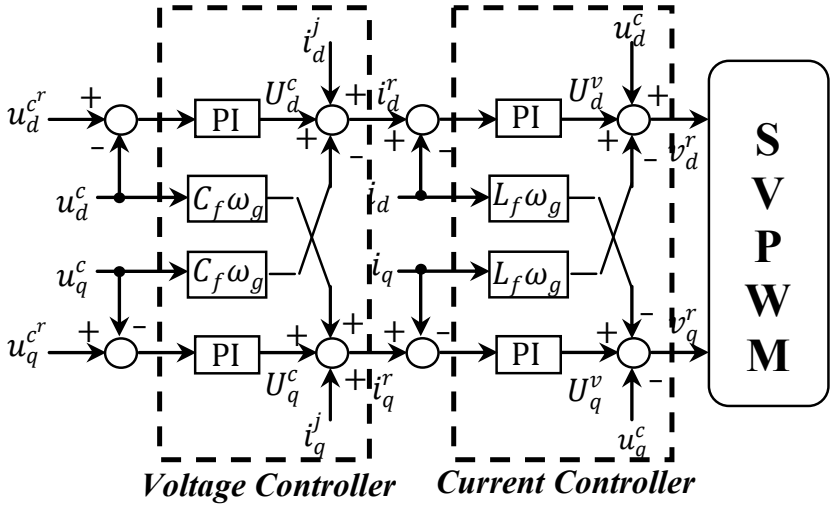

Fig. 5.8 VSI with LC-filter controller schematic diagram

5.6 Simulation and Experimental Results

In order to investigate the performance of the overall developed system, a simulation program using Simulink™ was carried out using simulation parameters shown in Table 5.1. Furthermore, an experimental setup for the developed WECS was constructed and connected to the local grid. A digital board containing a digital signal processor (DSP TMS320F240) was tested and used as the control heart of the system. Each unit of the system is built and tested alone, and then the whole system is connected and tested. The SVPWM presented in this chapter was used with a 5 kHz switching frequency. VOC strategy discussed in section 5.4 is utilized in the simulation. A low pass filter with LC elements and 205 Hz cut-off frequency is connected before the isolation transformer in order to have clean power injection. Figure 5.9 shows the experimental setup schematic diagram for the overall developed system connected to the grid. The experimental setup includes fabricated built circuit boards, a wind generator modeled by a VSPM coupled with SEIG, and grid connected VSI. The induction machine ratings are listed in Table 5.2.

5.6.1 Wind Speed Variation

In order to evaluate the performance of emulator in turbulent wind speed condition, an experimental test was carried out. The wind speed could be constant, or varying in a form of pulses, sinusoidal, or step change. Actually wind speed has a random variation according to the wind turbine location and its atmospheric conditions, but it can be set to operate within a given variation of speed. Figure 5.10 shows the monthly average wind speed at La Venta station.

Table 5.1 Specifications and parameters for VOC VSI with L and LC-filters

Symbol	Quantity	Value
f_g	Grid frequency	60 Hz
V_g	Grid voltage	120/208 V *r.m.s*
V_{dc}	DC-link voltage	350 V
C_{dc}	DC-link capacitance	1200 μf
L_f	Filter inductance	24 mH
C_f	Filter capacitance	40 μf
f_{sw}	Switching frequency	5 kHz
k_p^i	Proportional current controller	10
k_i^i	Integral current controller	100
k_p^c	Proportional voltage controller	0.07
k_i^c	Integral voltage controller	0.7

Table 5.2 Specifications and parameters for SEIG

Symbol	Quantity	Value
P_o	Output power	1/3 hp
C_g	SEIG capacitance	70 μf
V_n	Nominal voltage	120/208 V *r.m.s*
n	Nominal speed	1800 *rpm*
I_n	Nominal current	1.7 A
V_f	Field voltage	125 V

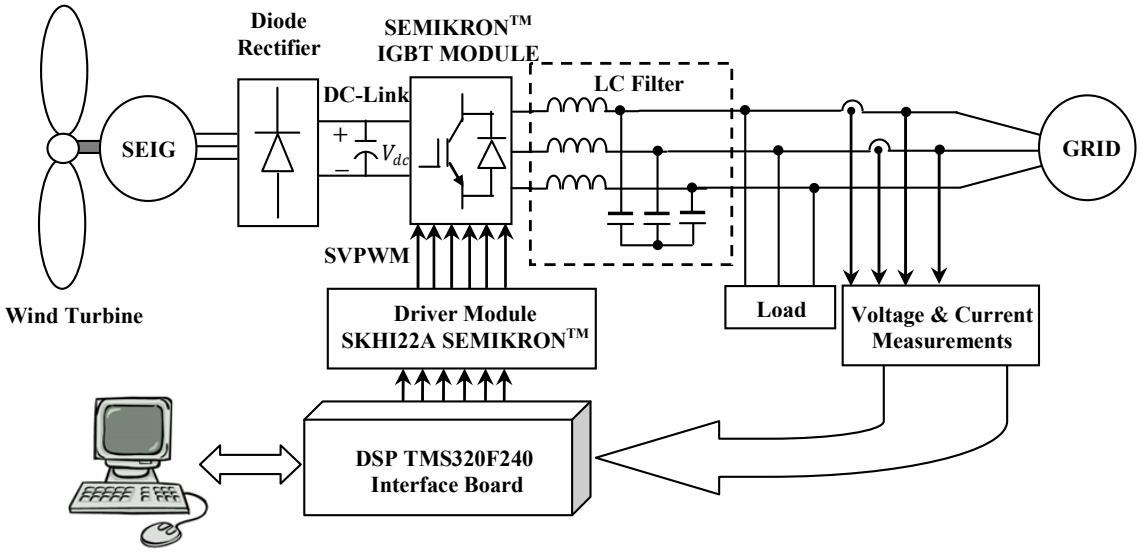

(a)

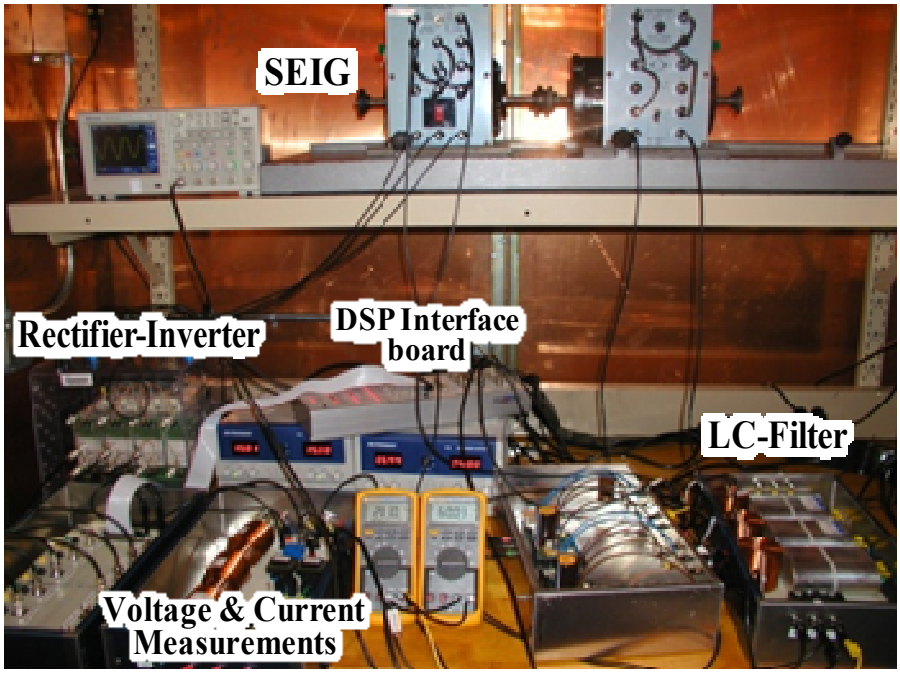

(b)

Fig. 5.9 The overall WECS control system connected to grid: (a) Schematic diagram and (b) Laboratory prototype setup

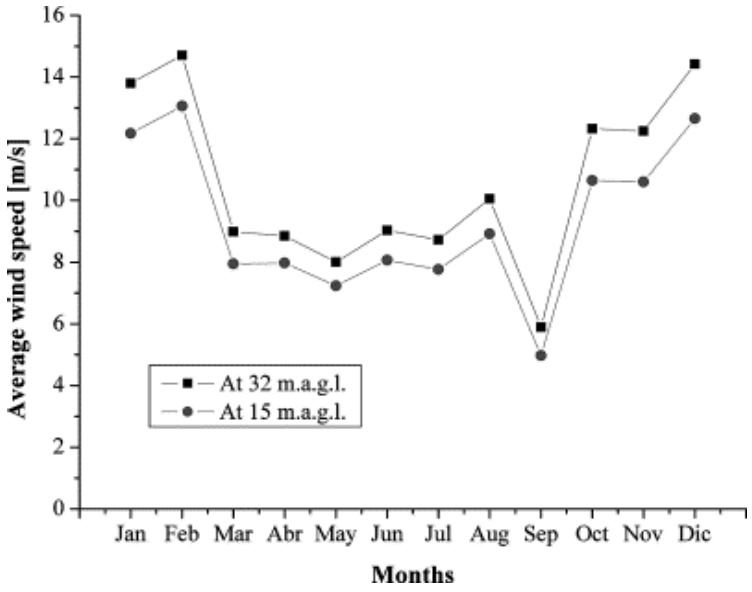

Fig. 5.10 Monthly average wind speed at La Venta station

5.6.2 Grid-Connected VOC VSI with L-Filter

In order to estimate the power injection characteristics, two types of tests are carried out. These tests have been done to compare L-filter performance that was introduced previously in the references [24, 50] with the developed LC-filter. The first is active power injection without any reactive power compensation. The second is injection of active power with reactive power compensation (lagging or leading). The terminal phase and line voltage of the VSI in *abc* frame are shown in Figs. 5.11, 12, respectively. The wind speed is variable according to the previous wind characteristics in Fig. 5.10. However, the output voltage has the rating of 208 V, 60 Hz which is synchronized with the utility grid rating. Figure 5.13 shows the first test of the power injection. A step change to the demanded active power from 125 W (half load) to 250 W (full load) while keeping the reactive power equal zero. Because the injected power is only active, the current appears in phase with grid voltage. The VSI phase voltage connected to utility grid through L- filter is shown in Fig. 5.14.We can notice that the voltage waveform has

large harmonic contents of 10.35%. The THD of the current injected in the electrical grid and output phase voltage with L-filter is shown in Fig. 5.15. It also shows large harmonic contents of 9.86% above the IEEE standards for grid connectivity protocol (5%).

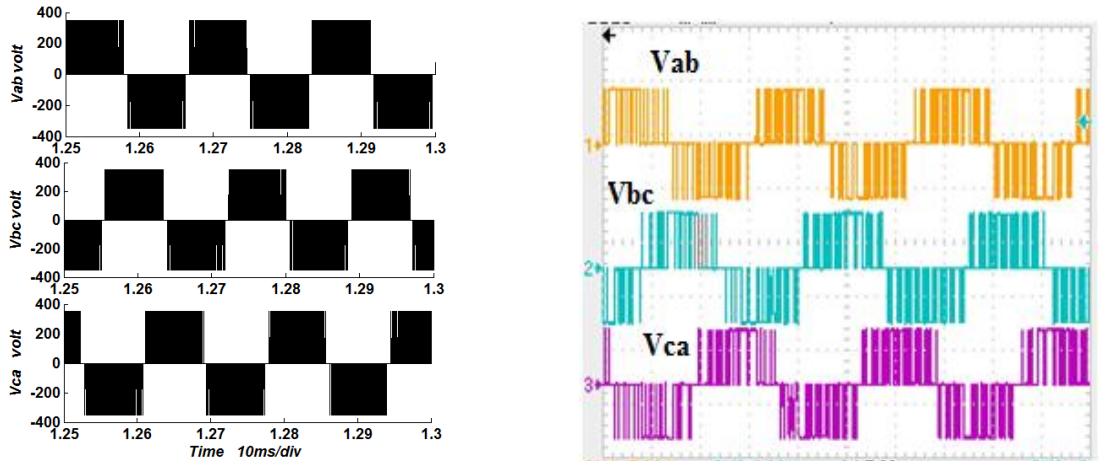

(a) (b)

Fig. 5.11 Line voltage of the VSI in *abc* frame (400 V/div-5ms): (a) Simulation and (b) Experimental

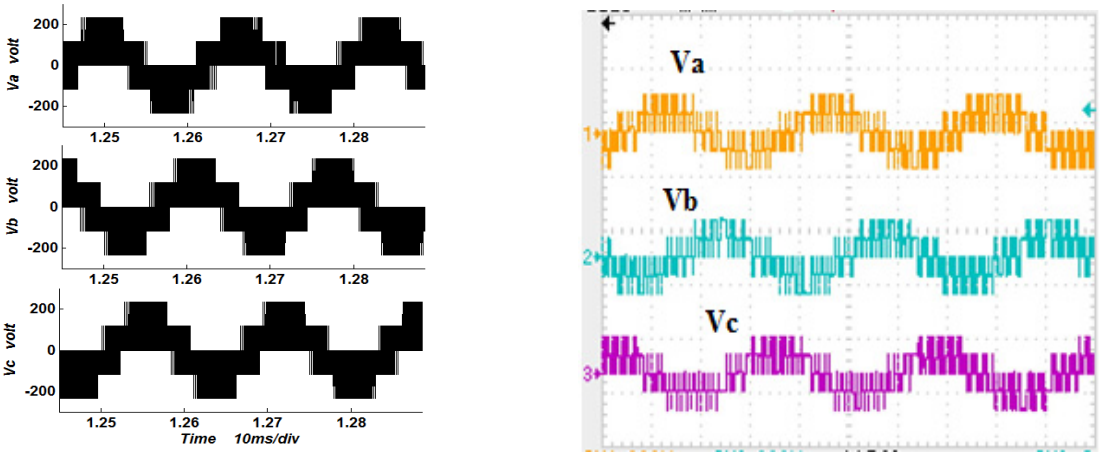

(a) (b)

Fig. 5.12 Phase voltage of the VSI in *abc* frame (400 V/div-5ms): (a) Simulation and (b) Experimental

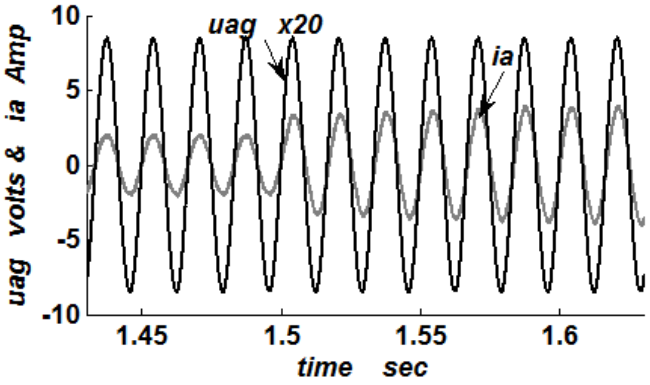

(a)

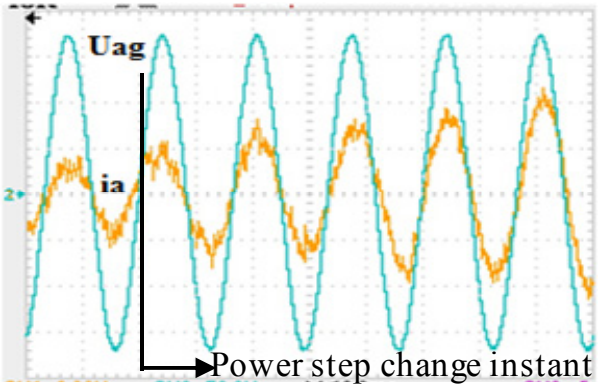

(b)

Fig. 5.13 Grid phase voltage (50 V/div-10ms) and injected current (1 A/div-10ms): (a) Simulation and (b) Experimental

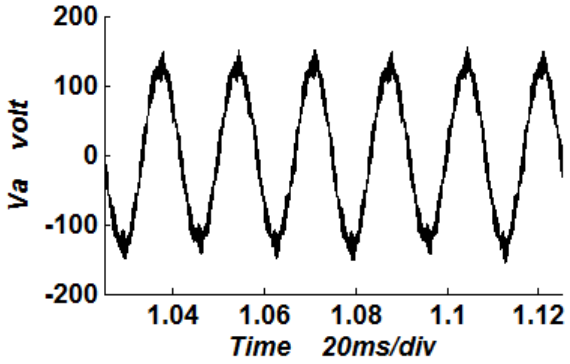

(a)

Fig. 5.14 Inverter phase voltage to be connected to the grid with only L-filter (50 V/div-10ms): (a) Simulation and (b) Experimental

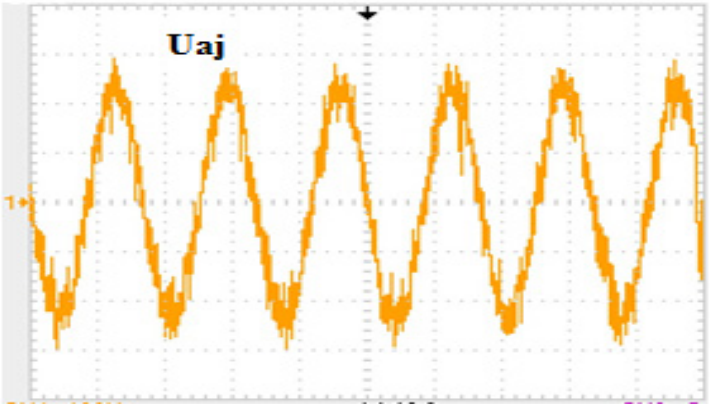

(b)

Fig. 5.14 Inverter phase voltage to be connected to the grid with only L-filter (50 V/div-10ms): (a) Simulation and (b) Experimental (continued)

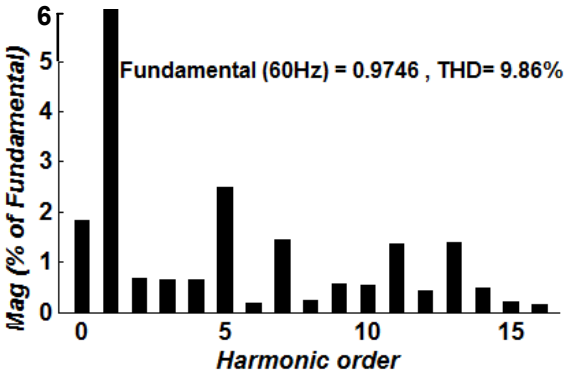

(a)

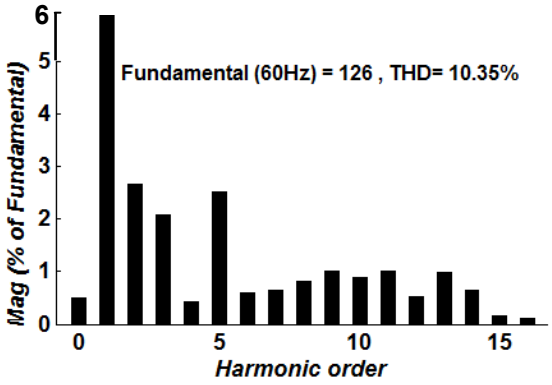

(b)

Fig. 5.15 The harmonic spectrum of: (a) Injected current and (b) Phase voltage

5.6.3 Grid-Connected VOC VSI with LC-Filter

An LC ($24mH$, $40\mu f$) filter with cut-off frequency of 205 Hz is used in the system between the WECS and utility grid. In the second test to investigate the controller performance and the capability of the system assumption of demanded active and reactive power is considered such that:

P^r = 125 *watt* over the test period. Q^r = 125 *VAR* from the start till 2 sec, and reversed to a positive reference (Q^r = -125 *VAR*) after that. The change between the modes of supplying and extracting reactive power is very clear with grid current and voltage waveforms as shown in Fig. 5.16. From the start until 2 sec, the VSI is considered as a capacitive load supplies reactive power to the grid. After that, the VSI absorbs reactive power from the grid causing the current to lag the voltage.

The in-phase injected current with grid and capacitor voltages $(i_a^j,\ u_a^g,\ u_a^c)$, the harmonic content of the injected current and filter capacitor voltage, and the measured efficiencies are shown in Figs. 5.17-5.19. Not like the L-filter, the voltage and current waveforms have less harmonic distortion.

Figure 5.17 shows the synchronization between the grid voltage and the filter capacitor voltage where they are almost the same. The current and voltage THD for the developed WECS with LC-filter is less than the 5% limit imposed by IEEE-519 standard [100], which does not occur when L-filter is considered. There is a significant change in the harmonic content for the output current and voltage of the WECS where the current and voltage THD% decreases from (9.86%, 10.35%) with L-filter to lower values as (2.67%, 0.12%) with LC-filter, respectively, as shown in Fig. 5.18. This demonstrates the expected improvement when compared with similar works.

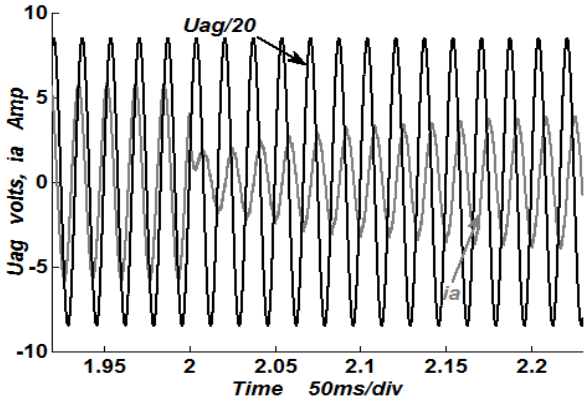

(a)

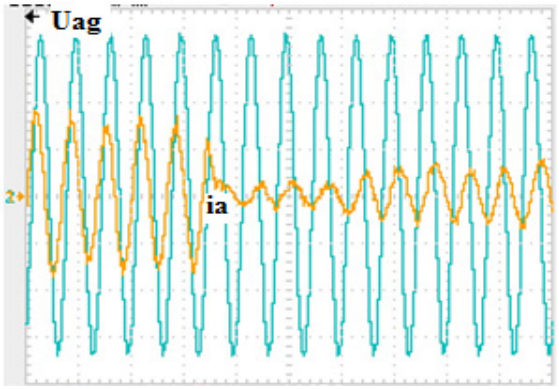

(b)

Fig. 5.16 Grid voltage (50 V/div-25ms) and injected current (1 A/div-25ms) under step change in the reactive power injected into grid: (a) Simulation and (b) Experimental

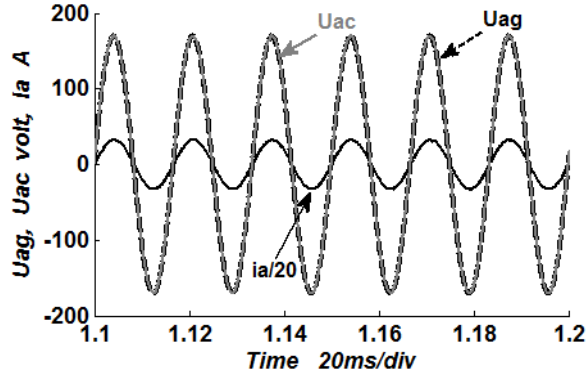

(a)

Fig. 5.17 VSI response with LC-filter for the grid and capacitor voltage (100 V/div-10ms) with the injected line current (5 A/div-10ms): (a) Simulation and (b) Experimental

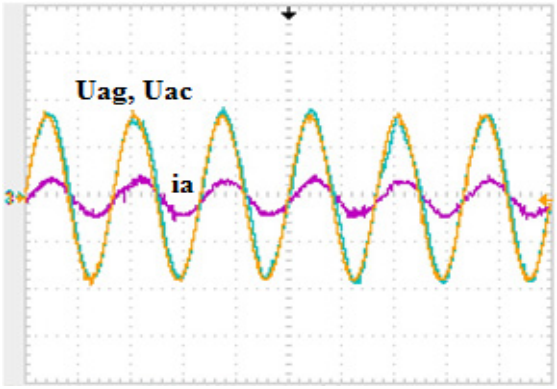

(b)

Fig. 5.17 VSI response with LC-filter for the grid and capacitor voltage (100 V/div-10ms) with the injected line current (5 A/div-10ms): (a) Simulation and (b) Experimental (continued)

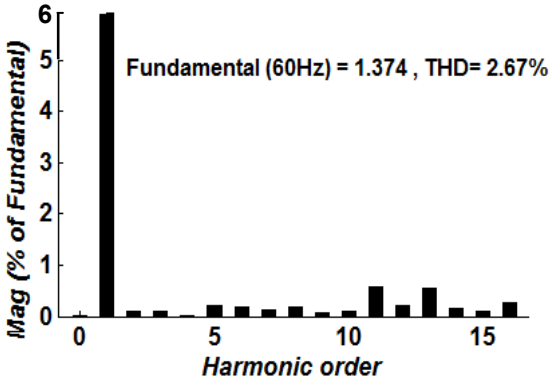

(a)

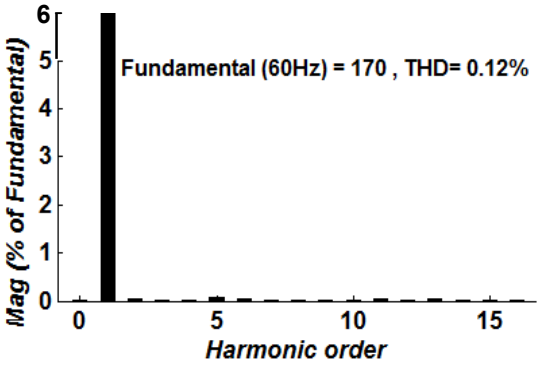

(b)

Fig. 5.18 The harmonic spectrum analysis with LC-filter: (a) Injected current harmonic content and (b) Filter capacitor voltage harmonic content

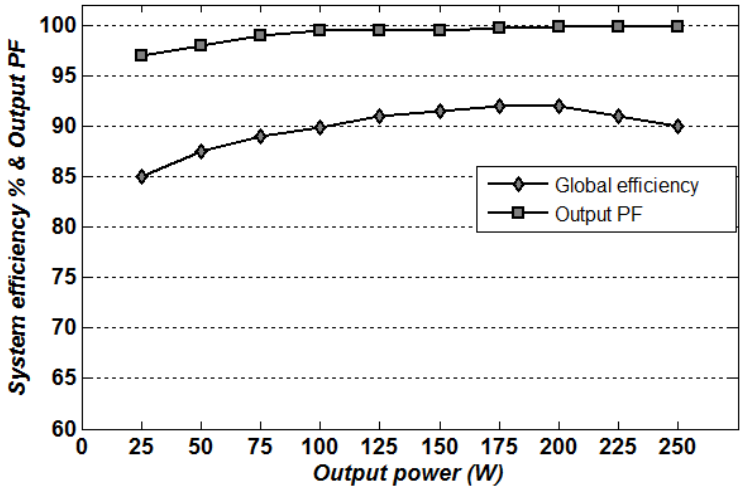

Fig. 5.19 Efficiency and output power factor versus output power

5.7 Conclusion

In this chapter, the VOC grid connected VSI was investigated for high performance control operation. The test results showed how the control scheme succeeded in injecting the wind power as active or reactive power in order to compensate the weak grid power state. An LC-filter is inserted between VOC VSI and grid to obtain a clean voltage and current waveform with negligible harmonic content and improve the power quality. Also, this technique achieved unity power factor grid operation (average above 0.975), very fast transient response within a fraction of second (0.4 sec) under different possible conditions (wind speed variation and load variation) and high efficiency due to reduced number of components (average above 90%) was achieved. The experimental results obtained from a prototype rated at 250 W showed that the current and voltage THD (2.67%, 0.12%), respectively, for the WECS with LC-filter is less than 5% limit imposed by IEEE-519 standard. All results obtained confirm the effectiveness of the developed system feasible for small-scale WECSs connected to weak grids.

Chapter 6 High Frequency versus Low Frequency Converter Operation Study for Hybrid Renewable Generation System

6.1 Introduction

Today's power converters generally operate in the low hundreds of kHz (the frequency at which power is shuffled through the circuit) with efficiencies between 60 and 90%. While higher efficiency power converters are currently technologically possible, their size and cost preclude them from practical application. Specifically, the size of the passive components (inductors and capacitors) in these converters is inherently tied to the frequency at which the converter operates. A power converter is like a bucket that transfers water from a one tank to another. To transfer water ("energy") between tanks, one could fill and then empty a large bucket once, or, to transfer the same amount of water in the same amount of time, one could fill and empty a smaller bucket several times very quickly. Similarly, by increasing the switching frequency of power converters, passive components – which make up the majority of the converter's volume – can be miniaturized significantly; thereby driving down the converter's cost. Unlike in the computing industry where Moore's law has driven switching frequencies into the Gigahertz range, high frequency operation has not been the focus of power electronics because the energy losses in the semiconducting switches and in the converter's magnetic components increase at higher frequencies. This means that in order to realize the miniaturization and low-cost benefits of high frequency power conversion, a new set of materials, circuit topologies, and component designs is needed. Achieving greater conversion efficiencies along with greater degrees of integration and miniaturization has

become the focus of research labs and corporations across the country as groups attempt to create the next generation of integrated power conversion systems.

High frequency operation for power converters became a mature technology with several international manufacturers of power electronic devices [101]. Recent power converters tend to increase switching frequency to reduce the size and volume of the passive components, such as inductors, transformers, and capacitors. However, a high-frequency switching operation increases the power semiconductor device switching loss, which is proportional to the switching frequency [102]. The latest technologies have a fast turn-on and turn-off capability to reduce the switching loss at a high frequency operation [103]. A major design aspect in high power converters is the selection of the inductor and capacitor. The major concern is the size, cost and weight of such a high power inductor that is perhaps the single heaviest component in the entire converter. In order to reduce the inductor size and weight, a small inductance value is preferred.

Figure 6.1 shows relation between output power density and power loss of converters (based on traced data by NTT for different types of power supplies). It is obvious that the output power density increases with the loss reduction [27, 165]. Figure 6.2 shows the relation between output power density and switching frequency [104, 166]. It is implied from this data that the output power density have been improved roughly in proportion to switching frequency increase. In 10 years of the future, the power density will 10 times increase according to the trend curve shown in Fig. 6.3 [30, 167]. According to the relation between output power density and power loss shown in Fig. 6.1, the power losses of power electronics systems will be reduced by half, and the switching frequency will be 10 times higher than that for present converters according to Fig. 6.2.

Figure 6.4 shows present switching frequencies for output power of power electronics systems. To achieve lower loss and higher switching frequency for higher output power density systems, semiconductor power device improvement is the key issue because the power loss generated in the power semiconductors shares about a half of total losses in the present power electronics system and increase of switching frequency directly increases the semiconductor power loss.

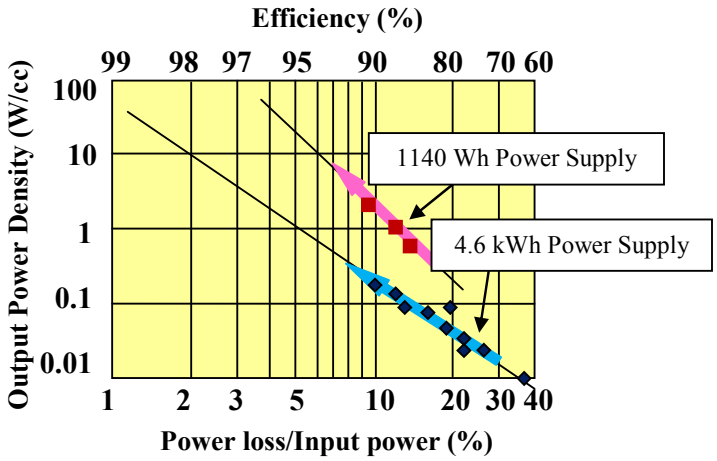

Fig. 6.1 Relation between output power density and power loss of converters according to traced data by manufacturer for different types of power supplies

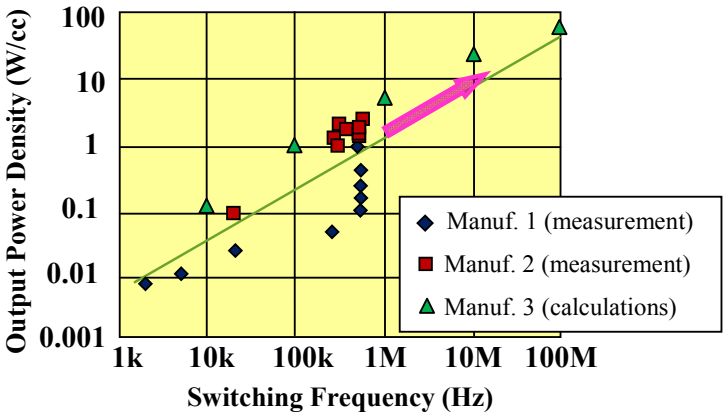

Fig. 6.2 Output power density versus switching frequency trends

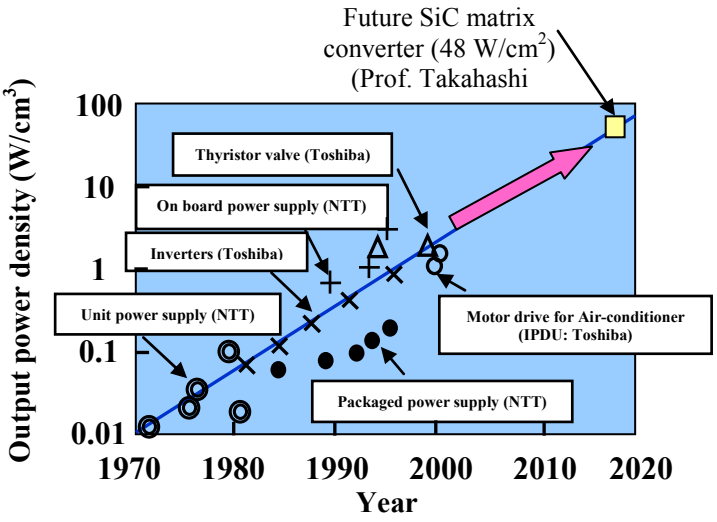

Fig. 6.3 Output power density improvement trends for 30-years

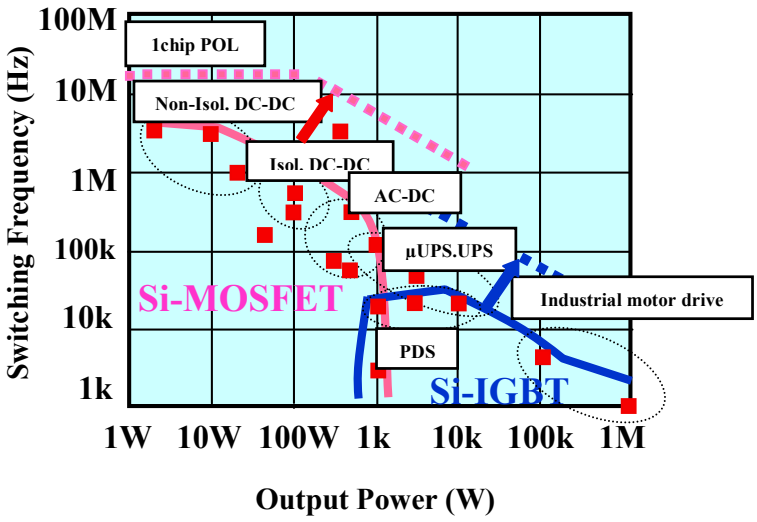

Fig. 6.4 Switching frequency for power electronics systems (broken line represents frequency prospect in 2010-2015)

In this chapter, a simple simulation comparative study between high frequency (HF) and low frequency (LF) switching is done to verify the advantages resulting from HF-operation and to confirm the effectiveness of the hybrid generation system with high frequency-high power converters for grid connection operation. This study is investigated for each conversion stage separately. Firstly, the rectification stage (AC/DC) between the

wind generator and DC-link. Secondly, the (DC/DC) conversion stage between PV-generator and DC-link. Finally, the inversion stage (DC/AC) between the DC-link and the local grid.

6.2 Electromagnetic Interference Effect

Two major sources of EMI in power electronics are *dv/dt* and *di/dt* during switching times. In fact, a DC-voltage of few hundred volts is chopped by a power switch in a fraction of microsecond. Thus, conducted emission is a major issue in most power electronic systems due to significant over voltage and leakage current generated by fast switching and stray components of the system.

High *di/dt* may create significant over voltage in power converters due to stray inductance of current loops. High *dv/dt* may create significant leakage current in magnetic elements and electric motors due to stray capacitive coupling between windings and a frame.

The switching loss can be reduced by decreasing the switching time, but fast switching increases *dv*/*dt* and *di*/*dt* which affects electromagnetic interference (EMI) noise. As previously discussed, decreasing *dv/dt* and *di/dt* means increasing the switching time which increases losses. Thus, it is a trade-off between losses and EMI to determine the switching time. The other alternative is to reduce stray inductance and capacitance of power electronics system using a better layout, interconnection and configuration.

6.3 Simulink Model Architecture

Figure 6.5 shows the Simulink model for the hybrid system which includes:

- PMSG wind generator (10 kW),
- PV generator (6-kW),

- 3-Line inductors (0.1 mH) mounted between wind generator and rectifier circuit,
- Rectifier circuit; semi-controlled topology is studied as an example,
- DC-DC boost converter to interface the PV-source to the DC-link,
- DC-link capacitor (1000 μf) as a voltage filter
- DC-resistive load (1 kW)
- PWM VSI topology for grid connectivity,
- LC-filter (0.3mH and 20 μf) as a low pass filter
- AC-resistive load (3 kW),
- AC-dynamic load (5 kW induction motor).

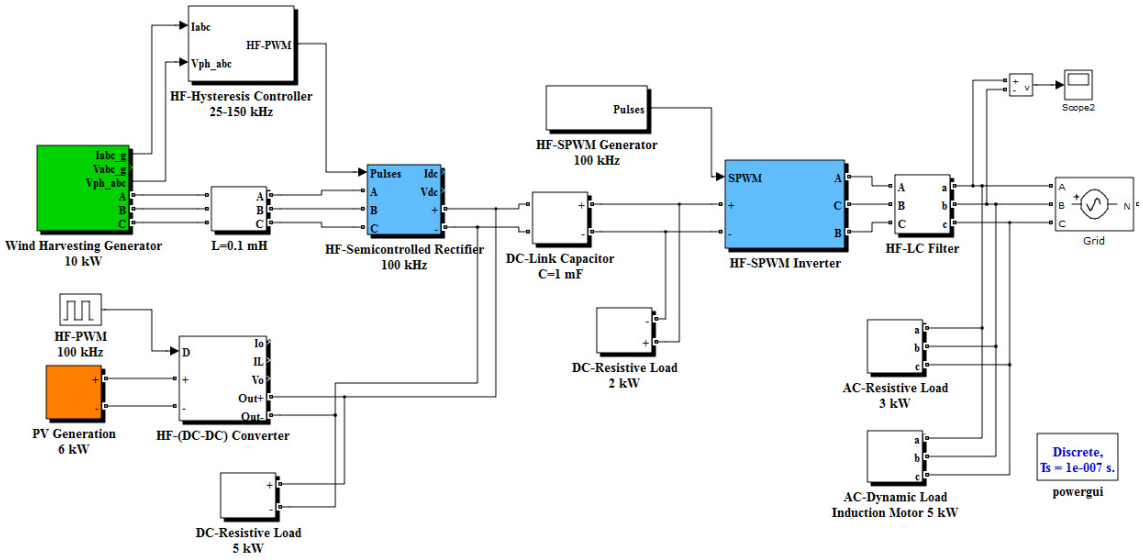

Fig. 6.5 The Simulink model for switching frequency comparative study

6.3.1 HF versus LF for Rectifier Operation Test

In this section, the comparison is made between HF and LF switching for the same rectifier topology. A semi-controlled rectifier topology is selected here as an example. The rectifier is controlled through hysteresis band controller to achieve lower current

harmonic distortion; since the duty cycle is discontinuous. The HF switching operation is set between 30-45 kHz while the LF switching operation is set between 1-5 kHz. Figure 6.6 show the rectifier input voltage and current waveforms for both switching operations. HF switching gives THD of (0.62, 21.79%) for generator voltage and current, respectively, while LF switching gives THD of (0.71, 63.78%) for rectifier voltage and current, respectively, as shown in Figs. 6.7, 8. It can be noticed that the harmonic distortion is significantly reduced with HF operation compared to LF operation.

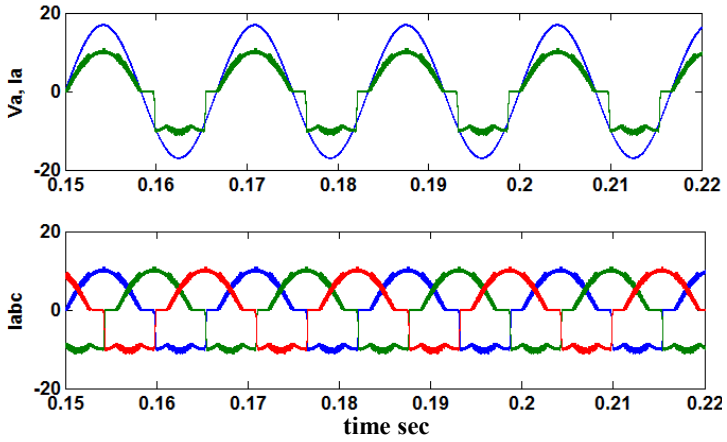

(a)

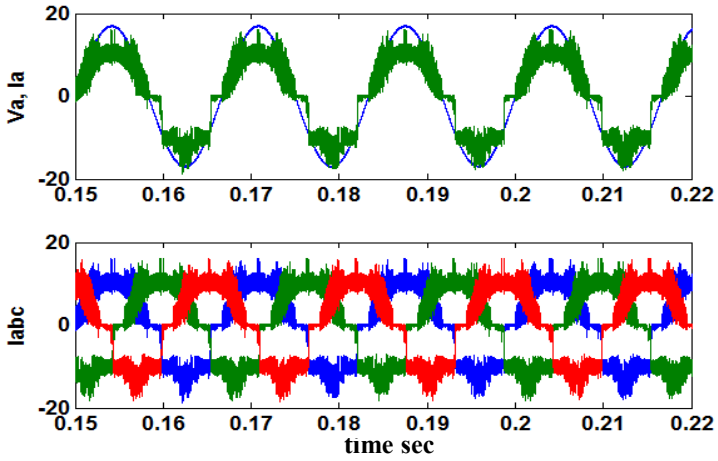

(b)

Fig. 6.6 Switching frequency comparison for the rectifier stage: (a) HF and (b) LF

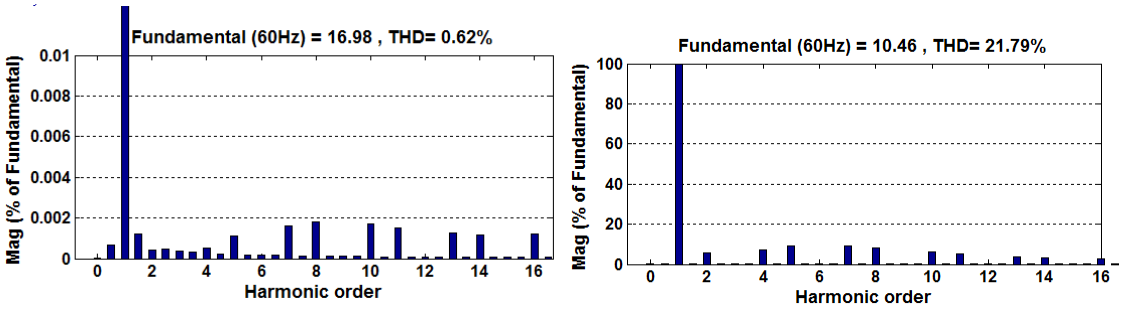

(a) (b)

Fig. 6.7 Harmonic spetcrum for rectifier under HF operation: (a) Voltage THD% and (b) Current THD%

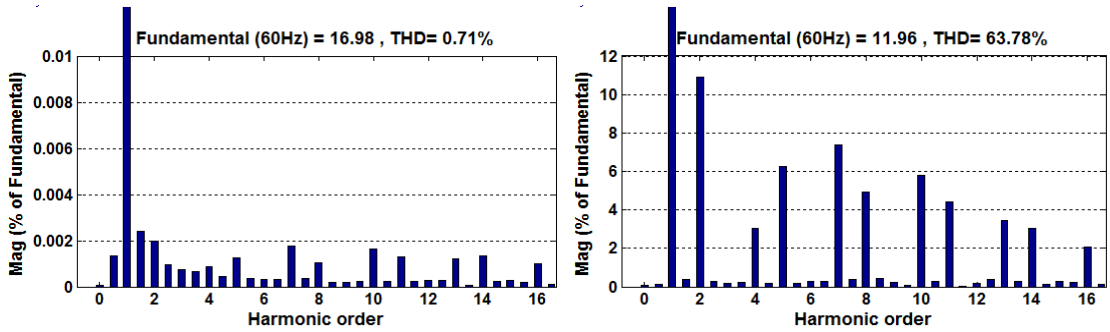

(a) (b)

Fig. 6.8 Harmonic spetcrum for rectifier under LF operation: (a) Voltage THD% and (b) Current THD%

6.3.2 HF versus LF for Inverter Operation Test

A simple sinusoidal (SPWM) switching technique was used for HF of 30 kHz versus LF of 3 kHz. This study was created for same passive element values in the circuit; where 0.3 mH, 20 µF are used in the VSI. Figure 6.9 shows the voltage and current waveforms. The harmonic spectrum for both operations is also shown in Fig. 6.10, 11. For HF operation, we can notice that voltage and current harmonic distortion (THD %) are 1.21 and 0.74%, respectively, which is below the 5% limit imposed by IEEE-519 standard

[100]. On the other hand, a 37 and 17.26% voltage and current harmonic distortion, respectively, resulted from LF operation.

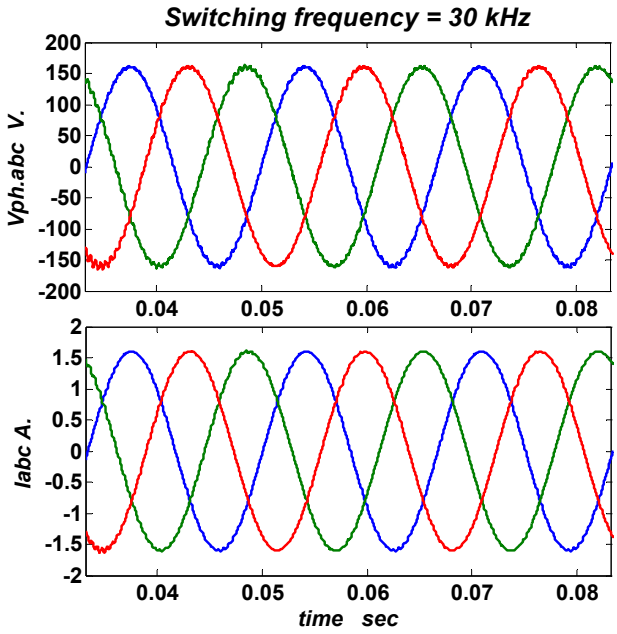

(a)

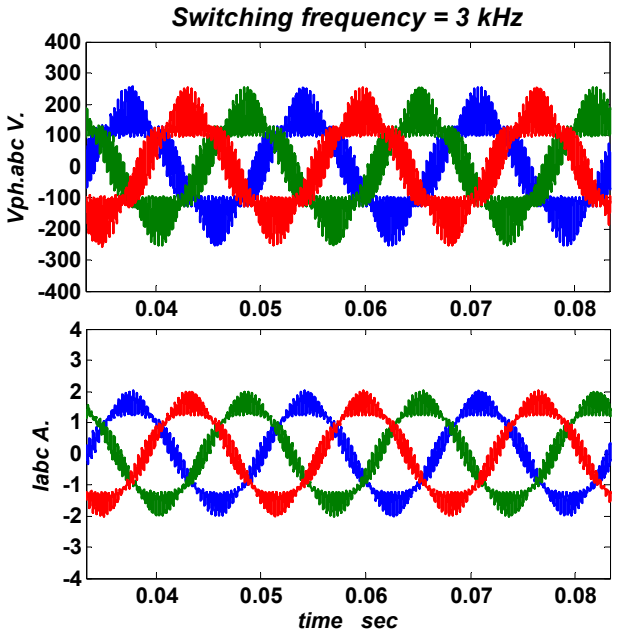

(b)

Fig. 6.9 Switching frequency comparison for the inverter stage: (a) HF and (b) LF

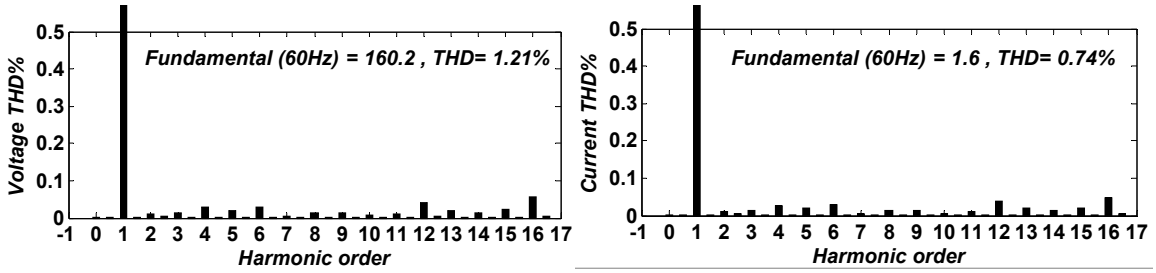

(a) (b)

Fig. 6.10 Harmonic spetcrum for inverter under HF operation: (a) Voltage THD% and (b) Current THD%

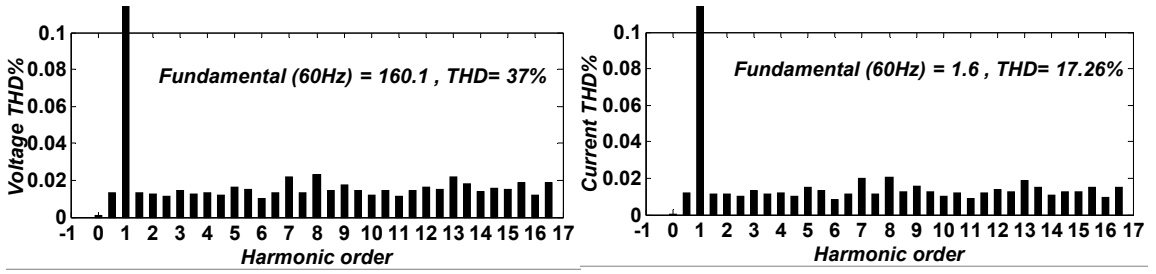

(a) (b)

Fig. 6.11 Harmonic spetcrum for inverter under LF operation: (a) Voltage THD% and (b) Current THD%

6.4 Conclusion

In this chapter, the HF switching operation was investigated and compared with the LF switching operation for hybrid systems applications. A Simulink model was built and tested under both operations. The system performance was evaluated through the voltage and current waveforms for the rectifier and inverter inside the system. It was noticed that under HF operation, reduced passive elements were used in addition to less harmonic distortion which leads to better power quality when compared to LF operation.

Chapter 7 High Frequency Three-Phase Semi-controlled Boost Rectifier for Grid-Connected Wind Generation Systems

7.1 Introduction

Low speed operation of direct-driven permanent magnet wind generation systems (PMWGS) is one of the major aspects that influence the generated voltage. However, direct drive operation is preferred for higher generation efficiency [48]. Also, low speed operation produces low voltage profile at the generator terminals. In this chapter, a new grid-connected dual-boost converter feasible for low speed direct-driven PMWGSs is introduced. A three-phase high frequency semi-controlled boost rectifier is used as the first interface stage for grid connection. Robustness, simplicity, low cost, and high efficiency are inherent characteristics because few semiconductor elements are used. Also, the size and weight of the passive elements (inductors and capacitors) are reduced proportionally to the switching frequency improving the overall efficiency. Furthermore, a DC-bus voltage control technique for parallel wind-based three-phase semi-controlled PWM rectifiers is developed with master-slave strategy. This technique involves hysteresis control algorithm in order to reduce the wind generator harmonic distortion due to duty cycle discontinuity. The topology structure, the principle of operation, and control scheme are presented. The general circuit model and loss model are derived with the aim to design the closed-loop control and to calculate the efficiency, respectively. These models consider the internal resistance of the inductor and capacitor for the rectifier. The PI-voltage controller is designed to accomplish the specifications of the voltage control loop based on the dynamics of the DC-bus. A 2^{nd} order SPLL technique is also used in the control loop to detect the angle of the generator and grid voltages.

Additionally, a three phase current source inverter (CSI) is employed in the grid connection.

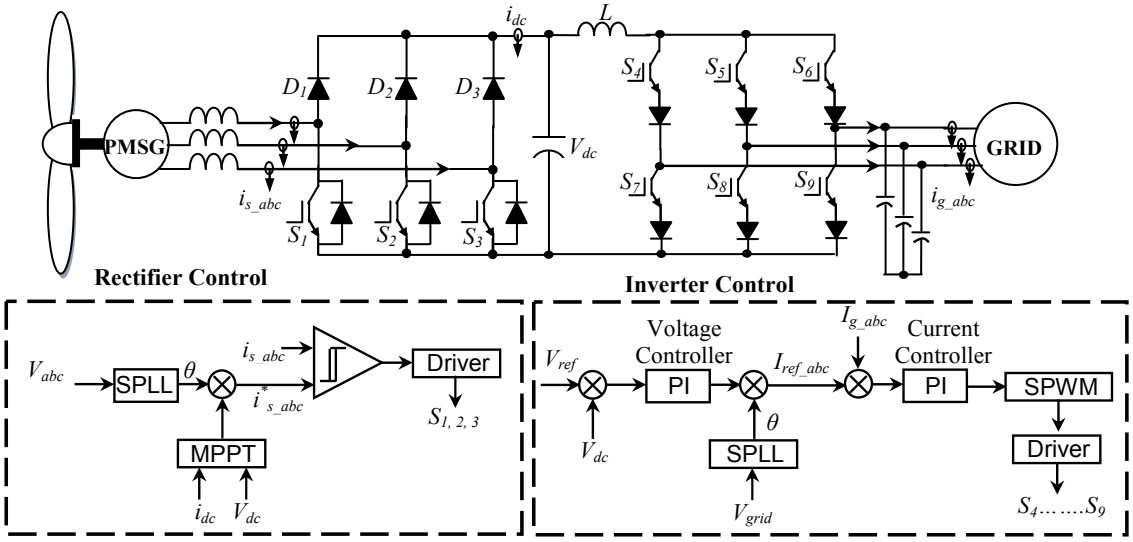

Fig. 7.1 Schematic diagram of the dual-boost low speed direct-driven PMWGS

7.2 Developed Conversion Topology

The developed system is shown in Fig. 7.1. Each wind emulator machine system is represented by a VSPM directly coupled to PMSG. With this configuration, the boost DC-DC converter (shown in Figs. 2.12, 15) is omitted without any change in the objectives of WGS. The developed semi-controlled rectifier topology only uses three insulated-gate bipolar transistors (IGBTs) and three diodes when compared to VSC topology (shown in Figs. 2.13, 16) [105]. Moreover, there is no need to add step-up transformer (shown in Figs. 2.12-14) between the inverter output and grid; since CSI is used as a boost inverter. The easy way to reduce the size of the inductor, capacitor and input /output EMI filter by means of increasing the frequency of inductor current ripple and the output voltage ripple. The operating switching frequency for rectifier is set between 30-45 kHz according to the designed hysteresis band and for inverter operation

is 50 kHz. The control scheme provides higher system bandwidth with the aim to achieve a fast dynamic response for the converter and to reduce the size of the passive components. To design the developed rectifier control system, it is necessary to model its dynamic behavior. Unfortunately, understanding of converter dynamic behavior is hampered by the nonlinear time-varying nature of the switching and PWM process.

7.2.1 Rectifier Power Transfer Operation

Three-IGBTs are only employed for controlling the amount of the power transferred from the wind generator inputs to DC-link. When any switch S1, S2, or S3 is turned on then the current will flow through it and respective input inductor current will increase, while respective diode D1, D2, or D3 is reverse biased (off). On the other hand, when S1, S2, or S3 is turned off then the current will flow through the respective diode D1, D2, or D3 (forward biased) and energy will be transferred to DC-link.

According to current direction, three states are representing each phase current I_a, I_b, and I_c. These states can be simplified as: zero (z), forward (f), and reverse current flow (r), resulting in 27 different states as shown in Fig. 7.2. Only 12 states are physically implemented as shown in Table 7.1. There are three states (10, 11, and 12) will not be implemented for rectification mode of operation; since no power will be transferred to DC-link. The other nine states can be subdivided into three groups; (1, 4, and 7), (2, 5, and 8), and (3, 6, and 9). Therefore, states 1-3 will be repeated with 4-6 as well as 7-9. Fig. 7.3 shows the current waveforms for all rectification possible states 1-9 where only the positive half cycle is modulated while negative half cycle is uncontrolled.

- Sector I: In this sector, currents I_a and I_b are forward, and current I_c is reverse. Thus, in this sector, the rectifier has two degree of freedom (DOF), associated to the states

of switches S1 and S2, resulting in the four possible topological states, as shown in Fig. 7.4.

- Sector II: In this sector, current I_a is forward, current I_b is zero, and current I_c is negative. Therefore, in this sector, the rectifier has only one DOF, which is associated to the state of the switch S1, resulting in the topological states of Fig. 7.5.
- Sector III: In this sector, current I_a is forward, current I_b is reverse, and current I_c is zero. Thus, in this sector, the rectifier has only one DOF, which is also associated to the state of switch S1, resulting in the topological states of Fig. 7.6. Applying the same criterion, similar sectors can be subdivided in three sets: (1, 4, and 7), (2, 5, and 8), and (3, 6, and 9). Hence, the description of sectors I–III is enough for deriving the remaining ones.

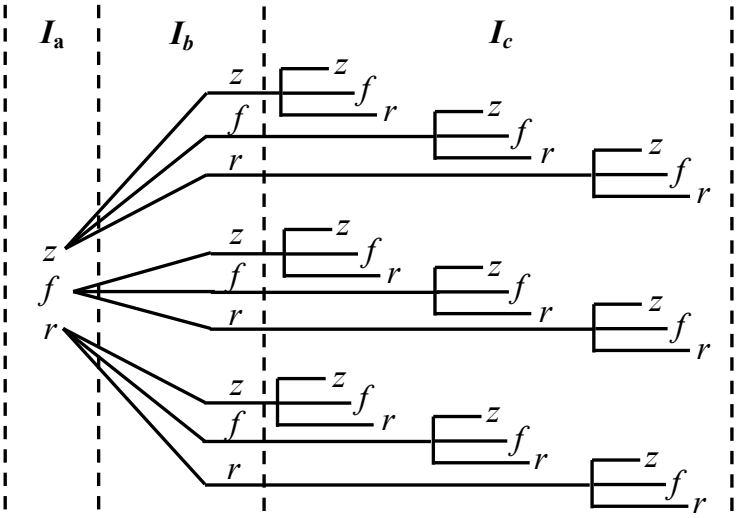

Fig. 7.2 All possible combinations for rectifier current flow

Table 7.1 The physical valid current flow for rectifier operation

	1	2	3	4	5	6	7	8	9	10	11	12
I_a	*f*	*f*	*f*	*f*	*z*	*r*	*r*	*r*	*z*	*f*	*r*	*r*
I_b	*f*	*z*	*r*	*r*	*r*	*z*	*f*	*f*	*f*	*r*	*f*	*r*
I_c	*r*	*r*	*z*	*f*	*f*	*f*	*f*	*z*	*r*	*r*	*r*	*f*

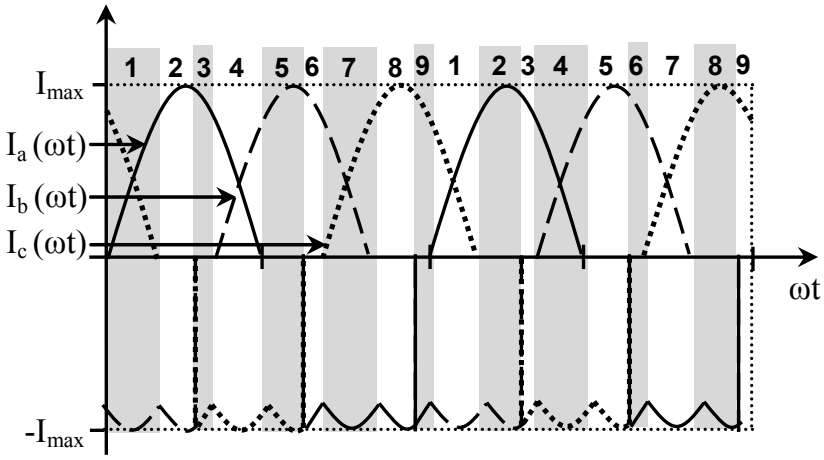

Fig. 7.3 Theoretical current waveforms for the nine rectification physical states

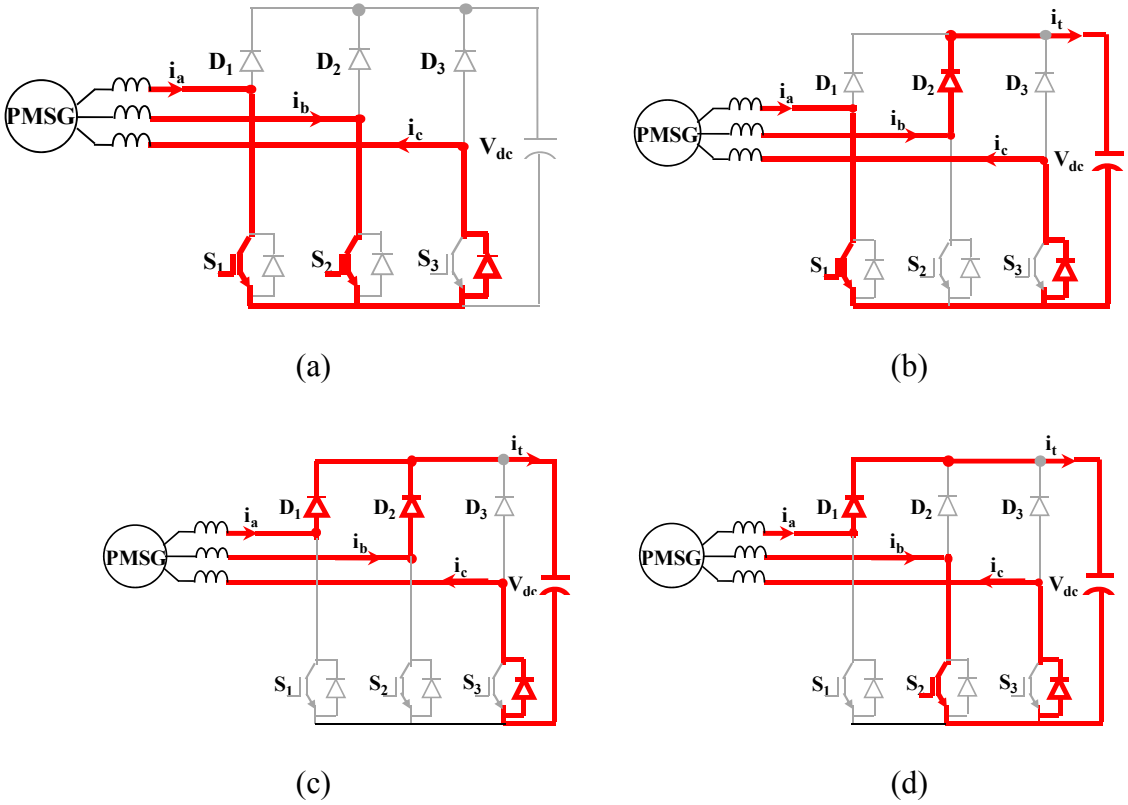

Fig. 7.4 Sector I topological states: (a) S1, S2 are ON, (b) S1, D2 are ON, (c) D1, D2 are ON and (d) D1, S2 are ON

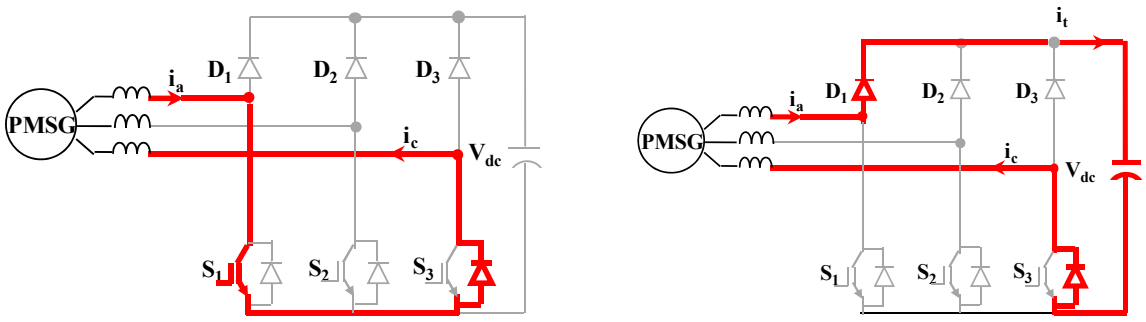

(a) (b)

Fig. 7.5 Sector II topological states: (a) S1 is ON, (S2, D2) are OFF and (b) D1 is ON, (S2, D2) are OFF

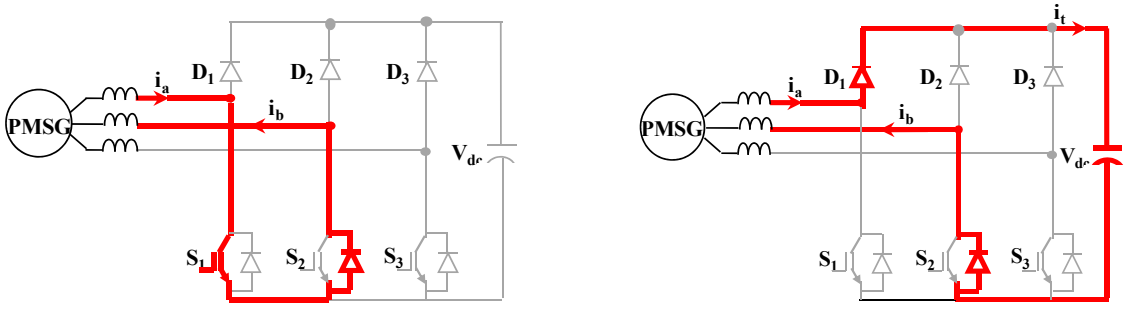

(a) (b)

Fig. 7.6 Sector III topological states: (a) S1 is ON, (S3, D3) are OFF and (b) D1 is ON, (S3, D3) are OFF

7.2.2 Rectifier Dynamic Model

The input and output equivalent circuits of a three-phase semi-controlled rectifier are shown in Fig. 7.7. It is assumed that a resistive load R_L is connected to the output terminal. The instantaneous average voltages (V_{ra}, V_{rb}, and V_{rc}) seen by each phase are given by:

$$\begin{bmatrix} V_{ra}(t) \\ V_{rb}(t) \\ V_{rc}(t) \end{bmatrix} = \begin{bmatrix} 1-D_{sa}(t) \\ 1-D_{sb}(t) \\ 1-D_{sc}(t) \end{bmatrix} \begin{bmatrix} V_a(t) \\ V_b(t) \\ V_c(t) \end{bmatrix} \tag{7-1}$$

Where $D_{sa}(t)$, $D_{sb}(t)$, and $D_{sc}(t)$ are instantaneous functions of the effective duty cycle of switches S1, S2, and S3, respectively, V_a, V_b, and V_c are the PMSG-phase voltages, I_a, I_b, *and* I_c are the AC-input currents, and R, L are the resistance and inductance of the boosting inductor, respectively. Considering the generator voltages balanced and the absence of the neutral conductor, and applying the Kirchhoff's law and Laplace transform, the dynamic model of the rectifier is obtained and given in matrix form by:

$$\begin{bmatrix} I_a(s) \\ I_b(s) \\ I_c(s) \end{bmatrix} = \frac{1}{3Ls} \begin{bmatrix} -2 & 1 & 1 \\ 1 & -2 & 1 \\ 1 & 1 & -2 \end{bmatrix} \begin{bmatrix} V_{ra}(s) \\ V_{rb}(s) \\ V_{rc}(s) \end{bmatrix} \tag{7-2}$$

For fast voltage control, the input power should supply instantaneously the sum of load power and charging rate of the capacitor energy. On the DC-output side in Fig. 7.7. b:

$$i_{dc} = C_{dc} \frac{dv_{dc}}{dt} + i_L \tag{7-3}$$

Where v_{dc}, i_{dc}, C_{dc} are the DC-link output voltage, current, and filter capacitor, respectively, i_L is the load current.

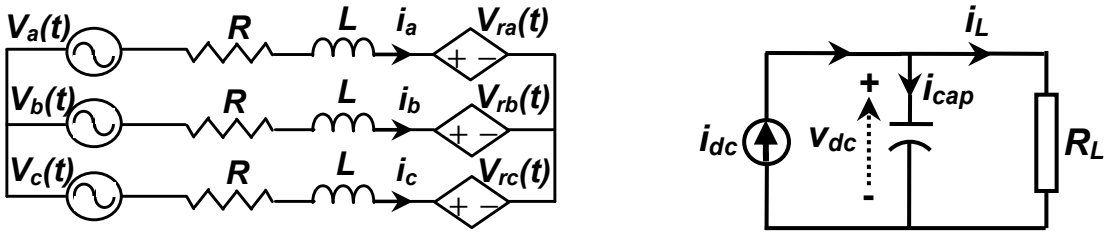

(a) (b)

Fig. 7.7 The equivalent circuit of the three-phase PWM semi-controlled rectifier. (a) Input side and (b) Output side

7.2.3 Rectifier Control

Through simulation studies, it was verified that constant frequency PWM controllers tend to increase the current THD due to the discontinuities duty cycle operation [106-109]. Among presented techniques and widely used for high performance current control is the hysteresis controller. The input currents through each phase (I_{s_abc}) are measured and compared to the respective reference currents ($I^{*}_{s\_abc}$). The reference current shapes are obtained from the respective input voltages, and their peak values are given by a MPPT algorithm as shown previously in Fig. 7.1. The employed MPPT algorithm consists of measuring the frequency of the generator voltage through a 2nd order SPLL technique [86]. Then, the current peak values are obtained from a preprogrammed table. Switching operation occurs when the current limits are reached, as shown in Fig. 7.8. With this technique, the obtained line currents achieve low THD with a simple control circuitry. The main disadvantage of the hysteresis control is the variable switching frequency. However, switching frequency can be maintained within acceptable range by adjusting the hysteresis band (HB).

The HB method switches the IGBTs (S1-S3) when the error between $I^{*}_{s\_abc}$ and I_{s_abc} exceeds a fixed magnitude: the hysteresis band. This type of control needs a single comparator with hysteresis per phase. In this case the switching frequency is not determined, but its maximum value can be evaluated such that [110]:

$$F_s^{\max} = \frac{V_{dc}}{4h \cdot L} \tag{7-4}$$

Where $F_s^{\max}$ is the maximum switching frequency, and *h* is the HB magnitude.

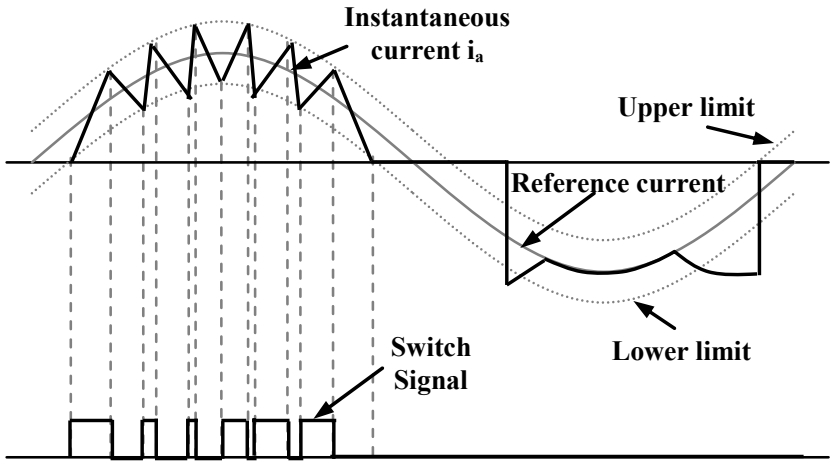

Fig. 7.8 Switching pattern of the hysteresis control applied to the rectifier stage

7.2.4 Rectifier Efficiency

In this section, the power losses of the rectifier are estimated with the aim to calculate the efficiency of the converter. The total losses in a power electronics system are the sum of all losses and the efficiency of a system (η) can be calculated based on input power (P_{in}), output power (P_{out}) and total losses (P_{loss}). The converter efficiency is expressed by:

$$Efficiency(\eta) = \frac{P_{out}}{P_{in}} = \frac{P_{out}}{P_{out} + P_{loss}} \tag{7-5}$$

$$P_{loss} = P_S + P_D + P_{LC} \tag{7-6}$$

The power loss in a switch (P_S) over one switching cycle is given by:

$$P_S = I_{srms}^2 r_{CE} + V_{CE} I_{sav} + \frac{V_{dc}}{V_{CC} I_C} \begin{bmatrix} E_{off}(I_{sav} + \Delta I/2) + \\ E_{on}(I_{sav} - \Delta I/2) \end{bmatrix} \tag{7-7}$$

The *IGBT* represents the switch in this study. The *IGBT* characteristics (e.g. r_{CE}, V_{CE}, V_{CC}, I_C, E_{off}, and E_{on}) are given in *IGBT* datasheet. The I_{Srms}, I_{Sav} and ΔI represent respectively the rms current of the *IGBT*, the average current of the IGBT and the current ripple. The losses of the diode (P_D) are evaluated as follows:

$$P_D = I_{Drms}^2 r_F + V_{F0} I_{Dav} + \frac{V_{dc}}{V_{CC} I_F} [E_{rr} I_{Dav}] \tag{7-8}$$

The *diode* characteristics (e.g. r_F, V_{F0}, V_{CC}, I_F, and E_{rr}) are given in datasheet. The I_{Drms} and I_{Dav} represent the rms current and the average of the diode. In a power electronics system, there are other circuits such as gate drives, controllers, sensors and passive filters which consume power. The losses of the passive components (P_{LC}) are approximately given by:

$$P_{LC} = I_{Lrms}^2 R_L + I_{Crms}^2 R_C \tag{7-9}$$

The DC-output power is calculated as follows:

$$P_{out} = V_{dc} I_{dc} \tag{7-10}$$

In order to estimate the efficiency of the rectifier, a loss analysis was performed, considering the developed equations, the semiconductors, and parameters given in Table 7.2 and the respective datasheets.

Table 7.2 Semiconductor devices and its parameters

Parameter	Specification
S_1-S_9, D_1-D_3	SKM 50GAL125D
V_{switch}	1200V
I_{switch}	50A

7.3 Rectifier Parallel Operation for Wind Farms

In this section, the rectifier topology is studied for parallel-integrated PMSG-based wind farms. A DC-bus voltage control technique is introduced based on a master-slave hysteresis control scheme in order to solve discrepancy problems that could happen

between the controllers. The developed system provides interconnection extension ability of multi wind converter units sharing the same DC-bus and more economic utilization of the wind generator; by insuring unity power factor operation.

To design the parallel-connected rectifier control system, it was necessary to model its dynamic behavior as introduced previously. It is assumed that the converters are rectifying the output voltage of two wind generator systems. It is not convenient to let each unit controlling the DC-bus voltage separately without any information from the other unit. A discrepancy could happen between the controllers. The Master-Slave scheme can solve this problem. One converter unit is selected to be a Master whereas the other is treated as a slave. The slave unit has a self governing system, i.e., it has its inner current control feedback loop. Only the master unit has the outer DC-voltage control feedback loop giving the reference current to the entire slave units. Figure 7.9 shows the DC-bus voltage controller operation. Using the master PI-voltage controller, the DC-voltage can be regulated by choosing the current reference, $i_{ref}(t)$ such that:

$$i_{ref}(t) = K_p^v \cdot [V_{dc}^r - V_{dc}(t)] + K_i^v \cdot \int [V_{dc}^r - V_{dc}(t)]dt \qquad (7\text{-}11)$$

Figure 7.10 shows the configuration of the overall PMWGS parallel system including its control strategy and hardware test setup.

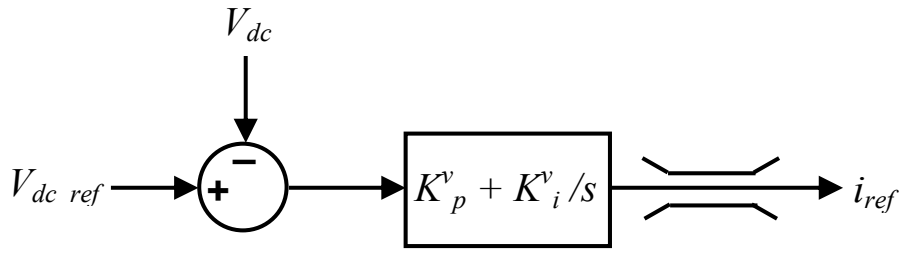

Fig. 7.9 DC-bus voltage controller for parallel rectifier operation

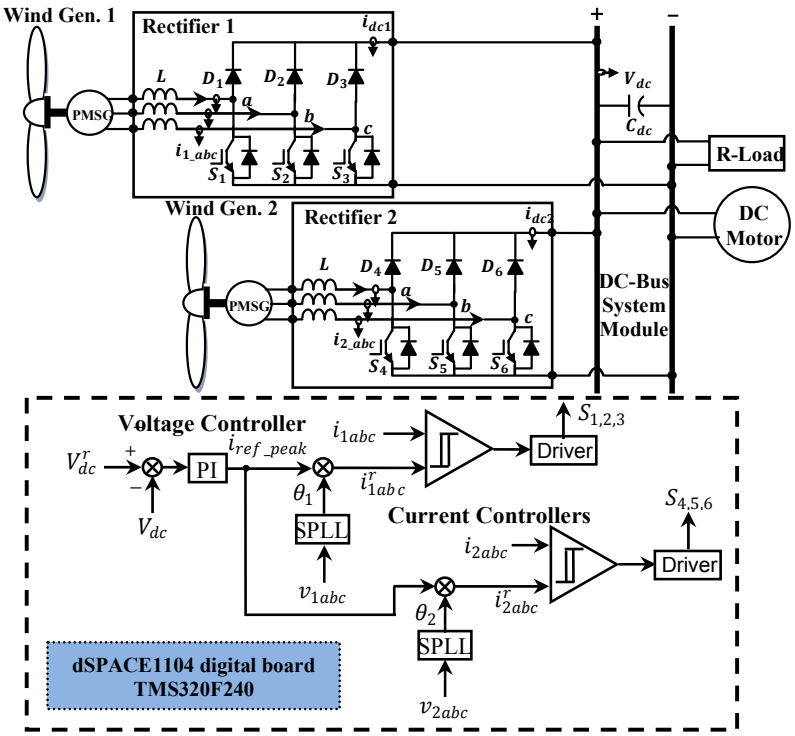

(a)

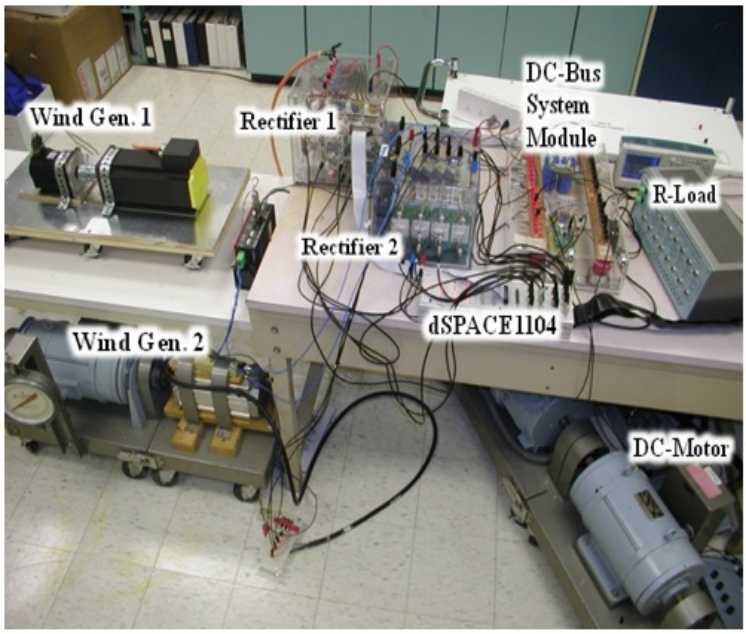

(b)

Fig. 7.10 The overall PMWGS parallel configuration and its developed control strategy: (a) Schematic diagram and (b) Experimental test setup

7.4 Test Results

In order to investigate the performance of the overall system, an experimental setup for the low-speed direct-driven PMWGS is constructed and connected to the local grid. The semi-controlled rectifier topology was tested. Master-Slave strategy discussed in section 7.3 is utilized in the control operation. The parameters for the PMSGs are listed in Table 7.3. The converters specifications and parameters used in the system are shown in Tables 7.4. The individual converters are controlled by their own control platforms. In this section, the experimental results of the semi-controlled rectifier are provided.

Table 7.3 Wind PMSGs Specifications and Parameters

PMSG1		**PMSG2**	
Parameter	Specification	Parameter	Specification
Output power	0-4.88 kW	Output power	0-7 kW
Rated voltage	208 Vrms	Rated voltage	460 Vrms
Rated speed	1200 rpm	Rated speed	1500 rpm
Resistance	0.46 Ω	Resistance	0.56 Ω
Inductance	4.86 mH	Inductance	5.9 mH

Table 7.4 Rectifier and CSI Specifications and Parameters

Rectifier		**CSI**	
Parameter	Specification	Parameter	Specification
Input voltage range	70-208 Vrms	Grid voltage	208 Vrms
Line input inductor	0.3 mH	Grid frequency	60 Hz
Internal resistance	0.012 Ω	Input inductor	1 mH
DC-bus capacitor	1200 μf	Internal resistance	0.04 Ω
DC-bus voltage	400 V	Filter capacitor	20 μf
Switching frequency	30-45 kHz	Switching frequency	50 kHz

7.4.1 Rectifier Performance

Figure 7.11 shows the DC-bus voltage, the current through phase "a," and the respective phase voltage at rated power of PMSG1 (4.88 kW). The DC-bus voltage has no overshoot and low voltage ripple of 2.3%. Figure 7.12 shows the harmonic spectrum of the generator voltage (THD=0.37%) and rectifier current (THD=17.03%) at rated power, where the second-, fourth-, and fifth-order components are the most relevant. This high current THD will affect the generator operation; since it creates more noise and vibration. This large harmonic content can be reduced either by decreasing the hysteresis band width or by increasing the input filter inductance value. UPF operation was investigated (PF=0.991); since the generator current and the phase voltage are in phase. In conventional diode bridge rectifiers, typical power factor and THD are about 0.94 and 35%, respectively. This improvement in the power factor represents a reduction of about 10% in the generator conduction losses. Considering that the THD for the rectifier is lower, additional gain due to the skin effect losses reduction is achieved. While the winding resistances tend to be smaller due to the reduced temperature of the generator, conduction losses are even more reduced.

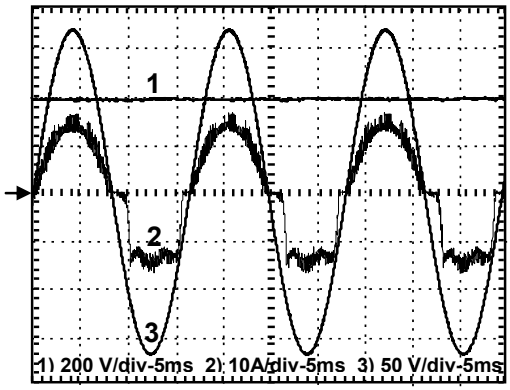

Fig. 7.11 DC-bus output voltage (200 V/div, 5ms), rectifier current (10 A/div, 5ms), and generator voltage (50 V/div, 5ms) for phase "a"

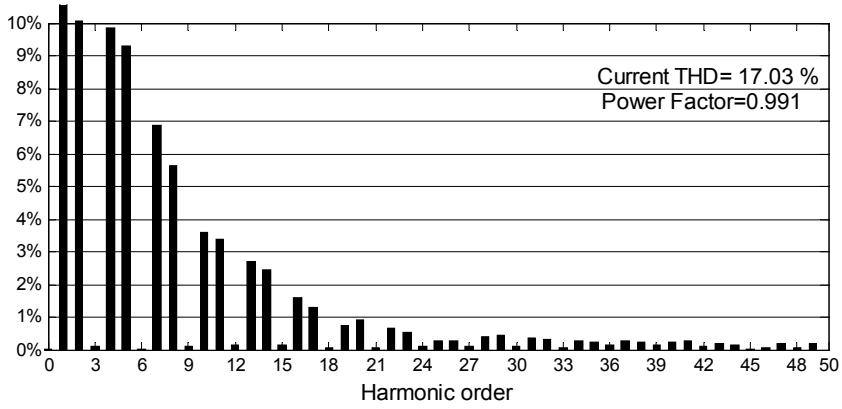

(a)

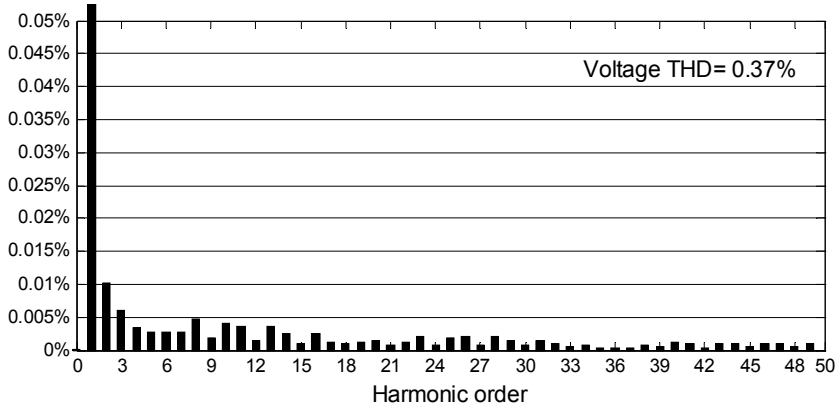

(b)

Fig. 7.12 Harmonic spectrum of: (a) The generator voltage and (b) The input current

7.4.2 Parallel Operation Test

The performance of the parallel operation is investigated using the developed control strategy. Two modular converter units are connected in parallel, sharing one DC-bus as shown in Fig. 7.10. Two different types of DC-loads have been connected to DC-bus; one is representing a static resistive load of 2.38 kW and the other is a dynamic DC-motor loaded at its rated power of 2.5 kW. Figure 7.13 shows the test results of the two parallel converters under step change in the load current (from 2.5 to 4.88 kW). We can notice that the total load current is equally shared between both converters according to the

master-slave scheme. On the other hand, DC-bus voltage still tracking its reference value (400 V) with a small transient dipping of 4 V (1%).

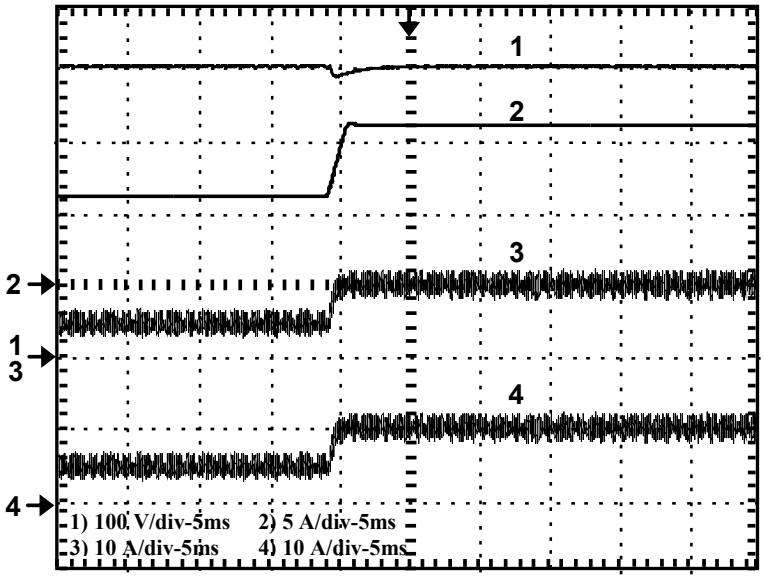

Fig. 7.13 Load current sharing among two parallel converters: (a) DC-bus output voltage (100 V/div, 5ms). (b) Load current (5 A/div, 5ms). (c) PMSG1 *d*-axis current (5 A/div, 5ms). (d) PMSG2 *d*-axis current (5 A/div, 5ms)

7.4.3 Rotor Speed Variation

In order to evaluate the performance of PMWGS emulator in turbulent wind speed condition, an experimental test has been carried out in order to imitate the wind behavior effect which leads to variation in the generator output voltage and frequency. Practically, wind speed has a random variation according to the location and atmospheric conditions. Step change is representing a severe condition for any WECS; since the instantaneous change from any speed to another is not physically possible. However, it is a good test to evaluate the overall control dynamic performance under the worst case. The random wind variation is even easier for the system performance to be tested. Figure 7.14 shows the DC-bus voltage, PMSG1, and PMSG2 phase voltages under step change in the generator output voltage and frequency. The generator voltage change is applied for both PMSGs

but at different instants. It can be noticed that DC-bus voltage has a limited effect at generator voltage variation instants. An 8 V (2%) transient change appears for a fraction of second (0.1 sec) and after that the DC-bus voltage restore its desired reference value at 400 V.

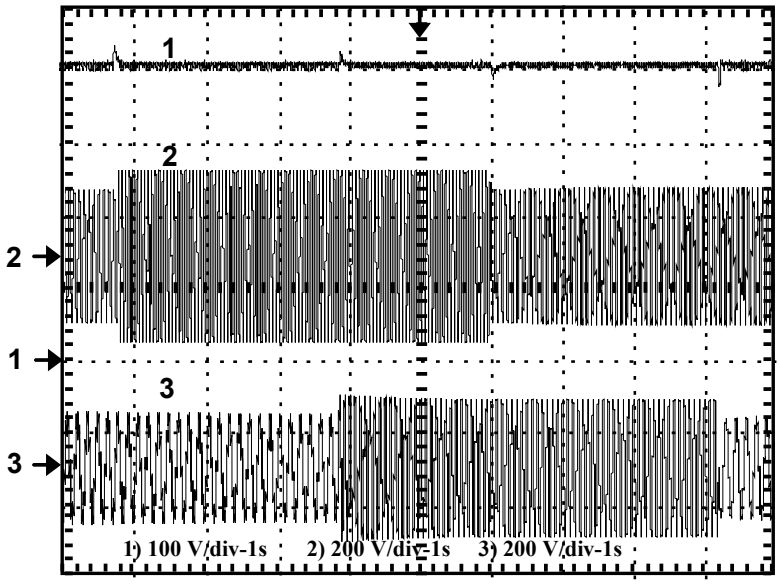

Fig. 7.14 DC-bus voltage (100 V/div, 1s), PMSG1 phase voltage (200 V/div, 1s), and PMSG2 phase voltage (200 V/div, 1s) under generators voltage and frequency change

7.4.4 Parametric Variations Effect

Once the developed parallel PMWGS and its controller was modeled as described above in section 7.3, various parametric variations have to applied to the rectifier circuit, so that a controller can be synthesized which will desensitize them and maintain good performance to achieve satisfactory voltage regulation. For modeling uncertainty, a ±10% variation in the component values of L and C_{dc} is considered. The effect of parameter variations on the control performance is shown in Fig. 7.15. The result shows a transient change of 7% in the DC-bus voltage then it changed back to the desired value according to the reference voltage. This test confirms the robustness of the controller.

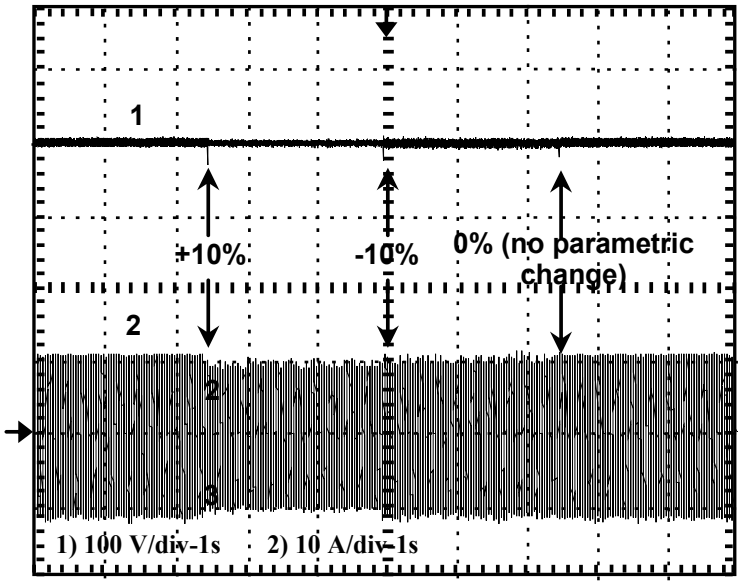

Fig. 7.15 DC-bus voltage (100 V/div, 1 s) and input rectifier current (10 A/div, 1 s) control response during parametric variation of ± 10%

7.4.5 CSI Performance

Figure 7.16 shows the inverter–grid current and the grid voltage for a power factor around 0.998. We can notice that the inverter current is shifted by 180^{o} from the grid voltage. This result confirms that PMWGS succeeded to inject the generated wind power into the utility grid. The THD of the grid voltage and grid-injected current of the CSI are about 1.09%, 0.64%, respectively. The 31^{st} harmonic is the most relevant component, as shown in Fig. 7.17. The power factor (PF) is equal to 0.988 with respect to inverter voltage; it means that the inverter is transferring only active power to the grid. Figure 7.18 shows the measured efficiencies and PF. This demonstrates the expected improvement when compared with similar works.

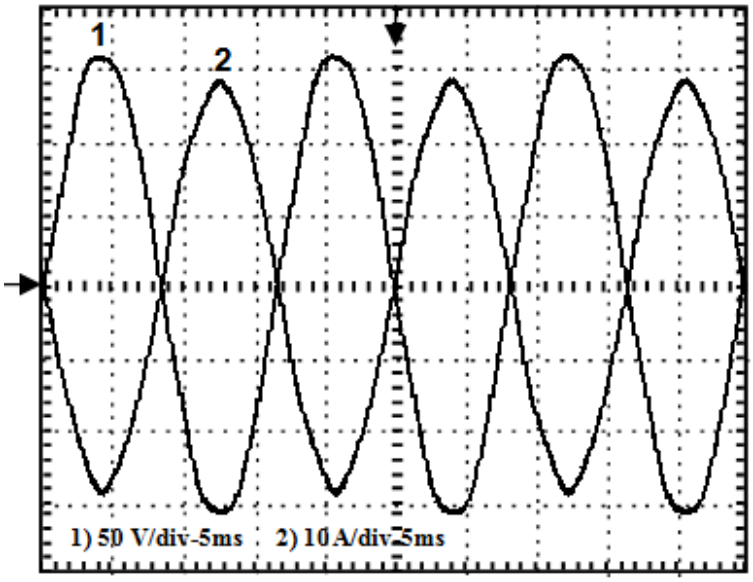

Fig. 7.16 Grid voltage for phase "a" (50 V/div, 5ms) and grid current (10 A/div, 5ms)

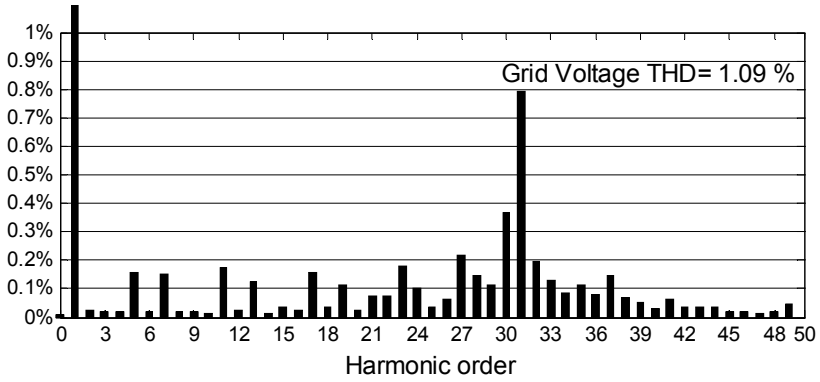

(a)

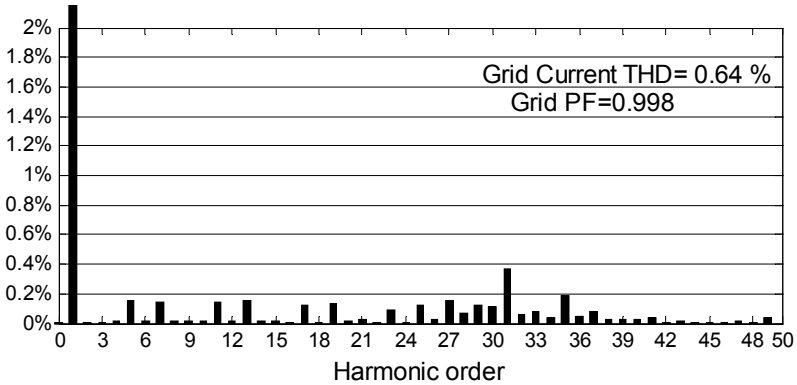

(b)

Fig. 7.17 Harmonic spectrum of: (a) The grid voltage and (b) Grid-injected current

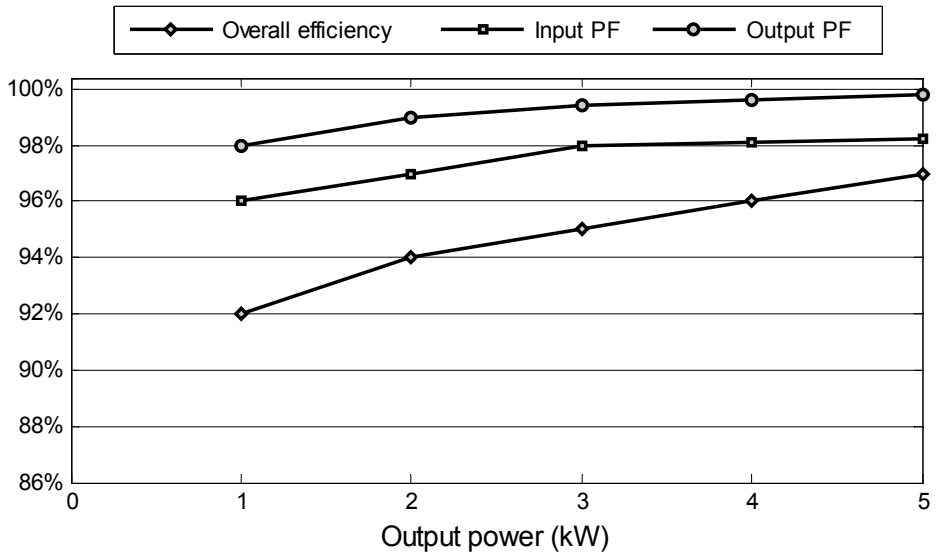

Fig. 7.18 Efficiency, input power factor, and output power factor versus output power

7.5 Application Considerations

Practically, during initial voltage controller adjustment with the DC-bus capacitor uncharged, the initial DC-level will be very high, if it is above the capacitor voltage rating, it can destroy it. Avoiding that can be done by initially charging the DC-bus capacitor to 60% of the reference DC-voltage. The free-wheeling diodes of the IGBT module is working as a diode bridge rectifier during an initial charging. Once the capacitor is charged, the converter switching control signals should be connected, allowing the total power to flow to the IGBT switches. A protection relay controlled from the DSP board should be mounted between the generator side and the converter side in order to avoid working above the voltage limit. The current controller discussed in section 7.3 should be tuned first while keeping the output DC-voltage level uncontrolled. That can be done by commanding the current controller to work with a constant value. Once the actual current tracks the command current, the DC-voltage controller can join

the control loop. Also, the impact of the large current harmonic contents should be considered for grid-connection operation.

7.6 Conclusion

This chapter discussed an effective high frequency semi-controlled boost rectifier topology feasible for grid-connected low speed direct-driven PMWGSs. This topology achieved high efficiency (average above 95%). This is due to the reduced number of components. Moreover, the passive elements (inductors and capacitors) are reduced proportionally to the frequency improving the overall efficiency for the system. The UPF (0.998) operation was verified for better economic utilization of the generator operation. The DC-bus voltage control technique was investigated for parallel integrated PMWGSs based on a Master-slave strategy. The hysteresis algorithm was used for reducing the generator harmonics.

The system was tested under different severe conditions including: full load parallel operation, hard wind speed variation, and parameter uncertainties. Load current sharing among the parallel converters was investigated with a small transient voltage dips (<5%). A fast control dynamic response was achieved (0.1 second) during wind speed variation. The use of parallel converters provides high reliability and power capability.

The inverter stage is based on a three-phase CSI which has higher power capability compared to voltage source inverter. High frequency operation was utilized to achieve low voltage and current THD (1.09% and 0.64%) for grid-connection, respectively. The test results obtained from a prototype have demonstrated the system effectiveness for a wide power range (0-5 kW).

Chapter 8 Novel Modularized High Frequency Multi-Input Bridgeless Boost Converter Topology

8.1 Introduction

In hybrid energy systems and its application such as PHEVs, multi-input boost converters became widely used to enhance the stability and reliability. The high power boost converter is an essential interface between the hybrid energy sources and the DC-bus that serves as the inverter input. However, conventional boost converters have difficulty of low efficiency and the implementation size problem as well as the cost. Therefore, the DC system with multiple input converters may play an important role in the future power system. The topology designs of boost converters were documented in many references examples of which are references [111-114]. In addition, the design of high power boost converters and their controller plays an important role to control power regulation particularly for a common DC-bus. Several DC/DC converters topologies based on their components count, advantages and disadvantages are discussed and compared in [115-117].

In this chapter, our scope of work focuses on the multiple input boost converter (MIBC), considering three hybrid AC/DC sources:

- AC- source; such as wind generator or AC-grid,
- DC-source; such as PV or FC,
- DC-source as energy storage; such as battery bank.

Figure 1 shows an application example for the MIBC topology feasibility with PHEVs [118, 119]. In MIBC, the AC-grid is connected to the DC-Bus via boost rectifier,

the FC is connected to the DC-Bus via boost converter and the energy storage system is connected to the DC-Bus through a bidirectional DC/DC converter. Another example is the MIBC topology instead of the individual converters inside the HF hybrid DC-link integration infrastructure systems which shown in Fig. 8.2.

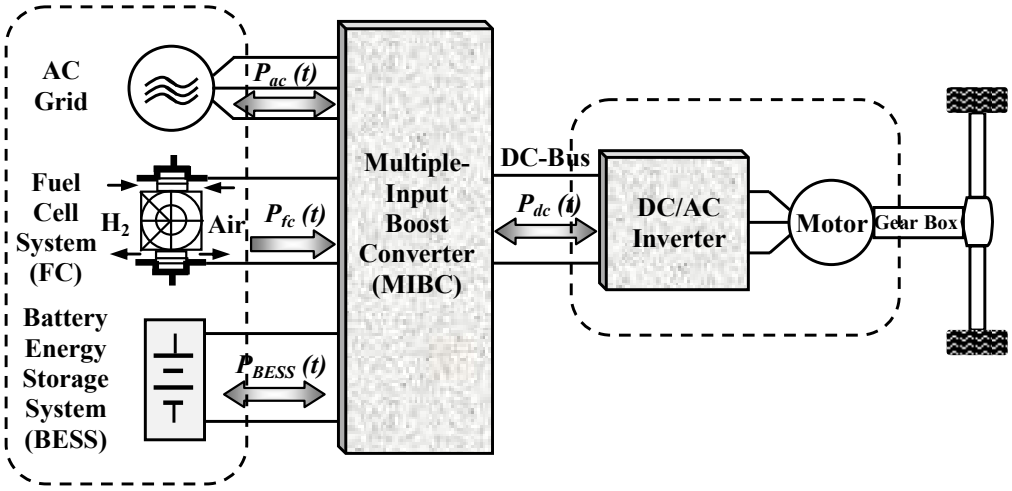

Fig. 8.1 The block diagram of the PHEV drive train including MIBC

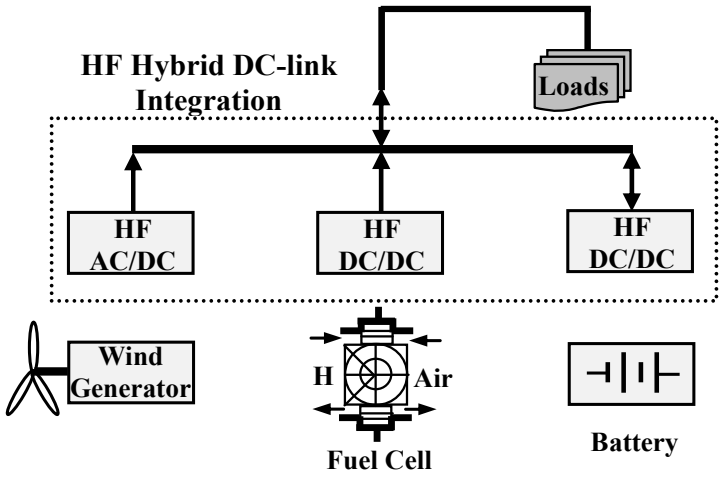

Fig. 8.2 The HF DC link integration hybrid system Configuration

In addition, the MIBC performance directly influences on the characteristics of the renewable sources or the energy storage system (e.g. Batteries) [120]. For example, the ripple and harmonic content of the current is one of the various phenomena influencing

fuel cell lifetime as well as batteries lifetime [117]. It is clear that, the main objective is to minimize such inductor size, capacitor, current /voltage ripple and harmonic content. The problems due to harmonics in conventional converters have resulted in the establishment of standards such as IEC 61000-3-2 and IEEE Std 519™-1992 [41, 121]. Thus, a PHEV charger with a Power Factor Correction (PFC) based AC-DC converter is desirable [122].

Furthermore, Bridge and bridgeless boost converter topologies have been well discussed in many literatures [25]-[35]. In [123], the bridge boost converter (BBC) topology was introduced as a simple and popular topology for PFC applications. It uses a dedicated diode bridge to rectify the AC input voltage to DC, which is then followed by the boost section, as shown in Fig. 8.3.a. In this topology, the output capacitor ripple current is very high [124]. Furthermore, as the power level increases, the diode bridge losses significantly degrade the efficiency, so dealing with the heat dissipation in a limited area becomes problematic. Due to these constraints, this topology is good for a low to medium power range up to approximately 1kW [125]. For power levels >1kW, typically, designers parallel semiconductors in order to deliver greater output power. The inductor volume also becomes a problematic design issue at high power.

On the other hand, the bridgeless power factor correction boost converter (BPFCC) topology avoids the need for the rectifier input bridge [126], yet maintains the classic boost topology, as shown in Fig. 8.3.b. It is an attractive solution for applications > 1kW, where power density and efficiency are important [127]. The bridgeless boost converter solves the problem of heat management in the input rectifier diode bridge, but it introduces increased EMI [128]. Another disadvantage of this topology is the floating input line with respect to the PFC stage ground, which makes it impossible to sense the

input voltage without a low frequency transformer or an optical coupler. Also in order to sense the input current, complex circuitry is needed to sense the current in the IGBT and diode paths separately, since the current path does not share the same ground during each half-line cycle.

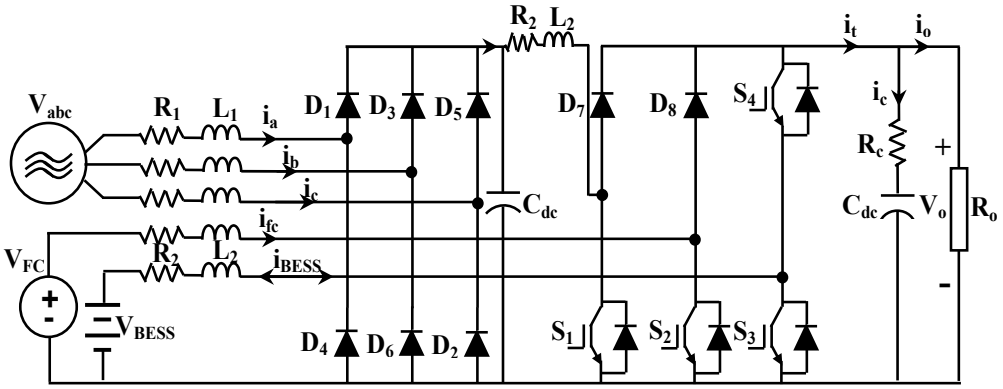

(a)

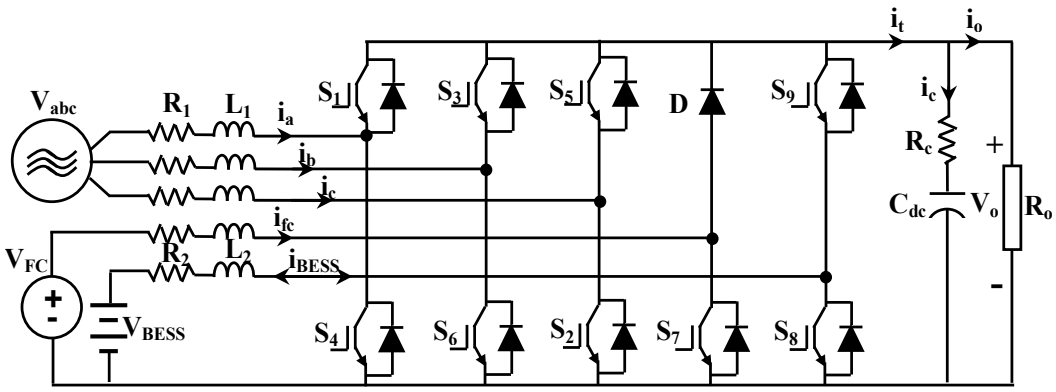

(b)

Fig. 8.3 Conventional MIBC topologies: (a) BBC and (b) BPFCC

In this chapter, a novel modularized multi-input bridgeless boost converter (MIBBC) is studied for possibility of reducing the size and weight of the passive components such as; inductor, capacitor and input/output electromagnetic interference (EMI) filter. Meanwhile, the input/output current/voltage ripple can still be minimized with high efficiency and reliability. Furthermore, the developed topology is compared with other

conventional MIBC converter topologies (e.g. BBC and BPFCC) in order to investigate its dynamic response. All topologies (BBC, BPFCC, and MIBBC) were built and tested in our laboratory. The MIBBC topology structure, the principle of operation, and control scheme are presented. The general circuit model and loss model are derived with the aim to design the closed-loop control and to calculate the efficiency, respectively. These models consider the internal resistance of the inductor and capacitor for these converters. A hybrid control strategy programmed on TMS320F28335 DSP was developed to implement the control strategy for the converters.

8.2 Developed MIBBC Topology

The MIBBC structure, which is developed here, uses six insulated-gate bipolar transistors (S1-S6 IGBTs) and four diodes (D1-D4), is shown in Fig. 8.4. (S1-S3) and (D1-D3) are used for the three-phase AC-input. (S4, D4) are used as for the fuel cell input. (S5, S6) are used for the battery input. The easy way to reduce the size of the inductor, capacitor and input /output EMI filter by means of increasing the frequency of inductor current ripple and the output voltage ripple. The developed converter is compared with two other converter topologies (BBC and BPFCC). The main advantages of the developed topology are:

- Higher efficiency; due to less number of switches,
- Smaller size; since passive elements are reduced proportionally due to high frequency operation,
- Unity power factor (UPF) operation can be achieved.

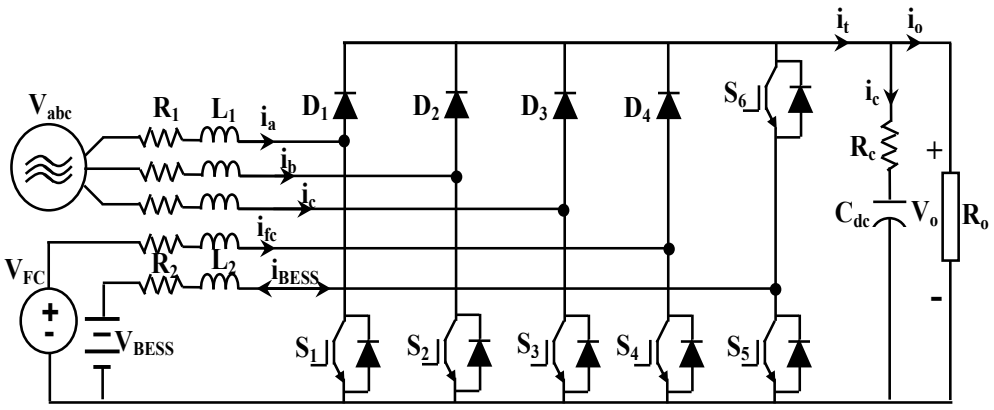

Fig. 8.4 The structure of the developed MIBBC topology

8.2.1 MIBBC Detailed Description

Figure 8.5 shows a detailed description for the developed MIBBC topology. It consists of 3-input ports and 1-output port. The first input port could be supplied from a three-phase AC-input source; such as wind generator or AC-grid…..etc. A three-phase semi-controlled rectifier topology was used for this input in order to regulate the ac-input and get a controlled DC-output voltage.

The second input port was designed to be supplied from any DC-source; for example PVs, FCs, DC-generators …etc. A step-up DC–DC converter was installed for boosting the input voltage to a higher level of common DC-voltage. The third input port was added for battery energy-storage system (BESS). According to operation mode, BESS mitigates power fluctuations of the DC and AC inputs, or shifts the power generation to regulate the power transferred to the load. The BESS is divided into battery storage and a buck–booster that is a bidirectional DC–DC converter for charging or discharging the battery storage. The battery converter links the battery-terminal bus and the common DC bus, whose voltage levels are mutually different, and controls the current flow between the two buses. In some previous applications [129], battery storage was directly linked to

common DC-bus without using a converter. This configuration requires more battery stacks than using a DC–DC converter, and so may lower the system economy. Also, the lifetime of battery may be degraded without appropriate control of battery current and voltage.

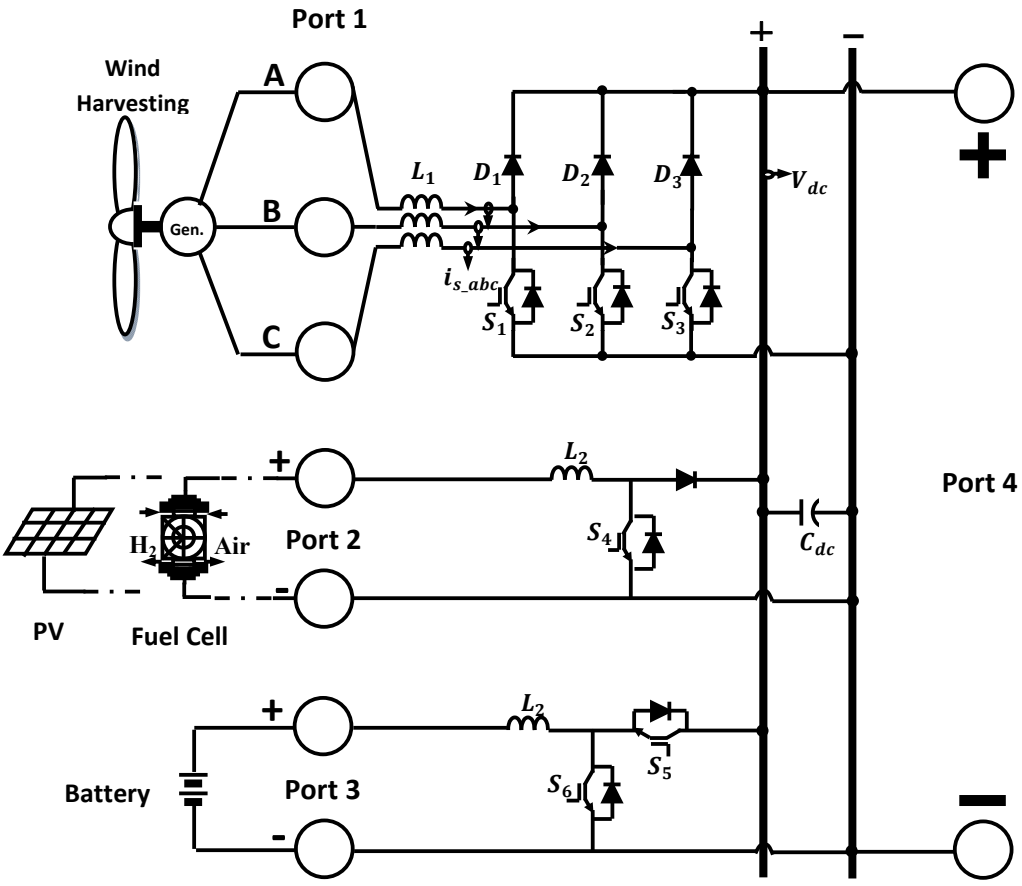

Fig. 8.5 The detailed power circuit configuration for the developed MIBBC topology

8.2.2 MIBBC Power Transfer Operation

Six-IGBTs are only employed for controlling the amount of the power transferred from the hybrid AC/DC inputs to DC-bus. Assuming that the battery is running under discharging mode of operation, then each input is connected to DC-bus via a boost converter. Figures 8.6-8 shows the different modes of operation for the MIBBC. This

operation was previously discussed in section 7.2.1; since same analysis can be used here under the battery discharging operation.

Assuming that the battery is running under charging mode of operation, the same operation is repeated for the developed topology; since S4 is running as a boost DC-DC fuel cell converter and S6 is running as a buck DC-DC battery converter. The corresponding sectors are given in Figs. 8.9-11.

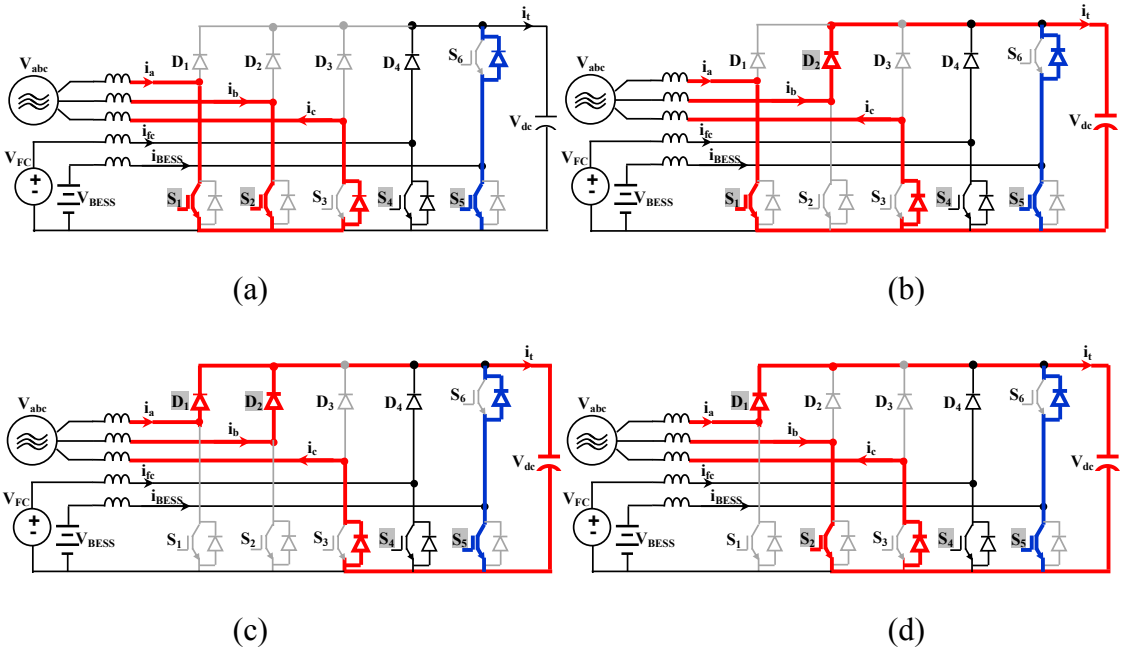

Fig. 8.6 Sector I topological states (discharging mode): (a) S1, S2 are ON, (b) S1, D2 are ON, (c) D1, D2 are ON and (d) D1, S2 are ON

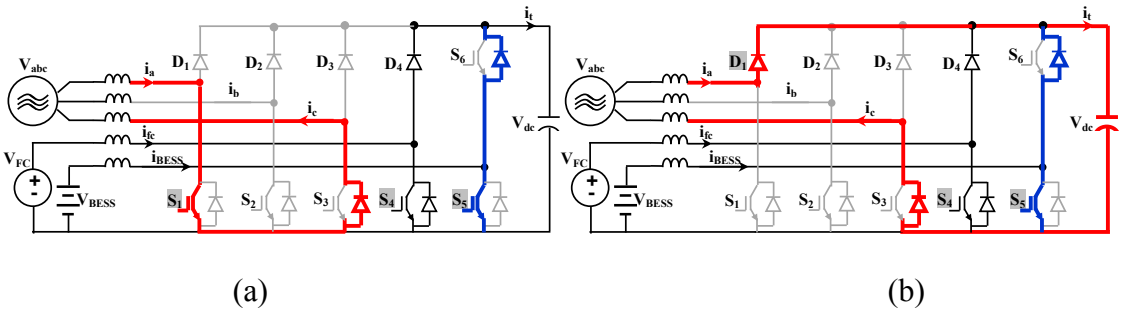

Fig. 8.7 Sector II topological states (discharging mode): (a) S1 is ON, (S2, D2) are OFF and (b) D1 is ON, (S2, D2) are OFF

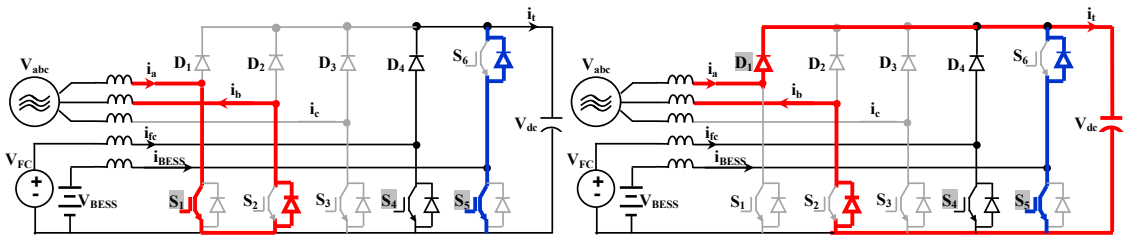

Fig. 8.8 Sector III topological states (discharging mode): (a) S1 is ON, (S3, D3) are OFF and (b) D1 is ON, (S3, D3) are OFF

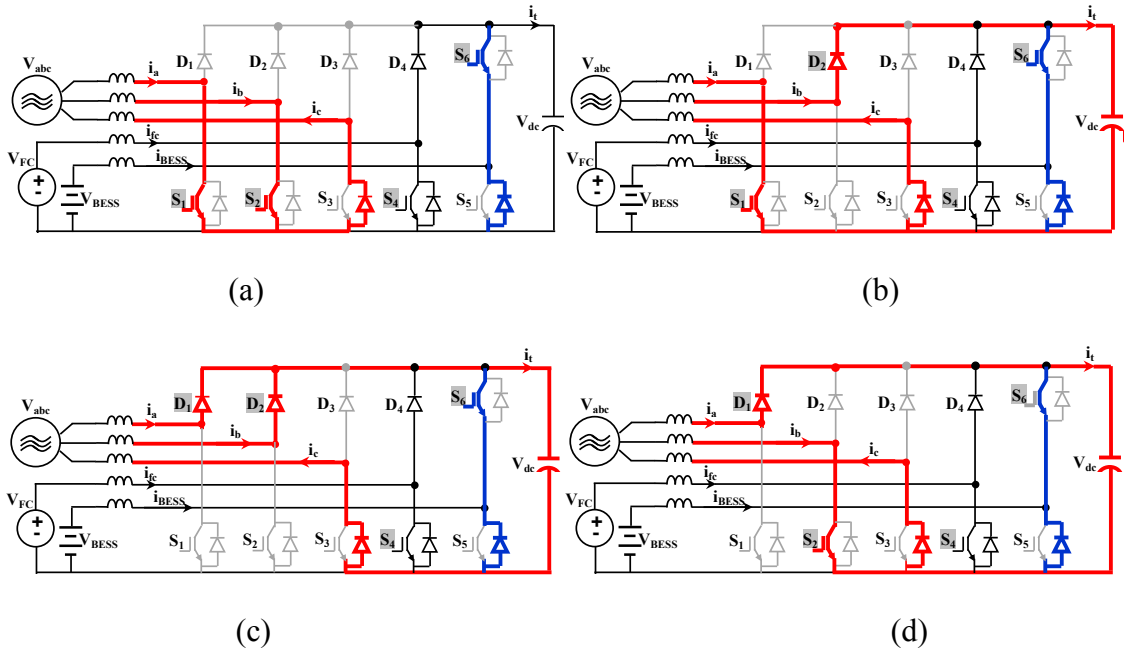

Fig. 8.9 Sector I topological states (charging mode): (a) S1, S2 are ON, (b) S1, D2 are ON, (c) D1, D2 are ON and (d) D1, S2 are ON

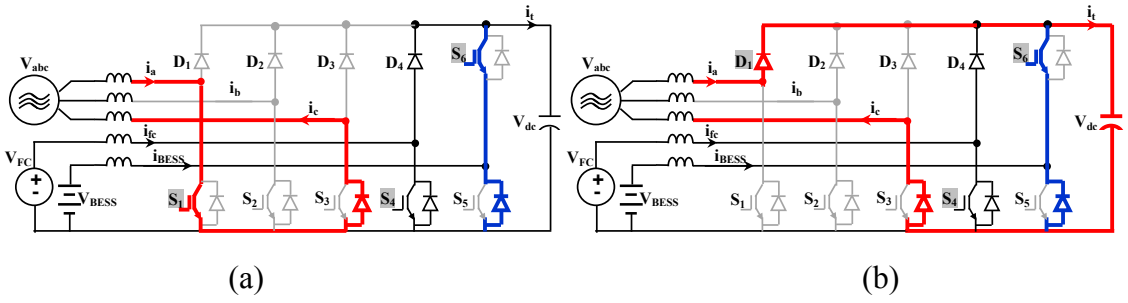

Fig. 8.10 Sector II topological states (charging mode): (a) S1 is ON, (S2, D2) are OFF and (b) D1 is ON, (S2, D2) are OFF

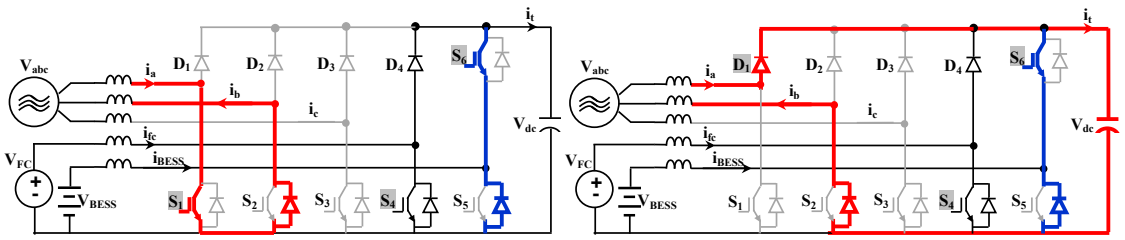

Fig. 8.11 Sector III topological states (charging mode): (a) S1 is ON, (S3, D3) are OFF and (b) D1 is ON, (S3, D3) are OFF

8.2.3 MIBBC Dynamic Model

To design the control system of a converter, it is necessary to model the converter dynamic behavior. Since the dynamic mathematical model semi-controlled rectifier topology was previously introduced in section 7.2.2. So, it is not necessary to repeat the modeling equations of this stage inside the developed MIBBC topology. For the DC-DC stage, bidirectional (regenerative) power flow can be obtained with a current-bidirectional two quadrant realization of the switch network. An example is illustrated in Fig. 8.12, in which a DC-DC converter interfaces batteries to the main DC-power bus of a spacecraft.

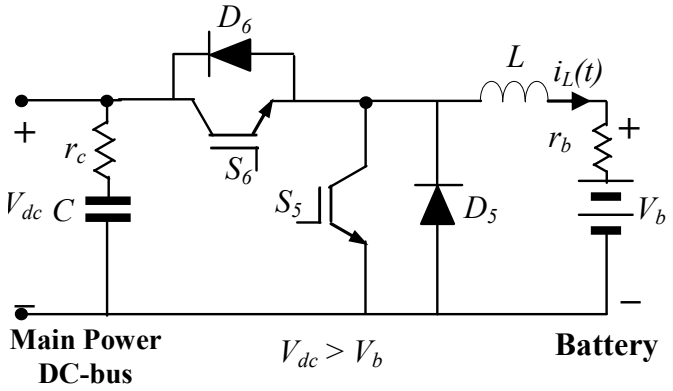

Fig. 8.12 Bidirectional DC-DC PWM converters power circuit

The anti-parallel-connected switches and diodes form current-bidirectional switches. Switch S5 is driven with the complement of the S6 drive signal, such that S5 is off when

S6 is on, and vice-versa. To charge the battery, the inductor current $i_L(t)$ is positive and flows through transistor S6 and diode D5. To discharge the battery, the current $i_L(t)$ reverses polarity, and flows through transistor S5 and diode D6. In both cases, the battery voltage is less than the main DC-bus voltage. The magnitude and polarity of the battery current can be controlled via adjustment of the duty cycle d.

In particular, it is of interest to determine how variations in the power input voltage, the load current i_L, and the duty cycle d affect the output voltage V_{dc}. Unfortunately, understanding of converter dynamic behavior is hampered by the nonlinear time-varying nature of the switching and pulse-width modulation (PWM) process. These difficulties can be overcome through the use of waveform averaging and small signal modeling techniques [130]. A well-known converter modeling technique known as state-space averaging is briefly described here. The model equations are derived below. When state switch S6 is on and S5 is switched off (buck converter), based on Kirchhoff's laws:

$$\begin{bmatrix} pV_c \\ pI_L \end{bmatrix} = \begin{bmatrix} -1/Cr_c & 0 \\ 0 & -r_b/L \end{bmatrix} \begin{bmatrix} V_c \\ I_L \end{bmatrix} + \begin{bmatrix} 1/Cr_c & 0 \\ 1/Lr_c & 1/L \end{bmatrix} \begin{bmatrix} V_{dc} \\ V_b \end{bmatrix} \tag{8-1}$$

The state space equation in the matrix form when S6 is off and S5 is on (boost converter) is given by:

$$\begin{bmatrix} pV_c \\ pI_L \end{bmatrix} = \begin{bmatrix} -1/Cr_c & 0 \\ 0 & -r_b/L \end{bmatrix} \begin{bmatrix} V_c \\ I_L \end{bmatrix} + \begin{bmatrix} 1/Cr_c & 0 \\ 0 & 1/L \end{bmatrix} \begin{bmatrix} V_{dc} \\ V_b \end{bmatrix} \tag{8-2}$$

Where p is the derivative operator, i.e. $p=d/dt$. V_b and V_c are the battery and capacitor voltages, respectively. r_b and r_c are the battery and capacitor internal resistances, respectively. The averaged state space equation can be written as:

$$\begin{aligned} \dot{X} &= Ax + bV_{dc} + eV_b \\ A &= A_1 d + A_2(1-d) \\ B &= b_1 d + b_2(1-d) \\ E &= e_1 d + e_2(1-d) \end{aligned} \tag{8-3}$$

The state space equation for the output can be written as:

$$\begin{aligned} Y &= Cx + Du \\ C &= C_1 d + C_2(1-d) \\ D &= D_1 d + D_2(1-d) \end{aligned} \tag{8-4}$$

Where d is the duty cycle and the matrices are given by:

$$\begin{aligned} A_1 &= \begin{bmatrix} -d/Cr_c & 0 \\ 0 & -dr_b/L \end{bmatrix}, \\ A_2 &= \begin{bmatrix} -(1-d)/Cr_c & 0 \\ 0 & -(1-d)r_b/L \end{bmatrix}, \\ b_1 &= \begin{bmatrix} d/Cr_c \\ d/Lr_c \end{bmatrix}, \quad b_2 = \begin{bmatrix} (1-d)/Cr_c \\ 0 \end{bmatrix}, \\ e_1 &= \begin{bmatrix} 0 \\ d/L \end{bmatrix}, \quad e_2 = \begin{bmatrix} 0 \\ (1-d)/L \end{bmatrix}, \\ C_1 &= \begin{bmatrix} 0 & 1 \\ 1 & 0 \end{bmatrix}, \quad C_2 = \begin{bmatrix} 0 & 1 \\ 1 & 0 \end{bmatrix}, \\ D_1 &= \begin{bmatrix} 0 & 0 \end{bmatrix}^T, \quad D_2 = \begin{bmatrix} 0 & 0 \end{bmatrix}^T \end{aligned} \tag{8-5}$$

The input to output transfer function can be written as:

$$\frac{\tilde{y}(s)}{\tilde{u}(s)} = C_{av}[SI - A_{av}]^{-1} B_{av} + D_{av} \tag{8-6}$$

Where $\tilde{y}(s)$ is the output and $\tilde{u}(s)$ is the input in Laplace form. Also the averaged matrices are given by:

$$C_{av}=\begin{bmatrix}0 & 1\\ 1 & 0\end{bmatrix},\qquad A_{av}=\begin{bmatrix}-1/Cr_c & 0\\ 0 & -r_b/L\end{bmatrix},$$
$$B_{av}=\begin{bmatrix}1/Cr_c & 0\\ d/Lr_c & 1/L\end{bmatrix},\qquad D_{av}=\begin{bmatrix}0\\ 0\end{bmatrix} \tag{8-7}$$

8.3 MIBBC Hybrid Control Strategy

A hybrid control strategy is used here in order to optimize the utilization of each input independently. The control strategy should be designed in order to satisfy the current and voltage requirements. In this section, a simple feedback hybrid PI-hysteresis controller is used to maintain a constant bus voltage of 400 V in converter output, irrespective of the variations in load and input voltage. Figure 8.13 shows the schematic diagram for the overall developed MIBBC system.

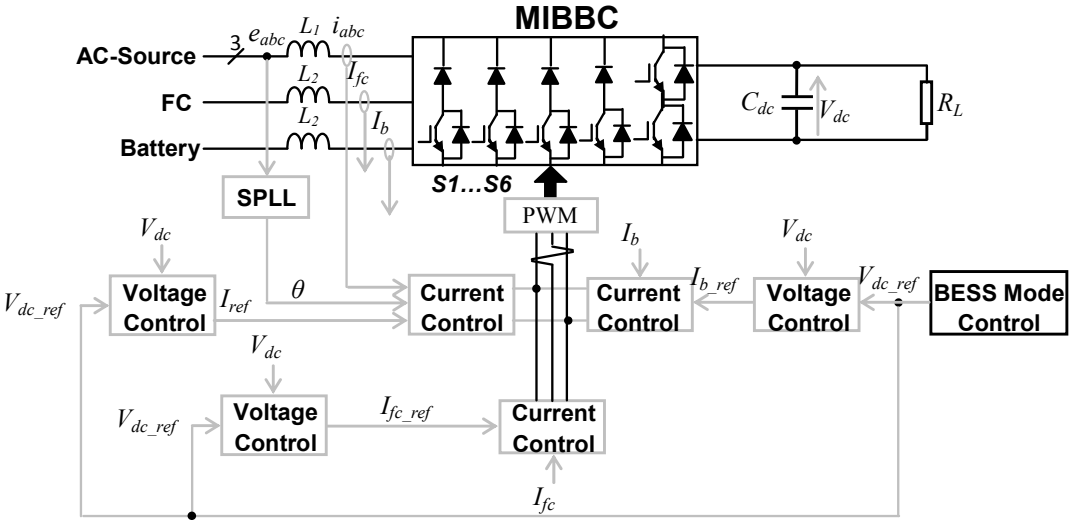

Fig. 8.13 The configuration of the overall MIBBC system and its local control schematic

The diagram is involving the control strategy for each conversion stage as follows:

8.3.1 AC-Input Source Control

The hysteresis control scheme is used for the AC-input stage to achieve low harmonic distortion of the AC-input current; since it operates at variable switching frequency due to duty cycle discontinuity operation. This strategy was previously well discussed in section 7.2.3.

8.3.2 Fuel Cell Control

The cascaded digital control strategy is more efficient than other techniques to achieve a high performance (stability, accuracy, and the response speed) for the PWM boost converter. Figure 8.14 illustrates the block diagram of the cascaded control structure in the s-domain. The series voltage controller ($H_v(s)$) is designed to maintain the DC-output voltage constant. The feed-forward inner current controller ($H_i(s)$) is used to achieve faster transient response. This controller requires the sampling of two variables, namely: DC-output voltage V_{dc}, FC-inductor current I_{fc}, which are obtain through conventional Hall Effect Transducers. A limiter on the inductor current reference is crucial in this controller. This is because during large signal transient like startup period, there is a big difference between the voltage reference and the DC-output voltage. As a result, the output of the voltage compensator could give a command to the current loop higher than the maximum allowable inductor current, resulting in the inductor saturation and damaging the device. There are in general two basic approaches in designing the digital controller for DC/DC PWM converters. The first approach, known as the Digital Redesign Approach (RDA), is to design the controller in the s-domain using conventional methods and the resulting controller is transformed into the z-domain using appropriate z-transformations. However, the RDA suffers from sampling and quantization errors,

computational time delay and discretization effects. The second approach, known as Direct Digital Control (DDC), is to design the controller directly in the z-domain itself. Since the DDC starts with the system discrete transfer functions, it is possible to include the effect of sampling, Zero-Order-Hold (ZOH) and computational time delay effects in order to guarantee the stability of the controller design [131]. Consequently, the final digital control more realistic and meet the design specifications without any tuning. In this section, a cascaded digital controller is designed using DDC approach.

In order to design the cascaded digital controller, the continuous time transfer functions ($G_v(s)$ and $G_i(s)$) of the boost converter are first discretized using one of the discretization methods, such as ZOH, matched pole-zero, backward difference and bilinear transformation methods. Therefore, the appropriate transformation method to be used here is the ZOH method. Once the discrete transfer functions of the system are available, the digital controller ($H(z)$) is directly designed in the z-domain using methods similar to the continuous-time frequency response methods. Figure 8.15 illustrates the entire cascaded system containing the outer voltage loop controller ($H_v(z)$), inner current loop controller ($H_i(z)$) , the ZOH and computational delay, e^{-sTd}, and the control to output transfer functions ($G_v(s)$ and $G_i(s)$) of the converter. The discrete-time transfer functions ($G_v(z)$ and $G_i(z)$) of the converter, that include the ZOH and e^{-sTd}, are given as follows:

$$G_v(z) = Z\left\{\frac{1-e^{-Ts}}{s}\cdot e^{-sTd}\cdot G_v(s)\right\} \tag{8-8}$$

$$G_i(z) = Z\left\{\frac{1-e^{-Ts}}{s}\cdot e^{-sTd}\cdot G_i(s)\right\} \tag{8-9}$$

The loop gains for inner current loop and outer voltage loop can be expressed as:

$$T_i(z) = H_i(z) \cdot G_i(z) \tag{8-10}$$

$$T_v(z) = \frac{H_v(z) \cdot H_i(z) \cdot G_i(z)}{1 + T_i(z)} \tag{8-11}$$

The digital PI-controllers are designed based on the required phase margin (ϕ_m) and critical frequency (ω_{cz}) by using the bode diagram in the discrete time domain, the transfer function of the digital PI-controller in z-domain is given by:

$$H(z) = k_p + \frac{k_i T_s z}{z - 1} \tag{8-12}$$

$$\text{Where } k_p = \frac{\cos\theta}{|G_o(z)|}, \quad k_i = \frac{-\omega_{cz} \sin\theta}{|G_o(z)|}, \quad \theta = \phi_m - \angle G_o(z) \tag{8-13}$$

The $G_o(z)$ is the discrete-time transfer function of the open loop system (e.g. G_v (z), or G_i (z))**.** For example, Figure 8.16 demonstrates the bode plots for the current loop gain and voltage loop gain, respectively, which are designed for MIBBC topology with converter parameters listed in Table 8.1. The plots demonstrate that the current loop gain has a crossover frequency as high as 2 kHz, with a phase margin of 40.4°. To avoid interaction between the sub-systems and to accommodate the slow fuel cell response, low control bandwidth is used for voltage loop outer voltage loop has a crossover frequency of 50 Hz and a phase margin of 73.4°.

Table 8.1 DC-DC converters parameters

Topology	***L (μH)***	***R_L (mΩ)***	***C (μF)***	***R_C (mΩ)***
BBC	600	25	2000	0.164
BPFCC	330	12	1500	0.212
MIBBC	300	10	1000	0.326

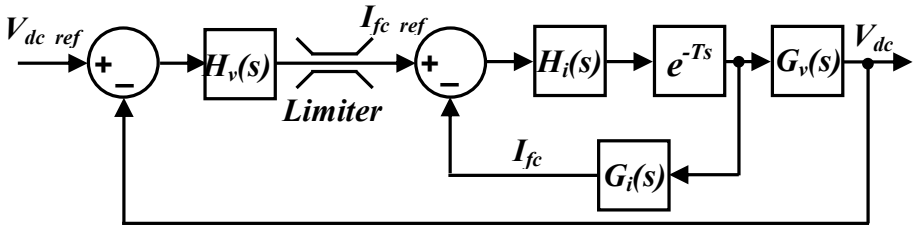

Fig. 8.14 Cascaded control structure

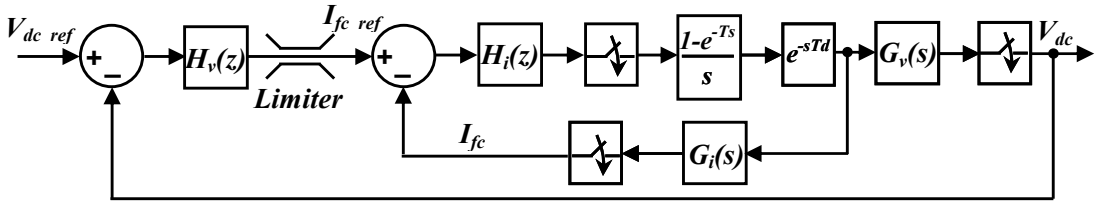

Fig. 8.15 Cascaded digital control structure using DDC approach

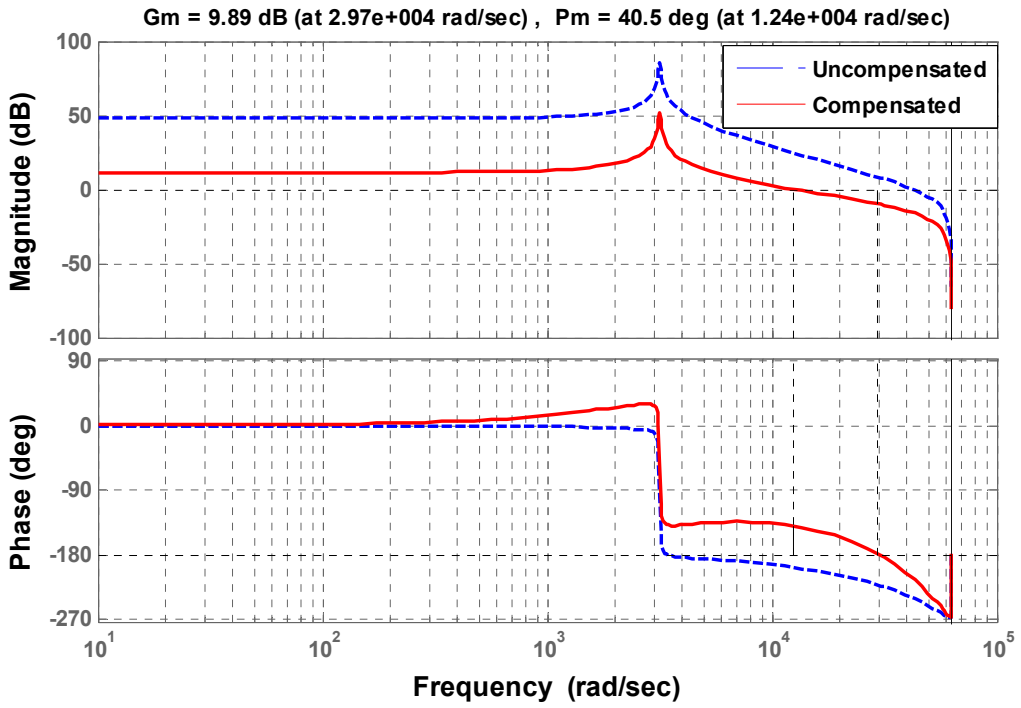

(a)

Fig. 8.16 The frequency response of cascaded digital control: (a) Current gain and (b) Voltage gain

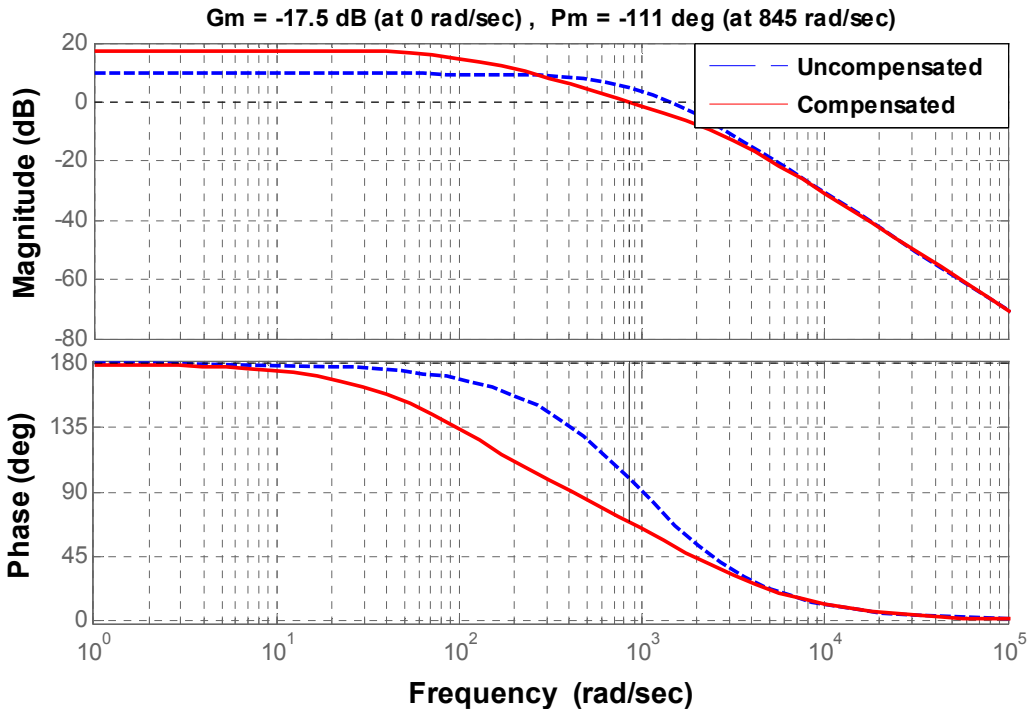

(b)

Fig. 8.16 The frequency response of cascaded digital control: (a) Current gain and (b) Voltage gain (continued)

8.3.3 Battery Energy Storage Control

The primary goal of the battery converter is to stabilize the common DC-bus voltage which must be regulated to stay within a stable region regardless of the battery-current variation. To do this, a modified hysteresis-control strategy is applied. The concept of this strategy is to regulate the common DC-voltage within a specific band, for example, a hysteresis band. Therefore, the battery charger/discharger is controlled in such a way that the DC-bus voltage should not violate the specified upper and lower limits, V_{dc_up} and V_{dc_low}, as shown in Fig. 8.16.a. A decision criterion for charging/discharging becomes the level of the common DC-bus voltage and the battery buck–booster operates according to the scheme as below:

If $V_{dc} > V_{dc\_up}$ then charging: $V_{dc\_ref} = V_{dc\_up}$

If $V_{dc} < V_{dc\_low}$ then discharging: $V_{dc\_ref} = V_{dc\_low}$ (8-14)

If $V_{dc\_low} \le V_{dc} \le V_{dc\_up}$ then control (rest).

When the common DC-voltage V_{dc} becomes larger than the upper limit, charging mode begins with the voltage command V_{dc_ref} equal to the upper limit and continues until the DC-voltage reaches the limit. If V_{dc} goes below the lower limit, then the voltage target is bound at the lower limit and the converter starts operating in boost mode.

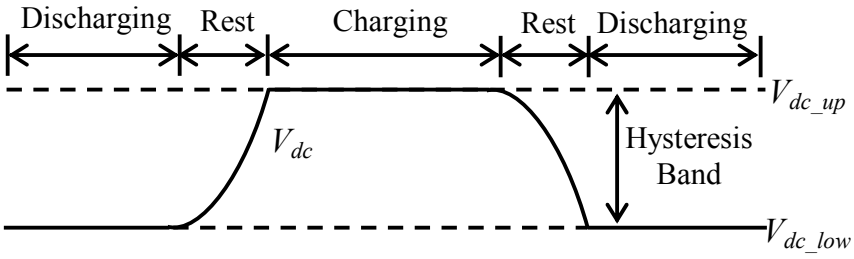

(a)

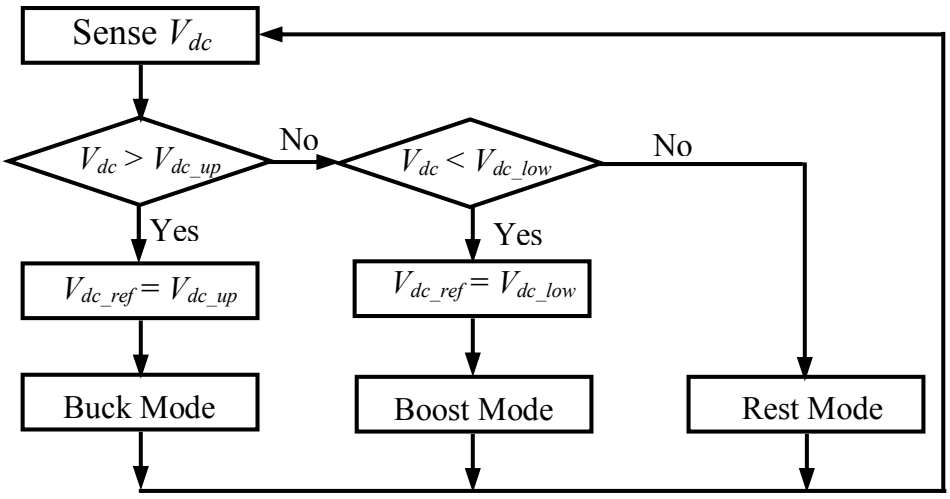

(b)

Fig. 8.17 Battery-mode control: (a) Modified hysteresis control strategy and (b) flow chart

Accordingly, the battery-mode control block in Fig. 8.13 can be built as shown in Fig. 8.17.b. There is another reason for such hysteresis control other than voltage regulation of the DC-bus. It is intended to protect the battery storage against excessive charging frequency and current variation. Not by bounding DC-bus voltage at a constant value but by allowing a hysteresis band; the battery can take a rest during the rest interval in Fig. 18. a. Energy that can be extracted or stored across the hysteresis band in a DC-bus capacitor ΔE_c is described as follows:

$$\Delta E_c = \frac{1}{2} C_{dc} (V_{dc\_up}^2 - V_{dc\_low}^2) \tag{8-15}$$

8.4 MIBBC Loss Estimation

A main part of total losses is the switching and conduction losses which depend on switching times and switching frequency. When a switch is turned on or off, energy is lost during the switching transients as the operating point of the switch is changed from on (off) to off (on) state through an active state. This type of energy loss is called switching loss of the power switch and it depends on voltage across the switch, current through the switch and the switching time. When a switch is off, normally a leakage current through the switch is very small and we ignore the energy loss associated with the off-state. But when the switch is on, the energy loss depends on current through the switch and a forward voltage of the switch. This type of energy loss is called conduction loss of the switch.

Figure 8.18 shows the waveforms for switching times. The average power loss in a switch over one switching cycle is given by the following equation which consists of the conduction and switching losses:

$$\overline{P_s} = \frac{1}{T_{sw}} \int_0^{T_{sw}} i_{sw} \cdot v_{sw} dt = \overline{P}_{cond} + \overline{P}_{sw} \tag{8-16}$$

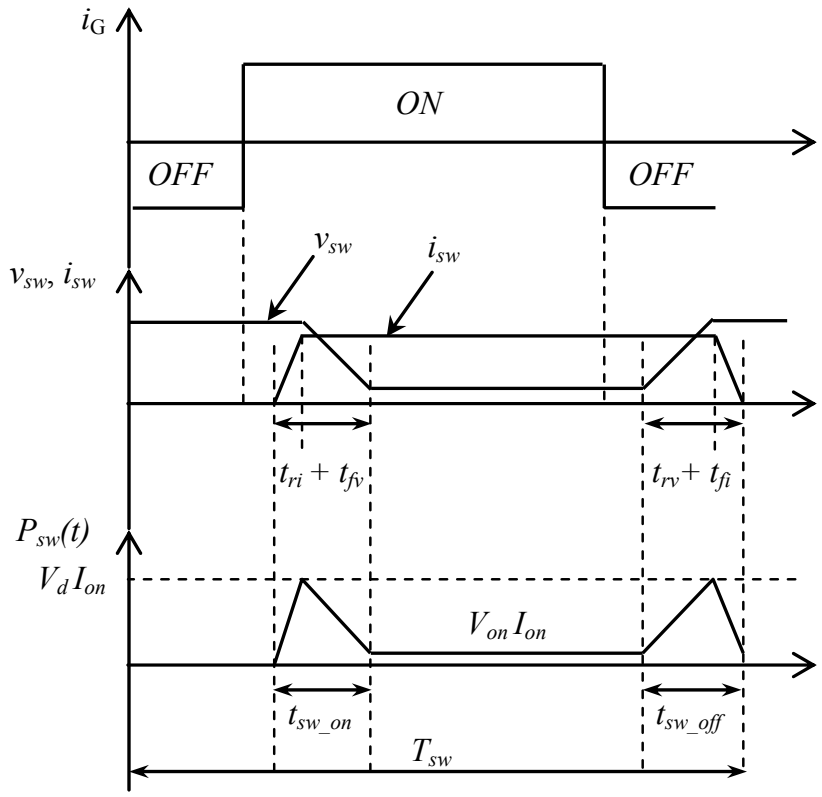

Fig. 8.18 The voltage, current, and power waveforms for power switches

Assuming that the on and off switching times are small compared to switching cycle, T_{sw}, and the leakage current is negligible, $I_{off} = 0$. Thus the conduction loss is given by:

$$\overline{P}_{cond} = V_{on} \cdot I_{on} \cdot D\,, \quad D = \frac{t_{on}}{T_{sw}} \tag{8-17}$$

Where t_{on} is the time when the switch is in on-state, V_{on} is a voltage drop across the switch, I_{on} is a current through the switch assuming it is constant in magnitude and D is a duty cycle. The switching loss should be calculated based on instantaneous current and voltage waveforms as follows:

$$\overline{P}_{sw} = f_{sw}\left(\int_{0}^{t_{sw\_on}} v_{sw} \cdot i_{sw} dt + \int_{0}^{t_{sw\_off}} v_{sw} \cdot i_{sw} dt \right) \tag{8-18}$$

Where t_{sw_on} and t_{sw_off} are turn- on and turn-off switching times. Also, the total average power losses can be calculated as follows:

$$\overline{P}_{av\_loss} = f_{sw}\left(\frac{1}{2} V_d \cdot I_{on} \cdot t_{sw\_on} + \frac{1}{2} V_d \cdot I_{on} \cdot t_{sw\_off} + V_d \cdot I_{on} \cdot D \right) \tag{8-19}$$

In a power electronic system, there are other circuits such as gate drives, controllers, sensors and passive filters which consume power. The total losses in a power electronic system are the sum of all losses and the efficiency of a system (η) can be calculated based on input power (P_{in}) and total losses (P_{loss}) as given below:

$$\eta = \frac{\overline{P}_{out}}{\overline{P}_{in}} = \frac{\overline{P}_{in} - \overline{P}_{loss}}{\overline{P}_{in}} = 1 - \frac{\overline{P}_{loss}}{\overline{P}_{in}} \tag{8-20}$$

In order to estimate the efficiency of the developed topology, a loss analysis was performed, considering the developed equations, the semiconductors, and parameters given in Table 8.2 and the respective datasheets. Figure 8.19 compares the estimated efficiency of the developed MIBBC topology (η_1) with the BPFCC topology (η_2). In the fully controlled structure, the currents can be modulated in both half cycles which leads to less input current harmonic distortion when compared to the developed topology. However, it has larger switching losses and it requires the use of bootstrap-integrated circuits. Moreover, the occurrence of eventual short-circuits through the leg is possible. It can be seen that MIBBC has improved efficiency over the entire power range.

Table 8.2 Semiconductor devices and its parameters

Parameter	Specification	Parameter	Specification
S_1-S_4, D_1-D_4	SKM 200GAL125D	S_5, S_6	SKM 200GB125D
V_{switch}	1200V	V_{switch}	1200V
I_{switch}	200A	I_{switch}	200A

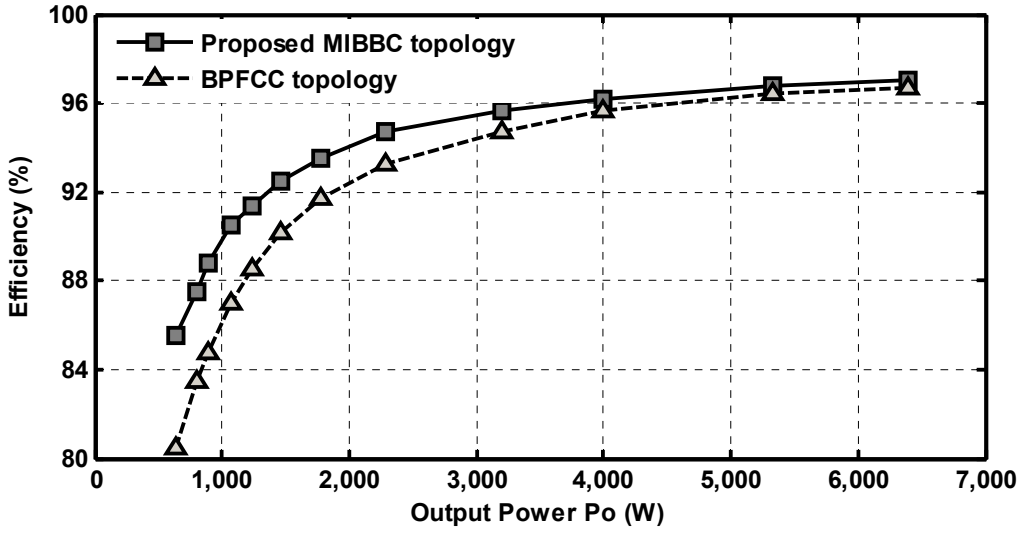

Fig. 8.19 The estimated efficiencies for the MIBBC topology (η_1) and the BPFCC topology (η_2) at load change based on loss model

8.5 Experimental Results

A hardware prototype of the developed high frequency power converter module was developed. Figure 8.20 shows the MIBBC prototype hardware implementation. It was designed, fabricated, and implemented in our laboratory. Ports 1-3 are designed for AC-source, fuel cell, and battery inputs, respectively. Port 4 is the DC-output. The individual converters are controlled by their own TMS320F28335-based control platforms. LEM voltage and current transducers are used for measuring feedback signals required for control strategy implementation. The specifications and parameters used in the prototype

are shown in Tables 8.3, 4. In this section, the experimental results of the BBC, BPFCC, and the developed converter (MIBBC) are provided.

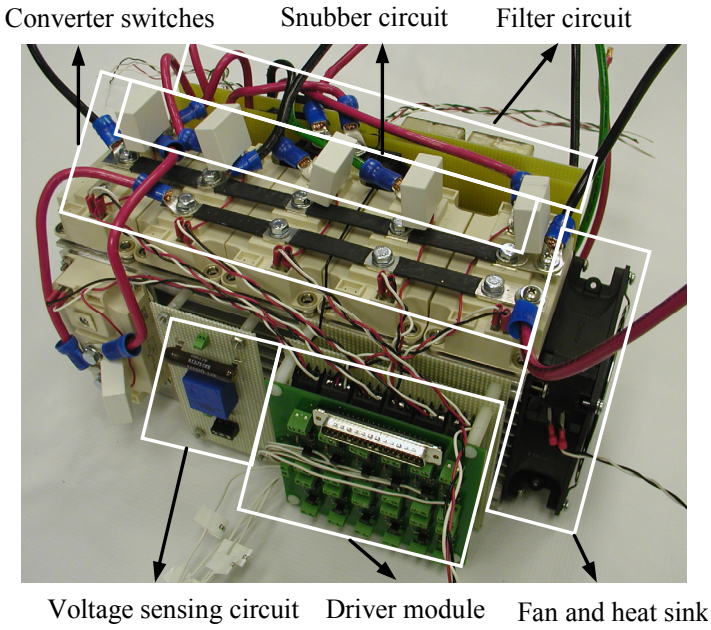

(a)

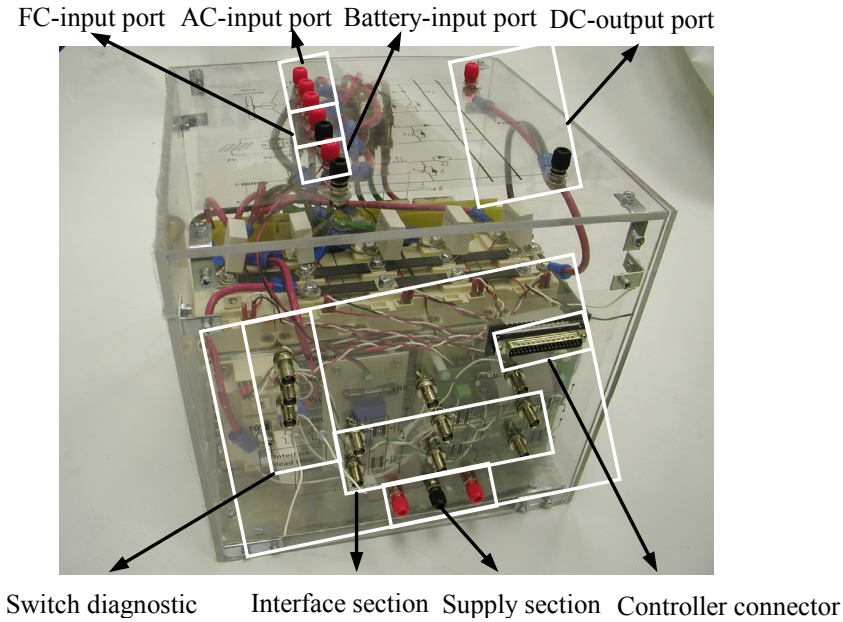

(b)

Fig. 8.20 The MIBBC topology hardware implementation: (a) Open-frame prototype, (b) Modularized frame and (c) Overall test setup

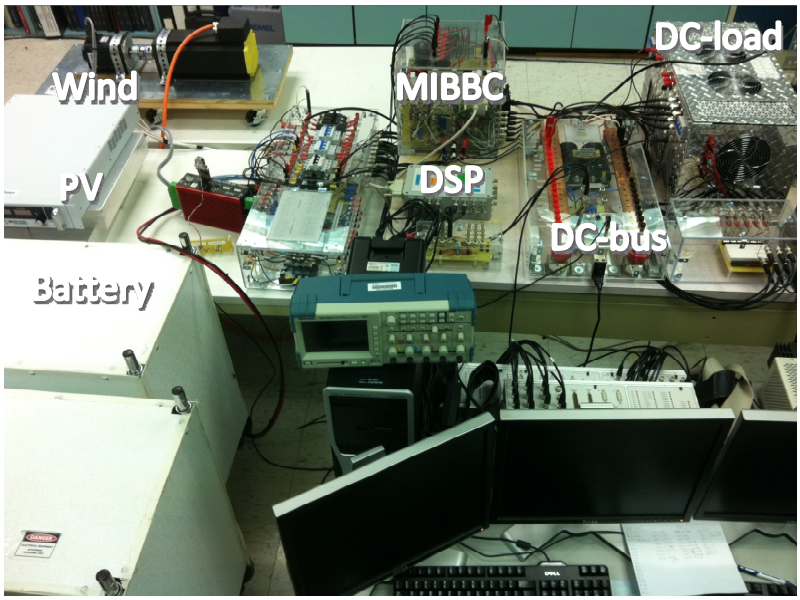

Fig. 8.20 The MIBBC topology hardware implementation: (a) Open-frame prototype, (b) Modularized frame and (c) Overall test setup (continued)

Table 8.3 PMSG wind generator AC-input specifications and control parameters

Parameter	Specification
Input power	0-4.88 kW
Rms input voltage range	80-208 V
Output voltage	400 V
Switching frequency	30-45 kHz
Input inductor	0.3 mH
Switching frequency	30-45 kHz

Table 8.4 FC and BESS Specifications and control Parameters

FC		Battery Bank	
Parameter	Specification	Parameter	Specification
Output Power	0-6 kW	rated voltage	160 V
Nom. operating point	(5 A,150 V)	Connection	10-series
Max. operating point	(60 A, 70 V)	rated capacity	100 AH
Switching frequency	50 kHz	Battery type	Lead-acid
Input inductor	0.33 mH	Total power	12 kW

8.5.1 MIBBC AC-Input Performance Evaluation

Figure 8.21 shows the DC-bus voltage, the current through phase "a," and the respective phase voltage at load power of 10-kW. The DC-bus voltage has no overshoot and low voltage ripple of 2.3%. In conventional bridge boost converter (BBC), the power factor and THD are about 0.835 and 35%, respectively, as shown in Fig. 8.22. In BPFCC, the power factor and THD are about 0.9983 and 7.95%, respectively, as shown in Fig. 8.23. In the developed MIBBC, the harmonic spectrum of the grid voltage (THD=0.3%) and rectifier current (THD=17.03%) at rated power, where the second-, fourth-, and fifth-order components are the most relevant, as shown in Fig. 8.24. Unity power factor (UPF) operation was investigated (PF=0.998); since the generator current and the phase voltage are in phase. This PF improvement represents more economic utilization of AC-power; since BPFCC achieved same advantage but with larger number of switches and losses.

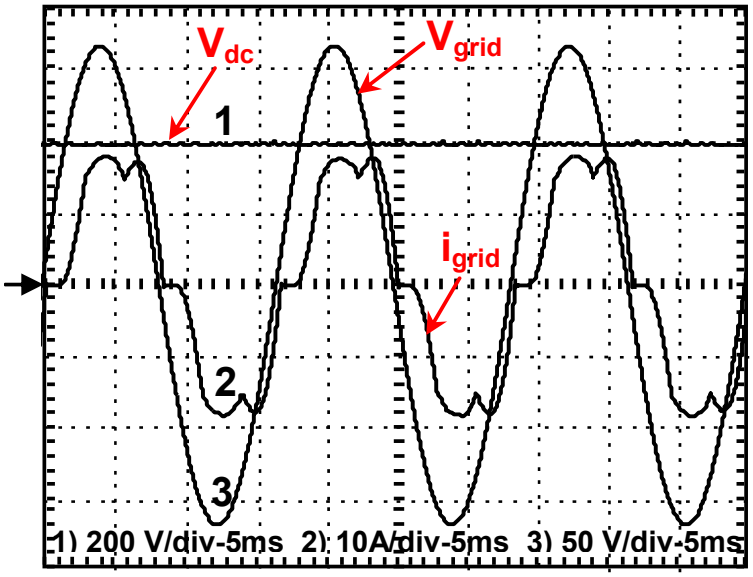

(a)

Fig. 8.21 DC-bus output voltage (200 V/div, 5ms), input AC-current (10 A/div, 5ms), and generator voltage (50 V/div, 5ms) for phase "a": (a) BBC, (b) BPFCC and (c) MIBBC

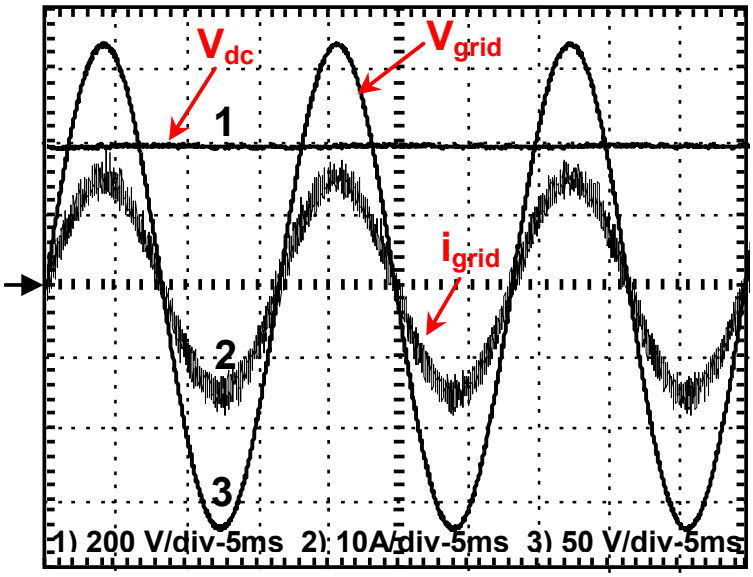

(b)

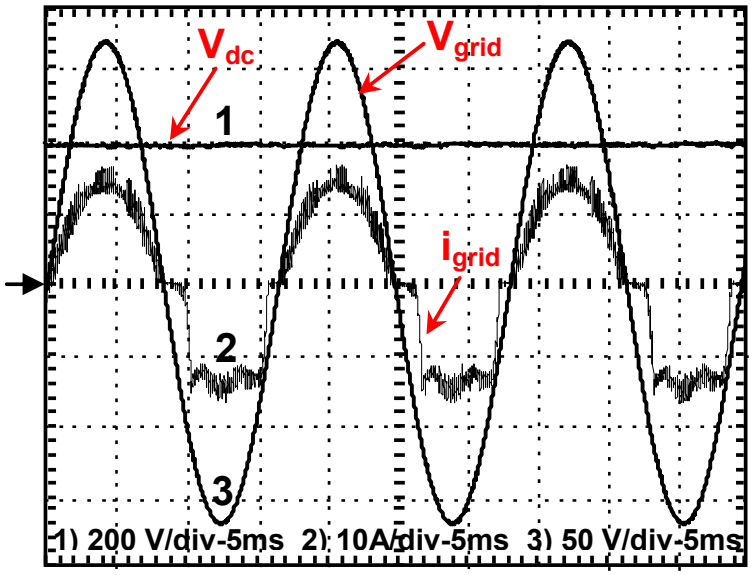

(c)

Fig. 8.21 DC-bus output voltage (200 V/div, 5ms), input AC-current (10 A/div, 5ms), and generator voltage (50 V/div, 5ms) for phase "a": (a) BBC, (b) BPFCC and (c) MIBBC (continued)

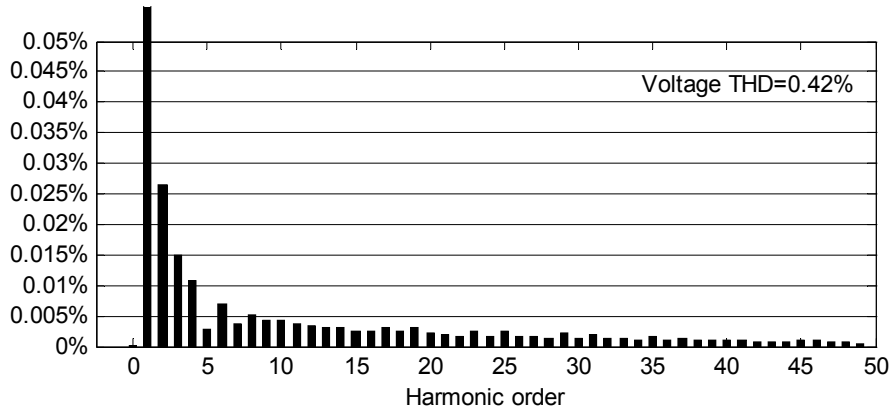

(a)

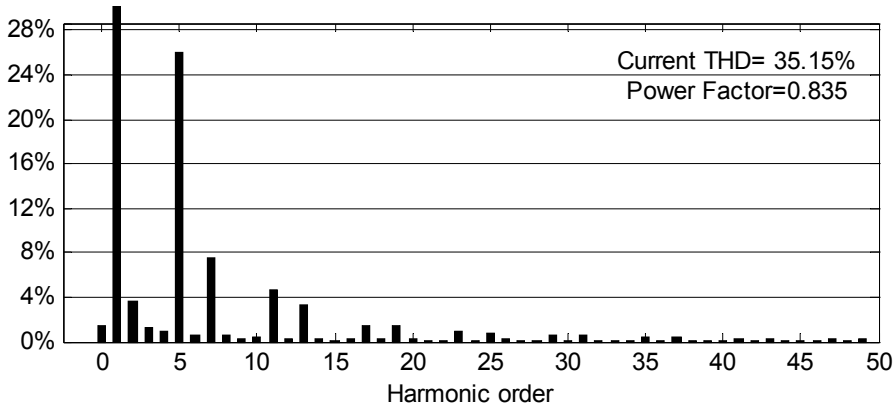

(b)

Fig. 8.22 BBC topology harmonic spectrum: (a) Grid voltage and (b) AC-current

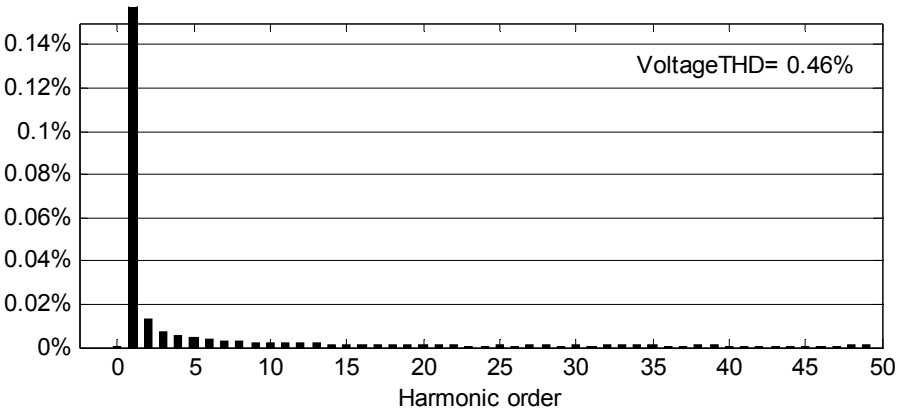

(a)

Fig. 8.23 BPFCC topology harmonic spectrum: (a) Grid voltage and (b) AC-current

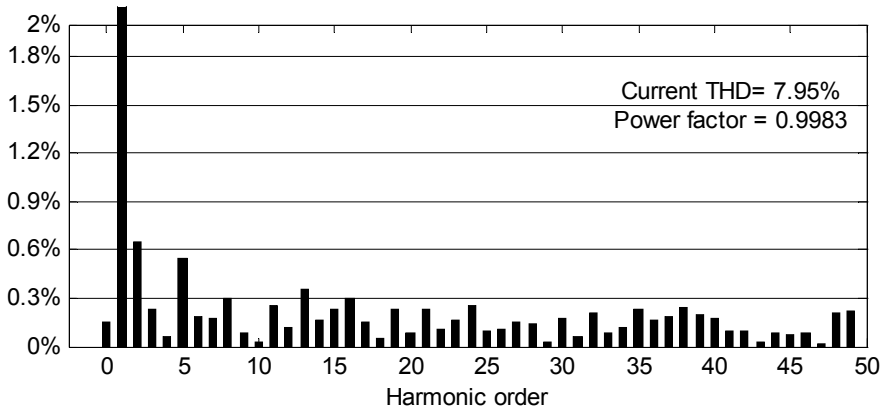

(b)

Fig. 8.23 BPFCC topology harmonic spectrum: (a) Grid voltage and (b) AC-current (continued)

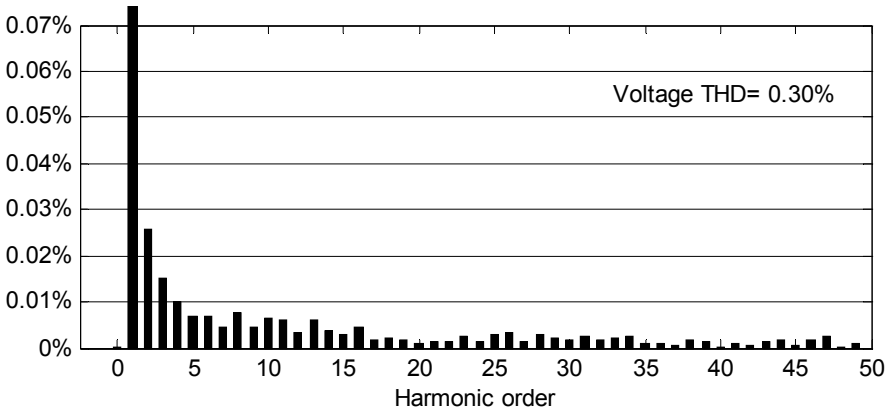

(a)

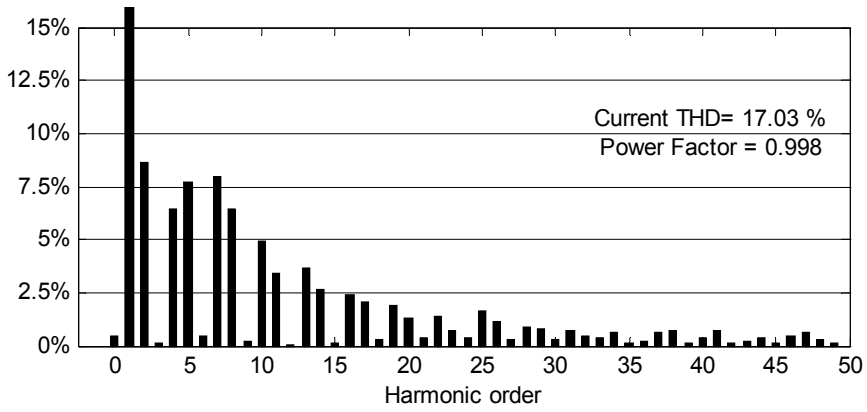

(b)

Fig. 8.24 MIBBC topology Harmonic spectrum: (a) Grid voltage and (b) AC-current

8.5.2 DC-Reference Change Test

Figure 8.25 shows the reference voltage, V_{dc_ref}, and the actual voltage, V_{dc} under DC-bus voltage reference change. The main objective of this test is to investigate the control system performance under DC-bus voltage level change to large values for medium-voltage distribution applications such as PHEV. A reference step change is applied and set to be increased from 400 to 500 V. The corresponding input current for the wind generator is also shown in Fig. 8.25. According to gain parameter design, it is noticed that the control operation has over damped transient response and there is no overshoot. The settling time is almost 0.05 sec which indicates to the fast response of the control system. Therefore, the overall dynamic performance was greatly improved.

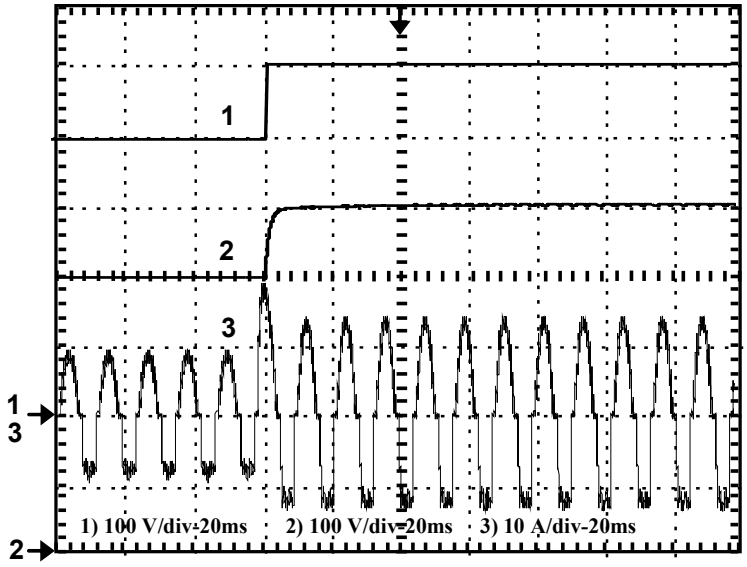

Fig. 8.25 Reference and actual DC-bus voltage (100 V/div, 20ms) and generator AC-current (10 A/div, 20ms) under DC-step change

8.5.3 Efficiency Comparison

Figure 8.26 illustrates the steady state battery DC-input inductor current of the MIBBC which shows that it works in the continuous mode of operation. As a result, the

instantaneous value of the inductor current can be easily controlled. This represents one of the main advantages for the MIBBC topology under high frequency operation; since the battery current is operate in the continuous mode which facilitates the control of the instantaneous value of the current instead of only controlling the average value. This leads to faster dynamic response during control operation. Figure 8.27 shows the comparative study of the efficiency between the converters based on laboratory measurements. In addition, the digital controller based DSP provides a good solution for achieving high accuracy under high frequency switching operation. As a result, the size of the passive components (inductor, output capacitor, and EMI Filter) is reduced by more than 50% compared with BBC at the same switching frequency. In addition, MIBBC and its digital control reduce the output voltage ripples and the inductor current ripple. Table 8.5 demonstrates the comparative study between the developed MIBBC topology the conventional converters (BBC and BPFCC) based on the experimental results.

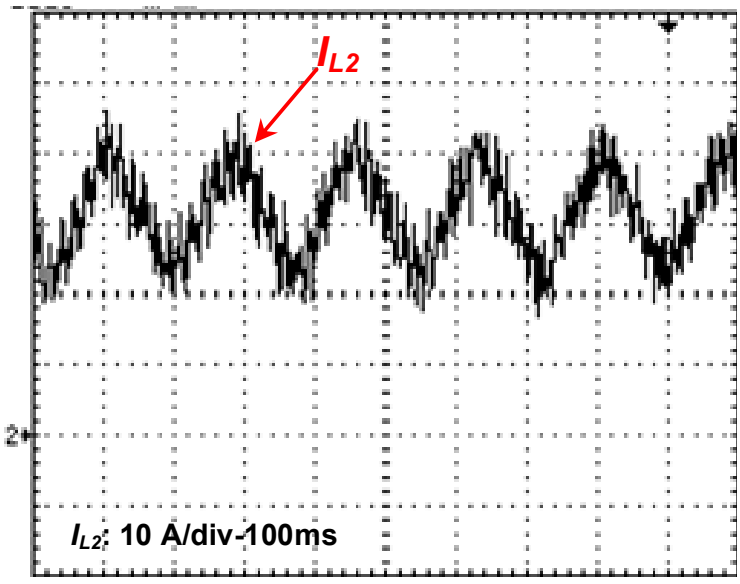

Fig. 8.26 The DC-inductor current of the MIBBC (10 A/div, 100 ms)

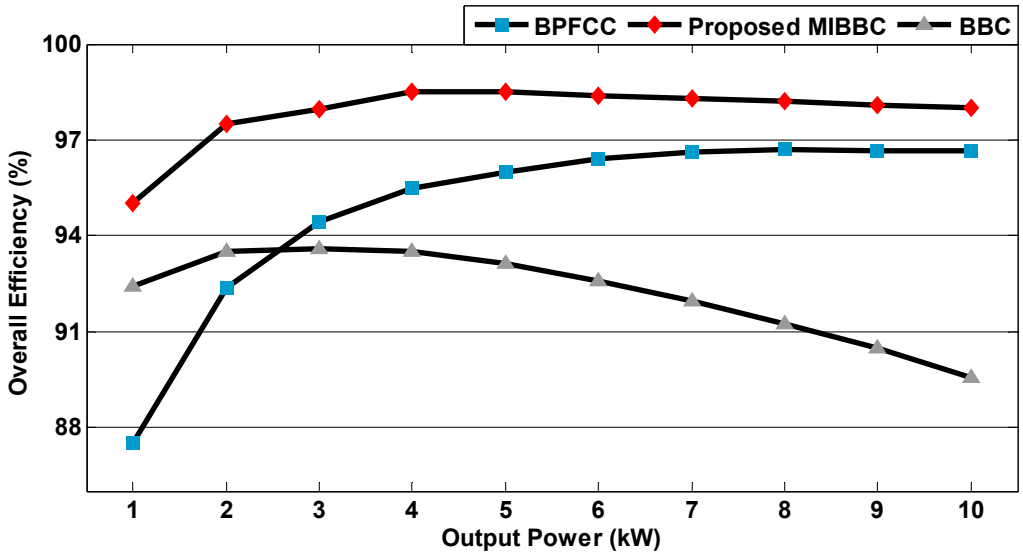

Fig. 8.27 The comparative efficiency between MIBCs at load change based on loss model

Table 8.5 Experimental topology comparisons of various MIBCs

Topology	BBC	BPFCC	MIBBC
PF	0.835	0.9983	0.998 (UPF)
Efficiency	92.2%	94.8%	97.8%
Input Inductor	2 mH	0.33 mH	0.3 mH (85% reduction)
THD%	35%	7.95%	17% (medium)

8.6 Conclusion

In this chapter, a novel modularized 4-port high frequency multi-input bridgeless boost converter (MIBBC) topology feasible for hybrid energy systems and PHEVs was developed in order to optimally utilize the amount of the generated energy. The hybrid PI-hysteresis control algorithm was designed for reducing the AC-input source harmonics. A direct digital control (DDC) approach was used for designing the cascaded digital control strategy to control the DC-input sources operation. The digital PI-

controllers were designed using a bode diagram to achieve the required phase margin and critical frequency. The MIBBC achieved higher efficiency (97.8%), when compared to BBC (92.2%) and BPFCC (94.8%). Also, the inductor size and weight (0.3 mH: 1.29 lbs) reduced proportionally to the frequency, compared to BBC (2 mH: 12.5 lbs), improving the overall efficiency for the system. In addition, less cost (more economic) was achieved compared to BPFCC; due to less number of switches. Smaller heat sink was needed compared to BPFCC; due to less switching losses which lead to less heat dissipation. High current THD (17.03%) was investigated but still lower than the compared BBC current THD (35%). Furthermore, UPF (0.998) operation was verified for generator input operation, compared to BBC (0.835). A fast control dynamic response was achieved (0.1 second) under DC-reference step change test. All the obtained results confirm the effectiveness of the developed topology for hybrid sustainable energy systems.

Chapter 9 Design and Implementation of Digital Signal Controller and Peripheral Interface Circuit for High Frequency Grid-Tie Inverters

9.1 Introduction

The digital signal controllers (DSCs) are finding wide application in many engineering fields especially the field of power electronics and these are suitable in almost all high frequency power conversion applications. This is because of their ability to perform complex mathematical computations within minimum amount of time and efforts. Furthermore, the digital controller is flexible as the implementation involves only software instructions and is independent of the converter size. An example of this is the dSPACE hardware and software programs which allow engineers to control projects through Matlab. However, a key setback presented by using dSPACE as the control interface is that the project or system must be constantly connected to the dSPACE interface board as well as the computer where the program is created. In addition, dSPACE controllers are expensive tools and have multiple components which occupy large space in the hardware system. Furthermore, it has a limited processing speed capability [132].

Some research studies for designing and implementing a DSP controller have been done on simulators and emulators for different applications [133-137]. In [133], a fuel cell (FC) emulator and the control are implemented in a Matlab/Simulink^{TM} environment and programmed into a dSPACE and/or DSP controllers. The control voltage from the FC model is fed into a power amplifier. Finally, the power amplifier drives either a load or a power-converter circuit. Reference [134] proposes a design and implementation of a power converter for an autonomous wind-powered SEIG feeding an isolated load through

the employment of a DSP-based rectifier-inverter circuit. Moreover, a DSP-based prototype platform used to support advanced power measuring algorithms, considering the definitions proposed in the new IEEE Standard 1459–2000, was presented in [135].

Reference [136] reports on the development of a laboratory prototype of a fully digital DSP-controlled 12-kVA unified power quality conditioner (UPQC), capable of compensating for both the supply voltage and the load current imperfections. A fully digital controller based on the TMS320F2812 DSP platform is implemented for the reference generation as well as control purposes. Also, an eZdsp development board was used to implement various PWM strategies on a fixed point DSP and compare their performances [137].

One of the most important applications that utilize digital signal processors is adjustable speed drives (ASDs) as discussed in [138-140]. A true single chip solution was proposed using DSP controller for multiple motor drives which significantly simplify the system design [138]. A speed control of DC motor using TMS320F240 DSP was done in [139] and [140]. In the previous application, an accurate and reduced part closed loop control was achieved through the fabricated DSP controller board.

In this chapter, a real-time digital control based on TMS320F28335 DSC is designed and implemented in order to achieve a fast response during transient operation. The control strategies are implemented using Code Composer Studio™ (CCStudio) and eZdsp TMS320F28335. The developed DSC board is highly suitable not only for high frequency-based power converters and wind turbine controllers but also for various industrial electronics applications such as; HEVs controllers and ASDs.

9.2 The DSC Developed Hardware Board

The DSC board is 150mm x 250mm four layers fabrication. The card is powered from regulated 5V DC switched mode power supply (SMPS) mounted on a separate analog board in the same box. It is plugged on the analog board for interfacing via 16 (12-Bit) ADCs BNC pins, 8 (8-Bit) DACs BNC pins, and 88 I/O pins female connectors. Figure 9.1 shows the block diagram of the developed DSC digital board. Figure 9.2 shows the board after assembling its components. The board has 7 major sections:

- TMS320F28335 DSP processor and 150 MHz crystal oscillator,
- On-card 256K x 16 Flash memory, 34K x 16 SARAM, and 8K x 16 Boot ROM,
- 16-channels 12Bit input Mux 80 ns/12.5 MSPS conversion rate,
- 8 Output Two DACs TLC7226 8Bit converter,
- 88 general purpose I/O pins with input filtering,
- Multiple output-SMPS with +5V or +/-15V Power Options,
- JTAG 1149.1 compliant emulation port compatible with XDS-510 USB or equivalent debugger using TI Code Composer Studio.

The DSC-board requires a 5V DC source. This 5 V DC source is obtained from the imbedded multiple output SMPS PCB which yields the required voltage as well as a +/-15V output, this 15V output can be accessed through three female banana connections which are placed on the DSC mainframe. These outputs are +15V, ground, and -15V. The SMPS powers both the DSC mother board as well as the internal fan with the 5V DC output. However, the DACs which are used for the analog outputs are powered by the +/-15V output. The SMPS is connected to a power receptacle of 120V AC.

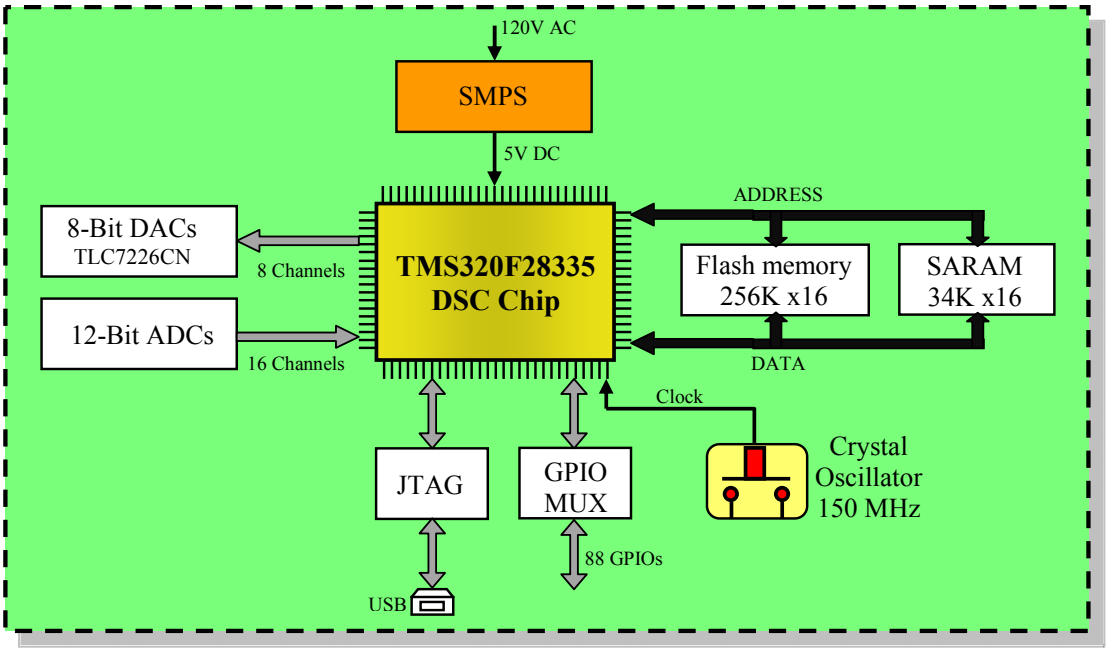

Fig. 9.1 Block diagram of the developed DSC digital board

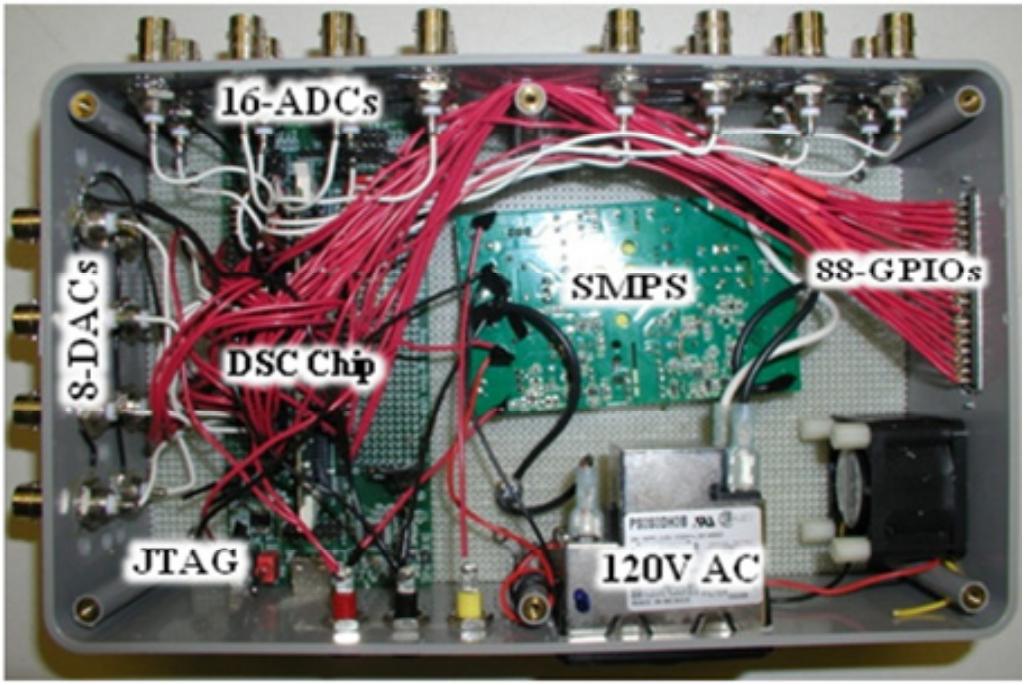

(a)

Fig. 9.2 DSC digital fabricated board: (a) Internal DSC-design with assembling its components and (b) Finalized version of the controller

(b)

Fig. 9.2 DSC digital fabricated board: (a) Internal DSC-design with assembling its components and (b) Finalized version of the controller (continued)

The cooling is implemented using a small 1.5” x 1.5” fan. The air in the DSC is able to circulate because across from the fan there are 9 strategically placed holes which allow air to flow easily. Furthermore, the fan can be controlled through a heat sensor which maintains the internal temperature at a desired value. The schematic diagram and the layout footprints are shown in Fig. 9.3.

The TLC7226CN is a four 8-bit output digital to analog converter (DAC). This chip is used to convert the output digital signals from the TMS320F fabricated board into analog signals. These analog output signals are amplified to control the speed of the prime-mover which acts as a wind turbine emulator. The DAC has a parallel input channel configuration, which means that it will work faster than the serial input channel configuration since the eight input digital bits will be sent to the chip at the same time. Out of one single DAC chip we can obtain up to four analog outputs (OUTA, OUTB,

OUTC and OUTD). Since the converter is an 8 bit converter, eight outputs from the I/O pins on the controller board will be used to send digital signal to the DB0 through DB7 pins on the chip to obtain four analog outputs. Figure 9.4 below shows the chip pin configuration [141].

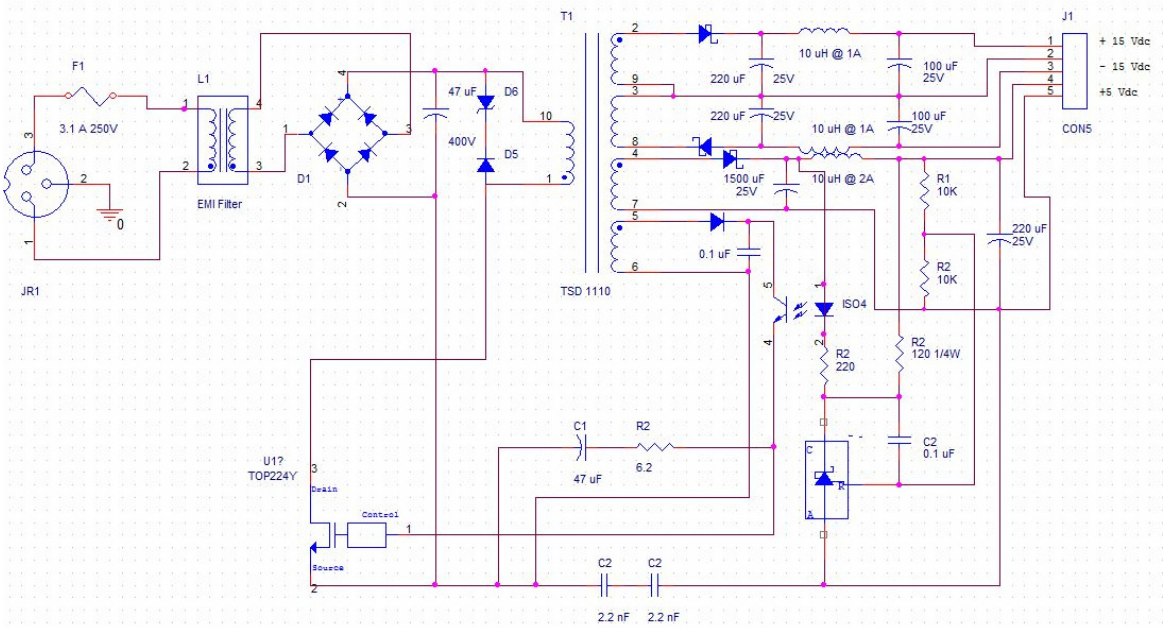

Fig. 9.3 SMPS design schematic diagram for DSC digital board

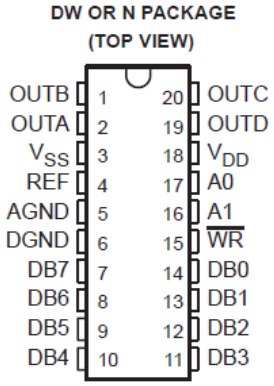

Fig. 9.4 The TLC7226CN digital to analog convertor pin configuration

9.3 Software Design

Software development environments such as Code Composer Studio™ (CCStudio), Matlab and Microsoft Visual C++ were used. This section gives a brief overview of the first two items. The Texas Instruments (TI) provides a royalty-free RTOS with its DSPs, called DSP/BIOS. For a list of features, the reader must refer to [142-144]. In view of the described application, the use of DSP/BIOS has three distinct advantages:

- The Code can be impeded and ported to a small fixed-point DSC, without substantially modifying the source code,
- It is a pre-emptive multitasking environment. Software expansion is easy and the real-time analysis (RTA) module provides detailed information in real-time about the running algorithms (tasks),
- It has a real-time data exchange (RTDX) module, that transfers data in real-time between the DSC and the PC.

At first, the "C" programming language was considered for the algorithm development. Given the fact that it takes significant time to master writing good quality "C" code, programming of an algorithm in a DSP/BIOS task is done by means of the Matlab IDE Link toolbox, thus avoiding tedious manual coding of the algorithms. The produced "C" code is compiled and linked with support software that runs the code as a single or multiple tasks, depending on whether the Matlab system has one or more sample rates. The tasks are either data- or interrupt-driven.

The DSP/BIOS provides streaming I/O objects (SIO) that handle this type of data acquisition and entirely hide process synchronization from the programmer. A task simply blocks when a request is made for data that is not yet available, releasing the

processor to other, lower-priority tasks. A low-level I/O driver (LIO) was written that uses the DSCs on-chip direct memory access (DMA) controller to transfer these blocks in the background without interrupting the DSC.

9.4 Peripheral Interface Circuit

The interface section is one of the most important parts in the real-time operation. It represents the connection point between the control circuit and power circuit. The designed interface board is 127mm x 114mm two layers fabrication. The board is powered from regulated 15V DC switched mode power supply (SMPS) mounted on a separate analog board outside the module box. The main objectives of this board are: (1) to make ground isolation between the controller board (low power) and power circuit (high power) which protects the controller against power circuit section faults, (2) to amplify the control voltage from 5V to 15 V in order to be able to switch on the IGBT power switches.

Figure 9.5 shows the circuit schematic of the developed interface circuit. The circuit was completely designed using the tools in Orcad Capture. A simple opt-coupler was obtained from the built-in libraries and it was modified to look like the 6N136. This one has a BJT inside and also had one more diode than a regular opt-coupler. This circuit was done exclusively on a PCB to reduce the size and bulkiness of breadboard built models. This circuit was repeated to create 12 inputs-12 outputs design as shown in Fig. 9.6. Figure 9.7 shows a photograph of the board after assembling its components.

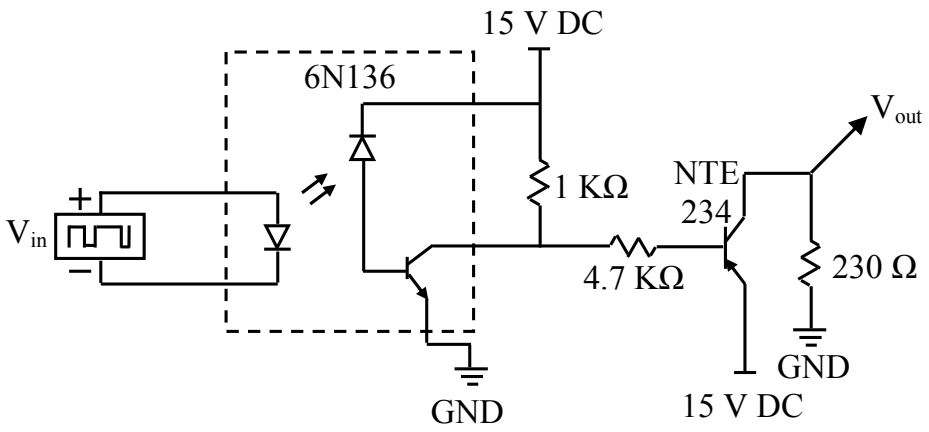

Fig. 9.5 Circuit schematic of one opt-isolator

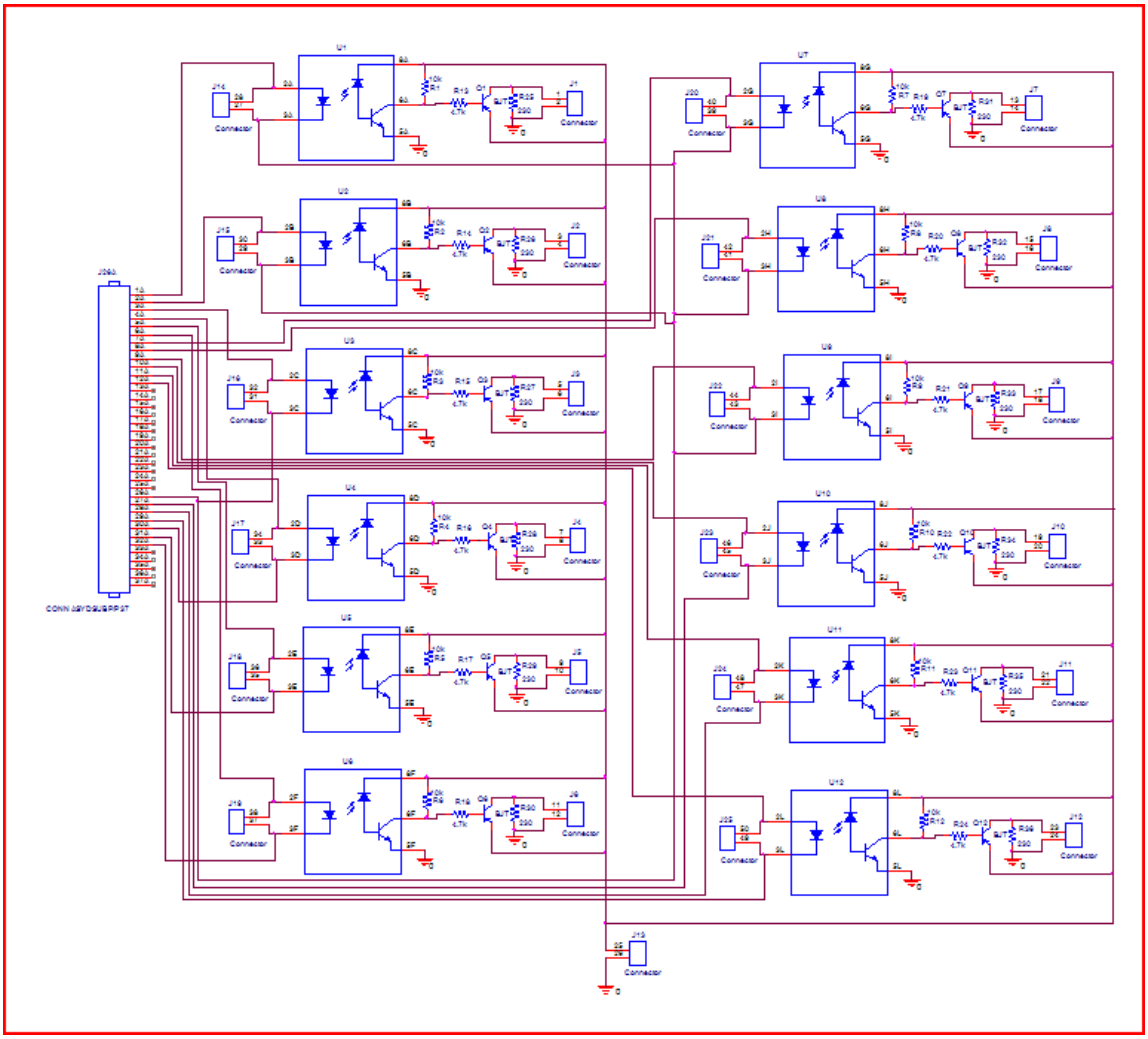

Fig. 9.6 The layout of the overall interface board before fabrication

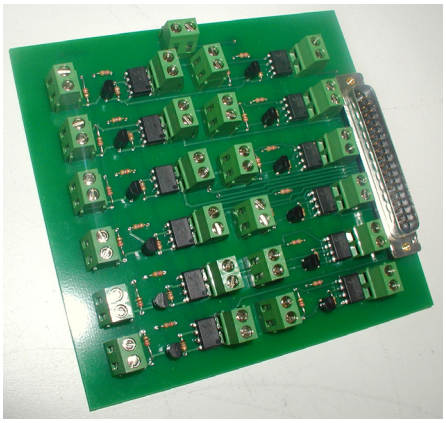

Fig. 9.7 The hardware interface board after assembling its components

9.5 Power Circuit Description

Figure 9.8 illustrates the schematic diagram of a grid-connected wind farm and its VOC control strategy that was previously discussed in chapter 3. This system is considered as an example to verify the advantages of the developed DSC over the commercial laboratory controllers such as dSPACE 1104. DSC is used here to investigate the performance of the control operation of the high frequency grid-tie-inverter.

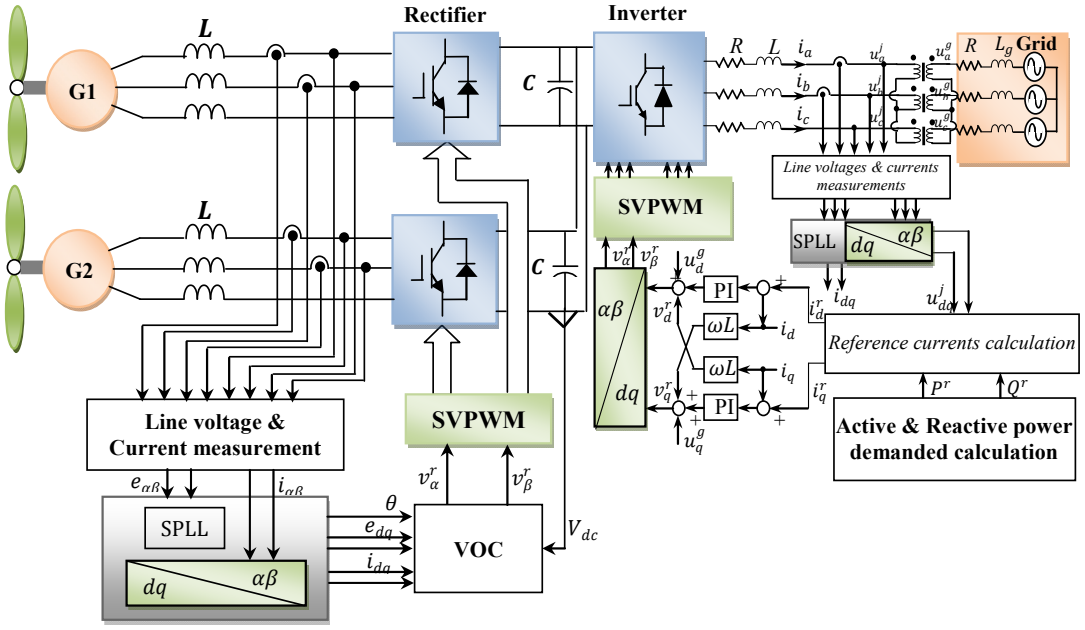

Fig. 9.8 Schematic diagram of the overall WECS control system connected to grid

9.6 DSC Test Results

In order to investigate the performance of the developed system, an experimental setup for WECS is constructed and connected to the local grid. A prototype experimental setup is designed and implemented including the developed DSC as the control heart of the developed system and all the interfacing circuits to the analog power circuits.

The control program using Matlab/Simulink™ was designed and downloaded to DSC-chip [145]. The HF-PWM presented in this section was used with a 30-kHz switching frequency. The VOC strategy discussed in chapter 3 is utilized in the control. Figure 9.9 shows a photo of the experimental test setup implemented in the laboratory for the developed system.

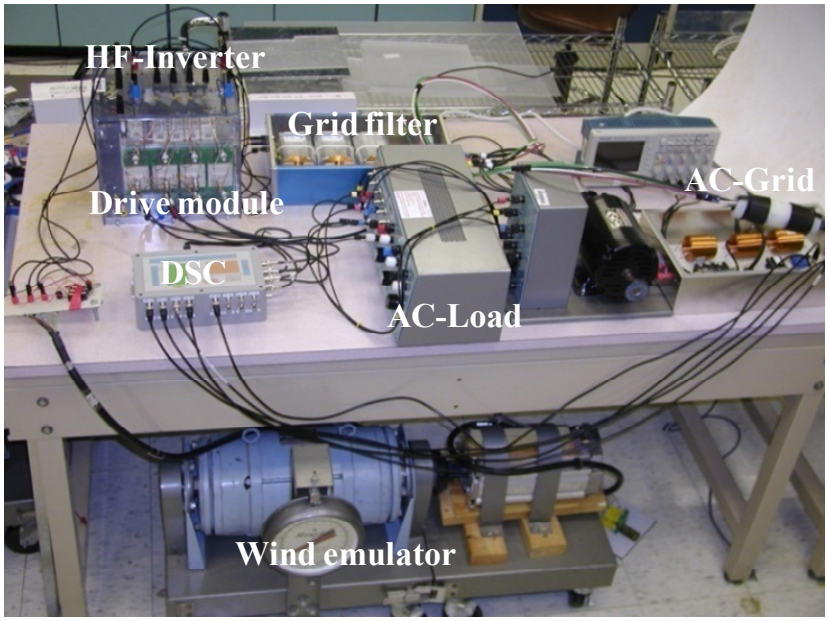

Fig. 9.9 The experimental setup of the overall WECS connected to grid (including DSC-controller board).

9.6.1 DSC-board performance

In order to test the DSC-board characteristics, two types of tests were carried out. The first is the DAC test for wind speed emulation. The second is the digital output test for high frequency operation capability.

In the first experiment, a sine wave is used as the input signal to be converted into eight bit digital values. This eight bit will then be sent to the DAC chip in order to obtain an analog sine wave on the output. Because the DAC has 8 bit inputs, then the state (11111111) will be equivalent to $2^8 = 256$ and the state (00000000) will be equivalent to 0. The states between these two values can be calculated by the formula $(2^8\text{-}1)/V_{IN}$. Figure 9.10 shows the Matlab/Simulink™ program that was designed to perform this operation.

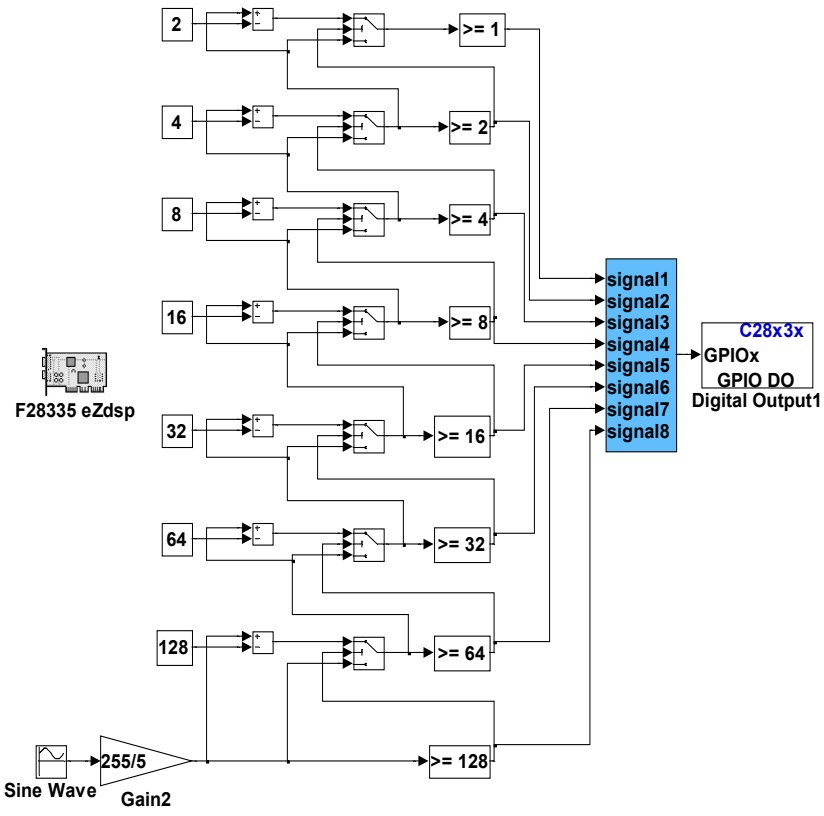

Fig. 9.10 Digital to analog converter- sine wave test

The sign wave signal at the input has amplitude of 2.5V and is biased by 2.5V in order to have the full sine wave on the positive side of the y-axis since the chip is set to work in the unipolar configuration. A gain of 255/5 is placed after the sine wave block to convert the analog voltage values between zero and 5V into a value between zero and two hundred and fifty five. The value obtained after the gain is then processed by eight different operations which gives eight different digital outputs of zeros and ones. A multiplexer is then used to send the eight outputs to the block named “Digital Output”. The Digital Output block sends the input values coming from the multiplexer to the I/O pins which are connected directly to the chip. Figure 9.11 shows the sine wave obtained from the analog output on the DSC- box.

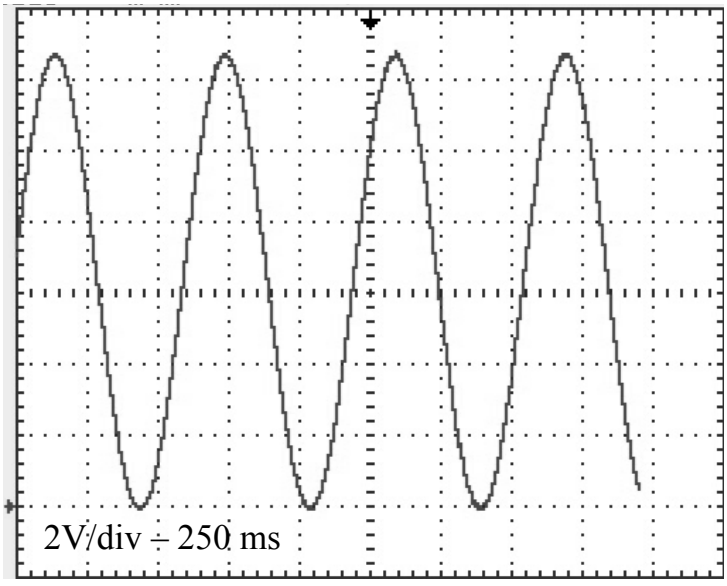

Fig. 9.11 Sine waveform obtained from the analog output of the DSC-board

In the second experiment, the digital outputs or I/O pins are tested with a very simple circuit design. The objective of this experiment is to measure the switching frequency of the output digital signal. Figure 9.12 shows the circuit schematic.

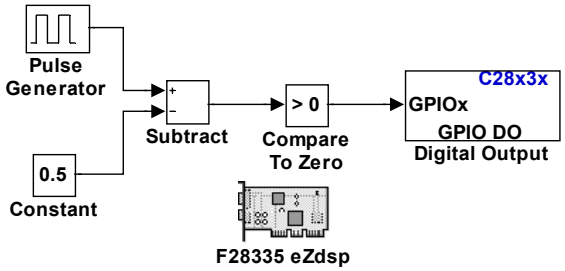

Fig. 9.12 Digital output test

A pulse generator is used as the input signal with amplitude of 1. Then, it is subtracted by a constant of 0.5 and the result is compared to 0. When the value from the pulse modulator is 1, then (1-0.5>0) and the output is 1. On the other hand, when the pulse modulator is 0, then (0-0.5<0) and the output is 0. The output from the comparator is sent to the "Digital Output" block and is assigned to a specific I/O pin on the board. The signal output from the circuit must be a pulse signal with amplitude of 3.3V (rated value). The frequency of the output signal depends on the frequency of the input pulse modulator. Figure 9.13 show the output signal from the I/O pins.

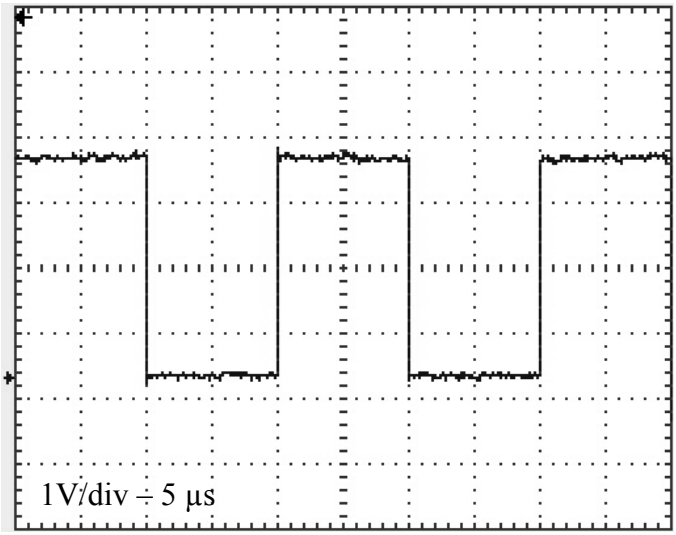

(a)

Fig. 9.13 Pulse signal from the digital outputs with amplitude of 3.3V and frequency of: (a) 50 kHz and (b) 100 kHz

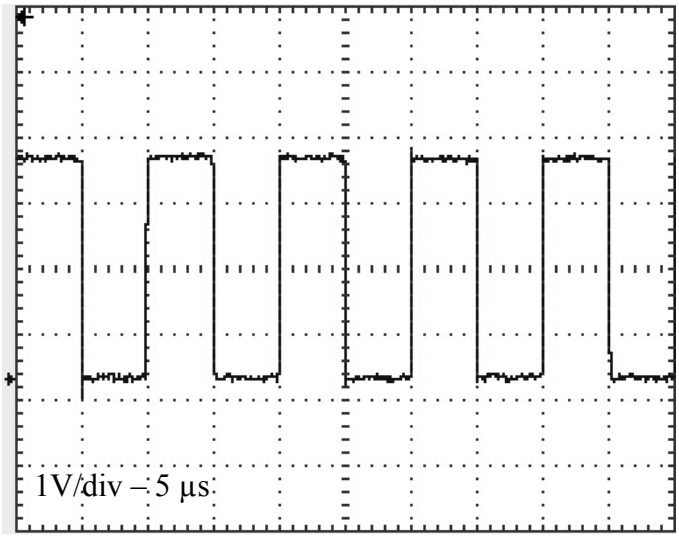

(b)

Fig. 9.13 Pulse signal from the digital outputs with amplitude of 3.3V and frequency of: (a) 50 kHz and (b) 100 kHz (continued)

9.6.2 Wind Emulator and HF-PWM Inverter Control

This part is composed of two main components. The first is the wind emulation section which can be seen on the lower left corner of Fig. 9.14. The block "Repeating Sequence Interpolate d" is used to simulate the wind speeds at one of Chicago's airports data 2009. This value is then converted to an analog output through the DAC subsystem which was previously explained on the first experiment. The second part is the inverter control which can be seen on the top left. The inverter control is composed of a high frequency PWM signals which sends digital outputs to control the IGBTs in the grid-tie inverter part of the wind emulation system. This HF-PWM signal can be seen in Fig. 9.15. The signal on the top half represents the wind speed simulation and the PWM digital output signal is represented on the bottom half.

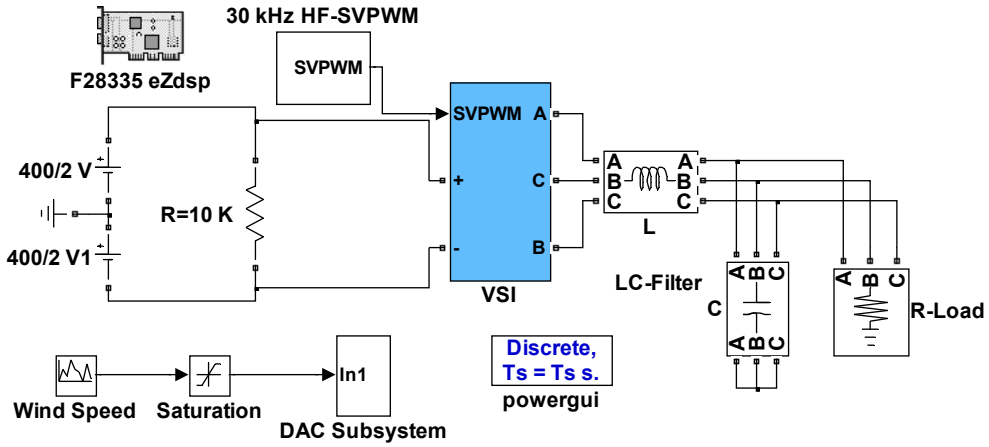

Fig. 9.14 Simulink program for the wind emulator and inverter control system

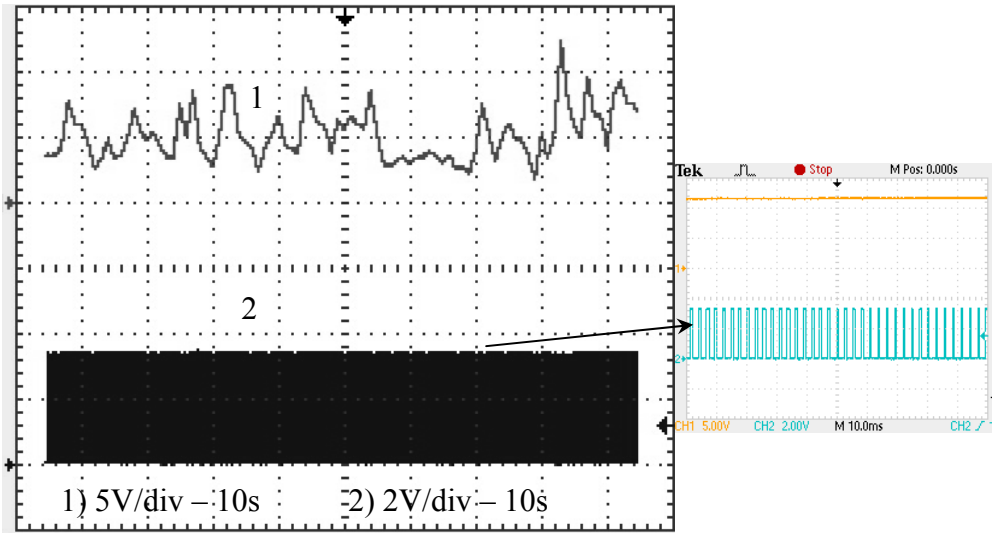

Fig. 9.15 Wind emulator speed (5 V/div, 10s) and inverter HF-PWM (30 kHz) control output signal (2 V/div, 10s)

9.6.3 Power Injection Test

In order to evaluate the performance of developed system, two types of loads are applied to the output of the WECS at the grid connection point. A 350 Ω resistive load and 1/3 hp induction motor load were connected together at the same time. Although loads are connected at the grid point, no current was drawn from the AC grid and WECS supplied the current for both loads as well as the wind generation system maintain stable

in synchronization process with the grid. Figure 9.16 shows the grid-tie inverter output voltage synchronized to the AC-grid voltage while the load current appears to be lagging to inverter output voltage.

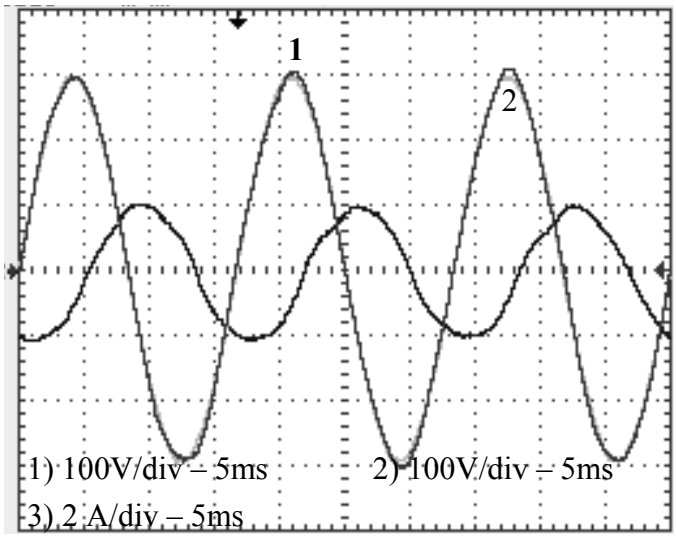

Fig. 9.16 Grid-tie inverter voltage and AC grid voltage (100 V/div, 5ms) versus load current (2 A/div, 5ms)

9.6.4 DSC Measured Efficiency and Power Factor

Figure 9.17 shows the measured efficiency and inverter output power factor (PF) for both controllers (DSC-development board versus dSPACE1103 board) according to the applied resistive load condition. For DSC, it is noticed that the average efficiency is above (91 %) while the PF is almost unity and these results agree with dSPACE controller results to a great extend.

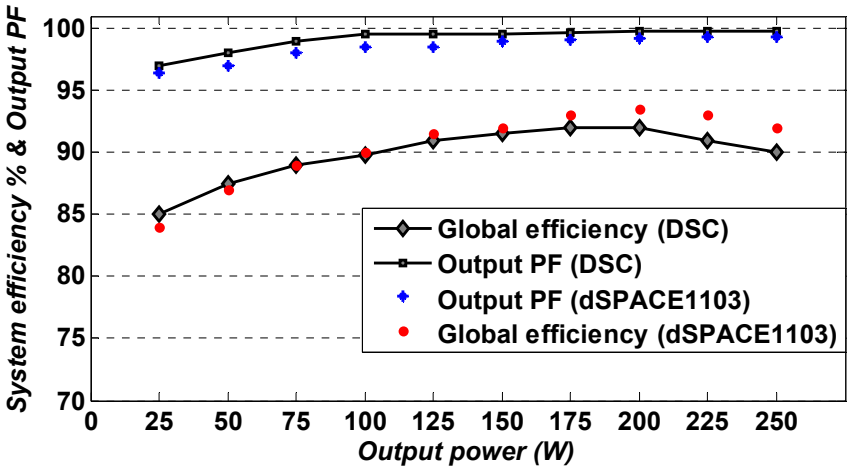

Fig. 9.17 Efficiency versus output power and output PF versus output power

9.7 Conclusion

In this chapter, the developed DSC-board proved its high performance and practical impact towards controlling high frequency-based power inverters for grid-connected wind emulator system. The high frequency operation was utilized for efficiency (above 91%) and power density improvement since the passive elements physical size and power losses have been reduced inversely with switching frequency. Different types of loads have been connected to the system (active and reactive) in order to test the power injection capability.

The designed controller achieved the following advantages; low cost (less that $100), comparing to other commercial controllers such as dSPACE 1103, which facilitate its availability for research work as well as educational purposes, high accuracy, where 150 MHz processor is used as the main heart of DSC-system, high reliability, since it is an embedded and computer independent with USB communication for program downloading process. The developed DSC-system confirmed its superiority for grid-connected sustainable energy systems.

Chapter 10 Practical Implementation of HFPCS

10.1 Introduction

Enabling modern power electronics solution for markets such as wind, solar, traction, welding, elevators and electric vehicles is a complete sub-assembly. The decision to select an all-round solution which includes a complete sub-assembly, the specification and design, production, arduous testing and after-sales support and service is time-saving, cost-effective and so simple with an experienced partner.

Through the whole dissertation study, the high frequency power converter system HFPCS was designed, implemented, and investigated in our Energy Systems Research Laboratory (ESRL) as a high-level-integration power electronics system from the multi-converter system family that was developed in line with customer specifications. The system comprises multiple converters used to control power flow under harsh ambient conditions. Different operating modes are possible, e.g. the system can be supplied with electric power by way of a 3-phase wind generator, a PV, Fuel cell, and Batteries. The system is housed in an air-cooled case (with thermal protection) and communicates with the master controller via a D-connector bus. The signal interface features analogue and digital I/Os to allow for the connection of a wide variety of sensors, e.g. temperature sensors, resolver inputs.

This new enabling technology has ability for hybrid sustainable energy sources connection representing DC-microgrid and sharing same DC-bus voltage level. Also, DC-Power can be injected into local single-phase or three-phase AC-grid through a power inverter module system. The main advantages of this high frequency developed

module when compared to the conventional low frequency power converters for other manufacturers are:

- Higher efficiency due to less power losses and reduced number of switching elements,
- Lower total harmonic distortion (THD %) which leads to better power quality,
- Larger output power density realization,
- The power circuit passive elements were reduced proportionally to the frequency, with a corresponding reduction in size and weight,
- Smaller size and weight,
- Voltage/current measurements and interface board are internally imbedded,
- Less overall operational cost,
- The harmonics are of higher orders and can be easily filtered out,
- Higher reliability because of parallel sources and thermal protection.

Figure 10.1 illustrates the developed HFPCS schematic diagram and its hardware implementation. High frequency multi-input boost converter (MIBC) was successfully tested, as a prototype of its initial 72kW hybrid converters technology. The power handling capability was calculated according to the maximum designed features for the developed converter. However, this converter was tested for 10 kW loading condition considering the available loads in our laboratory and the amount of the heat dissipation that will occur during larger power operation. Accordingly, there are some important recommended rules explained in this chapter must be considered to upgrade the developed converter for testing it under larger power ratings up to 72 kW.

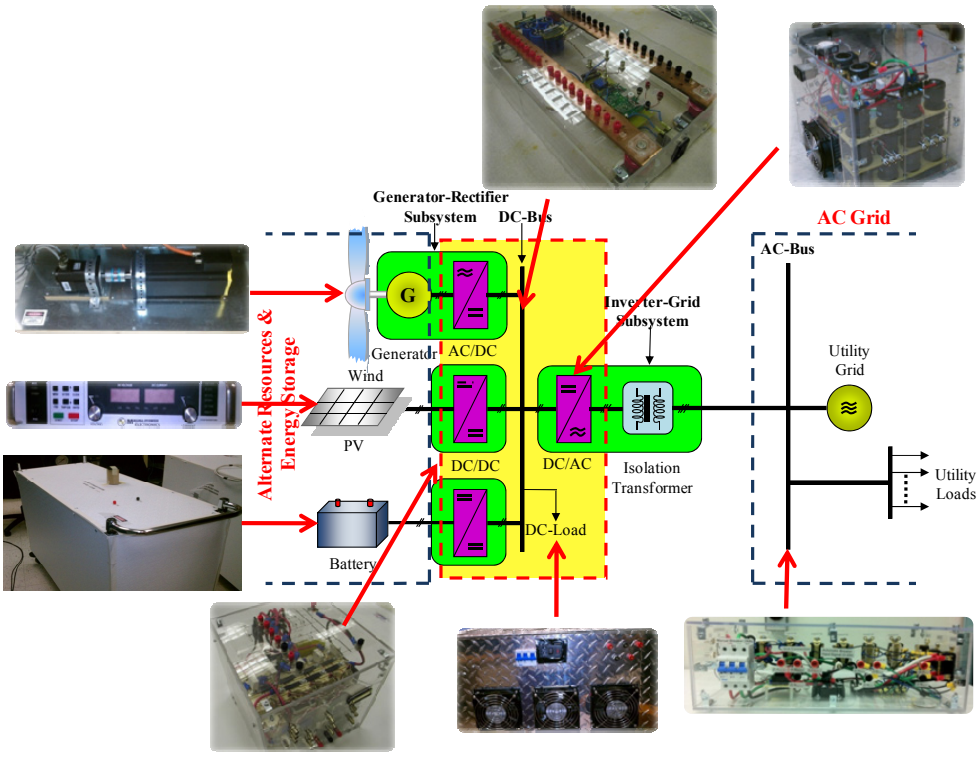

(a)

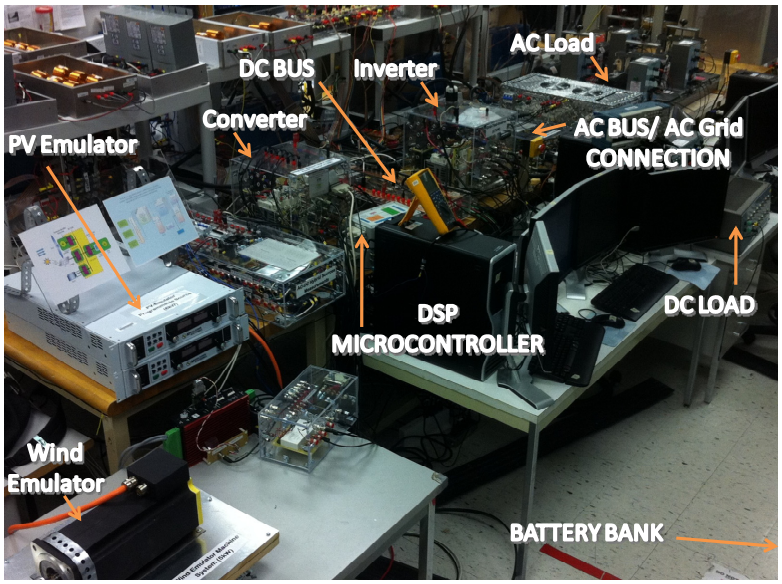

(b)

Fig. 10.1 The overall high frequency-based power converter system configuration: (a) Schematic diagram. (b) Hardware implementation

10.2 Commercialized MIBC Description

The developed HF MIBC is a power electronics platform solution meeting market demands for a standardized, compact, maintainable, flexible and above all cost-effective system for forced air-cooled converters of 1200V, 72 kW. Figure 10.2 shows a photograph of the first modularized version of the MIBC.

The diode rectifier with intermediate DC-DC boost converters and the fully-controlled converters are the dominant power converter topologies used in AC-sustainable energy conversion systems. MIBC uses a completely new topology called high frequency semi-controlled converter topology. This topology uses similar components and materials as the conventional converters, but operates in a completely unique method. Although HF MIBC was designed as a standard platform it was also designed to allow customization, such as changing the power modules, the type and orientation of the fans without changing the whole concept. The dramatically smaller size and lower weight of the MIBC prototype converter is proven in this pilot project.

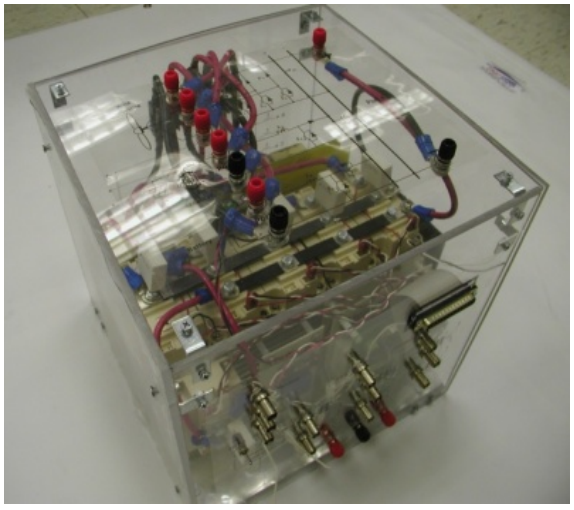

Fig. 10.2 MIBC developed prototype

10.3 MIBC Main Features

The main features of the developed MIBC topology can be summarized as:

- Reduced cost industrial platform is achieved; parts used within the range of 60A, (at 50kHz switching frequency) are reduced to the minimum according to the available components of the shelf (COTS), the whole range can be covered with only one reference of IGBT module, line input inductor filter, heat sink, fan, and voltage sensor.
- The module design with the latest NPT-IGBT chip generation is optimal for the HF MIBC range.
- The gate driver along with close protection scheme gate boards protects the devices with electrical isolation, V_{ce} monitoring, short pulse suppression, under-voltage monitoring and interlocking.
- The MIBC range has forced air-cooling of the system guaranteeing long lifetime expectancy and avoiding the occurrence of hot spots.
- The excellent symmetry of the bus-bar system between the Snubber blocks and the IGBT modules ensure a current sharing between the modules.
- All five sizes use the same spare parts; this ensures easy integration, plug and play and easy maintenance.
- Four of these sizes have a half controlled rectifier. All removable parts weigh less than 66 lbs and all screwing points are accessible from the left side, while conventional converters with similar capability have about 364 lbs of magnetic-metal.
- For a large installation with multiple power ratings less spares are required due to the modularity of the MIBC.

- The same parts are used through the whole range, which simplifies training of the after sales team and allows an improved availability of the parts.
- All technical performances result in a power/volume ratio, which was previously only achievable through water cooling.
- Reduced weight and cost; this is achieved by reducing inductive filter requirements.
- Higher efficiency due to less power losses and reduced number of switching elements, maximizing energy harvesting.

The developed MIBC detailed technical specifications are shown in Table 10.1.

Table 10.1 MIBC technical specifications and parameters

Technology	**MIBC**
Max. DC-Voltage	550 Vdc
Max. Input Current	60A
Max. Input Power	11 kW
Efficiency	97.8% Average
Weight	<66 lbs (>80% reduction)
Size (Dimension)	11.8”x11.8”x12.2”
Multi-access	Yes
Switching Frequency	50 kHz
Passive elements	Filters included
Interface circuit	Yes (TTL & CMOS)
Voltage measurements	Yes (+/- 0.8% accuracy)
Current measurements	Yes
Cooling	Yes (Forced-air heatsink)
Thermal Protection	Yes (through thermal sensor)
Accessories Self-Supply	Yes (Through battery bank)
Signal Error Monitoring	Yes
Snubber circuit	Yes (0.22 μF)
Load Control	Yes (6-outputs)
Controller Connectivity	BNCs or D-connector
Battery voltage sensor	Yes
Total Costs	<$3,000

10.4 MIBC Application Area

The developed converter is designed to provide superior power management for rapid control prototyping and is highly suitable for various applications such as:

- Hybrid sustainable energy conversion systems,
- Grid connected systems,
- Grid-tie inverters,
- DC-distribution infrastructure systems,
- Hybrid electric vehicles,
- Adjustable speed drives.

10.5 The Practical Rules for MIBC Scaling-up

It is not viable to simply resort to increasing the switching frequency to limit the size, weight, and cost of the converter since the core and copper loss of the inductor will go up as a result of the increased switching frequency and the power rating. In addition, the semiconductor heat dissipation in the converter limits the switching frequency [169]. For example, the inductor design is still a challenging issue for increasing the converter efficiency and power density. Besides its large size and heavy weight, the lossy inductor limits the operating temperature. As a result, a compact size (11.8 in. × 11.8 in. × 12.2 in.) and light weight (<66 lbs) were achieved. Furthermore, the power density of the developed converter is considerably increased.

On the other hand, research labs around the US have taken many different approaches and rules, which represent the potential innovation, to scale-up to the full utilization for larger power ratings (up to 72 kW) of our developed MIBC converter and obtaining more efficient and better integrated power converters:

10.5.1 Improved High Frequency Circuit Topologies

The Perrault lab at MIT has focused much of their recent efforts on new circuit topologies – the arrangement of components in a circuit – that can limit the losses in the semiconducting switches used in power converters. This group has developed a new class of converters which operate at high frequencies with minimal switching losses. Many of these new designs rely on Gallium Nitride-based (GaN) semiconductors currently under development. The GaN switches will likely replace silicon-based semiconductors as the building block for tomorrow's converters [169].

Also, the replacement of silicon carbide (SiC) devices instead of the present NPT-IGBT will have merit because of their high-temperature capability, high-power density, and high efficiency, which has been indicated by some previous works [170, 171].

Moreover, the use of the clustered insulated gate bipolar transistor (CIGBT) in cascaded manner is another option to increase the power rating through larger voltage levels (> 3.3 kV) [172]. However, some issues, such as short circuit, could be arisen from the series connection which must be taken into consideration [173]. In addition, the multiphase multilevel connection is highly recommended for high-current, high power HEVs and fuel cell vehicles (FCVs) [174].

10.5.2 Switched Capacitor Circuits

Groups such as the Sanders lab at Berkeley have been researching a new circuit topology called switched capacitor circuits that eliminate magnetic devices completely from the switching circuit (remember that losses in magnetic components generally scale with frequency). Work is still underway to produce switched capacitor systems which can be efficiently regulated, but miniaturization is easily attainable with these new

designs [175]. There is still great potential to make the converter even lighter by replacing the film capacitors with multilayer ceramic capacitors (MLCCs).

10.5.3 Integrated Magnetics Designs

Building miniaturized magnetic devices with manageable losses at high frequencies has been the recent focus of the Lang (MIT) and Allen (Georgia Tech) labs. Designing magnetics which are smaller and much more integrated with the converters' other components can require both new materials and complex microfabrication approaches. This has convinced MEMS (micro electromechanical systems) experts, such as Lang and Allen, to focus their work on building efficient micro-scale inductors for power converters. Magnetic components that are integrated on-chip with other power conversion components could bring low-cost and efficient power conversion to a myriad of industries.

10.5.4 Heat Sink Design Considerations

In fact, the heat sink is one of the major parts that directly affect heat transfer characteristics inside the converter module [176]. With the increase in heat dissipation from microelectronic devices and the reduction in overall form factors, thermal management becomes a more and more important element of electronic product design.

Both the performance reliability and life expectancy of electronic equipment are inversely related to the component temperature of the equipment. The relationship between the reliability and the operating temperature of a typical silicon semiconductor device shows that a reduction in the temperature corresponds to an exponential increase in the reliability and life expectancy of the device. Therefore, long life and reliable performance of a component may be achieved by effectively controlling the device

operating temperature within the limits set by the device design engineers. The developed MIBC employs SEMITRANS®3 SKM 200GAL125D Ultra Fast NPT IGBT Modules. Form the respective data sheet, the effect of temperature change on the output current and switching frequency is shown in Fig. 10.3. It is clearly appeared that for larger switching frequency, the maximum current is proportionally reduced. Meanwhile, the temperature reduction is increasing the current capability for high switching frequencies.

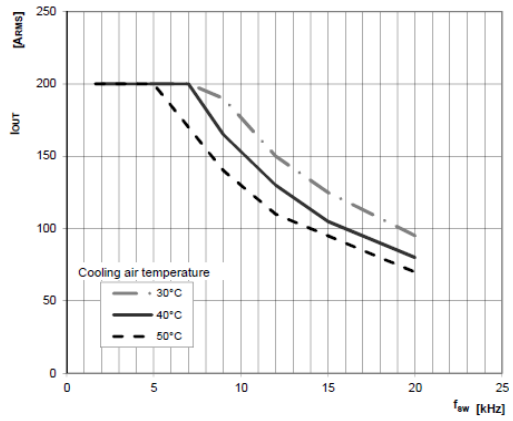

Fig. 10.3 Maximum output current versus switching frequency (during temperature change)

Figure 10.4 shows that the temperature is also related to the DC-bus voltage level which also limits the corresponding current value.

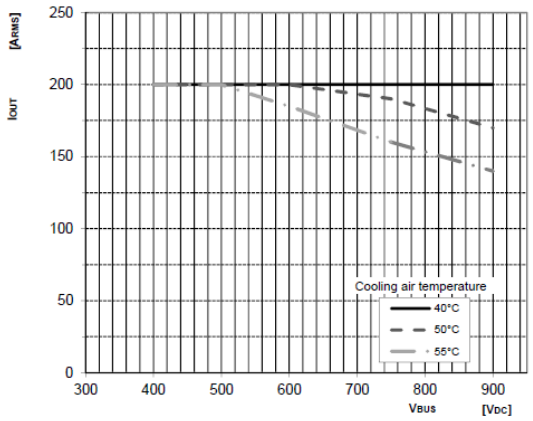

Fig. 10.4 Maximum output current versus DC-bus voltage (during temperature change)

Heat sinks are devices that enhance heat dissipation from a hot surface, usually the case of a heat generating component, to a cooler ambient, usually air.

For the following discussions, air is assumed to be the cooling fluid. In most situations, heat transfer across the interface between the solid surface and the coolant air is the least efficient within the system, and the solid-air interface represents the greatest barrier for heat dissipation. A heat sink lowers this barrier mainly by increasing the surface area that is in direct contact with the coolant. This allows more heat to be dissipated and/or lowers the device operating temperature.

The primary purpose of a heat sink is to maintain the device temperature below the maximum allowable temperature specified by the device manufacturer. The heat sink geometry is affecting the performance of the heat dissipation. Rectangular fins have better performance than square fins, whose back edges have poor air flow past them. Rectangular fins also have better performance than round fins; however, pressure drop is also higher for rectangular fins. Round fins are good if you don't know which direction your airflow will be from or if airflow may not be straight through the heat sink.

Longer fin heights mean increased surface area but with a fixed volumetric flow rate performance may actually decrease with fin height. Also, longer heat sinks in the direction of flow and more fins both mean increased surface area but both have adverse affects on pressure drops and flow bypass, and the average heat transfer coefficient goes down [177]. The developed MIBC uses P3/300B-Semikron rectangular Heat Sink, 135x125x300mm with axial fan, 119mm, 115VAC, 190mA as shown in Fig. 10.5. This design is considered for a maximum power rating of 10 kW continuous operation and 15 kW pulse operation.

For larger power ratings (maximum 72 kW), a larger rectangular poly heat sink (P16) with forced cooled radial fan that provide the thermal characteristics shown in Fig. 10.6. It can be noticed that for longer operation time, the power dissipation capability is reduced. For example, if the converter runs for short period of 5 seconds, then the power rating becomes large 1/0.005 (200 kW). Also, if the converter runs for long period of 600 seconds, then the power rating becomes smaller 1/0.02 (50 kW). It can be noticed that the curve reaches saturation level after 400 seconds.

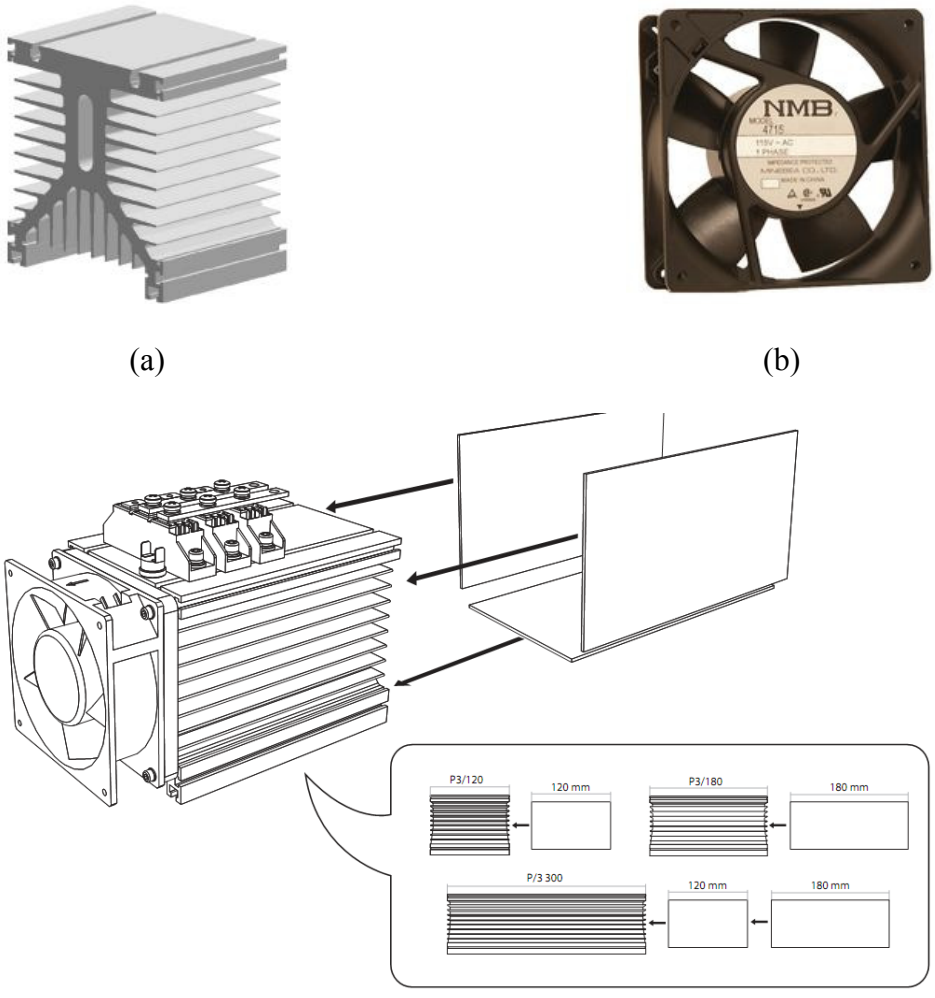

(a) (b)

(c)

Fig. 10.5 The photograph of the rectangular heat sink with axial fan employed in the developed MIBC: (a) Heat sink, (b) Fan and (c) Installation schematic

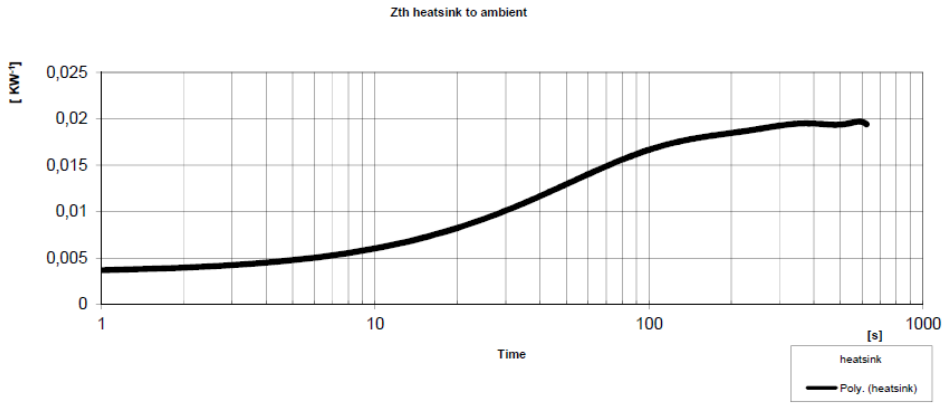

Fig. 10.6 The thermal characteristics of the P16 poly heat sink

10.6 MIBC Grid Connectivity

In this section, an experimental study is performed to confirm the practical validity of the developed MIBC for AC-grid connection through the grid-tied-inverter. This study is also implemented to verify the active-reactive power control capability through the developed VOC control algorithm that was previously discussed in Chapter 5. The MIBC output is connected as the inverter stage input while the DC-bus is representing a common connection point for supplying the DC-microgrid local loads as shown in Fig. 10.1. The filter design is directly affecting the power quality of the grid-connection operation. Accordingly, different inductor values are designed and its results are discussed. Three values are mounted (6, 12, and 24 mH) and each inductor is tested within 1-6 kW power range. A variable filter was designed by using two 12mH inductors and three switches as shown in Fig. 10.7. The detailed operation is explained in Table.10.2. The harmonic contents of the injected current are analyzed and compared in order to select the proper filter value. In addition, the active-reactive power flow control operation is investigated by applying different reference power values.

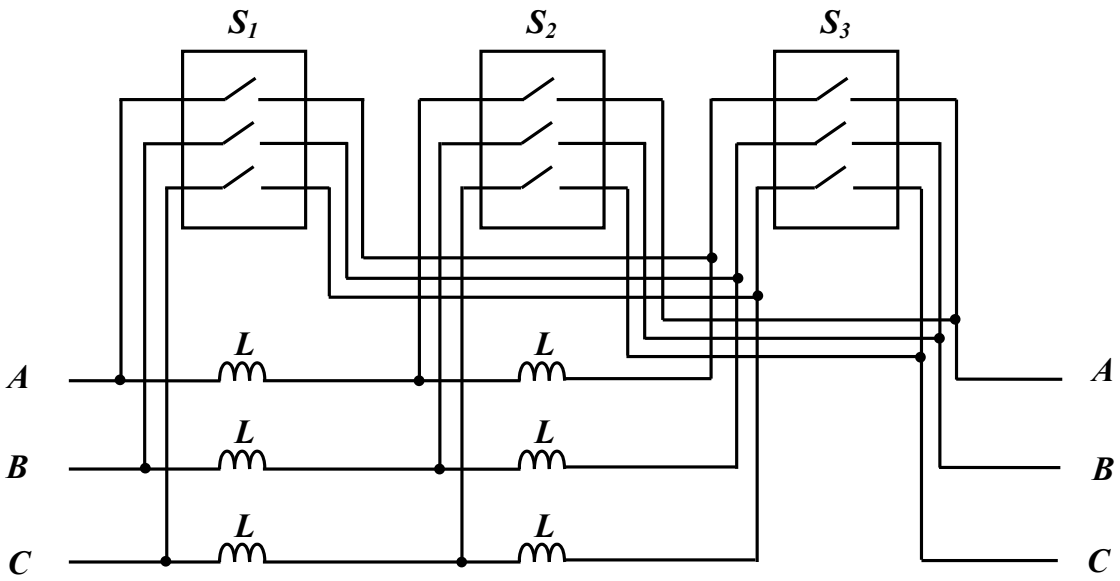

(a)

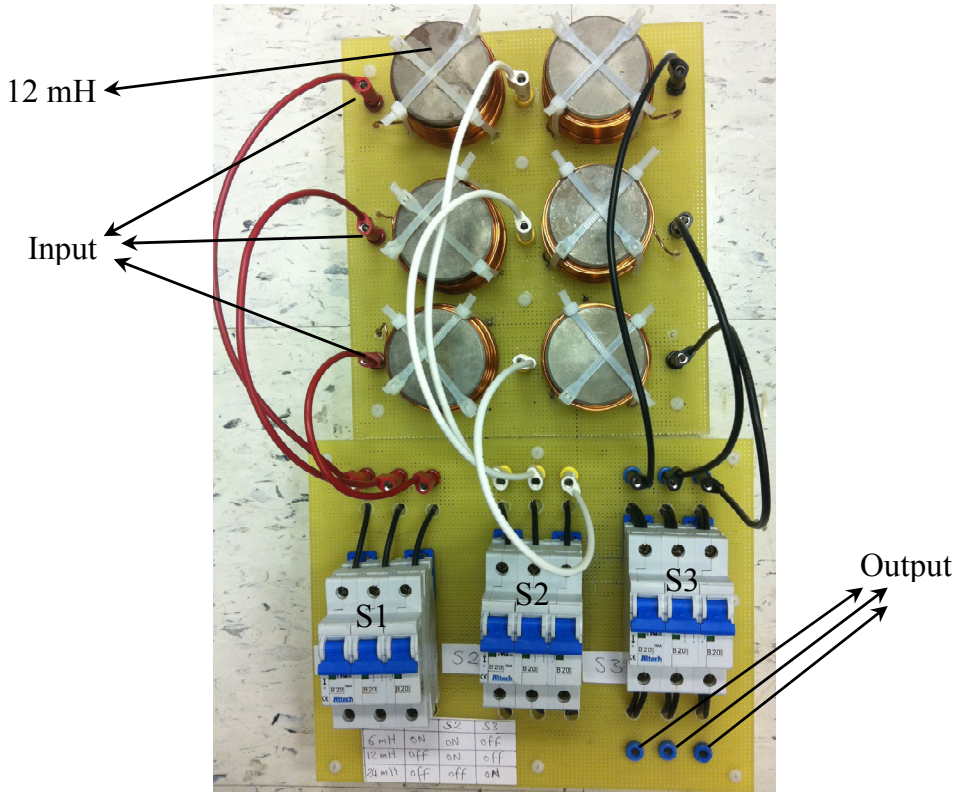

(b)

Fig. 10.7 The developed variable inductor filter design: (a) Schematic diagram and (b) Real hardware circuit.

Table 10.2 The three switching states for the variable filter

Inductance value	S_1	S_2	S_3
6 mH	ON	ON	OFF
12 mH	OFF	ON	OFF
24 mH	OFF	OFF	ON

10.6.1 6 mH Line Filter

This test is investigating the grid connection system performance with 6 mH inductor filter. According to Table 10.2, when S1, S2 are ON and S3 is OFF, then the parallel connection between the two 12 mH is achieved resulting a total of 6 mH inductance value as shown in Fig. 10.8. When S1, S3 are OFF and S2 is ON, then the connection gives a 12 mH inductance value as shown in Fig. 10.9. When S1, S2 are OFF and S3 is ON, then the series connection between the two 12 mH is achieved resulting a total of 24 mH inductance value as shown in Fig. 10.10. The experimental test results with 6 mH filter are shown in Figs. 10.11, 12. Figure 10.11 shows the injected active current with different reference active power from 1-6 kW. It can be noticed that the current appears to be in phase with grid voltage which means a pure active power injection with a unity power factor operation. It is also clearly appeared that the current increased proportionally with the reference required active power value. The harmonic spectrum analysis of the injected current is illustrated in Fig. 10.12. At low power of 1 kW, the current THD is 31.2% (large). However, at larger power of 6 kW, the current THD is 3.26% (low) which is accepted within the IEEE 929 standard that allows a limit of 5% with individual limits of 4% for each odd harmonic from 3^{rd} to 9th and 2% for 11^{th} to 15^{th}. We can notice that the harmonic distortion effect is decreased with larger power ranges.

10.6.2 12 mH Line Filter

This test is investigating the grid connection system performance with 12 mH inductor filter. The experimental test results with 12 mH filter are shown in Figs. 10.13, 14. Figure 10.13 shows the injected active current with different reference active power from 1-6 kW. The harmonic spectrum analysis of the injected current is illustrated in Fig. 10.14. At low power of 1 kW, the current THD is 21.8% (large) but less that the compared 6 mH inductor (31.2%) that was previously tested. However, at larger power of 5 kW, the current THD is 1.97% which is lower than the compared 6 mH (3.64 %) for the same power value. On the other hand, it can be noticed that the current did not increase when the reference power changed from 5 to 6 kW. The main reason is that at larger inductance values, the same sampling time is not sufficient to store the energy at larger current values. Accordingly, the controller failed to satisfy the required referenced power which limits the use of larger inductors at certain power ranges.

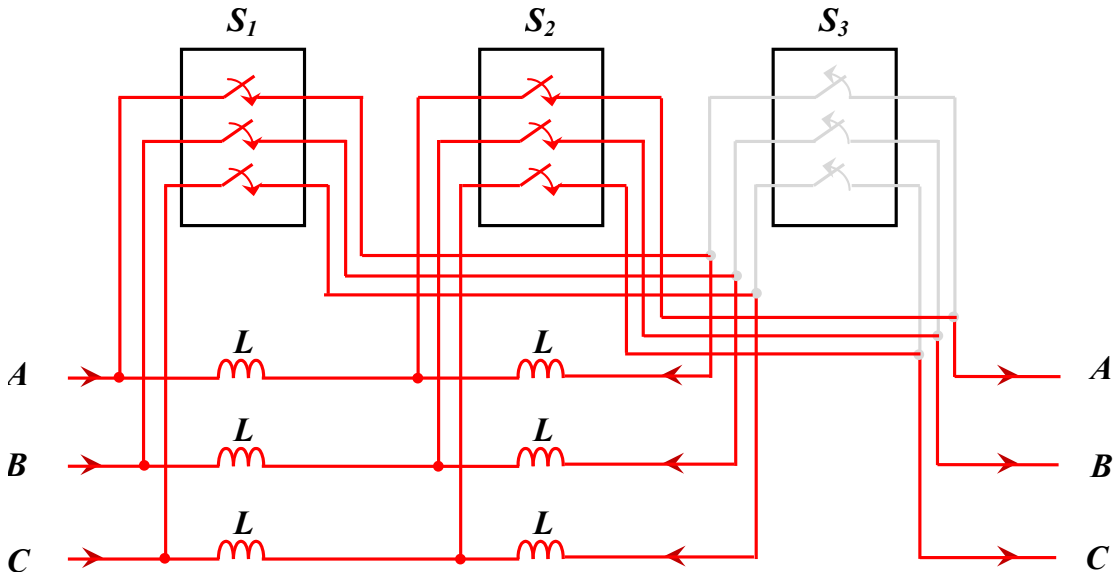

Fig. 10.8 The schematic diagram of the 6 mH line filter connection.

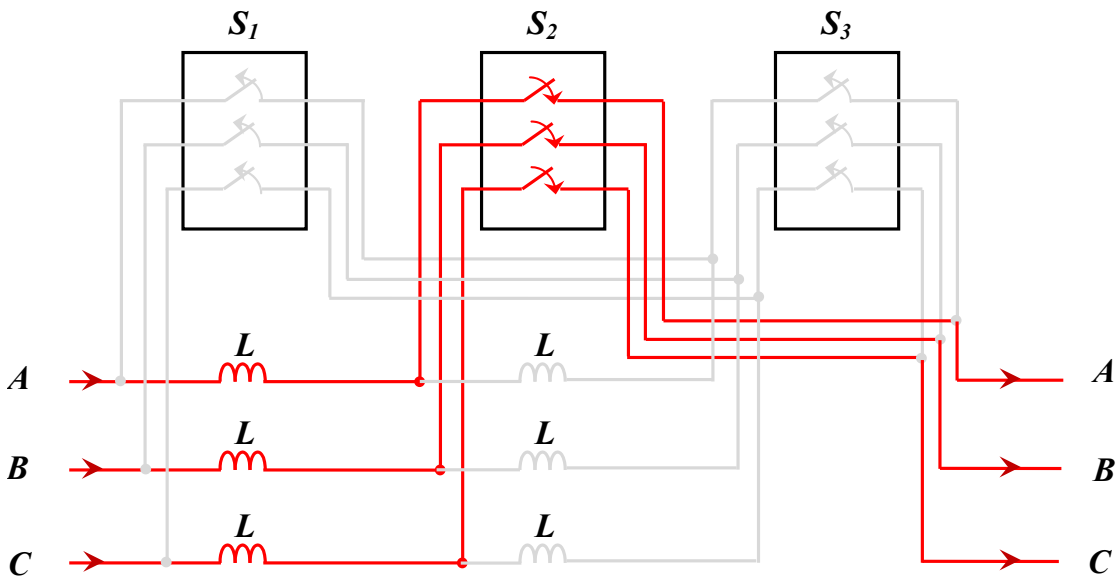

Fig. 10.9 The schematic diagram of the 12 mH line filter connection.

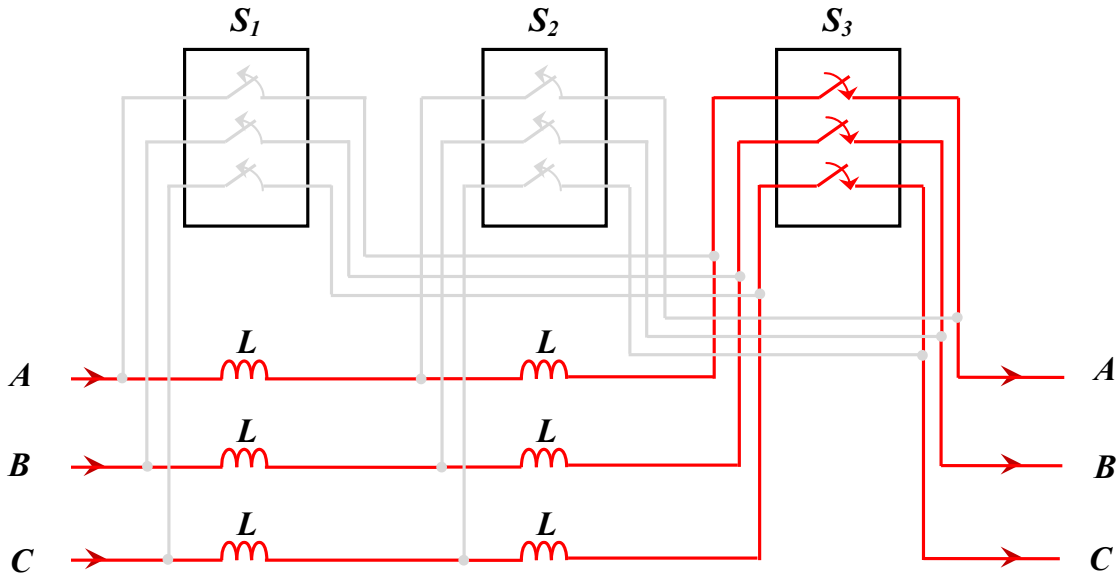

Fig. 10.10 The schematic diagram of the 24 mH line filter connection.

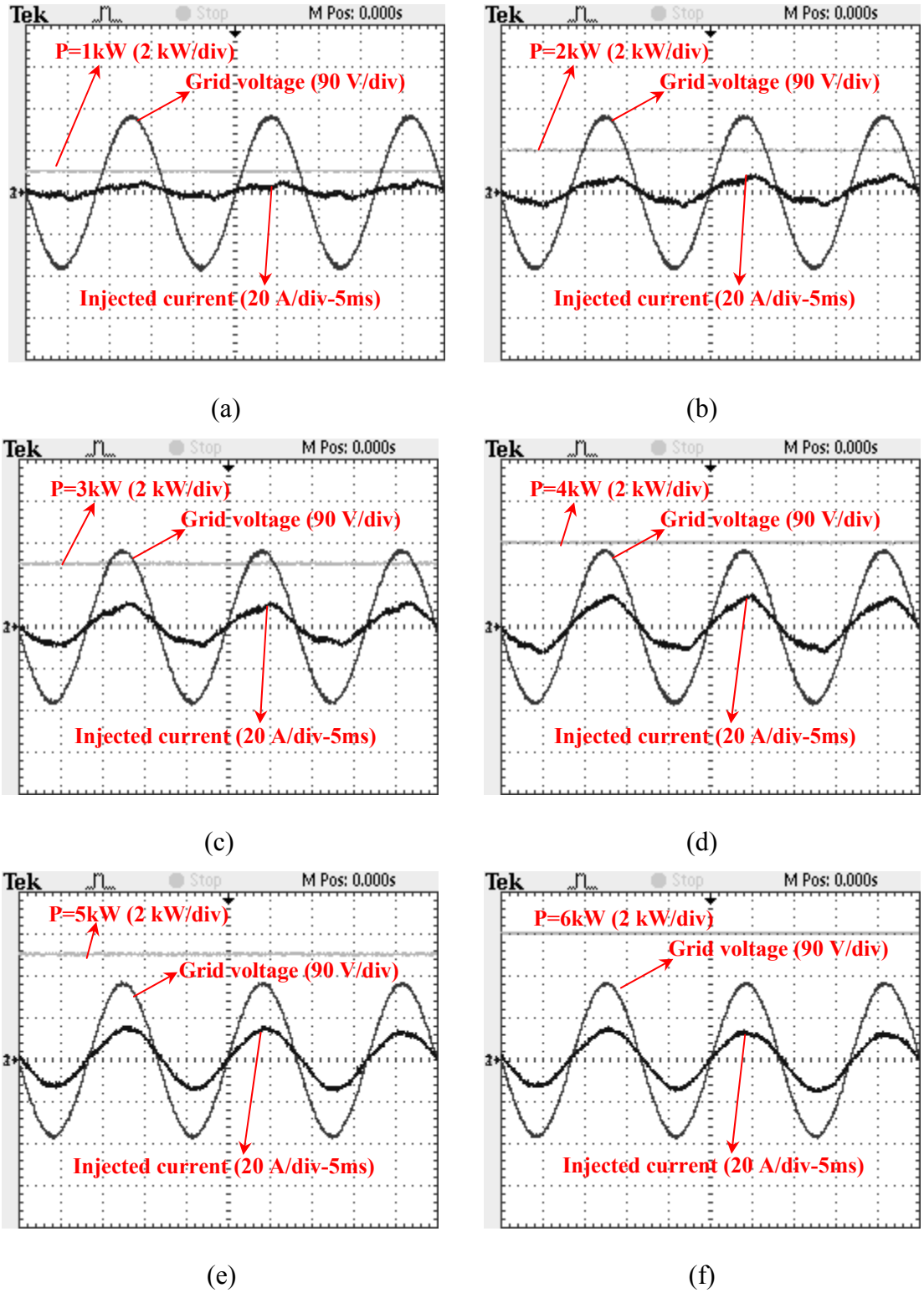

Fig. 10.11 The grid voltage (90 V/div-5 ms), the injected current (20 A/div-5ms), and the desired power (2 kW/div-5ms) with 6 mH: (a) 1 kW, (b) 2 kW, (c) 3 kW, (d) 4 kW, (e) 5 kW and (f) 6 kW.

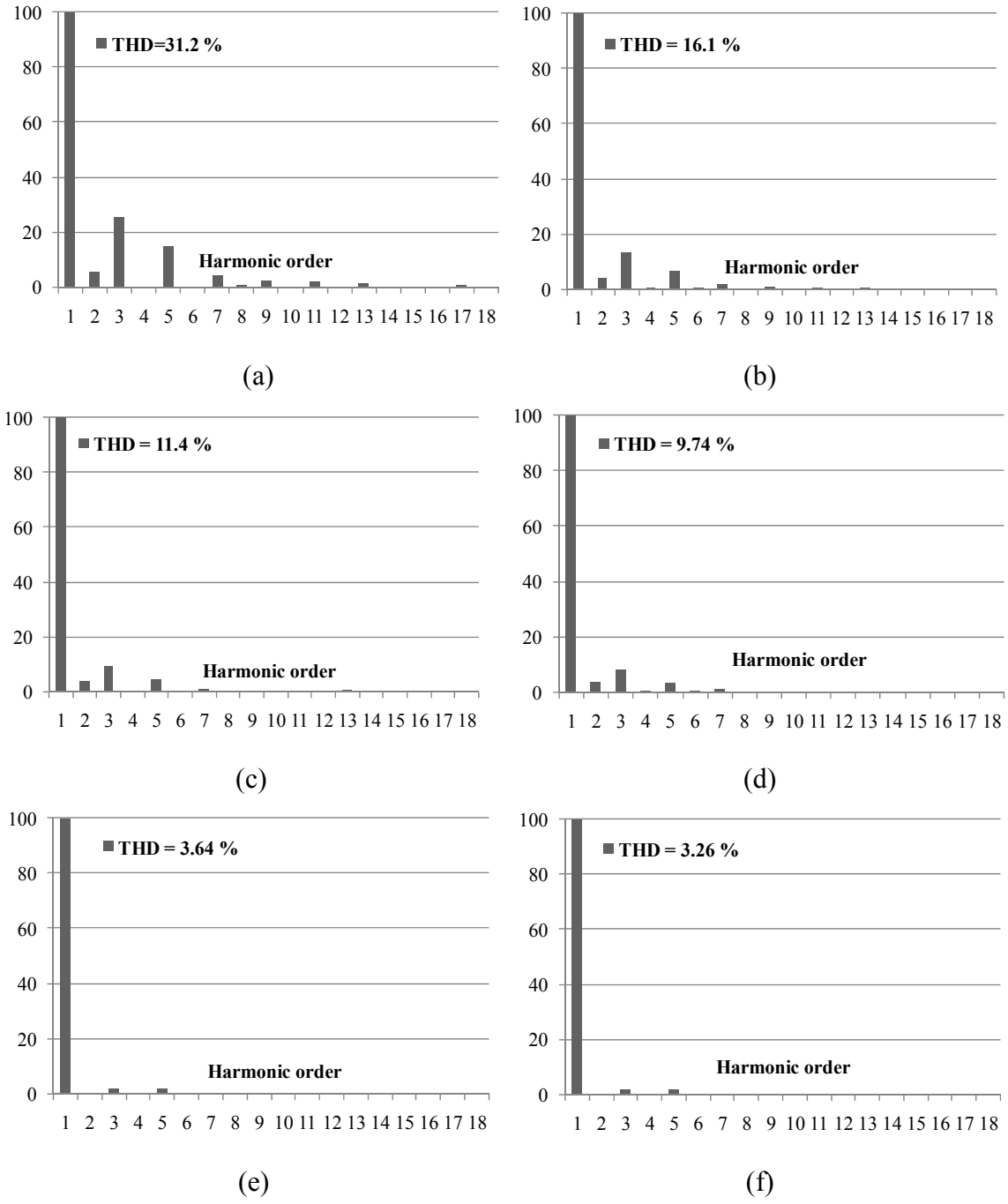

Fig. 10.12 The injected current harmonic spectrum analysis with 6 mH: (a) 1 kW, (b) 2 kW, (c) 3 kW, (d) 4 kW, (e) 5 kW and (f) 6 kW.

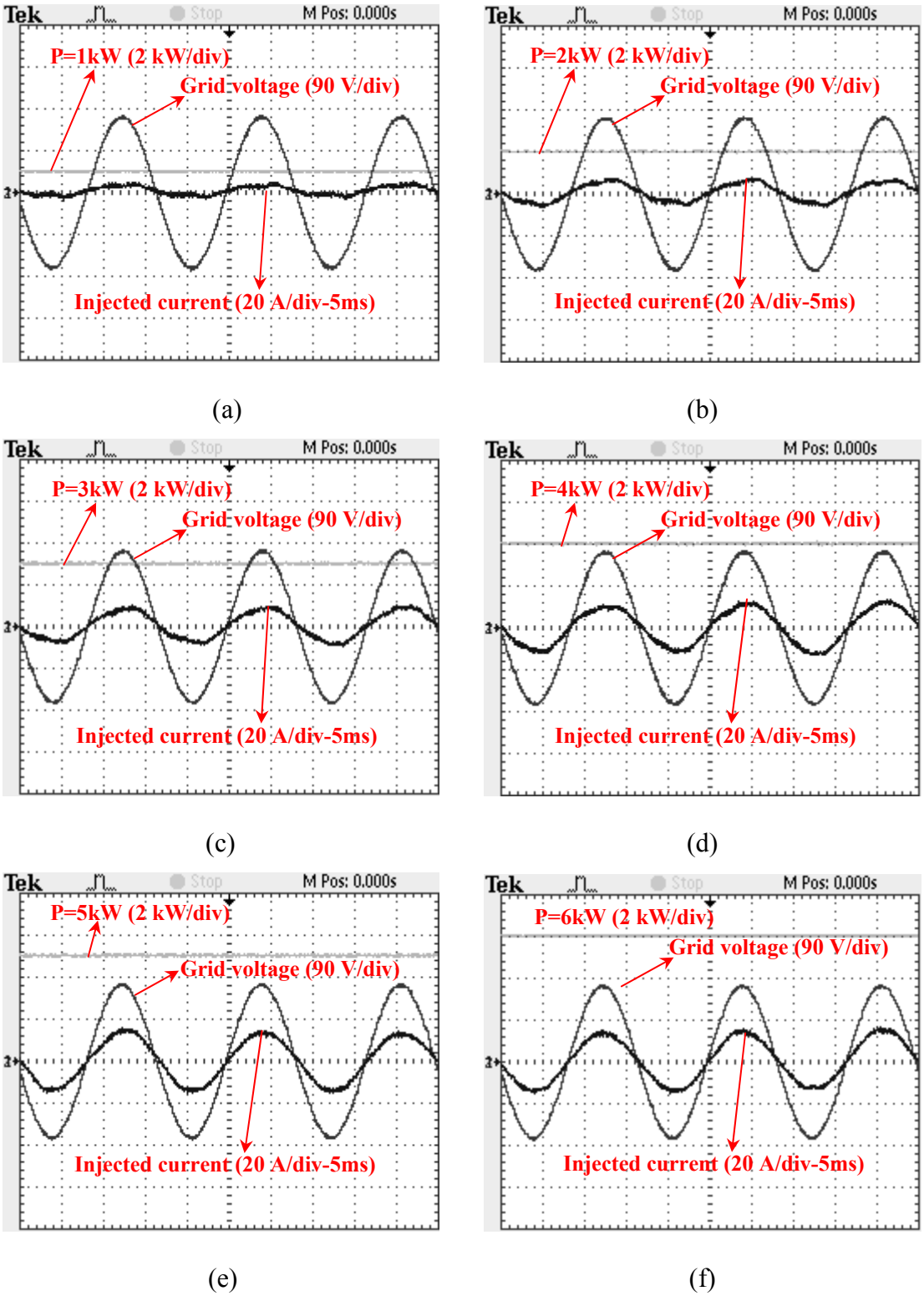

Fig. 10.13 The grid voltage (90 V/div-5 ms), the injected current (20 A/div-5ms), and the desired power (2 kW/div-5ms) with 12 mH: (a) 1 kW, (b) 2 kW, (c) 3 kW, (d) 4 kW, (e) 5 kW and (f) 6 kW.

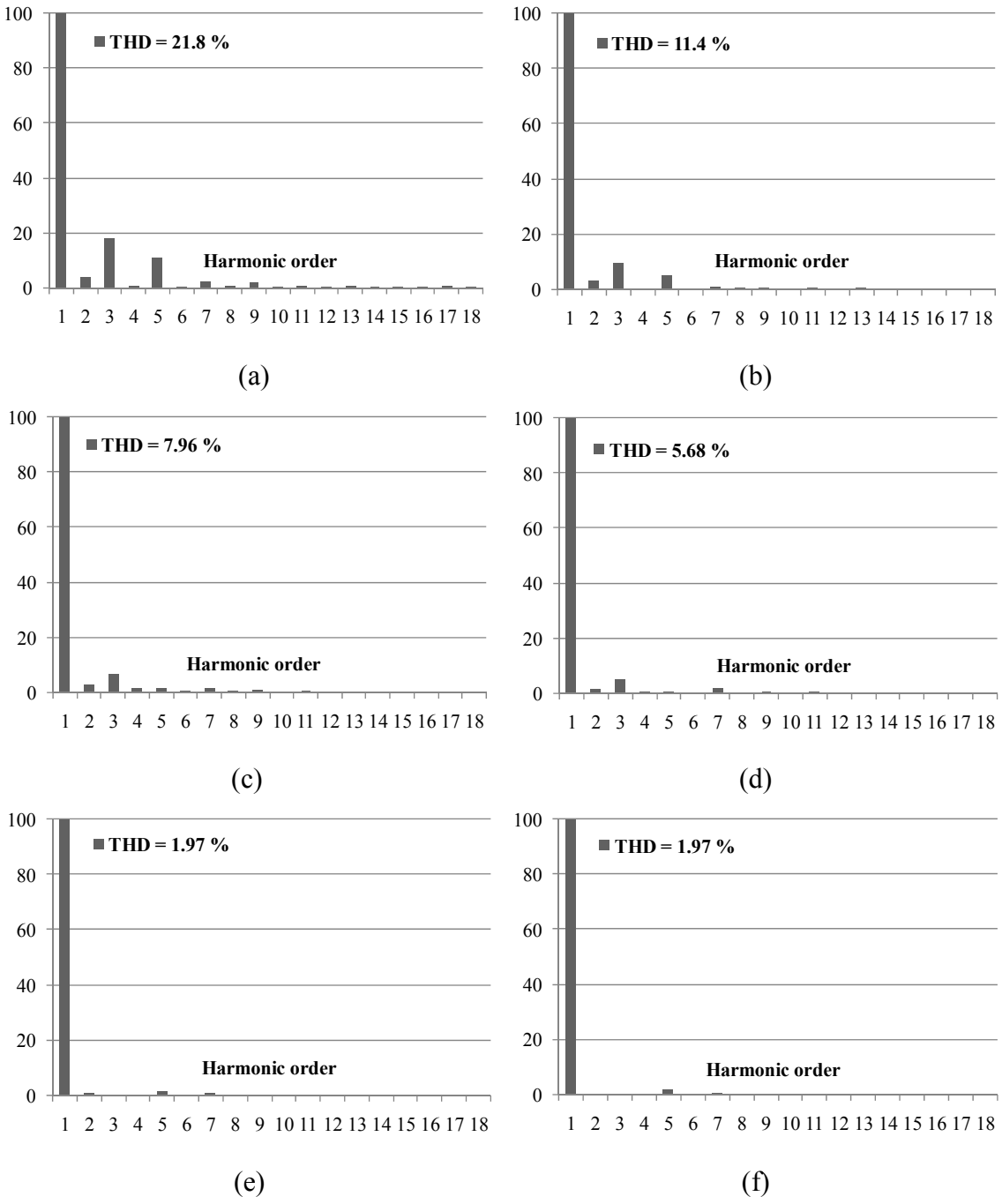

Fig. 10.14 The injected current harmonic spectrum analysis with 12 mH: (a) 1 kW, (b) 2 kW, (c) 3 kW, (d) 4 kW, (e) 5 kW and (f) 6 kW.

10.6.3 24 mH Line Filter

This test is investigating the grid connection system performance with 24 mH inductor filter. The experimental test results with 24 mH filter are shown in Figs. 10.15,

16. Figure 10.15 shows the injected active current with different reference active power from 1-6 kW. The harmonic spectrum analysis of the injected current is illustrated in Fig. 10.16. At low power of 1 kW, the current THD is 12.3% (large) but less than the other compared 6 mH (31.2%) and 12 mH (21.8%) inductors that were previously tested. However, at larger power of 2 kW, the current THD is 5.93% which is lower than the other compared 6 mH (16.1 %) and 12 mH (11.4%) for the same power value. For 3 kW, the 24 mH gives a very low harmonic distortion of 1.36 % compared to the 6 mH (11.4%) and the 12 mH (7.96%). On the other hand, it can be noticed that the current did not increase when the reference power changed from 4 to 6 kW for the same reason that was previously mentioned in section 10.6.2. Accordingly, the controller failed to satisfy the required referenced power which limits the use of larger inductors at certain power ranges. Table 10.3 shows the total values resulted from the comparison between all the three filters. We can conclude that the large filter value (24 mH) is feasible for small power range (1-2.5 kW) while smaller filter values (12 mH) are recommended for larger power range (3-5 kW). Meanwhile, the 6 mH is feasible for power ≥ 5 kW.

Table 10.3 The comparative test results for the grid line filter

Filter value / Reference power	%THD		
	6 mH	**12 mH**	**24 mH**
1 kW	31.2	21.8	12.3
2 kW	16.1	11.4	**5.93**
3 kW	11.4	7.96	**1.36**
4 kW	9.74	**5.68**	1.24
5 kW	**3.64**	**1.97**	1.2
6 kW	**3.26**	1.97	1.01

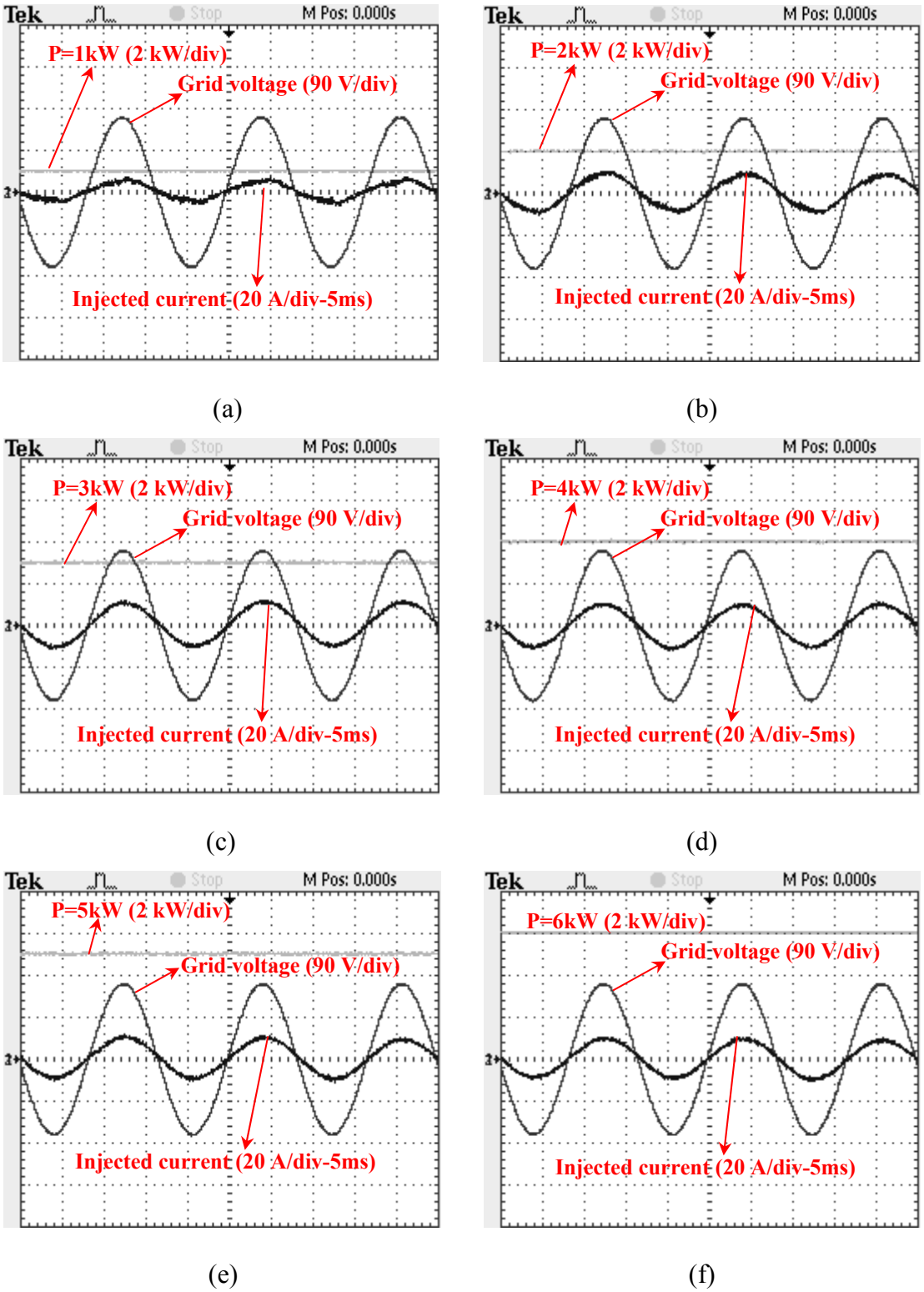

Fig. 10.15 The grid voltage (90 V/div-5 ms), the injected current (20 A/div-5ms), and the desired power (2 kW/div-5ms) with 24 mH: (a) 1 kW, (b) 2 kW, (c) 3 kW, (d) 4 kW, (e) 5 kW and (f) 6 kW.

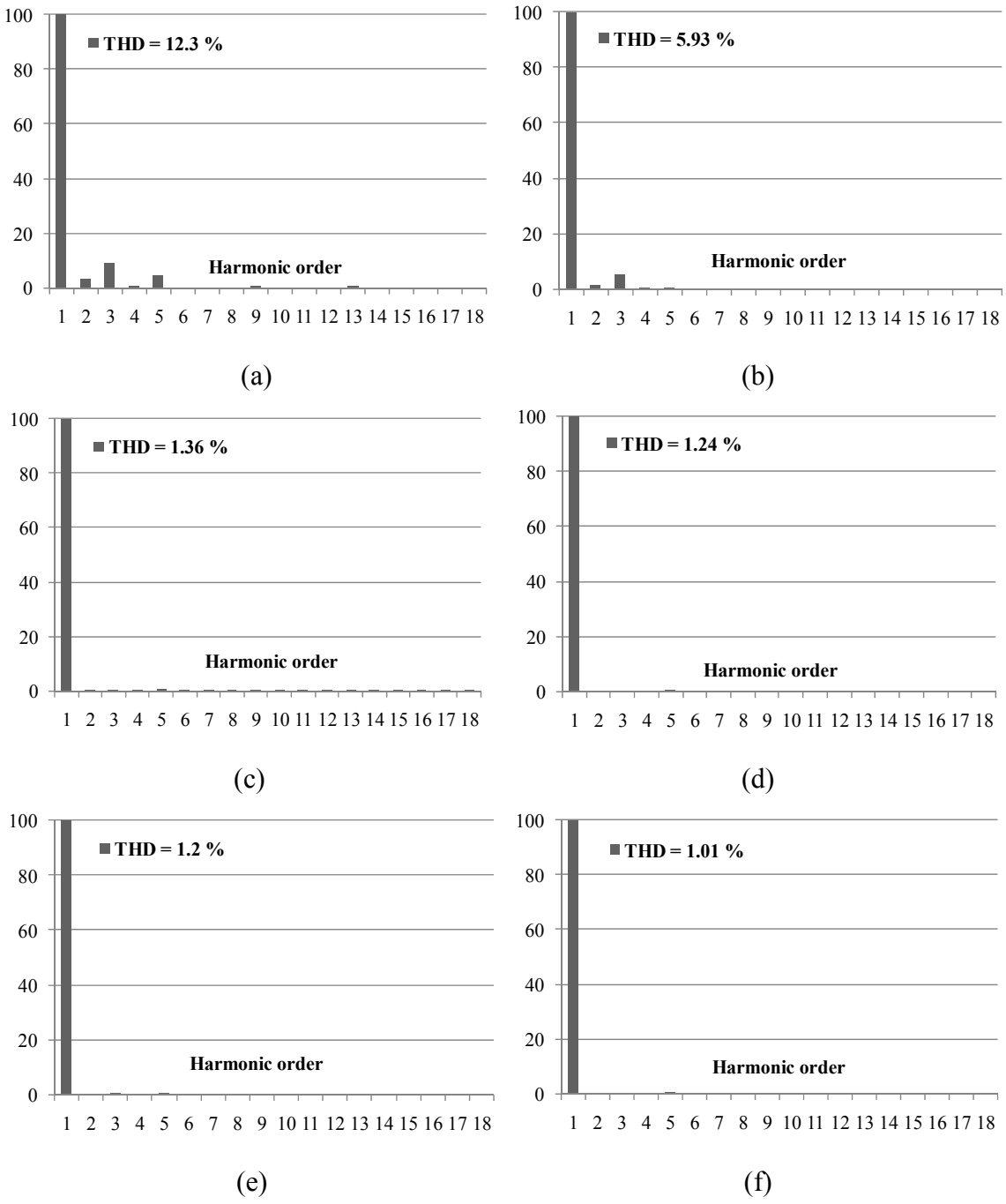

Fig. 10.16 The injected current harmonic spectrum analysis with 24 mH: (a) 1 kW, (b) 2 kW, (c) 3 kW, (d) 4 kW, (e) 5 kW and (f) 6 kW.

10.6.4 Active-Reactive Power Injection Capability with MIBC

An inverter grid-tie system has been designed to verify the effectiveness of the MIBC injection capability for AC-power into the grid. The inverter has been tested under

various power factor and command step conditions with 12 mH grid filter. The switching frequency of the devices is set to be 3 kHz. If more inverter units are connected in cascade while adopting the phase-shifted PWM control, the equivalent switching frequency of the inverter is 6 kHz for two-unit and 9 kHz for three-unit cascade inverters, respectively. With more cascade units, the equivalent switching frequency will be higher, which leads to less output current ripple and possibility of smaller passive filter component selections. On the other hand, the system efficiency will suffer if the switching frequency is set too high because this topology is still hard switching [178].

The grid voltage is 120V, 60 Hz. The system controller and PWM generation are conducted by DS1103 PPC Controller Board. The passive filter components are selected as: L = 12 mH. Figure 10.17 shows the grid-tie inverter control under pure active power, pure leading and lagging reactive power conditions. The output is 5 kW active power (0^o), 2.5 kVar lag reactive power (-90^o), or 5 kVar lead reactive power (90^o).

Figure 10.18 shows the grid-tie inverter control with equal active power and reactive power command. The active power is 3 kW with either lagging (1.5 kVar) or leading reactive power (3 kVar).

Figure 10.19 shows the grid-tie inverter control with active power command and reactive power command step changes. The experimental results proved that the control system has fast dynamics and good stability. The active power step change test was made from 3 to 5 kW as shown in Fig. 10.19a. The lead reactive power step change test was made from 2 to 4 kVar as shown in Fig. 10.19b. It can be noticed that the current is quickly responding to this severe condition within one cycle (millisecond) which indicates the control system robustness.

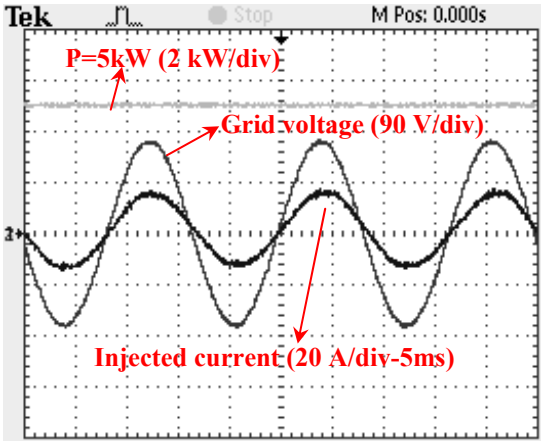

(a)

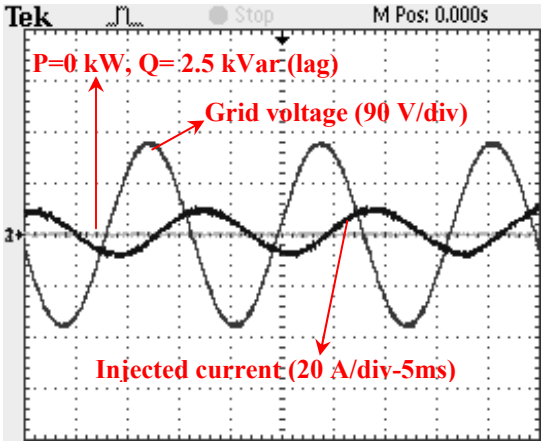

(b)

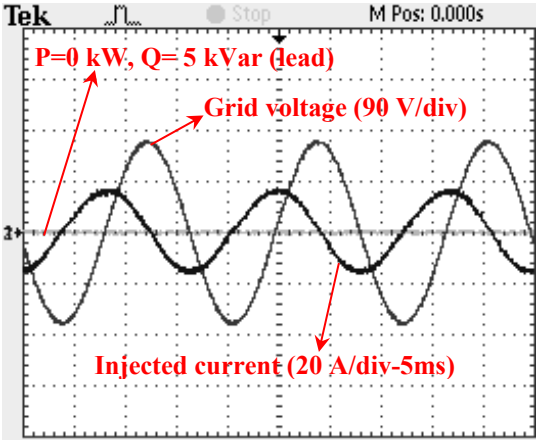

(c)

Fig. 10.17 The test results for the pure active-reactive power injection: (a) 5 kW active, (b) 2.5 kVar lag reactive, and (c) 5 kVar lead reactive powers.

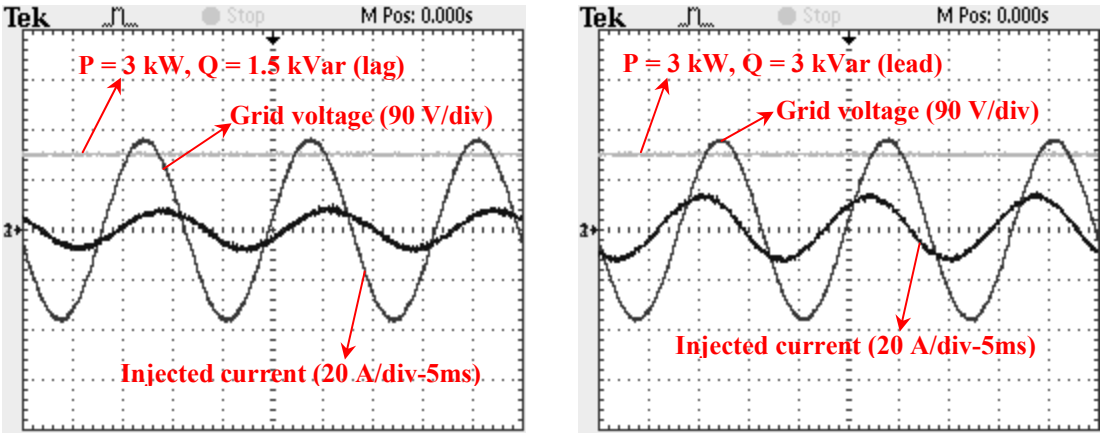

(a) (b)

Fig. 10.18 The test results for the hybrid active-reactive power injection: (a) 3 kW active with 1.5 kVar lag reactive powers and (b) 3 kW active with 3 kVar lead reactive powers.

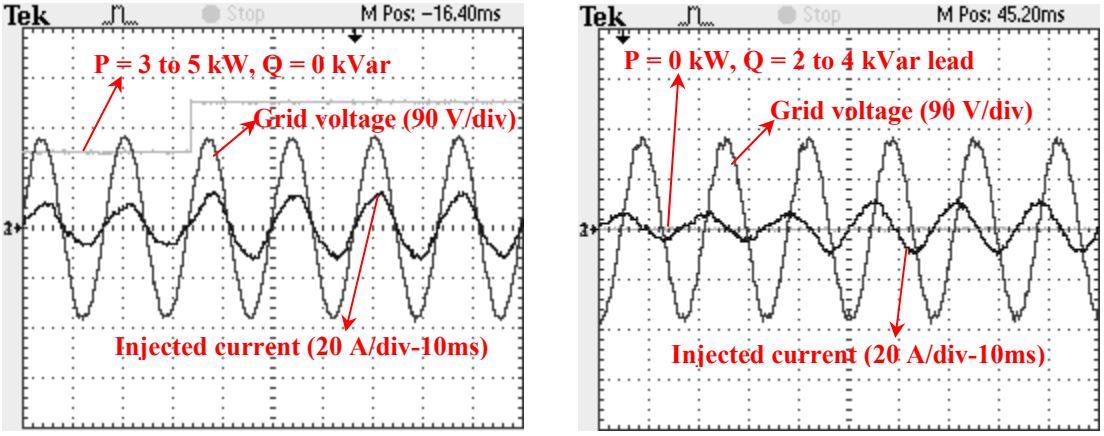

(a) (b)

Fig. 10.19 The test results for the step change active-reactive power injection: (a) 3 to 5 kWactive power and (b) 2 to 4 kVar lead reactive power.

10.7 Conclusion

HFPCS successful pilot test proved that its new power converter technology improved the efficiency as well as the power density by reducing the weight and size of converters. The MIBC converter will improve the direct cost, indirect cost, efficiency and

reliability of commercial-scale hybrid systems. The isolated gate drive with fault monitoring and protection confirmed its interface ability with any peripheral controller.

Moreover, MIBC verified the multi-access input comprehensive connectivity which enables the power interface to hybrid sources through one converter. Also, MIBC included the power circuit, measurements board, filter circuit, and interface circuit all imbedded inside the converter which leads to its compact design. The forced air cooling capability gave more protection to the developed converter against high temperature rise which can easily damage the switching semiconductor devices. Additionally, the thermal protection is added to the design to detect the over temperature case and run the fan according to the thermal sensor setting value. The snubber circuit was designed and connected to the switching elements in order to protect it against the fast overvoltage/overcurrent excessive operation.

The grid-tie control of inverter operation for MIBC system was presented and discussed. The control system ensures wide-range power flow capability, from pure active power to pure reactive power delivery. Detailed analysis and design of the grid filter were conducted for inverter system. The VOC compensation controller was incorporated into the control loop to achieve better dynamic and steady-state performances. It was confirmed that smaller inductance value is feasible for larger power ranges while larger inductance value is recommended for smaller power ratings. A 6 kVA inverter grid-tie system was built and tested to verify the developed control operation. Wide-range power flow experimental results proved the feasibility and effectiveness of the designed control system.

This technology can be applicable to other clean energy infrastructure markets, including microgrids, utility-scale converters, plug-in hybrid electric vehicles (PHEVs), and adjustable speed drives (ASDs). The basic rules for scaling-up the developed MIBC for larger power rating operation were discussed.

Chapter 11 Implementation in a Wide Area Measurement System for Smart Grid Involving Hybrid Energy Sources: An Application Study

11.1 Introduction

Wide area measurement system (WAMS) became one of the most recent technologies that are quite popular for upgrading the traditional electric grid. This upgrade has become a necessity to modernize the electricity delivery system following the occurrence of major blackouts in power systems around the world. Although many algorithms were developed in the past for online monitoring of transmission and distribution systems including the estimation of operating frequency, the required level of details for real-time online assessment is yet to be achieved [146-148]. In the early 1980s, synchronized phasor measurement units (PMUs) were first introduced and since have become the ultimate data acquisition technology, which will be used in wide area measurement systems with many applications currently under development around the world [149].

Synchronized phasor measurements, or synchrophasors, provide a method for comparing the phase and sequence values from anywhere on a power system which can be integrated with phasor data concentrators (PDCs) at substations in a hierarchical structure [150, 151].

The precise and accurate data that can be acquired from PMUs in a WAMS built on the power system confirms the need for a robust, reliable communication network with secure and high speed capabilities for online data access. As smart grid applications, utility power grid analysts can benefit from WAMS in the validation of system models and components which was one of the first uses of synchrophasors. This validation occurs through the use of inter-area communication or simultaneous data collection of conditions at a single point in time [152].

In addition, real-time system monitoring (RTSM) for stability assessment and state measurement is another application where phasor measurements at nodes help the system operators to gain a dynamic view of the power system and initiate the necessary measures at the proper time. This is done in accordance with the latest IEEE standard (C37.118-2005) developed to standardize data transmission format and sampling rates of PMUs. This can significantly be supported by the stability assessment algorithms, which are designed to take advantage of the phasor measurement information [153].

In the past, post-event analysis was an application of synchrophasors (PMUs) without wide-area communication where data was archived locally. However, it was not a useful tool for online (dynamic) control. Recently, real-time control (RTC) of WAMS became a powerful control and analysis tool which provides a new view of power systems [154]. This is achieved by improving the communication network capabilities while maintaining

PMUs as a main component in the network. The use of PMUs for RTC will increase the control accuracy since the data are measured online. Also, it will enhance the power system stability and delivery automation capabilities after challenges of new data communication requirements across the system are firstly resolved [155-156]. The depth of observability is another advantage for PMUs. It means that the ability of measuring the bus voltage phasor directly or calculating it using the PMU voltage and line current of the nearest connected bus. This is the cost effective part since it reduces the number of data acquisition instruments and tools needed across the network as the measuring line currents can extend the voltage measurements to buses where no PMU is installed. In Fig. 9.1, a simple generalization of the PMU block diagram is shown. This serves as the basis of simulating such unit [157, 158].

In this chapter, the developed WAMS network is studied and discussed to utilize this type of data collection to check the health state of hybrid power system networks. The purpose is to increase the overall system reliability for all power stages via significant dependence on WAMS as distributed intelligence agents with improved monitoring, protection, and control capabilities of the power networks [159]. This is achieved through building WAMS infrastructure communication network. The performance of the overall developed system is investigated through a Matlab simulation of the PMUs in a small system scenario of a WAMS network based on a 6-bus power utility network along with the associated communication network. Such a system is shown in Fig. 9.2. Moreover, the developed WAMS power network was experimentally built in the laboratory in order to dynamically interact (online) with the PMUs readings. The PMU functions were

programmed in the Matlab/Simulink environment based on the Hardware-in-The loop (HIL) concept.

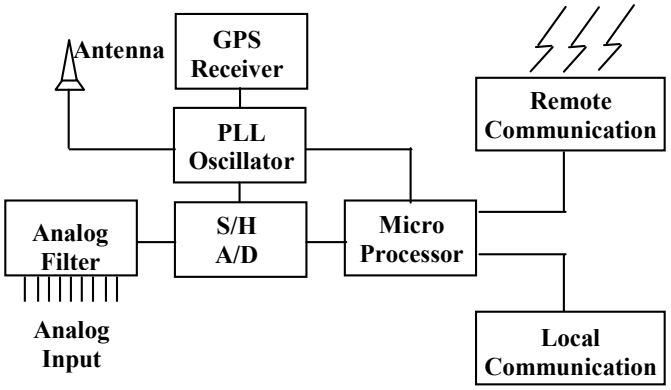

Fig. 11.1 The block diagram of PMU

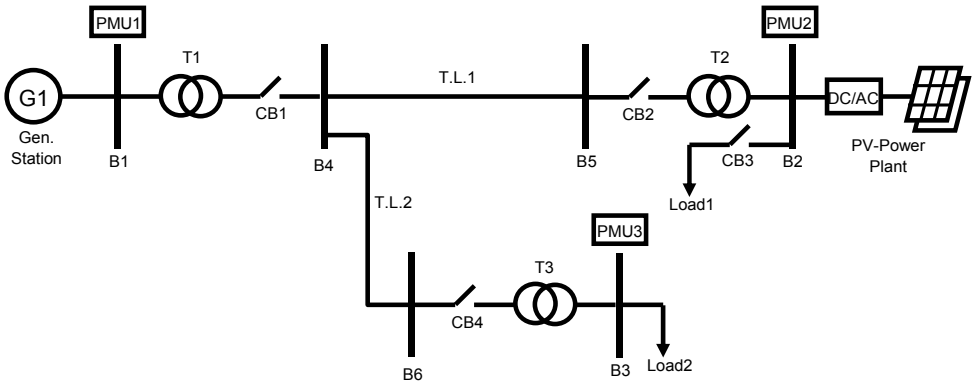

Fig. 11.2 Single-line diagram of the developed hybrid AC/DC network

11.2 WAMS System Description

The principle of a WAMS network based on synchrophasors data with the aid of a broadband communication network is described in this section. The system consists mainly of two layers as shown in Fig. 11.3. First, the electrical power system layer, which consists of line-line 208V generating station with 50-kW output rated power, a PV-power renewable source of 24-kW rated power, 3-power transformers (T1, T2, and T3) linking the different parts of the electrical system, 2-short transmission lines (T.L.1 and T.L.2), 6-buses (B1-B6), 4- circuit breakers (CB1, CB2, CB3, and CB4) and 2-loads each of 30-

kW. Secondly, the WAMS layer which consists of 3-PMUs, located at generation and load buses, and one phasor data concentrator (1-PDC) which collects the data received from the remote PMUs. The PDC performs protocol conversion from IEEE C37.118 to a number of common power system protocols suitable for analysis and control actions in the control center.

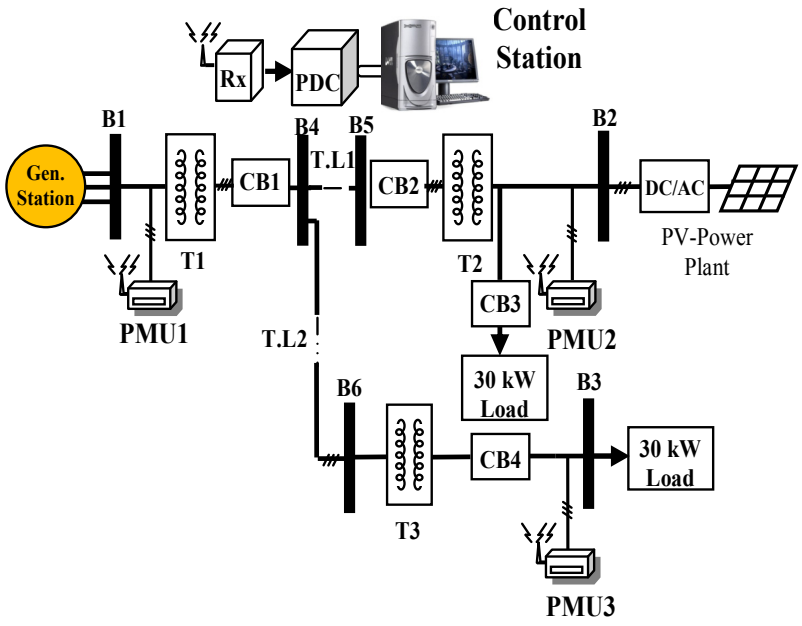

Fig. 11.3 Schematic diagram of the developed WAMS involving the PV-sustainable power plant

11.3 WAMS Mathematical Modeling

A small size WAMS platform was designed and built on a 208-V, 60-Hz test-bed network that was modeled as shown in Fig. 11.4. This developed communication network was implemented in the lab by locating one PMU at each generation or load bus. All PMUs will send their measured voltage and current measurements to the PDC to monitor the system status and take the proper control action if required. Furthermore, the depth of observability can be utilized here to significantly reduce the system costs through the reduction of the number of PMUs. This is, since one PMU can read the voltage and

current measurements at its bus location with other bus measurements, located in same area, can be calculated. However, this algorithm has less accuracy than installing one PMU at each bus. A simulation of the PMU units was done with using the sampling clock pulses to achieve synchronization between the synchrophasors which are phase locked to the signal provided by the global positioning system (GPS) receiver built inside or outside the PMU. The GPS module is simulated as a clock enabling pulses sent to all PMUs at the same time so that all of them will have the same time tags. Accordingly, the same reference wave can be used at all different PMU locations through the WAMS.

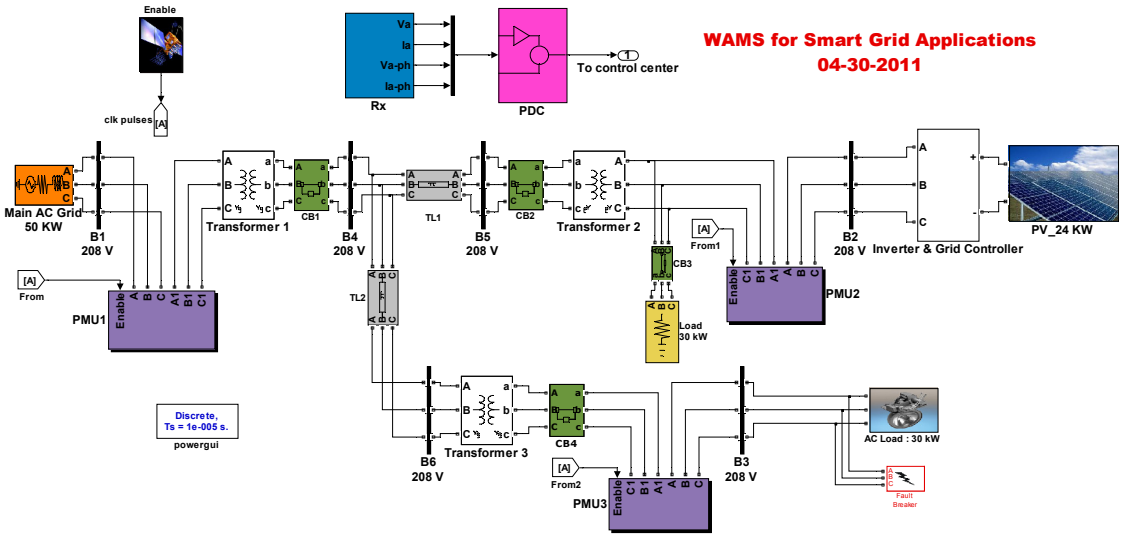

Fig. 11.4 Simulink model for a scenario of the developed PMUs communication network layer on a hybrid AC/DC power system smart grid

11.3.1 PMU Network Analysis

The PMU must separate the fundamental frequency component from other harmonics and find its phasor representation. The Discrete Fourier transform (DFT) method is then applied on the sampled input signal to compute its phasor. Also, it should compensate for the phase delay introduced to the signal by the antialiasing filters present in the input to

the PMU. For $x_k\{k = 0,1,\cdots,N\}$ where N is the number of samples taken over one period, the phasor representation is given by:

$$X = \frac{\sqrt{2}}{N}\sum_{K=0}^{N-1} x_k \varepsilon^{-jk\frac{2\pi}{N}} \tag{11-1}$$

Since the components for the real input signals at a given frequency appears in DFT and are complex conjugates of each other, they can be combined giving the factor of 2 in front of the summation in (11-1). The rms value of the fundamental frequency is obtained by dividing the peak value by $\sqrt{2}$. In steady state, all generators have the same frequency (f_{ss} Hz). Accordingly, the voltage at all points in the power system will have the same frequency f_{ss} which is measured by the PMU through to the following equation:

$$e_i(t) = E_i \cos(2\pi f_{ss} + \delta_i) \tag{11-2}$$

In case of frequency disturbance, the power system generators will run at different frequencies and each generator may be considered as a voltage source with different values of E_i, f_{ss} and δ_i as slow time varying functions. It can be assumed that for a small time interval ($\Delta t = n\ cycles$), the E_i, f_{ss} and δ_i are constants. As a result, the power system can be represented as a circuit with several voltage sources of different frequencies. The actual voltage at any bus *i* using superposition becomes as follows [160]:

$$v_i^{act} = v_{i,1}(t) + \cdots + v_{i,N_G}(t) = \sum_{j=1}^{N_G} v_{i,j}(t) = \sum_{j=1}^{N_G} V_{i,j} \cos(2\pi f_{N_G} t + \theta_{i,N_G}) \tag{11-3}$$

Where $V_{i,j}$ represents the voltage at bus *i* due to generator *j*. This indicates that this bus will have a multi frequency voltage that is close to 60 Hz. In dynamic power system studies, this can be estimated as:

$$v_i^{est}(t) = V_i^{est} \cos(2\pi f_i^{est} t + \theta_i^{est}) \tag{11-4}$$

In equation (11-4), the frequency f_i^{est} represents the frequency of the system at this location. It equals the frequency measured by the PMU at that bus. This is done by assuming that $v_i^{est}(t) = v_i^{act}(t)$ and having access to the sampled data of $v_i^{act}(t)$; so f_i^{est} can be easily evaluated [161].

11.3.2 Communication Channel Analysis

The IEEE PC37.118 16 protocol format is usually used in PMUs' communication. This standard format includes the frequency and the rate of change of frequency in each message. Once the frequency and size of the messages are known, the following equation can be used to determine the bit-per-second (bps) rate at which the data can be sent [162]:

$$bps = 1.2(nn \cdot L \cdot f) \tag{11-5}$$

Where *nn* is the message size (bytes), *L* is the frame length (1 start bit, 8 data bits, 2 stop bits, 1 parity=12), *f* is the messages frequency, 1.2 is a factor to account for system delays (based on typical experience). The PMU data can be sent at various rates, depending on the application requirements. Most PMUs have Ethernet cards that use the IEEE PC37.118 16 protocol for data exchange on the physical layer. The physical layer of the Ethernet can be unshielded twisted pair (UTP) or fiber optical network that support data speeds up to 100 Mbit/s in each data stream. The communications link connecting the

substations could be a fiber-optic multiplexer. The relays communicate with the multiplexer via EIA-232 asynchronous interface.

11.3.3 The Communication System Constraints

Communication networks suitable for smart grid applications—even in a loose sense—need to provide distinct qualities and services which are closely related to application requirements and distinguish them from other networks [163]:

- High reliability and availability are standard requirements for nearly every communication system; Nodes should be reachable under all circumstances. While this is normally not a problem in a wired network, it may be challenging for wireless or power line infrastructures because communication channels can change during operation. In the particular case of power line systems, such a change may be introduced by distribution network management which balances the power consumption load on the power grid, particularly on the medium-voltage (MV) level. Switching actions are initiated via various supervisory control and data acquisition (SCADA) and controlling systems (or even manually) using specific communication protocols that may not be modified.
- High coverage and distances. Evidently; the nodes to be connected by the communication network are distributed in a wide area. Network concepts based on telecommunication systems or power lines have the potential to fulfill this requirement.
- Large number of communication nodes; If we assume that only one energy meter per customer is connected, a primary station can supply up to tens of thousands of nodes, particularly in areas of large apartment block concentration. Even though

the commands and data packets are usually short, total data volume to be transferred in the network is substantial, and communication overheads can become an issue.

- Appropriate communication delay and system responsiveness; The Quality-of-Service (QoS) needs to take care of different data classes such as metering, control, or alarm data. Even if the predominant communication relationship is client/server (i.e., an application server polls the meter data or issues control commands), it may be necessary to foresee something like a fast event channel to transmit.
- Communication security; Data related to smart grid applications are considered critical, in particular, when they are relevant for billing purposes or grid control. Secure communication is therefore important. Surveys among utilities showed that integrity (no malicious modification) and authenticity (origin and access rights are guaranteed) are the most important security goals for energy transmission and distribution networks, whereas the confidentiality aspect is not considered to be an issue.
- Ease of deployment and maintenance. For any distributed communication system, mechanisms must be foreseen which facilitate not only the initial installation but particularly the maintenance of the infrastructure during the operation. Features like error mode analysis and error localization, easy update of firm- and software and remote configuration are essential.

11.4 Simulation and Experimental Results

A Matlab Simulink model was constructed to investigate the performance of the developed WAMS for smart grid applications. The model was carried out according to the operation described in section 11.2. The simulation parameters are shown in Table 11.1. Furthermore, a reduced scale experimental setup of 6 kW (4:1 scale) programmable power supply was utilized as a PV-characteristics emulator connected to AC-grid network. The setup was designed and implemented in the laboratory to verify the obtained simulation results. The experimental verification is based on HIL concept utilizing real-time DSP controller. The dSPACE1104 R&D TMS320F240 DSP controller board was used for interfacing the simulated PMUs with the hardware circuit to achieve fast real time response during the transient and steady state operations. An LEM (LA 25-NP) current and voltage (LV 25-P) transducers were used for measuring the actual power network bus-signals. The required measuring and interface circuits were designed and built. All the measurements from across the scaled model are time tagged using GPS synchronization clock. These measurements are then transmitted to the simulated PMUs that communicate with the setup. The measurements and the signals received from the power network communicating with the scaled model are transmitted to a local host through an Ethernet network. The interface software and the simulation algorithms are located on the host computer. This information is then used as inputs to the state estimator and estimates the state of the system considering all the imbalances, asymmetries, faults, and instrumentation errors. The results can then be compared with the actual measurements from the system.

In this section, the simulation and the experimental results of the developed WAMS are given. The experimental ratings and parameters are listed in Table 11.2. Figure 11.5 shows the descriptive schematic diagram and the overall experimental setup for the developed reduced scale HIL WAMS network. To estimate the PMUs characteristics, two types of tests were carried out. The first is a normal operation test without any fault or unbalanced conditions in the network. The second test is a fault test which was used as an extreme case to show the behavior of the network under this condition.

Table 11.1 Simulation parameters

Parameter	Specification
Rated voltage and frequency	208 Vrms, 60 Hz
Generation station rated power	50 kW
PV-plant rated power	24kW
Total load rated power	60 kW
No. of loads	2 (at B2, B3)
No. of transformers (Y/Y)	3 (208V/11 kV)
No. of transmission lines	2 (10km each)
No. of buses	6
PMU message report rate	60 msg./sec.

Table 11.2 Experimental parameters

Parameter	Specification
Grid voltage and frequency	208 Vrms, 60 Hz
Programmable power supply	6 kW (4:1)
Total load rated power	6 kW (10:1)
Inverter power rating	10 kW
Inverter L-filter	1 mH
Inverter C-filter	40 μf
Switching frequency	20 kHz

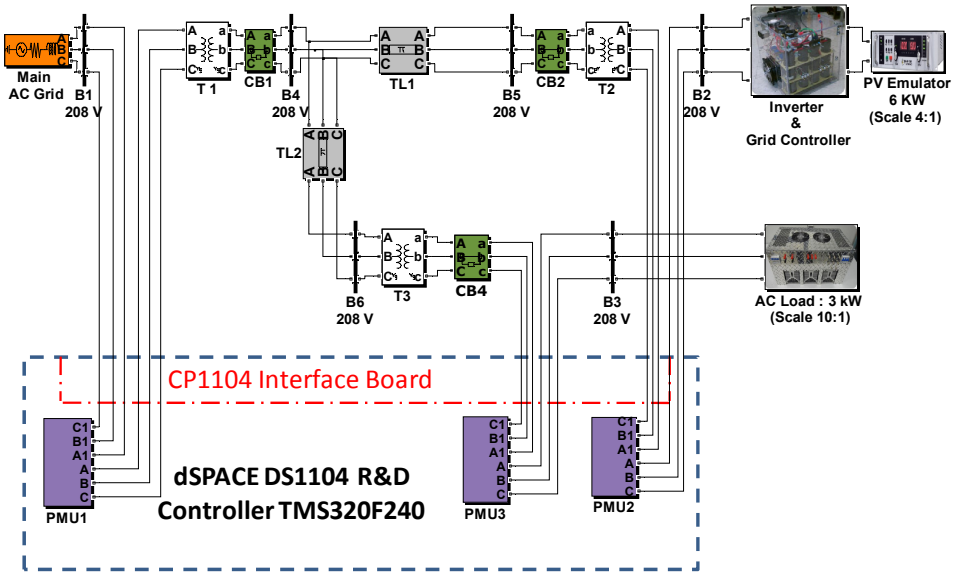

Fig. 11.5 The schematic diagram of the HIL WAMS hardware implementation

11.4.1 Normal Operation Test

In this test, the system was observed under normal operation condition. The 30 kW load on bus 2 was supplied locally from the PV-power plant and the other 30 kW load on bus 3 was supplied by the generating station sharing the PV-energy. In this case, all the PMUs show stable readings within the references. From Figs. 11.6-11, the three PMUs read accurate information about line voltage V_{ab}, the voltage amplitude of about 296 V starting from 0 sec for buses 1 and 2. At bus 3, zero voltage amplitude for the first 0.1 sec; since load bus was not connected to the network. After 0.1 sec, breaker 4(CB4) will connect load bus 3 to the network, the same average voltage amplitude level appears at other buses with a phase difference of 2.65 degrees under stable operation for all readings. The exported data by the simulated PMUs to the control center show that the developed WAMS succeeded to accurately reflect the system status in real-time (online). For a complete verification of its performance, another test with a fault occurrence is required.

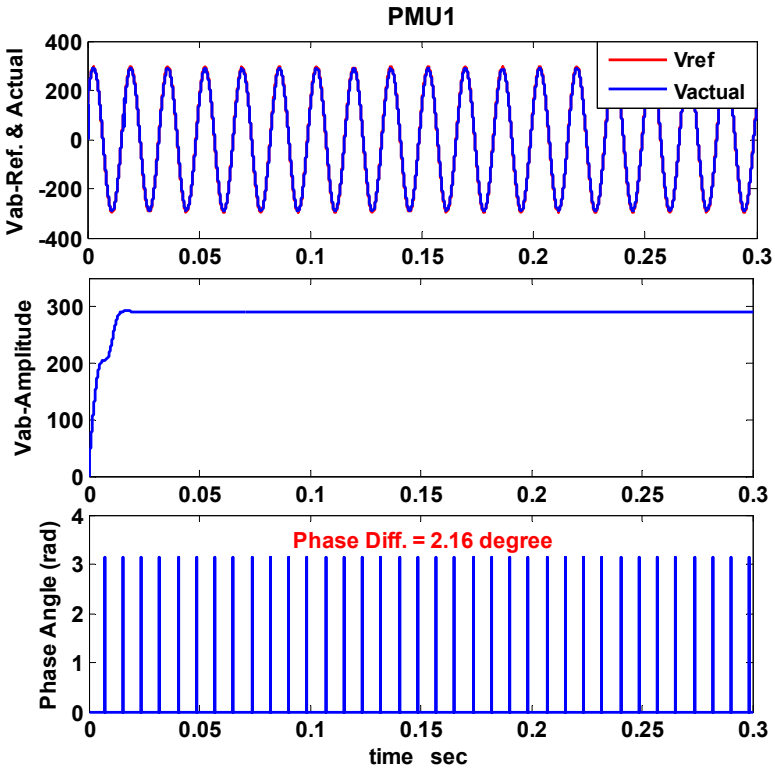

Fig. 11.6 PMU1 readings under normal operation condition (simulation)

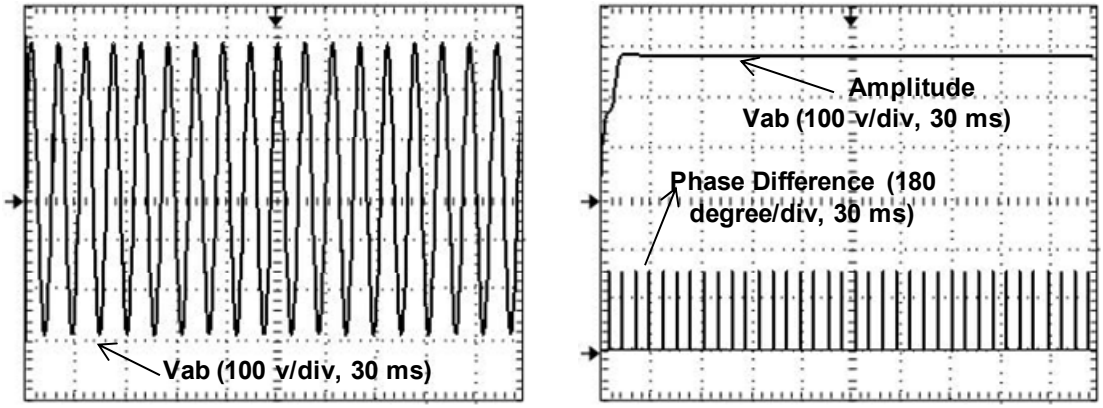

(a) (b)

Fig. 11.7 PMU1 readings under normal operation condition (experimental): (a) The line voltage (100 V/div, 30ms) and (b) The voltage amplitude (100 V/div, 30 ms) and phase difference (180 degree/div, 30 ms)

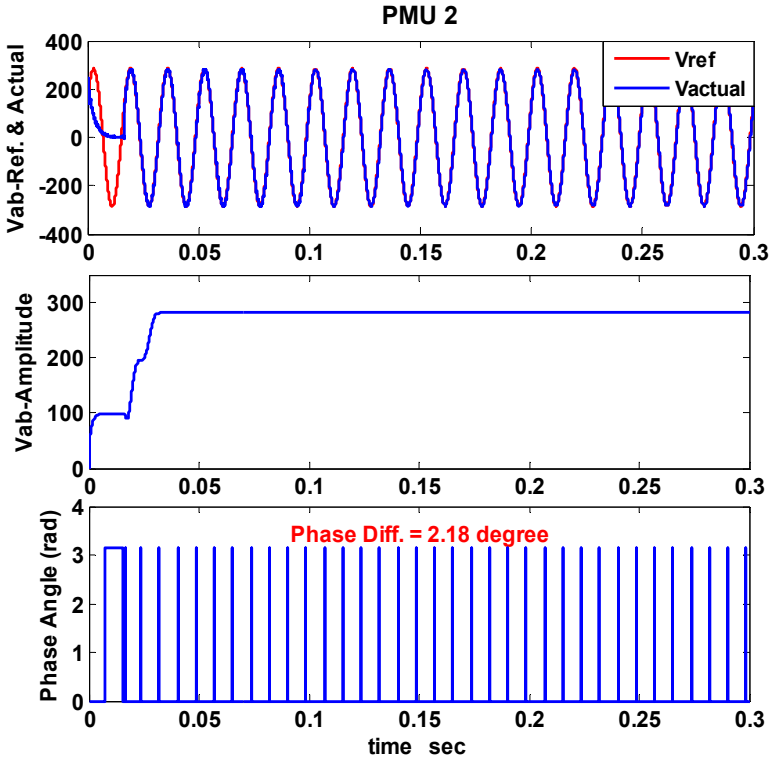

Fig. 11.8 PMU2 readings under normal operation condition (simulation)

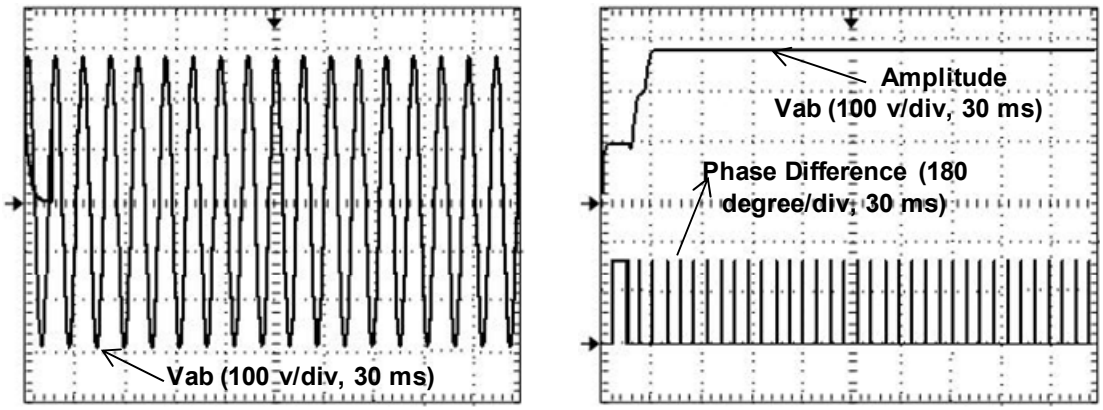

(a) (b)

Fig. 11.9 PMU2 readings under normal operation condition (experimental): (a) The line voltage (100 V/div, 30ms) and (b) The voltage amplitude (100 V/div, 30 ms) and phase difference (180 degree/div, 30 ms)

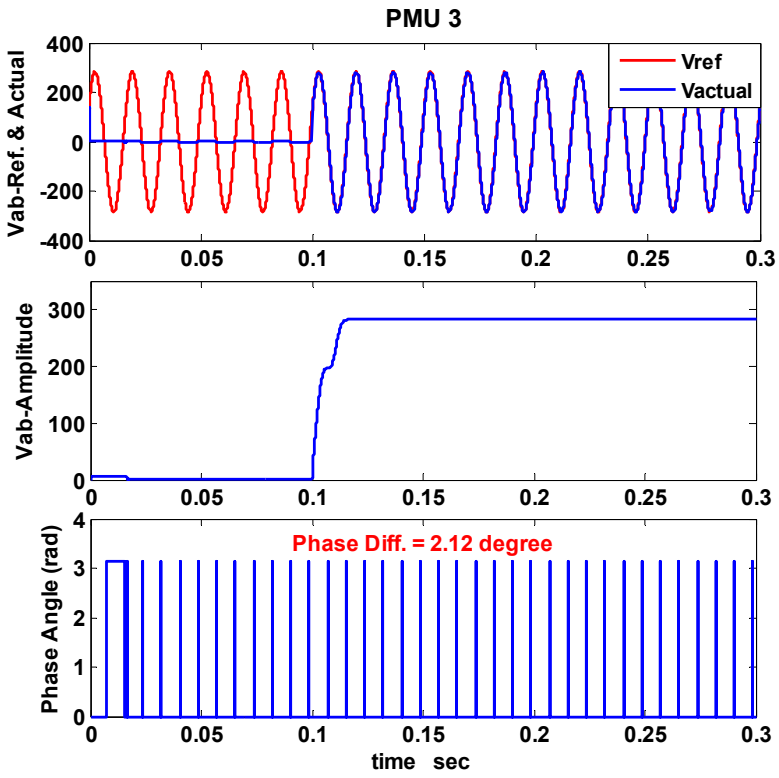

Fig. 11.10 PMU3 readings under normal operation condition (simulation)

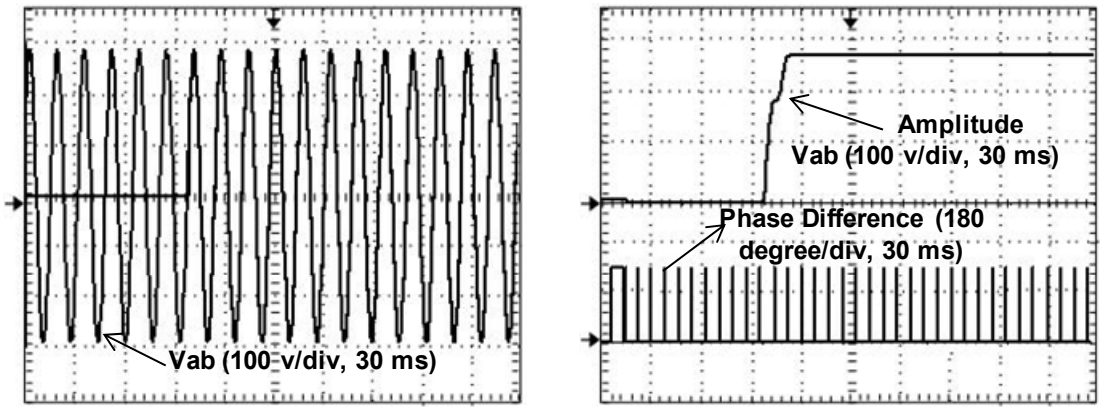

(a) (b)

Fig. 11.11 PMU3 readings under normal operation condition (experimental): (a) The line voltage (100 V/div, 30ms) and (b) The voltage amplitude (100 V/div, 30 ms) and phase difference (180 degree/div, 30 ms)

11.4.2 Fault Operation Test

In this test, a three phase to ground short circuit fault occurred at bus 3 then was repeated for bus 2. Figures 11.12, 13 show the single-line diagram for the hybrid AC/DC power network during fault occurrence at B3 and B2, respectively.

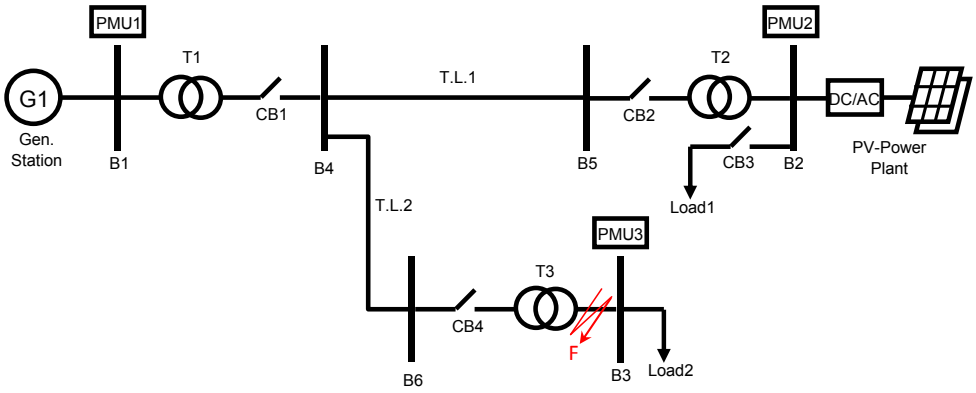

Fig. 11.12 Hybrid AC/DC power network during fault occurrence located at bus 3

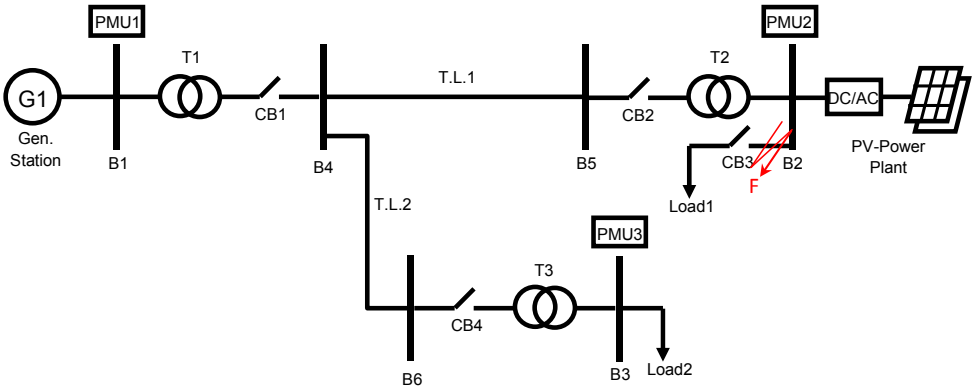

Fig. 11.13 Hybrid AC/DC power network during fault occurrence located at bus 2

Figures 11.14, 15 show the readings for all PMUs at the 3-buses. The whole system shows normal operation for 0.2 sec while bus 3 was loaded after 0.1 sec. The fault has occurred after 0.2 sec and it is cleared after 0.05 sec later. PMUs 1 and 2 read larger phase differences (10.8 and 11 degrees, respectively) than in the normal mode (2.16 and 2.18 degrees, respectively). Accordingly, the voltage amplitude dropped by 40 V which means that the fault is not located on those buses area. On the other hand, PMU 3 has

extremely large phase difference change (54 degrees) associated with a large drop in the voltage amplitude as a result of the fault that occurrence in this area. Consequently, the control center must send a control signal to the relay to release the circuit breaker at that bus upon receiving these data in real time from the PMUs to protect the other generation stations which are the most valuable part in the power network. Protecting against such damage prevents cascaded turnoff of stations which may result in major blackouts in the power system [164]. Furthermore, it helps analysts to determine the type of fault that has occurred using the data transmitted from PMUs. Additionally, the fault test is repeated for bus 2 (PV-plant area) to confirm the validity of PMU readings in showing the behavior for the system health status. Figures 11.16, 17 show the system response while the fault occurred at bus 2. We can notice that PMU2 observed the fault status at B2 while PMU1 and PMU3 indicate the fact that the fault is located inside the network but neither at B1 nor B3. This test can be utilized for studying the depth of observability for each PMU which will optimize the number of PMUs inside the WAMS network. Also, it leads to better economic operation and higher system reliability [165].

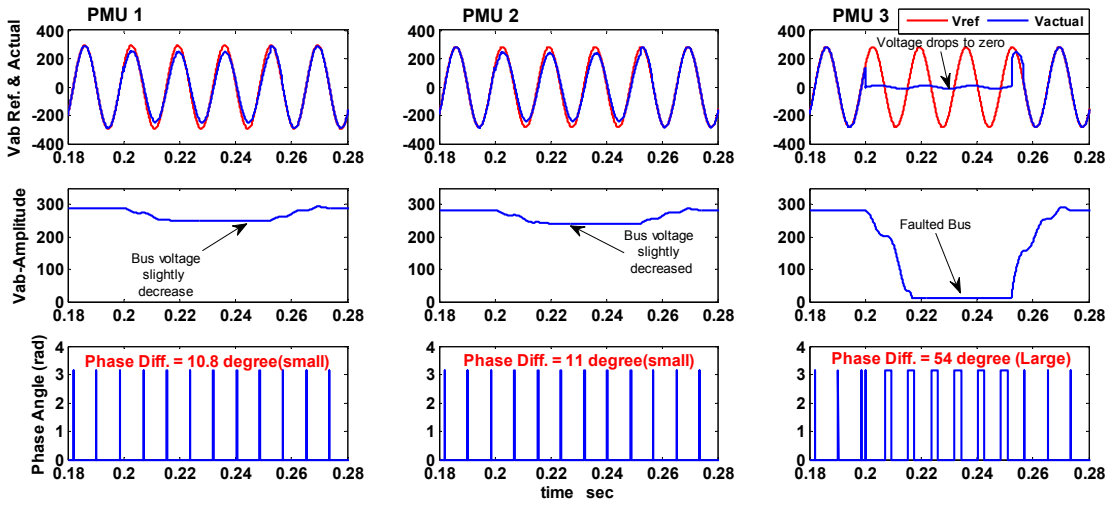

Fig. 11.14 PMUs readings during fault occurrence located at bus 3 (simulation)

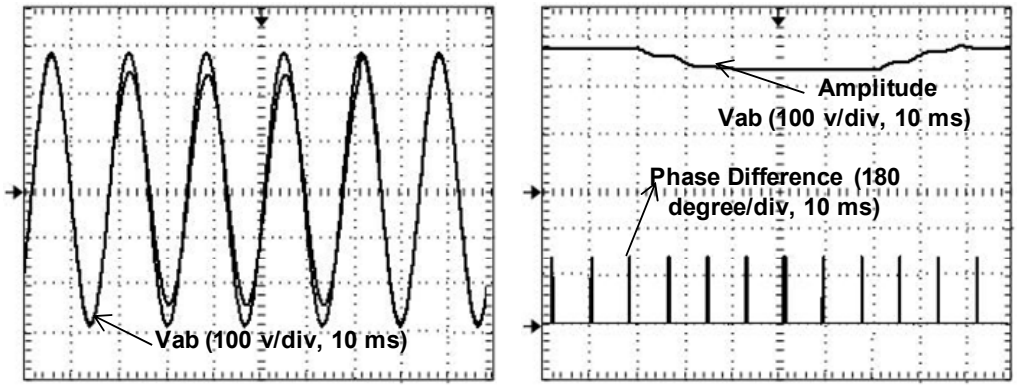

(a)

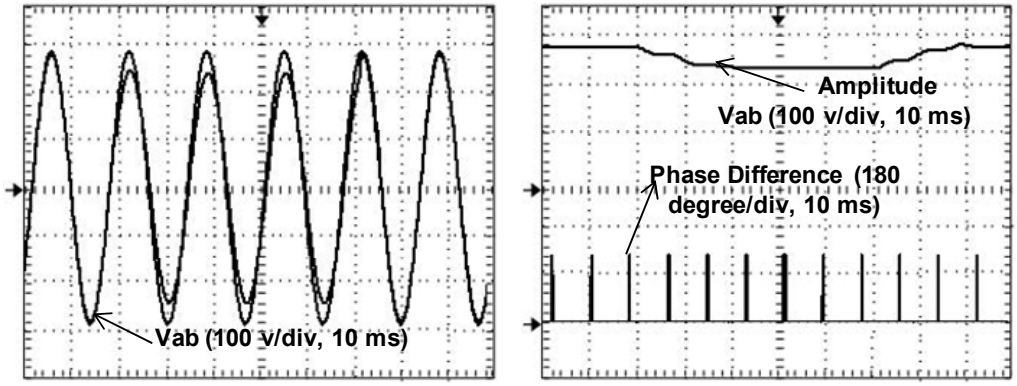

(b)

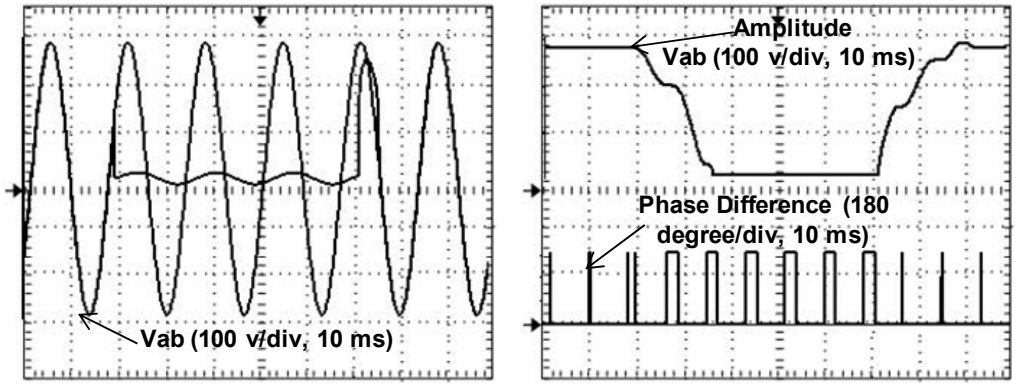

(c)

Fig. 11.15 PMUs readings during fault occurrence located at bus 3 (experimental): (a) PMU1, (b) PMU2 and (c) PMU3

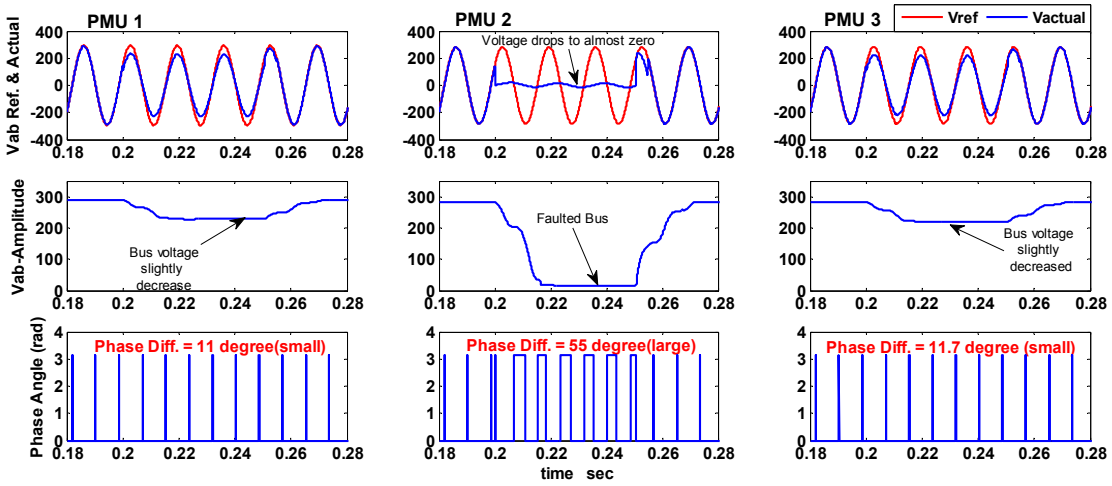

Fig. 11.16 PMUs readings during fault occurrence located at bus 2 (simulation)

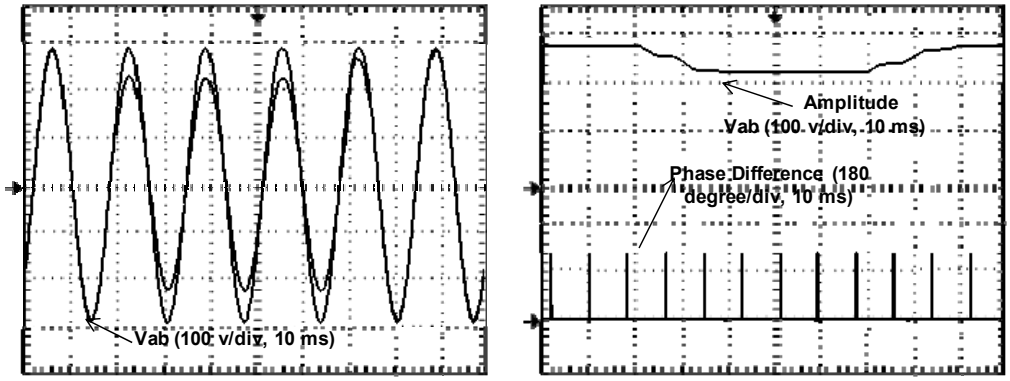

(a)

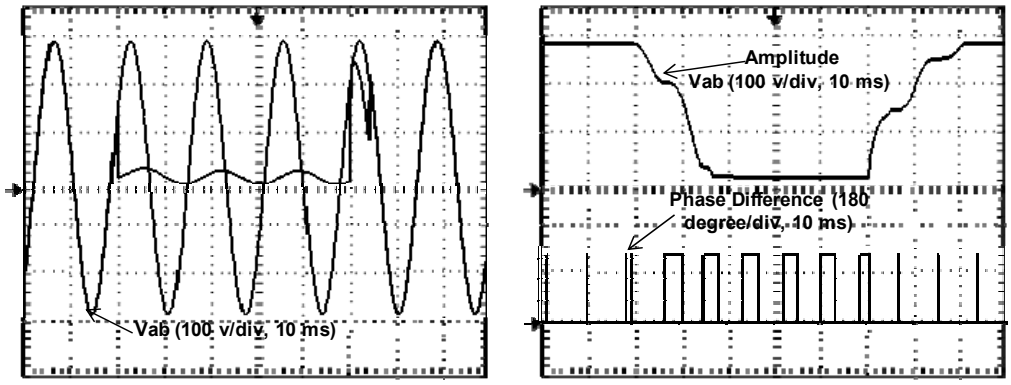

(b)

Fig. 11.17 PMUs readings during fault occurrence located at bus 2 (experimental): (a) PMU1, (b) PMU2 and (c) PMU3

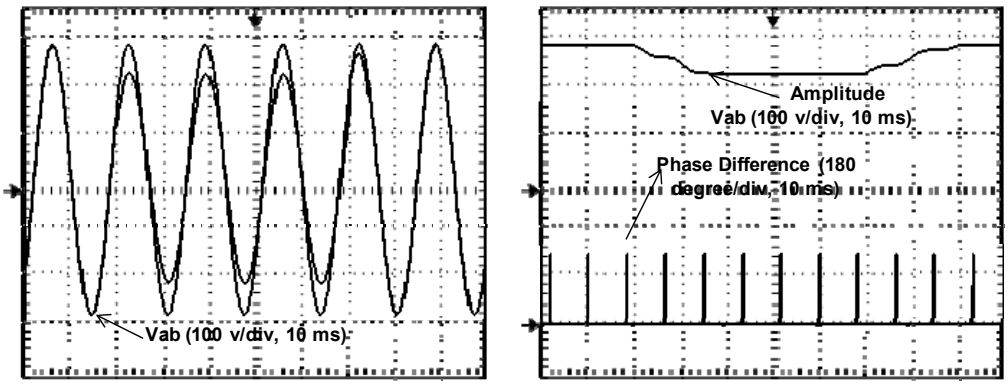

(c)

Fig. 11.17 PMUs readings during fault occurrence located at bus 2 (experimental): (a) PMU1, (b) PMU2 and (c) PMU3 (continued)

11.5 Conclusion

A performance analysis for a PMU based WAMS network was presented. The developed system was tested under two different possible conditions. The simulated PMUs show the real values of a maximum phase difference of 2.18 degrees and normal average amplitude reading showing the system stability. In this case, no action is to be taken from the control center during dynamic system monitoring.

During fault state, the PMUs data shows that the system has an unstable part with about 55 degrees phase difference. Additionally, a large voltage drop was observed in the area of the fault occurrence. This area was isolated via dynamic control signals before spreading to other parts resulting in catastrophic failure in some parts of the power system or blackouts. Furthermore, the fault test was repeated at different locations to study the behavior of each PMU. The depth of observability was identified through different fault locations; one PMU can give the status indications for each area. PMU2 was able to observe B2 locally and give indication for fault located at B3.

Furthermore, the developed HFPCS was utilized inside a reduced scale HIL-based experimental verification system was test as an experimental verification in this chapter. The real-time code for the PMU function was automatically generated using embedded target in dSPACE and real time workshop facility (RTW) in the Matlab/Simulink. All results obtained confirm the robustness of the HFPCS under severe conditions and the effectiveness of the developed WAMS network for smart grid applications.

Chapter 12 Discussion of Results, Conclusions and Recommendations for Future Work

12.1 Discussion of Results

This dissertation presented the dynamic mathematical model of the grid-connected hybrid renewable energy system utilizing high-frequency power converters. The VOC technique was developed to achieve high performance DC-bus voltage control operation as well as active-reactive power injection control. This technique achieved unity power factor grid operation (average above 0.975), very fast transient response within a fraction of second (0.4 sec) under different possible conditions (wind speed variation and load variation) and high efficiency due to reduced number of components (average above 90%) was achieved. The experimental results obtained from a prototype rated at 250 W showed that the current and voltage THD (2.67%, 0.12%), respectively, for the WECS with LC-filter is less than 5% limit imposed by IEEE-519 standard.

A high frequency semicontrolled rectifier topology was developed. This topology achieved high efficiency (average above 95%). The UPF (0.998) operation was verified for better economic utilization of the generator operation. The system was tested under different severe conditions including; full load parallel operation, hard wind speed variation, and parameter uncertainties. Load current sharing among the parallel converters has been investigated with a small transient voltage dips (<5%). A fast control dynamic response was achieved (0.1 second) during wind speed variation.

The inverter stage is based on a three-phase CSI which has higher power capability compared to voltage source inverter. High frequency operation was utilized to achieve low voltage and current THD (1.09% and 0.64%) for grid-connection, respectively. The

test results obtained from a prototype have demonstrated the system effectiveness for a wide power range (0-5 kW).

A new modularized 4-port high frequency multi-input bridgeless boost converter (MIBBC) topology feasible for hybrid energy systems and PHEVs was developed in order to optimally utilize the amount of the generated energy. The MIBBC achieved higher efficiency (97.8%), when compared to BBC (92.2%) and BPFCC (94.8%). Also, the inductor size and weight (0.3 mH: 1.29 lbs) reduced proportionally to the frequency, compared to BBC (2 mH: 12.5 lbs), improving the overall efficiency for the system. In addition, less cost (more economic) was achieved compared to BPFCC; due to less number of switches. Smaller heat sink was needed compared to BPFCC; due to less switching losses which lead to less heat dissipation. High current THD (17.03%) was investigated but still lower than the compared BBC current THD (35%). Furthermore, UPF (0.998) operation was verified for generator input operation, compared to BBC (0.835). A fast control dynamic response was achieved (0.1 second) under DC-reference step change test.

The AC-grid connection system performance was investigated with 24 mH inductor filter. The experimental test results showed the injected active current with different reference active power from 1-6 kW. At low power of 1 kW, the current THD is 12.3% (large) but less than the other compared 6 mH (31.2%) and 12 mH (21.8%) inductors. However, at larger power of 2 kW, the current THD is 5.93% which is lower than the other compared 6 mH (16.1 %) and 12 mH (11.4%) for the same power value. For 3 kW, the 24 mH gives a very low harmonic distortion of 1.36 % compared to the 6 mH (11.4%) and the 12 mH (7.96%). On the other hand, it can be noticed that the current did

not increase when the reference power changed from 4 to 6 kW. Accordingly, the controller failed to satisfy the required referenced power which limits the use of larger inductors at certain power ranges. We can conclude that the large filter value (24 mH) is feasible for small power range (1-2.5 kW) while smaller filter values (12 mH) are recommended for larger power range (3-5 kW). Meanwhile, the 6 mH is feasible for power $\geq$ 5 kW. All the obtained results confirm the effectiveness of the developed topology for hybrid sustainable energy systems.

12.2 Conclusions

The main objective of the dissertation was to develop a high frequency-based power converter system (HFPCS), which optimizes the utilization of the hybrid renewable power injected into the power grid. Studies and verifications on the developed HFPCS confirmed high efficiency, reduced size of the passive components, which leads to high output power density realization, low harmonic distortion, high reliability, and low cost.

A discussion was given on the simulated dynamic model of the developed converter starting from the dynamic formulations. Various types of simulations were performed and various algorithms were developed and tested. The results were verified for several factors including various power conversion topologies. The VOC technique was used for high performance control operation. The simulation results showed the response of the converter at different power outputs (1-10 kW). The Master-Slave control scheme was developed for a uniform current distribution among parallel converters when connected to cover higher power ratings than that of the currently available semiconductor power switches. The simulation results showed uniform current operation when using two converters. The synchronous frame 2^{nd} order SPLL was developed to give a fast detection

for the variable speed operation resulting in the phase and frequency variation. The test results confirmed the required performance.

The VOC technique was used for grid connected a voltage source inverter. The simulation and experimental results showed the validity of the control scheme in injecting the wind power as active or reactive power in order to compensate the grid power state. A VSI was introduced to work as a dynamic VAR compensator for regulating the system's voltage and stabilizing grid unbalance issues. The simulation and experimental tests for different situations of grid disturbance verified the compensator's instantaneous reaction to stabilize the grid voltage and allow sensitive loads to operate safely.

An effective high frequency semi-controlled boost rectifier topology feasible for grid-connected low speed direct-driven PMWGS was developed. The UPF operation was verified for better economic utilization of the generator operation. The DC-bus voltage control technique was developed for parallel integrated PMWGSs based on a hysteresis algorithm. This algorithm was used for reducing the generator harmonics. The developed topology was tested under various severe conditions including: full load parallel operation, hard wind speed variation, and parameter uncertainties in wind patterns.

A DSC-board containing a digital signal processor was designed to imbed the control scheme. The controller was fabricated and tested for use as the control unit of the system to satisfy all performance requirements. Each component of the system was built and tested separately, and then the whole system was connected and tested in the laboratory.

The experimental tests were implemented on line using a PC as a user interface tool. Appropriate software was developed, interfacing the experimental setup in the power

system test bed. The most important practical considerations were taken into consideration for HFPCS operation and the power injection into the grid.

A novel modularized 4-port high frequency multi-input bridgeless boost converter (MIBBC) topology feasible for hybrid energy systems and PHEVs was developed to optimally utilize the amount of the generated energy. The hybrid PI-hysteresis control algorithm was designed for reducing the AC-input source harmonics. A direct digital control (DDC) approach was used for designing the cascaded digital control strategy to control the DC-input sources operation. The digital PI-controllers were designed to achieve the required phase margin and critical frequency in a complete control scheme. The simulation and experimental results confirm the effectiveness of the developed HFPCS for the grid-connected hybrid renewable energy systems.

12.3 Future Work and Recommendations

Suggestions for further studies that can be conducted as future additions or studies are numerous. Such future works and/or additions can be used to extend this work in the following ways:

- Utilization of intelligent controllers instead the conventional PI-controllers may give more flexibility to the power system.
- Enhancing the functionality of the developed HFPCS through the new communication aspects that promote the converter to be a smart element engaged in larger networks (WAMS) and fault diagnosis operations.
- Studying multiphase converters to reduce the ripple-current notches (for minimum-size inductors according to the component of the shelf and also for reduced switching losses).

- Studying the cascading structure possibility in order to reach larger voltage levels with less stress on the switching devices.
- Testing and comparing different types of the advanced semiconductor switching devices (SiC and GaN) under high frequency operation as a promising way for reducing switching losses as well as enhancing the power density.
- Applying the recommended steps mentioned in chapter 10 in order to scale up the utilization of the developed HFPCS for larger power rating operation.
- Investigating the system performance under the disturbances that might happen to the converter behavior due to the unbalance wind generator state or during fault condition.
- Focusing on parallel converters' operation that may rise to a problem such as a circulating current among the converter units.
- Optimizing the size of the HFPCS by replacing the existing components with the advanced components, packaging and manufacturing technologies.
- Improving the MIBBC large current harmonic distortion through studying an additional filter that can be connected between the grid and the converter circuit to reduce the harmonic contents.
- Developing usable, high-fidelity models of advanced high frequency power converter topologies for PHEVs, which are gaining popularity because of the environmental consideration "go green" factor.

LIST OF REFERENCES

[1] F. A. Farret and M. G. Simoes, Integration of Alternative Sources of Energy. New York: John Wiley, 2006.

[2] S. R. Guda, "Modeling and power management of a hybrid wind micro-turbine power generation system," MSc. dissertation, Montana State Univ., Bozeman, Montana, July 2005.

[3] M. Godoy Simoes and Felix A. Farret, Renewable Energy Systems-Design and Analysis with Induction Generators, CRC Press, 2004, ch. 3-6.

[4] J. Jensen and B. Sorensen, Fundamentals of Energy Storage, Wiley, New York, 1984.

[5] H. M. Godah, "A digital control system for optimum utilization of renewable energy sources with the utility grid," Ph.D. Dissertation, Faculty of Engineering, Al Azhar Univ., Cairo, 2003.

[6] D. S. Oliveira, M. M. Reis, C. A. Silva, L. S. Barreto, F. M. Antunes, and B. L. Soares, "A Three-Phase High-Frequency Semicontrolled Rectifier for PM WECS," IEEE Transactions on Power Electronics, Vol. 25, No. 3, March 2010.

[7] B. K. Bose, Modern Power Electronics and AC Drives, Prentice Hall, Upper Saddle River, NJ, 2001.

[8] S. Nonaka and Y. Neba, "A PWM GTO current source converter–inverter system with sinusoidal inputs and outputs," IEEE Transactions on Industry Applications, Vol. 25, No. 1, pp. 76–85, January–February 1989.

[9] Z. Chen and E. Spooner, "Voltage source inverters for high-power variable-voltage dc power sources," IEE Proceedings: Generation, Transmission and Distribution, Vol. 148, No. 5, pp. 439–447, September 2001.

[10] M. A. Rahman, R. S. Radwan, A. M. Osheiba, and A. E. Lashine, "Analysis of current controllers for a voltage source inverter," IEEE Transactions on Industrial Electronics, Vol. 44, No. 4, pp. 477–XXX, August 1997.

[11] M. Mohr, B. Bierhoft, and F.W. Fuchs, "Dimensioning of a current source inverter for the feed-in of electrical energy from fuel cells to the mains," Paper 41, presented at the Nordic Workshop on Power and Industrial Electronics, NORPIE 2004, Trondheim, Norway, June 14–16, 2004.

[12] F. Z. Peng, X. Yuan, X. Fang, and Z. Qian, "Z-source inverter", IEEE Transactions on Industry Applications, Vol. 39, pp. 504–510, March/April 2003.

[13] P. C. Loh, D. M. Vilathgamuwa, Y. S. Lai, G. T. Chua, and Y. Li, "Pulse-width modulation of Z-source inverters," in Conference Record of the IEEE 39th Industry Applications Annual Meeting Conference, October 3–7, 2004, Vol. 1, pp. 155–162.

[14] R. D. Middlebrook, “Power electronics: topologies, modeling, and measurement,” Proc. IEEE Int. Symp. Circuits Syst., April 1981.

[15] S. Cuk, “Basics of switched-mode power conversion: topologies, magnetics, and control,” in Advances in Switched-Mode Power Conversion, vol. 2, pp. 279-310, Irvine: Teslaco, 1981.

[16] R. W. Erickson, Fundamentals of Power Electronics, New York: Chapman and Hall, 1997.

[17] R. Severns and G. E. Bloom, Modern DC-to-DC Switch mode Power Converter Circuits, New York: Van No strand Reinhold, 1985.

[18] N. Mohan, T. Undeland, and W. Robbins, Power Electronics: Converters, Applications, and Design, New York: John Wiley & Sons, 2003.

[19] H. Van der Broeck, “Analysis and realization of pulse width modulator based on voltage space vectors,” IEEE Trans. on Ind. Appl., Vol. 24, No.1, pp. 142-150, 1988.

[20] P. Vas, “Electrical machines and drives: A space vector theory approach” Oxford Science Publications, 1992.

[21] Global Wind Energy Outlook 2006. (2006). Global Wind Energy Council, Bruxelas [Online].Available:http://www.gwec.net/fileadmin/documents/Publications/Global_ Wind_Energy_Outlook_2006.pdf

[22] V. Kumar, R. R. Joshi, and R. C. Bansal, “Optimal control of matrix-converter-based WECS for performance enhancement and efficiency optimization,” IEEE Transactions on Energy Conversion, Vol. 24, No. 1, pp. 264-272, March 2009.

[23] Yi Zhou, P. Bauer, J. A. Ferreira, and J. Pierik, “Operation of grid connected DFIG under unbalanced grid voltage,” IEEE Transactions on Energy Conversion, Vol. 24, No. 1, pp. 240-246, March 2009.

[24] S. M. Dehghan, M. Mohamadian, and A. Y. Varjani, “A new variable-speed wind energy conversion system using permanent-magnet synchronous generator and z-source inverter,” IEEE Transactions on Energy Conversion, Vol. 24, No. 3,pp. 714–724, Sep. 2009.

[25] K. Tan and S. Islam “Optimum control strategies for grid-connected wind energy conversion system without mechanical sensors” WSEAS Transactions on Systems and Control, Vol. 3, Issue 7, pp. 644-653, ISSN:1991-8763, July 2008.

[26] B.C. Rabelo, W. Hofmann, J.L da Silva, R.G. de Oliveira, and S.R Silva, “Reactive power control design in doubly fed induction generators for wind turbines,” IEEE Transactions on Industrial Electronics, Vol. 56, No. 10, pp. 4154-4162, Oct. 2009.

[27] T. Yachi, NEDO technological survey on ultra low loss power device, pp. 170-190, 2001(in Japanese).

[28] P. Cheasty, J. Flannery, M. Meinhardt, A. Alderman, and S. O. Mathuna, "Benchmark of power packaging for dc/dc and ac/dc converters," IEEE Transactions on Power Electronics, Vol. 17, No. 1, pp. 141-150, Jan. 2002.

[29] Mitsubishi Intelligent Power Module Data Manual: PM50RVA120, Mitsubishi Elect. Electron. USA, Cypress, CA, 2003.

[30] H. Ohashi, "Recent power devices trend," IEEJ, Vol. 102, No. 3, pp. 168-171, 2002 (in Japanese).

[31] M. K. Mishra and K. Karthikeyan, "An investigation on design and switching dynamics of a voltage source inverter to compensate unbalanced and nonlinear loads," IEEE Trans. on Ind. Appl., Vol. 56, No. 8, pp. 2802–2810, August 2009.

[32] G. Resch, H. Auer, M. Stadler, C. Huber, L. H. Nielsen, J. Twidell, and D. J. Swider, "Dynamics and basic interactions of RES with the grid, switchable loads and storage," Work Package 1 within the 5th Framework Programme of the European Commission, supported by DG TREN, Contract NNE5-2001-660, October 2003.

[33] EREC (Integration of Renewable Energy Sources), "Targets and benefits of large-scale deployment of renewable energy sources," presented at the Workshop on Renewable Energy Market Development Status and Prospects, Workshops in the New Member States, April–May 2004.

[34] J. S. Rohatgi and V. Nelson, "Wind characteristics: An analysis for generation of wind power," Alternative Energy Institute, West Texas A&M University, Canyon, TX, 1994.

[35] P. Novak, T. Ekelund, I. Jovik, and B. Schmidtbauer, "Modeling and control of variable speed wind-turbine drive-system dynamics," Proceedings of the IEEE Control Systems Society Conference, 1995, pp. 28–38.

[36] M. R. Patel, Wind and Solar Power Systems, CRC Press, Boca Raton, FL, 1999.

[37] MR Dubois, H. Polinder, and JA Ferreira, "Comparison of generator topologies for direct-drive wind turbines," Proc. Nordic Countries Power and Industrial Electronics Conf. (NORPIE), Aalborg, Denmark, June 2000, pp. 22–26.

[38] G. Bywaters, V. John, J. Lynch, and ET AL., "Northern power systems wind PACT drive train alternative design study report," NREL, Golden, Colorado, Report no. NREL/SR-500-35524, October 2004.

[39] H Li and Z. Chen, "Overview of different wind generator systems and their comparisons," Renewable Power Generation, IET, vol.2, no.2, pp.123-138, June 2008.

[40] Paul C. Krause, Oleg Wasynczuk, and Scott D. Sudhoff, "Analysis of electric machinery and drive systems" Purdue University, second edition, IEEE Press, Wiley-Interscience, 2002.

[41] IEEE Recommended Practices and Requirements for Harmonic Control in Electrical Power Systems, IEEE Standard 519, 1992, 2010.

[42] H. M. Suryawanshi, M. R. Ramteke, K. L. Thakre, and V. B. Borghate, "Unity-power-factor operation of three-phase ac–dc soft switched converter based on boost active clamp topology in modular approach," IEEE Transactions on Power Electronics, Vol. 23, No. 1, pp. 229–236, Jan. 2008.

[43] A. B. Raju, B.G. Fernandes, and K. Chatterjee, "A UPF power conditioner with maximum power point tracker for grid connected variable speed wind energy conversion system," in Proc. 1st Int. Conf. Power Electron. Syst. Appl., pp. 107–112, Nov. 2004.

[44] G. T. Kim and T. A. Lipo, "VSI-PWM rectifier/inverter system with a reduced switch count," IEEE Transactions on Industrial Applications, Vol. 32, No. 6, pp. 1331– 1337, Nov./Dec. 1996.

[45] M. B. de Correa, C. B. Jacobina, E. R. C. da Silva, and A. M. N. Lima, "A general PWM strategy for four-switch three-phase inverters," IEEE Transactions on Power Electronics, Vol. 21, No. 6, pp. 1618–1627, Nov. 2006.

[46] C. B. Jacobina, E. C. dos Santos, E. R. C. da Silva, M. B. de Correa, A. M. N. Lima, and T. M. Oliveira, "Reduced switch count multiple three-phase AC machine drive systems," IEEE Transactions on Power Electronics, Vol. 23, No. 2, pp. 966–976, Mar. 2008.

[47] K. Tan and S. Islam, "Optimum control strategies in energy conversion of PMSG wind turbine system without mechanical sensors," IEEE Trans. on Energy Conv., Vol. 19, No. 2, pp. 392–399, Jun. 2004.

[48] J. Sopanen, V. Ruuskanen, J. Nerg, and J. Pyrhönen, "Dynamic torque analysis of a wind turbine drive train including a direct-driven permanent-magnet generator," IEEE Transactions on Industrial Electronics, Vol. 58, No. 9, pp. 3859-3867, Sep. 2011.

[49] Alejandro Garcés and Marta Molinas, "A study of efficiency in a reduced matrix converter for offshore wind farms," IEEE Transactions on Industrial Electronics, Vol. 59, No. 1, pp. 184-193, Jan. 2012.

[50] M. Chinchilla, S. Arnaltes, and J. C. Burgos, "Control of PMSG applied to VSWE systems connected to the grid," IEEE Transactions on Energy Conversion, Vol. 21, No. 1, pp. 130– 135, Mar. 2006.

[51] Hua Geng, Geng Yang, Dewei (David) Xu, and Bin Wu, "Unified power control for PMSG-based WECS operating under different grid conditions," IEEE Transactions on Energy Conversion, Vol. 26, No. 3, pp. 822–830, Sep. 2011.

[52] D. S. Oliveira, M. M. Reis, C. A. Silva, L. S. Barreto, F. M. Antunes, and B. L. Soares, "A three-phase high-frequency semicontrolled rectifier for PM WECS,", IEEE Transactions on Power Electronics, Vol. 25, No. 3, pp. 677-685, March 2010.

[53] F. Gao, P. C. Loh, F. Blaabjerg, and D. M. Vilathgamuwa, "Five-level current-source inverters with buck–boost and inductive-current balancing capabilities," IEEE Transactions on Industrial Electronics, Vol. 57, No. 8, pp. 2613-2622, August 2010.

[54] M. H. Rashid, Power Electronics Handbook, San Diego, CA: Academic Press, 2001.

[55] R. Messenger and J. Ventre, Photovoltaic Systems Engineering, CRC Press, Boca Raton, FL, 2000.

[56] R. Boylestad and L. Nashelsky, Electronic Devices and Circuit Theory, 6th ed., Prentice Hall, Upper Saddle River, NJ, 1996.

[57] R. R. Spencer and M. S. Ghausi, Introduction to Electronic Circuit Design, Prentice Hall, Upper Saddle River, NJ, 2003.

[58] R. M. Nelms, D. R. Cahela, and B. J. Tatarchuk, "Modeling double-layer capacitor Behavior using ladder circuits," IEEE Transactions on Aerospace and Electronic Systems, Vol. 39, No. 2, pp. 430-438, April 2003.

[59] J. M. Correa, F. A. Farret, L. N. Canha, and M. G. Simoes, "An electrochemical-based fuel-cell model suitable for electrical engineering automation approach," IEEE Transactions on Power Delivery, Vol. 17, No. 2, pp. 467–476, April 2002.

[60] Y. Kim and S. Kim, "An electrical modeling and fuzzy logic control of a fuel cell generation system," IEEE Transactions on Energy Conversion, Vol. 14, No. 2, pp. 239– 244, June 1999.

[61] C. J. Hatziadoniu, A. A. Lobo, F. Pourboghrat, M. Daneshdoost, J. T. Pukrushpan, A. G. Stefanopoulou, and Huei Peng, "A simplified dynamic model of grid-connected fuel-cell generators," IEEE Transactions on Industrial Electronics, Vol. 51, No. 5, pp. 1103–1109, October 2004.

[62] J.T. Pukrushpan, A.G. Stefanopoulou, and H. Peng, "Modeling and control for PEM fuel cell stack system," in Proceedings of the American Control Conference, Anchorage, AK, pp. 3117–3122, May 2002.

[63] C. Wang, M. H. Nehrir, and S. R. Shaw, "Dynamic models and model validation for PEM fuel cells using electrical circuits," Vol. 20, No. 2, pp. 442-451, June 2004.

[64] W. Friede, S. Rael, and B. Davat, "Mathematical model and characterization of the transient behavior of a PEM fuel cell," IEEE Transactions on Power Electronics, Vol. 19, No. 5, pp 1234–1241, September 2004.

[65] A. W. Stienecker, M. A. Flute and T. A. Stuart, "Improved battery charging in an ultracapacitor - lead acid battery hybrid energy storage system for mild hybrid electric vehicles", *SAE Paper* No. 2006-01-1123, 2006.

[66] B. Spier and G. Gutmann, "42-V battery requirements lead-acid at its limits," Journal of Power Sources 116, pp. 99-104, 2003.

[67] M. Anderman, "The challenge to fulfill electrical power requirements of advanced vehicles," Journal of Power Sources 127, pp. 2-7, 2004.

[68] C. Kim, H. Park, C. Kim, G. Moon, and J. Lee, "Individual charge equalization converter with parallel primary winding of transformer for series connected lithium-ion battery strings in an HEV," Journal of Power Electronics, Vol. 9, No. 3, pp. 472-480, 2009.

[69] B. Lee, D. Shin, H. Song, H. Heo, and H. Kim, "Development of an advanced hybrid energy storage system for hybrid electric vehicles," Journal of Power Electronics, Vol. 9, No. 1, pp. 51-60, 2009.

[70] O. Tremblay, A. Dessaint, and I. Dekkiche, "A generic battery model for the dynamic simulation of hybrid electric vehicles," IEEE Vehicle Power and Propulsion Conference VPPC 2007, pp. 284-289, 9-12 Sept. 2007.

[71] T. Takaku, G. Homma, T. Isobe, S. Igarashi , and Y. Shimada "Improved wind power conversion system using magnetic energy recovery switch (MERS)" IAS IEEE conference, Vol. 3, pp. 2007 – 2012, 2-6 Oct, Kowloon, Hong Kong, 2005.

[72] A. Knight and G. Peters, "Simple wind energy controller for an expanded operating range," *IEEE Trans. on Energy Conv.*, Vol. 20, No. 2, pp. 459–466, June 2005.

[73] M. Amin and O. A. Mohammed, "DC-bus voltage control of three-phase PWM converters connected to wind powered induction generator," IEEE Power and Energy Society General Meeting 2010, pp.1-7, Minneapolis, 25-29 July 2010.

[74] M. M. Neam (Amin), F. F. El-Sousy, M. A. Ghazy and M.A. Abu-Adma, "The dynamic performance of an isolated self-excited induction generator driven by a variable-speed wind turbine," International Conference on Clean Electrical Power (ICCEP '07), pp. 536-543, Capri, Italy, 21-23 May 2007.

[75] R. Leidhold, G. Garcia, and M. Valla, "Field-oriented controlled induction generator with loss minimization," IEEE Trans. on Ind. Elec., Vol. 49, No. 1, pp. 147-156, Feb. 2002.

[76] V. Blasko and V. Kaura, "A new mathematical model and control of a three-phase AC–DC voltage source converter," IEEE Trans. on Power Electronics, Vol. 12, No. 1, pp. 116–123, Jan. 1997.

[77] H. Sugimoto, S. Moritomo, and M. Yano, "A high performance control method of a voltage-type PWM converter," in Conf. Rec. IEEE PESC'88, pp. 360–368, Apr. 1988.

[78] S. Fukuda, Y. Iwaji, and T. Aoyama, "Modeling and control of sinusoidal PWM rectifiers," in Proc. EPE, Brighton, U.K., pp. 115–120, Sept. 1993.

[79] Yang Ye, M. Kazerani, and V. H. Quintana, "Modeling, control and implementation of three-phase PWM converters," IEEE Tran. on Power Electronics ,Vol. 18, No. 3, pp. 857-864, May 2003.

[80] S. H. Song, S. Kang, and N. K. Hahm, "Implementation and control of grid connected AC–DC–AC power converter for variable speed wind energy conversion system," Appl. Power Electron. APEC'03 Conf. Expo., Vol. 1, pp. 154–158, Feb. 2003.

[81] S. Fukuda and T. Yoda, "A novel current-tracking method for active filters based on a sinusoidal internal model," IEEE trans. On Ind. App., Vol., 37, No.3, pp. 888-895, May /June 2001.

[82] L. J. Borle, M.S. Dymond, and C. V. Nayar, "Development and testing of a 20 kW grid interactive photovoltaic power conditioning system in Western Australia," IEEE Trans. on Ind. App., Vol. 33, No. 2, pp. 502-508., 1997.

[83] D. W. Novotny and T. A. Lipo, "Vector control and Dynamic of AC Drive," Copyright by Clarendon Press Oxford University, 1996.

[84] Z. Jovan "A method of synchronizing microprocessor-controlled pulse width modulation inverter with the mains voltage" EPE, Conf. Proce., Sevilla, Spain, pp. 347-350, 1995.

[85] M. Amin, B. Mirafzal, and O. A. Mohammed, "A DC-bus voltage regulation for parallel wind-based synchronous generators," 36th Annual Conference on IEEE Industrial Electronics Society (IECON 2010), pp. 3161-3166, Phoenix, Nov. 2010

[86] M. Amin and O. A. Mohammed, "Software phase locked loop technique for grid-connected wind energy conversion systems," 2010 IEEE 12th Workshop on Control and Modeling for Power Electronics (COMPEL), pp.1-8, Boulder, 28-30 June 2010

[87] N. Hamrouni, M. Jraidi, and A. Chérif, "New control strategy for 2-stage grid-connected photovoltaic power system," Renewable Energy, Elsevier, Vol. 33, Issue 10, pp. 2212-2221, Oct. 2008.

[88] M. Kazmierkowski, R. Krichnen, F. Belaabjerg, Control in power electronics—selected problems. New York: Academic Press, 2002.

[89] O. Alonso, P. Sanchis, E. Gubia, L. Marroyo, "Cascaded H-bridge multilevel converter for grid connected photovoltaic generators with independent maximum power point tracking of each solar array," IEEE power electronics specialist conference (PESC '03), 2003.

[90] B. M. Hasaneen and Adel A. Elbaset, "Design and simulation of DC/DC boost converter," in Proc. IEEE Power System Conf., MEPCON 2008, pp. 335-340, March 2008.

[91] Y. Huang and S. Yasunobu, "A general practical design method for fuzzy PID control from conventional PID controller," in *Proc.* FUZZ IEEE *Conf.*, pp. 969-972, Vol. 2, 2000.

[92] M. Amin, M. Elshaer, and O. A. Mohammed, "DC bus voltage control for PV sources in a DC distribution system infrastructure," 2010 IEEE Power and Energy Society General Meeting, pp.1-5, Minneapolis, 25-29 July 2010.

[93] Jinn-Chang Wu, "Novel circuit configuration for compensating for the reactive power of induction generator," IEEE Transactions on energy conversion, Vol. 23, No. 1, pp. 156-162, March 2008.

[94] Juergen K Steike "Use of an LC filter to achieve a motor-friendly performance of the PWM voltage source inverter," IEEE Trans. on Energy Conversion, Vol. 14, No.3, pp. 649-654, September 1999.

[95] M.A. Chaudhari and H.M. Suryawanshi, "High-power-factor operation of three-phase AC-to-DC resonant converter," *IEE Proc.-Electr*. Power Appl., Vol. 153, No. 6, pp. 873-882, November 2006.

[96] T. Ahmed, E. Hiraki, M. Nakaoka, and O. Noro, "Three-phase self-excited induction generator driven by variable-speed prime mover for clean renewable energy utilization and its terminal voltage regulation characteristics by static VAR compensator," IEEE Trans. on Ind. App., Vol. 40, No. 4, pp. 978-988, July 2004.

[97] M. Amin and O. A. Mohammed, "Development of high-performance grid-connected wind energy conversion system for optimum utilization of variable speed wind turbines," IEEE Trans. on Sustainable Energy, Vol. 2, No. 3, pp.235-245, July 2011.

[98] M. Amin and O. A. Mohammed, "Power quality improvement of grid-connected wind energy conversion system for optimum utilization of variable speed wind turbines," 36th Annual Conference on IEEE Industrial Electronics Society (IECON 2010), pp. 3287-3292, Phoenix, 7-10 Nov. 2010.

[99] M. Amin and O. A. Mohammed, "Vector oriented control of voltage source PWM inverter as a dynamic VAR compensator for WECS connected to utility grid," 2010 Twenty-Fifth Annual IEEE Applied Power Electronics Conference and Exposition (APEC), pp. 1640-1650, Palm springs, California, 21-25 Feb. 2010.

[100] IEEE guide for harmonic control and reactive compensation of static power converters, IEEE Standard 519-1992.

[101] J. Napoles, J. Leon, R. Portillo, L. Franquelo, and M. Aguirre, "Selective harmonic mitigation technique for high-power converters," IEEE Trans. on Ind. Electron., Vol. 57, No. 7, pp. 2315-2323, July 2010.

[102] H. Fujita, "A resonant gate-drive circuit capable of high-frequency and high-efficiency operation," IEEE Trans. on Power Electronics, Vol. 25, No. 4, pp. 962-969, April 2010.

[103] N. King, E. Narayanan, L. Coulbeck, A. Crane, and R. Dudley, "Comparison of trench gate IGBT and CIGBT devices for increasing the power density from high power modules," IEEE Trans. on Power Electronics, Vol. 25, No. 3, pp. 583-591, March 2010.

[104] I. Omura, W. Saito, T. Domon, and K. Tsuda, "Gallium nitride power HEMT for high switching frequency power electronics," International Workshop on Physics of Semiconductor Devices (IWPSD 2007), pp. 781-786, Mumbai, Dec. 2007.

[105] M. Amin and O. A. Mohammed, "Development of a grid-connected wind generation system utilizing high frequency-based three-phase semicontrolled rectifier-current source inverter," the 26th IEEE APEC annual conference 2011, pp. 645-652, 6-11 March 2011.

[106] M. P. Kazmierkowski, and L. Malesani, "Current control techniques for three-phase voltage-source PWM converters: a survey," IEEE Trans. on Ind. Elect., Vol. 45, No. 5, pp. 691-703, Oct. 1998.

[107] D. Lee, G. Lee, and K. Lee, "DC-bus voltage control of three-phase ac/dc PWM converters using feedback linearization," IEEE Trans. on Ind. Appl., Vol. 36, No. 3, pp. 826-833, May/June 2000.

[108] H. Song and K. Nam, "Dual current control scheme for PWM converter under unbalanced input voltage conditions," IEEE Trans. on Ind. Elect., Vol. 46, No. 5, pp. 953-959,Oct. 1999.

[109] T. Ohnuki, O. Miyashita, P. Lataire, and G. Maggetto, "Control of a three-phase PWM rectifier using estimated ac-side and dc-side voltages," IEEE Trans. on Power Elect., Vol. 14, No. 2, pp. 222-226, May 1999.

[110] A. Tilli and A. Tonielli, "Sequential design of hysteresis current controller for three-phase inverter," IEEE Trans. on Ind. Electron., Vol. 45, No. 5, pp. 771-781, Oct. 1998.

[111] F. Musavi, W. Eberle, and W. G. Dunford, "Efficiency evaluation of single-phase solutions for AC-DC PFC boost converters for plug-in-hybrid electric vehicle battery chargers," IEEE Vehicle Power and Propulsion Conference (VPPC), pp. 1-6, 1-3 Sep. 2010.

[112] Chen Zheng, Nie Ziling, Fu Yuhong, and C. C. Mi, "A bidirectional power converter for battery of plug-in hybrid electric vehicles," the 36th Annual Conference on IEEE Industrial Electronics Society (IECON 2010), pp. 3049-3053, 7-10 Nov. 2010.

[113] Lijun Hang, SenSen Liu, Gang Yan, Bo Qu, and Zheng-yu Lu, "An improved deadbeat scheme with fuzzy controller for the grid-side three-phase PWM boost rectifier," IEEE Trans. on Power Elect., Vol. 26, No. 4, pp. 1184-1191, Apr. 2011.

[114] L. Huber, Yungtaek Jang, M. M. Jovanovic, "Performance Evaluation of Bridgeless PFC Boost Rectifiers," IEEE Transactions on Power Electronics, Vol. 23, No. 3, pp. 1381-1390, May 2008.

[115] Wuhua Li and Xiangning He, "Review of Nonisolated High-Step-Up DC/DC Converters in Photovoltaic Grid-Connected Applications", IEEE Trans. Ind. Electron., Vol. 58, No. 4, pp. 1239–1250, April 2011.

[116] M. Kabalo, B. Blunier, D. Bouquain, and A. Miraoui, "State-of-the-art of dc-dc converters for fuel cell vehicles", IEEE Vehicle Power and Propulsion Conference (VPPC), Lille, France 2010, 1-3 Sept, 2010

[117] M. Al Sakka, J. V. Mierlo, H. Gualous, and P. Lataire, "Comparison of 30KW DC/DC converter topologies interfaces for fuel cell in hybrid electric vehicle", The 13th European Conference on Power Electronics and Applications (EPE '09), 8-10 Sept. 2009, Barcelona-Spain.

[118] L. Solero, A. Lidozzi, and J. A. Pomilio, "Design of multiple-input power converter for hybrid vehicles", IEEE Transactions on Power Electronics, Vol. 20, No. 5, pp. 1007 – 1016, September 2005.

[119] S. H. Choung and A. Kwasinski "Multiple-input DC-DC converter topologies comparison", IEEE IECON 2008, pp. 2359 – 2364, 10-13 Nov. 2008.

[120] W. Liu, J. Chen, T. Liang, and R. Lin, "Multicascoded sources for a high-efficiency fuel-cell hybrid power system in high-voltage application," IEEE Trans. on Power Electronics, Vol. 26, No. 3, pp. 931-942, March 2011.

[121] J. Rodríguez, J. Dixon, J. Espinoza, J. Pontt and P. Lezana, "PWM regenerative rectifiers: state of the art," IEEE Trans. on Ind. Elect., Vol. 52, No. 1, pp. 5-22, Feb. 2005.

[122] M. Amin and O. A. Mohammed, "A three-phase high frequency semi-controlled battery charging power converter for plug-in hybrid electric vehicles," Journal of Power Electronics, Vol. 11, No. 4, July 2011.

[123] Burak Akin and Haci Bodur, "A new single-phase soft-switching power factor correction converter," IEEE Trans. on Power Electronics, Vol. 26, No. 2, pp. 436-443, Feb. 2011.

[124] Y. Lee, A. Khaligh, and Ali Emadi, "Advanced integrated bidirectional AC/DC and DC/DC converter for plug-in hybrid electric vehicles," IEEE Trans. on Vehicular Tech., Vol. 58, No. 8, pp. 3970-3980, Oct. 2009.

[125] B. A. Mather, and D. Maksimovi´, "A simple digital power-factor correction rectifier controller," IEEE Trans. on Power Electronics, Vol. 26, No. 1, pp. 9-19, Jan. 2011.

[126] W. Choi, J. Kwon, E. Kim, J. Lee, and B. Kwon, "Bridgeless boost rectifier with low conduction losses and reduced diode reverse-recovery problems," IEEE Trans. on Ind. Elect., Vol. 54, No. 2, pp. 769 -780, Apr. 2007.

[127] M. Ordonez and J. E. Quaicoe, "Soft-switching techniques for efficiency gains in full-bridge fuel cell power conversion," IEEE Trans. on Power Electronics, Vol. 26, No. 2, pp. 482-492, Feb. 2011.

[128] P. Kong, S. Wang, and F. C. Lee, "Common mode EMI noise suppression for bridgeless PFC converters," IEEE Trans. on Power Electronics, Vol. 23, No. 1, pp. 291-297, Jan. 2008.

[129] F. Valenciaga and P. F. Puleston, "Supervisor control for a standalone hybrid generation system using wind and photovoltaic energy," IEEE Trans. Energy Convers., Vol. 20, No. 2, pp. 398–405, June 2005.

[130] P. Krein, J. Bentsman, R. Bass, and B. Lesieutre, "On the use of averaging for the analysis of power electronic systems," IEEE Transactions on Power Electronics, Vol. 5, No. 2, pp. 182-190, April 1990.

[131] Y. Lui, E. Meyer, and X. Liu, "Recent Developments in digital control strategies for DC/DC switching power converters," IEEE Transactions on Power Electronics, Vol. 24, No. 11, pp. 2567-2577, Nov. 2009.

[132] "DS1104 R&D Controller Board," Catalog 2010, dSPACE, info@dspace.de, www.dspace.com

[133] A. Gebregergis and P. Pillay, "Implementation of fuel cell emulation on dsp and dspace controllers in the design of power electronic converters," IEEE Transactions on Industry Applications, Vol. 46, No.1, pp. 285-294, Jan.-Feb. 2010.

[134] Li Wang, He Wen Chen, and Dong Jing Lee, "Implementation of a DSP-based power converter for a wind induction generator," Power and Energy Society General Meeting - Conversion and Delivery of Electrical Energy in the 21st Century, 2008 IEEE , pp.1-6, 20-24 July 2008.

[135] C. Gherasim, J. Van den Keybus, J. Driesen, and R. Belmans, "DSP implementation of power measurements according to the IEEE trial-use standard 1459," IEEE Transactions on Instrumentation and Measurement, Vol. 53, No. 4, pp. 1086- 1092, Aug. 2004.

[136] I. Axente, J. N. Ganesh, M. Basu, M. F. Conlon, K. Gaughan, "A 12-kVA DSP-controlled laboratory prototype UPQC capable of mitigating unbalance in source voltage and load current," IEEE Transactions on Power Electronics, Vol. 25, No. 6, pp.1471-1479, June 2010.

[137] B. Vafakhah, J. Salmon, A. M. Knight, "A new space-vector PWM with optimal switching selection for multilevel coupled inductor inverters," IEEE Transactions on Industrial Electronics, Vol.57, No.7, pp. 2354-2364, July 2010.

[138] W. Shireen, M. S. Arefeen, D. Figoli, "Controlling multiple motors utilizing a single DSP controller," IEEE Transactions on Power Electronics, Vol. 18, No. 1, pp. 124- 130, Jan. 2003.

[139] V.K. Chinnaiyan, J. Jerome, J. Karpagam, S. Shiek Mohammed, "Design and implementation of high power DC-DC converter and speed control of DC motor using TMS320F240 DSP," India International Conference on Power Electronics IICPE 2006, pp. 388-392, 19-21 Dec. 2006.

[140] A. H. Niasar, H. Moghbeli, A. Vahedi, "Implementation of four-switch brushless dc motor drive based on TMS320lf2407 DSP," IEEE International Conference on Signal Processing and Communications (ICSPC 2007), pp. 332-335, 24-27 Nov. 2007.

[141] Texas Instrument: TLC7226CN Datasheet, January, 2003, www.ti.com.

[142] D. Dart, “DSP/BIOS Kernel Technical Overview,” Texas Instruments, Application Report, Document SPRA780, Aug.

[143] Texas Instruments: TMS320C2000TM Experimenter Kit Overview, August, 2009.

[144] The Mathworks, Inc.: Embedded IDE Link™ User’s Guide, Version 4.1, May, 2010, www.mathworks.com.

[145] M. Amin, A. Herrera, J. Seijo, and O. A. Mohammed, “A Digital signal controller for high frequency-based grid-tie inverter connected to wind emulator system: design and implementation,” IEEE/PES Power Systems Conference and Exposition (PSCE) 2011, pp.1-8, 20-23, Phoenix, March 2011.

[146] A. Girgis and F. M. Ham, “A new FFT-based digital frequency relay for load shedding,” IEEE Trans. on Power App. & Syst., Vol. PAS-101, No. 2, pp.433–439, Feb. 1982.

[147] M. S. Sachdev and M. M. Giray, “A least error squares technique for determining power system frequency,” IEEE Trans. Power App. & Syst., Vol. PAS-104, No. 2, pp. 437–443, Feb. 1985.

[148] S. Paul, S. K. Basu, and U. S. Hazra, “Novel frequency factor method for power system frequency measurement and estimation of load shedding,” IEE Proc. Inst. Elect. Eng., Gen., Transm., Distrib., Vol. 134, No. 6, pp. 389–395, Nov. 1987.

[149] H. Hrasnica, A. Haidine, and R. Lehnert, “Broadband powerline communications networks: Network Design” Wiley Books Pub. Co., 2004, Germany.

[150] A. R. Metke and R. L. Ekl., “Security technology for smart grid networks” IEEE Transactions on Smart Grid, Vol. 1, No. 1, pp. 99-107, June 2010.

[151] M. Pipattanasomporn, H. Feroze, and S. Rahman, “Multi-agent systems in a distributed smart grid: design and implementation,” IEEE PES 2009 Power Systems Conference and Exposition (PSCE’09), Seattle, USA.

[152] Z. Zhong, C. Xu, B. Billian, L. Zhang, S. Tsai, R. Conners, V. Centeno, and Y. Liu, “Power system frequency monitoring network (FNET) implementation,” IEEE Trans. on Power Syst., Vol. 20, No. 4, pp. 1914–1921, Nov. 2005.

[153] X. Liu, G. Liu, M. Sherwood, and V. Venk., “Wide-area monitoring and control algorithms for large power systems using synchrophasors,” Bulk Power System Dynamics and Control (iREP) - VIII (iREP) Symposium, pp.1-5, Aug. 2010.

[154] J. De La Ree, V. Centeno, J. S. Thorp, and A. G. Phadke, “Synchronized phasor measurement applications in power systems,” IEEE Transactions on Smart Grid, Vol. 1, No. 1, pp. 20-27, June 2010.

[155] A. Bose, "Smart transmission grid applications and their supporting infrastructure," IEEE Transactions on Smart Grid, Vol. 1, No. 1, pp. 11-19, June 2010.

[156] Y. Zhang and A. Bose, "Design of wide area damping controllers for interarea oscillations," IEEE Trans. on Power Syst., Vol. 23, No. 3, pp. 1136–1143, Aug. 2008.

[157] A. G. Phadke, D. Novosel, and S. H. Horowitz, "Wide area measurement applications in functionally integrated power systems," presented at the CIGRE B-5 Colloq., Madrid, Spain, 2007.

[158] R. F. Nuqui and A. G. Phadke, "Phasor measurement placement techniques for complete and incomplete observability," IEEE Trans. on Power Del., Vol. 20, No. 4, pp. 2381–2388, Oct. 2005.

[159] Mahmoud Amin and Osama Mohammed, "Wide area measurement system for smart grid applications involving hybrid energy sources," Springer Journal on Energy Systems, DOI: 10.1007/s12667-011-0047-4, Jan. 2012.

[160] J. Ning, W. Gao, G. Radman, and J. Liu, "The application of the groebner basis technique in power flow study," presented in North American Power Symposium (NAPS), pp.1-7, Oct. 2009.

[161] R. Malpani, Z. Abbas, and K. S. Swarup, "High precision frequency estimation using internet-based phasor measurement unit," IEEE Transactions on Power Systems, Vol. 25, No. 2, pp. 607-614, Oct. 2009.

[162] V.K. Sood, D. Fischer, M. Eklund, and T. Brown, "Developing a communication infrastructure for the smart grid," presented in Elect. Power & Energy Conf. (EPEC), pp. 1-7, Montreal, 2009.

[163] T. Sauter and M. Lobashov, "End-to-end communication architecture for smart grids," IEEE Trans. on Ind. Elec., Vol. 58, No. 4, pp. 1218–1228, April 2011.

[164] S. H. Horowitz and A. G. Phadke, "Boosting immunity to blackouts," IEEE Power Energy Mag., Vol. 1, No. 5, pp. 47–53, Oct. 2003.

[165] M. M. Amin, H. B. Moussa, and O. A. Mohammed, "Development of a wide area measurement system for smart grid applications," The 18th World Congress of the International Federation of Automatic Control (IFAC) Invited Session (Aug. 28-Sep.2, 2011) in Milano, Italy.

[166] A. Miyasaka, K. Akiyama, R. Kitano, and A. Yamashita, "Technical approaches to clean-energy power systems," NTT Technical Review, Vol. 4, No. 3, pp. 38-41, March 2006.

[167] K. Takao and T. Shinohe, "Demonstration of 25 W/cm3 class all-SiC three phase inverter," EPE 2011, pp.1-10, Aug. 30 2011-Sept. 1 2011.

[168] Y. Hayashi, K. Takao, T. Shimizu, and H. Ohashi, "Power loss design platform for high output power density converters," 2007 European Conference on Power Electronics and Applications, pp.1-10, 2-5 Sept. 2007.

[169] V. Pala, H. Peng, P. Wright, M. M. Hella, and T. P. Chow, "Integrated high-frequency power converters based on GaAs pHEMT: technology characterization and design examples," IEEE Transactions on Power Electronics, Vol. 27, No. 5, pp. 2644-2656, May 2012.

[170] H. Zhang, L. M. Tolbert, and B. Ozpineci, "Impact of sic devices on hybrid electric and plug-in hybrid electric vehicles," IEEE Transactions on Industry Applications, Vol. 47, No. 2, pp. 912-921, March/April 2011.

[171] J. Rabkowski, G. Tolstoy, D. Peftitsis, and H.-P. Nee, "Low-loss high-performance base-drive unit for SiC BJTs," IEEE Transactions on Power Electronics, Vol. 27, No. 5, pp. 2633-2643, May 2012.

[172] R. Withanage and N. Shammas, "Series connection of insulated gate bipolar transistors (IGBTs)," IEEE Transactions on Power Electronics, Vol. 27, No. 4, pp. 2204-2212, April 2012.

[173] H. Y. Long, N. L.-King, M. R. Sweet, and E. M. S. Narayanan, "Numerical evaluation of the short-circuit performance of 3.3-kV CIGBT in field-stop technology," IEEE Transactions on Power Electronics, Vol. 27, No. 5, pp. 2673-2679, May 2012.

[174] D. Cao and F. Z. Peng, "Multiphase multilevel modular dc–dc converter for high-current high-gain TEG application," IEEE Transactions on Industry Applications, Vol. 47, No. 3, pp. 1400-1408, May/June 2011.

[175] H.-P. Le, S. R. Sanders, and E. Alon, "Design techniques for fully integrated switched-capacitor dc-dc converters," IEEE Journal of Solid-State Circuits, Vol. 46, No. 9, pp. 2120-2131, Sep. 2011.

[176] M. B. Chaudhari, B. Puranik, and A. Agrawal, "Heat transfer characteristics of a heat sink in presence of a synthetic JET," IEEE Transactions on Components, Packaging and Manufacturing Technology, Vol. 2, No. 3, pp. 457-463, March 2012.

[177] Serri Lee, "Optimum design and selection of heat sinks," IEEE Transactions on Components, Packaging, and Manufacturing-Part A, Vol. 18, No. 4, pp. 812-817, December 1995.

[178] P. W. Sun, C. Liu, J.-S. Lai, and C.-L. Chen, “Cascade dual buck inverter with phase-shift control,” IEEE Transactions on Power Electronics, Vol. 27, No. 4, pp. 2067–2077, April 2012.

VITA

MAHMOUD AMIN

April 23, 1981	Born, Cairo, Egypt
1998-2003	B.Sc., Helwan University, Cairo, Egypt
2004-2007	Demonstrator, Helwan University, Cairo, Egypt
2007-2008	Assistant Researcher, Electronics Research Institute, Giza, Egypt
2004-2008	M.S., Helwan University, Cairo, Egypt
2008-2009	Research Assistant, Electronics Research Institute, Giza, Egypt
2009-2011	Research Assistant, Florida International University, Miami, Florida
2011-2012	Dissertation Year Fellowship, Florida International University, Miami, Florida

SELECTED PUBLICATIONS AND PRESENTATIONS

M. Amin and O. A. Mohammed, "Vector Oriented Control of Voltage Source PWM Inverter as A Dynamic VAR Compensator for WECS Connected to Utility Grid," 2010 Twenty-Fifth Annual IEEE Applied Power Electronics Conference and Exposition (APEC), pp.1640-1650, Palm springs, California, 21-25 Feb. 2010.

M. Amin and O. A. Mohammed, "Software Phase Locked Loop technique for Grid-Connected Wind Energy Conversion Systems," 2010 IEEE 12th Workshop on Control and Modeling for Power Electronics (COMPEL), pp.1-8, Boulder, m28-30 June 2010.

M. Amin, M. Elshaer, and O. A. Mohammed, "DC Bus Voltage Control for PV Sources in A DC Distribution System Infrastructure," 2010 IEEE Power and Energy Society General Meeting, pp.1-5, Minneapolis, 25-29 July 2010.

M. Amin and O. A. Mohammed, "DC-Bus Voltage Control of Three-Phase PWM Converters Connected to Wind Powered Induction Generator," 2010 IEEE Power and Energy Society General Meeting, pp.1-7, Minneapolis, 25-29 July 2010.

M. Amin and O. A. Mohammed, "Power Quality Improvement of Grid-Connected Wind Energy Conversion System for Optimum Utilization of Variable Speed Wind Turbines," 36th Annual Conference on IEEE IECON 2010, pp. 3287-3292, Phoenix, 7-10 Nov. 2010.

M. Amin and O. A. Mohammed, "Development of a Grid-Connected Wind Generation System Utilizing High Frequency- Semicontrolled Rectifier-Current Source Inverter," 2011 Twenty-Sixth Annual IEEE Applied Power Electronics Conference and Exposition (APEC), pp. 645-652, Fort Worth, 6-11 March 2011.

M. Amin, A. Herrera, J. Seijo, and O. A. Mohammed, "A Digital Signal Controller for High Frequency-Based Grid-Tie Inverter Connected to Wind Emulator System: Design and Implementation," IEEE/PES Power Systems Conference and Exposition (PSCE) 2011, pp.1-8, 20-23, Phoenix, March 2011.

M. Amin and O. A. Mohammed, "DC-Bus Voltage Control for Hybrid 4-Port High Frequency Parallel-Connected Sustainable Energy Conversion System," IEEE International Electric Machines and Drives Conference (IEMDC), pp. 89-94, Niagara Falls, May, 2011.

M. Amin and O. A. Mohammed, "Design and Implementation of DC-Bus System Module for Parallel Integrated Sustainable Energy Conversion Systems," The 2011 IEEE Power and Energy Society General Meeting (PES GM 2011), pp. 1-8, Detroit, 24-28 July, 2011.

M. Amin and O. A. Mohammed, "A Three-Phase High Frequency Semi-controlled Battery Charging Power Converter for Plug-in Hybrid Electric Vehicles," The third IEEE Energy Conversion Congress and Exposition (ECCE 2011) conference at Phoenix, pp. 2641 – 2648, 17-22 Sep. 2011.

M. Amin and O. A. Mohammed, "A Novel Grid-Connected Multi-Input Boost Converter for HEVs: Design and Implementation," This paper has been presented for the first IEEE International Electric Vehicle Conference (IEVC 2012) conference at Greenville, South Carolina 4-8 March 2012.

Mahmoud Amin and Osama Mohammed, "Development of High-Performance Grid-Connected Wind Energy Conversion System for Optimum Utilization of Variable Speed Wind Turbines," IEEE Transactions on Sustainable Energy, Vol. 2, No. 3, pp. 235-245, July 2011.

Mahmoud Amin and Osama Mohammed, "A Three-Phase High Frequency Semi-Controlled Battery Charging Power Converter for Plug-In Hybrid Electric Vehicles," Journal of Power Electronics, Vol. 11, No. 4, pp. 490-498, July 2011.

Mahmoud Amin and Osama Mohammed, "DC-Bus Voltage Control Technique for Parallel-Integrated Wind Energy Conversion Systems," IEEE Transactions on Energy Conversion, Vol. 26, No. 4, pp. 1140-1150, December 2011.

Mahmoud Amin and Osama Mohammed, "Wide Area Measurement System for Smart Grid Applications Involving Hybrid Energy Sources," Springer Journal on Energy Systems, DOI: 10.1007/s12667-011-0047-4, Jan. 2012.